Identity of Iron-Carbon Associations across a Permafrost Thaw Gradient and their Contribution to Greenhouse Gas Release

Dissertation

der Mathematisch-Naturwissenschaftlichen Fakultät

der Eberhard Karls Universität Tübingen

zur Erlangung des Grades eines

Doktors der Naturwissenschaften

(Dr. rer. nat.)

vorgelegt von

M.Sc. Eva Voggenreiter

aus Hildburghausen

Tübingen

2024

Gedruckt mit Genehmigung der Mathematisch-Naturwissenschaftlichen Fakultät der Eberhard Karls Universität Tübingen.

Tag der mündlichen Qualifikation: 22.10.2024
Dekan: Prof. Dr. Thilo Stehle
1. Berichterstatter/-in: Prof. Andreas Kappler
2. Berichterstatter/-in: Prof. Carsten Müller

II

I've got this music in my mind /

Saying it's gonna be alright

Swift et al. *1989*

Table of Contents

Summary

Permafrost soils store ca. one third of the global soil organic carbon (OC) stock. Increasing soil temperatures due to climate change are causing rapid thaw of permafrost soils, leading to waterlogging of previously dry soils and higher microbial activity. It is estimated that greenhouse gas (GHG) emissions will rise as a consequence, leading to higher release of carbon dioxide (CO_2) and methane (CH_4). However, accurate predictions of permafrost-derived GHG emissions are still not possible since they depend on the degradation of OC which is largely influenced by its bioavailability. In particular, the bioavailability of OC can be decreased by association with ferric iron (Fe(III)) (oxyhydr)oxides.

Organic carbon can both adsorb to and coprecipitate with poorly crystalline Fe(III) (oxyhydr)oxides, forming Fe(III)-OC associations. Under oxic conditions in permafrost soils, these associations are thought to protect the OC from degradation, thus limiting GHG release. In contrast, microbial reductive dissolution of Fe(III)-OC associations could take place under anoxic conditions in thawed permafrost soils, thereby releasing the previously bound OC again to the aqueous phase. However, it is not clear yet, (i) how the potentially Fe-bound OC quantity and its composition changes along the thaw gradient, (ii) what the effect of Fe(III)-OC associations on GHG emissions is during initial permafrost thaw, and (iii) how the presence of Fe(III)-OC associations in fully thawed permafrost soils impacts net CH_4 release.

To investigate these knowledge gaps, we employed a space-for-time approach, by taking representative soil samples across a permafrost thaw gradient at Stordalen Mire (Abisko, Sweden). This actively thawing permafrost peatland encompasses three different thaw stages: intact, oxic permafrost soils (palsa), seasonally anoxic, partly thawed soils (bog) and fully thawed, permanently anoxic soils (fen). We carried out various lab-based experiments using the sampled soils and complemented our findings by performing field-based experiments.

We found that the capacity of Fe(III) (oxyhydr)oxides to adsorb water-extractable OC diminished by more than 50% from palsa and bog (226 ± 3 and 204 ± 19 mg C g^{-1} ferrihydrite, respectively) to fen ecosystems (81 ± 4 mg C g^{-1} ferrihydrite). Abiotic coprecipitation of water-extractable OC from palsa and bog ecosystems with initially dissolved Fe(II) bound up to three times more OC than by adsorption. The resulting C:Fe ratios in the solid matched well with values based on previous extractions from soil samples, demonstrating that coprecipitation is likely the dominant formation mechanism of Fe(III)-OC associations in permafrost peatlands. Both adsorption and coprecipitation lead to preferential binding of OC, meaning that more aromatic, oxygen-rich and high molecular weight OC compounds were selectively bound. As a consequence, more aliphatic, low molecular weight compounds are disproportionally left in solution. Since these compounds are considered to be easier to degrade for microorganisms,

they might still be respired, contributing to CO_2 emissions. Therefore, Fe(III) mineral binding might provide less of an effective protection for OC in permafrost soils as previously thought.

Next, we tracked the fate of Fe(III)-OC associations during initial permafrost thaw by adding Fe(III)-OC coprecipitates to palsa and bog soils within a microcosm and field experiment. The coprecipitates were synthesized using water-extractable OC from the same sites. In the microcosm experiment, we simulated the initial collapse and development of anoxic conditions in palsa soils and the anoxic phase of water table fluctuations in bog soils. We found that Fe(III)-OC coprecipitates were fully reduced within several weeks. This led to an increase of CO_2 emissions by 43±16% compared to a no-coprecipitate amended control, showcasing that reduction of Fe(III)-OC coprecipitates makes up a large fraction of anaerobic respiration in thawing permafrost soils. Several microorganisms capable of degrading complex OC (*Sphingomonas*, *Firmicutes*) were enriched in coprecipitate-amended reactors compared to the no-coprecipitate controls, likely because they were stimulated by the release of previously Fe-bound OC. In bog soils, Fe(III)-OC coprecipitates were also fully reduced, albeit slower than in palsa soils. Net emissions of CO_2 did not change after coprecipitate addition, hinting at a counter-acting effect to anaerobic respiration. We speculate that the release of previously Fe-bound phenolic-rich OC, which could have anti-microbial properties, could be the reason for this observation. The findings of the field-based experiment complemented our microcosm experiment, in the sense that Fe(III)-OC coprecipitates are stable under oxic conditions in intact palsa soils, but reductively dissolved once conditions turn anoxic in bog soils. In conclusion, our results demonstrate that Fe(III)-OC associations are no stable sink for OC during thaw-induced waterlogging of permafrost peatlands.

Finally, we added Fe(III)-OC coprecipitates to fully thawed permafrost soils in order to test the effect on net CH_4 emissions. Using a combination of laboratory microcosm and *in situ* experiments, we found that Fe(III)-OC coprecipitates were partly (22% in microcosm experiment) to almost fully reduced (92±4.0% in field experiment) over weekly timescales. This ongoing Fe(III) reduction decreased net CH_4 emissions by at least 40% in comparison to a no-coprecipitate control. A majority of the inhibition of CH_4 emissions was attributable to methanogenesis suppression due to thermodynamic favorability of Fe(III) reduction, as detected by a decrease in the copy numbers of a methanogenesis marker gene in the coprecipitate-added treatment compared to the no-coprecipitate control. A minor portion of the decrease in net CH_4 release could also stem from anaerobic methane oxidation. We detected an intermediate increase in copy numbers of a methanotrophic marker gene and an increasing abundance of a genus belonging to the putatively anaerobic methane-oxidizing taxa *Methylomirabilales*. The added coprecipitates might have been used as electron acceptors for anaerobic methane oxidizers. Overall, the findings show that Fe(III)-OC associations might

play a crucial role in mitigating CH_4 release in thawing, anoxic permafrost peatlands, despite the release of additional OC.

Within this work, we expanded the knowledge of Fe(III)-OC associations in permafrost peatlands from the characterization of field samples and correlations of geochemical parameters to a process-based understanding of the future fate of Fe(III)-OC associations during permafrost thaw. The results of this thesis thereby help to assess future feedbacks of permafrost thaw to GHG emissions induced by Fe mineral reduction, and could be used to improve climate models simulating permafrost thaw.

Zusammenfassung

Ein Drittel des weltweiten Bestandes an organischem Kohlenstoff (OC) in Böden befindet sich in Permafrostböden. Die steigenden Bodentemperaturen aufgrund des Klimawandels führen zu einem raschen Auftauen von Permafrostböden, was zu einer Staunässe von zuvor trockenen Böden und einer erhöhten mikrobiellen Aktivität führt. Man geht davon aus, dass die Emissionen von Treibhausgasen ansteigen und somit mehr Kohlendioxid (CO_2) und Methan (CH_4) von Permafrostböden freigesetzt wird. Genaue Vorhersagen über die von Permafrostböden verursachten Treibhausgasemissionen sind jedoch noch nicht möglich, da der Abbau von OC weitgehend von der Bioverfügbarkeit des OC abhängt, die durch die Assoziation mit Eisen(III)-(oxyhydr)oxiden (Fe(III)-(oxyhydr)oxiden) verringert werden kann.

Organischer Kohlenstoff kann sowohl an wenig kristalline Fe(III)-(oxyhydr)oxide adsorbieren als auch mit ihnen kopräzipitieren und so Fe(III)-OC Verbindungen bilden. Es wird angenommen, dass diese Verbindungen unter oxischen Bedingungen in Permafrostböden den OC vor dem Abbau schützen und damit die Freisetzung von Treibhausgasen begrenzen. Im Gegensatz dazu könnte unter anoxischen Bedingungen in aufgetauten Permafrostböden eine mikrobielle reduktive Auflösung von Fe(III)-OC Verbindungen stattfinden, wodurch das zuvor gebundene OC wieder in die wässrige Phase freigesetzt wird. Es ist jedoch noch nicht klar, (i) wie sich die potenziell Fe-gebundene OC-Menge und ihre Zusammensetzung entlang eines Permafrosttau-Gradienten verändert, (ii) welche Auswirkungen Fe(III)-OC Verbindungen auf die Treibhausgasemissionen während des anfänglichen Auftauens des Permafrostes haben und (iii) wie sich das Vorhandensein von Fe(III)-OC Verbindungen in vollständig aufgetauten Permafrostböden auf die Freisetzung von CH_4 auswirkt.

Um diese Wissenslücken zu untersuchen, haben wir repräsentative Bodenproben über einen Permafrosttau-Gradienten in Stordalen Mire (Abisko, Schweden) genommen. Dieses aktiv auftauende Permafrostgebiet umfasst drei verschiedene Taustadien: intakte, oxische Permafrostböden (Palsa), saisonal anoxische, teilweise aufgetaute Hochmoore (Bog) und vollständig aufgetaute, permanent anoxische Niedermoore (Fen). Wir haben verschiedene Experimente mit den beprobten Böden im Labor durchgeführt und diese mit Experimenten im Feld ergänzt.

Wir fanden heraus, dass die Kapazität von Fe(III)-(oxyhydr)oxiden zur Adsorption von wasserextrahierbarem OC um mehr als 50% von Palsa und Bog (226±3 bzw. 204±19 mg C g^{-1} Ferrihydrit) zu Fen (81±4 mg C g^{-1} Ferrihydrit) abnimmt. Durch die abiotische Kopräzipitation von wasserlöslichem OC aus Palsa- und Bog-Böden mit ursprünglich gelöstem Fe(II) wurde bis zu dreimal mehr OC gebunden als durch Adsorption. Die resultierenden C:Fe Verhältnisse in den Partikeln stimmten gut mit Werten überein, die auf früheren Extraktionen aus

Bodenproben beruhen. Dies zeigt, dass die Kopräzipitation wahrscheinlich der vorherrschende Bildungsmechanismus von Fe(III)-OC Verbindungen in Permafrostgebieten ist. Sowohl Adsorption als auch Kopräzipitation führen zu einer bevorzugten Bindung von OC, was bedeutet, dass mehr aromatische, sauerstoffreiche und hochmolekulare OC Verbindungen selektiv gebunden wurden. Infolgedessen blieben mehr aliphatische Verbindungen mit niedrigem Molekulargewicht unverhältnismäßig stark in Lösung. Da man davon ausgeht, dass diese Verbindungen für Mikroorganismen leichter abbaubar sind, könnten sie dennoch zu den CO_2 Emissionen beitragen. Daher könnte die Bindung von Fe(III) Mineralen einen weniger wirksamen Schutz für OC in Permafrostböden bieten als bisher angenommen.

Als Nächstes untersuchten wir das Schicksal von Fe(III)-OC Verbindungen während des Auftauens von Permafrostböden, indem wir Fe(III)-OC Kopräzipitate zu Palsa- und Bog-Böden innerhalb Mikrokosmos- und Feld-Experimenten hinzugaben. Die Kopräzipitate wurden mit wasserextrahierbarem OC von denselben Böden synthetisiert. In dem Mikrokosmos-Experiment simulierten wir den anfänglichen Zusammenbruch und die Entwicklung anoxischer Bedingungen in Palsa-Böden sowie die anoxische Phase von Wasserspiegelschwankungen in Bog-Böden. Wir. Wir stellten fest, dass Fe(III)-OC Kopräzipitate innerhalb mehrerer Wochen vollständig reduziert wurden. Dies führte zu einem Anstieg der CO_2 Emissionen um 43±16% im Vergleich zu einer Kontrolle ohne Kopräzipitate. Dieses Resultat zeigt, dass die Reduktion von Fe(III)-OC Kopräzipitaten einen großen Teil der anaeroben Atmung in auftauenden Permafrostböden ausmacht. Mehrere Mikroorganismen, die in der Lage sind, komplexe OC Verbindungen abzubauen (*Sphingomonas*, *Firmicutes*) hatten eine höhere Abundanz in den mit Kopräzipitaten angereicherten Reaktoren im Vergleich zu den Kontrollen ohne Kopräzipitate. Diese Mikroorganismsen haben wahrscheinlich den von Fe-freigesetzten OC für ihren Metabolismus genutzt. In Bog-Böden wurden Fe(III)-OC Kopräzipitate ebenfalls vollständig abgebaut, wenn auch langsamer als in Palsa-Böden. Die Freisetzung von CO_2 änderte sich nach der Zugabe von Kopräzipitaten nicht, was auf einen der anaeroben Atmung entgegenwirkenden Effekt hindeutet. Wir vermuten, dass die Freisetzung von zuvor Fe-gebundenem phenolreichem OC, das antimikrobielle Eigenschaften haben könnte, womöglich der Grund für diese Beobachtung ist. Die Ergebnisse des Feld-Experimentes waren ähnlich zu denen des Mikrokosmos-Experimentes, in dem Sinne, dass die Fe(III)-OC Kopräzipitate unter oxischen Bedingungen in Palsa-Böden stabil waren, aber in anoxischen Bog-Böden reduktiv aufgelöst wurden. Zusammenfassend zeigen unsere Resultate, dass Fe(III)-OC Verbindungen keine stabile Senke für OC während der auftauungsbedingten Staunässe von Permafrostböden darstellen.

Letztendlich haben wir Fe(III)-OC Kopräzipitate zu vollständig aufgetauten Permafrostböden gegeben, um die Auswirkungen auf die Freisetzung von CH_4 zu testen. Mit einer Kombination aus Mikrokosmos-Experimenten und einem Experiment vor Ort im Feld fanden wir heraus, dass Fe(III)-OC Kopräzipitate teilweise (22 % im Mikrokosmos-Experiment) bis fast vollständig (92±4.0 % im Feldexperiment) über einen Zeitraum von mehreren Wochen reduziert wurden. Diese kontinuierliche Fe(III)-Reduktion verringerte die Freisetzung von CH_4 um mindestens 40% im Vergleich zu einer Kontrolle ohne Kopräzipitate. Der größte Teil der Hemmung der CH_4 Emissionen war auf die Unterdrückung der Methanogenese wegen der thermodynamisch günstigeren Fe(III)-Reduktion zurückzuführen, was durch eine Abnahme der Anzahl der Genkopien eines Methanogenese-Markergens zu sehen war. Ein geringerer Teil der Verringerung der CH_4 Freisetzung könnte auch auf die anaeroben Methanoxidation zurückzuführen sein. Wir stellten einen zwischenzeitlichen Anstieg der Anzahl der Genkopien eines methanotrophen Markergens und eine zunehmende Abundanz einer Gattung fest, die zu dem vermutlich anaeroben methanoxidierenden Taxa *Methylomirabilales* gehört. Die zugesetzten Kopräzipitate könnten als Elektronenakzeptoren für anaerobe Methanoxidierer verwendet worden sein. Insgesamt zeigen die Ergebnisse, dass könnten Fe(III)-OC Verbindungen eine entscheidende Rolle bei der Abschwächung der CH_4 Freisetzung in auftauenden, anoxischen Permafrostgebieten spielen, trotz der Freisetzung von zusätzlichem OC von den Kopräzipitaten.

Im Rahmen dieser Arbeit haben wir das Wissen über Fe(III)-OC Verbindungen in Permafrostgebieten von der Charakterisierung von Feldproben und Korrelationen geochemischer Parameter zu einem prozessbasierten Verständnis des zukünftigen Schicksals während des Auftauens von Permafrostböden erweitert. Die Ergebnisse dieser Arbeit helfen dabei, zukünftige Rückkopplungen des Permafrosttauens auf Treibhausgasemissionen durch die Auflösung von Fe(III)-OC Verbindungen abzuschätzen, und könnten somit zur Verbesserung von Klimamodellen verwendet werden, die das Permafrosttauen simulieren.

Chapter 1: Introduction

Permafrost soils during climate change – a vast organic carbon sink under threat

Permafrost soils represent globally significant organic carbon (OC) stocks which store twice as much carbon (1300±200 Pg C) as in the atmosphere[1]. They accumulated OC over thousands of years[2] and are mostly present in the circum-Arctic region, with OC stocks of up to 260 kg m^{-2} in the upper 3 m (

Figure **1**)[2]. Permafrost soils are generally defined as frozen ground that maintains temperatures at or below 0°C for at least two consecutive years[3,4]. These conditions favor the storage of OC since the microbial degradation of OC is slowed down at low temperatures and is near-zero under frozen conditions[5]. Besides the low temperatures, the vegetation cover and methanotrophic microbial communities in oxic soil layers also contribute to the C sink function by decreasing the net emission of greenhouse gases (GHGs)[6–8]. Plants perform photosynthesis, capturing carbon dioxide (CO_2) and storing it as OC and methanotrophic microorganisms oxidize methane (CH_4) to CO_2[7,9]. Since CH_4 has a 28 times higher global warming potential over 100 years compared to CO_2[10], the microbial oxidation of CH_4 thereby decreases the global warming potential of net GHG emissions.

Arctic regions are warming at a rate two to four times higher than the global average due to ongoing climate change[11,12]. The resulting higher air temperatures are causing soil warming, leading to the deepening of the active layer, which is the upper soil layer that annually thaws and refreezes[3]. Thawing causes not only previously frozen, high-OC, nutrient-rich soil layers to become available for microbial decomposition[13,14], but also increases the rate of microbial degradation due to higher temperatures[4,15]. Permafrost thaw therefore leads to a higher OC release, both by emission of GHGs[14,16] and by export of dissolved or solid OC into other riverine systems[17,18]. It has been projected that 67-237 Pg OC will be released as GHGs due to thawing of permafrost soils until the year 2100[19]. A substantial part of the radiative forcing is expected to come from CH_4 emissions in the future due to the increasing anoxic soil layers in the permafrost landscape[20]. These emissions therefore contribute to the so-called permafrost-carbon feedback. This process describes how the release of permafrost-derived GHGs has a positive feedback on climate warming, leading to even greater permafrost thaw and more decomposition of OC, thereby closing the cycle[2]. While these general trends are agreed upon within the scientific community, major uncertainties exist about the range and timing of GHG emissions from thawing permafrost soils[19,21].
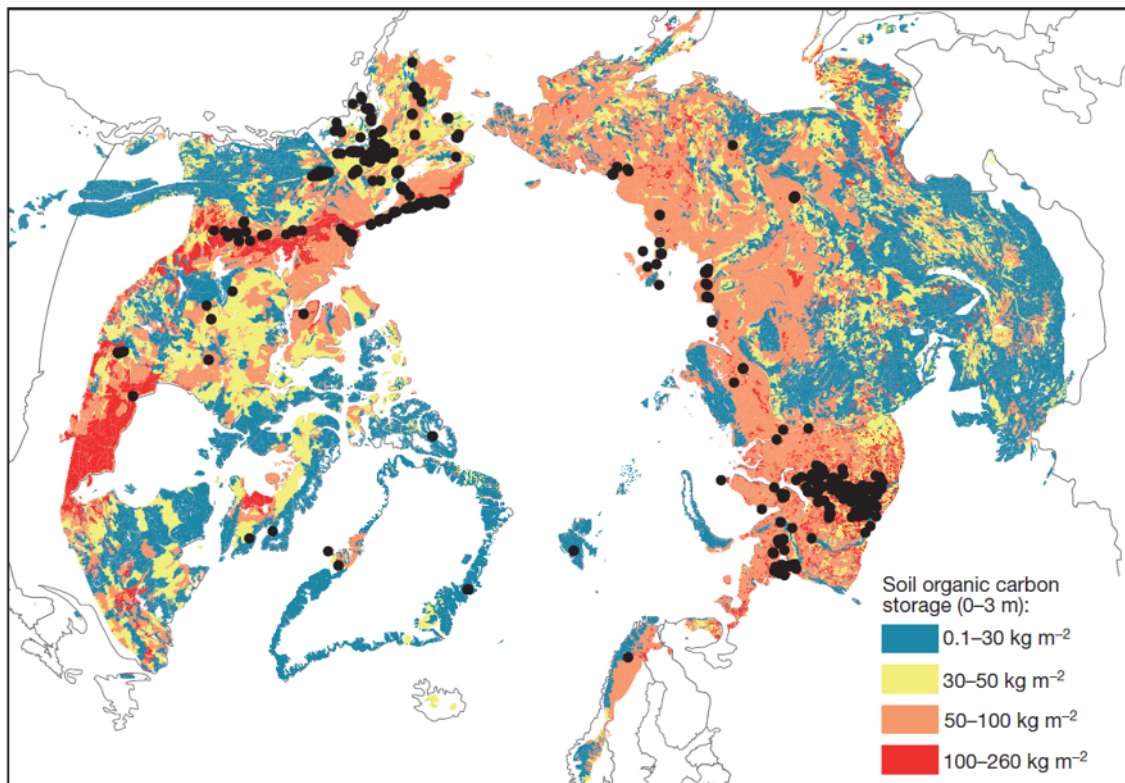
Figure 1. Distribution of soil OC pool (kg C m^{-2}) in the upper 3 m of permafrost soils in the circum-Arctic region. Different colors denote the range of soil OC stocks (blue: 0.1-30, yellow: 30-50, orange: 50-100, red: 100-260 kg C m^{-2}) and black dots indicate locations of soil measurements. The figure is taken from Schuur et al. (2015)[2].

The high uncertainty of released GHGs from permafrost soils is particularly due to the complex biogeochemical shifts of permafrost areas during climate change: Precipitation shifts, changes to hydrological conditions induced by abrupt thaw and thermokarst formation or draining of thaw lakes, vegetation changes to more productive plant species, and wildfires all shape future GHG release[19,21–23]. Most of these factors are poorly understood and not yet implemented in earth system models due to insufficient spatial and temporal datasets[24]. One of the core knowledge gaps is the change in bioavailability of OC within the continuum of these changing conditions (e.g. from oxic to anoxic soil conditions during abrupt thaw). The factors influencing bioavailability of OC are not only its chemical properties but also its association with mineral surfaces, which have been known to decrease microbial degradation[25–27].

Mineral-bound organic carbon in permafrost soils

Mineral-bound OC is generally more difficult to degrade for microorganisms because the binding energy of the mineral is stronger than the affinity to the active site of exoenzymes[28].

Therefore, the presence of mineral-OC associations is an important control on degradation of OC during permafrost thaw. Mineral-OC associations limit the bioavailability of OC, thus decreasing the resulting GHG emissions[29,30]. As a consequence, they decrease the temperature sensitivity of OC degradation[31,32], meaning that less OC is degraded per increase in soil temperature.

Mineral-OC associations can make up a substantial fraction of the total soil OC in permafrost soils (33-74%)[29,33–35]. These estimates vary due to different parent material of the soil[33], the climatic and redox conditions across soil development stages[29] as well as the mass ratio of soil OC to available minerals[35]. Binding can occur directly or indirectly (via cation bridges) to phyllosilicates and metal (oxyhydr)oxides, such as aluminum or iron (Fe)[36]. Poorly crystalline Fe(III) (oxyhydr)oxides (e.g. ferrihydrite) are especially known for their large OC binding capacity[37], due to their high specific surface area[38]. Those minerals typically make up the majority of Fe(III) phases in OC-rich environments, such as peatlands[39,40], since high OC concentrations hinder their transformation to more crystalline minerals[41,42]. Poorly crystalline Fe(III) have been known as an OC sink in many environmental settings[43–45], but only recently has more attention been given to Fe(III)-OC associations in permafrost soils within the context of permafrost thaw[29,30,34,46–48]. It has even been advocated that the presence of Fe(III)-OC associations should be included in future climate models simulating thaw[49], due to their multifaceted role in the C cycle.

Interactions between iron and organic carbon influence the carbon cycle in permafrost environments

Associations between Fe(III) and OC are mostly found in oxic soil layers or at oxic-anoxic transitions of permafrost soils[46,48]. Current estimates are that ca. 10-20% of soil OC in intact, oxic permafrost soils is bound to Fe(III) minerals[34,46,50,51]. Iron(III)-OC associations can be formed abiotically through adsorption of OC onto an existing Fe(III) (oxyhydr)oxide or by coprecipitation of initially dissolved Fe(II) and OC by oxygen (O_2) at redox interfaces[36] (Figure 2). Microorganisms capable of Fe(II) oxidation, such as microaerophilic, nitrate-reducing, or phototrophic Fe(II) oxidizers, can also initiate coprecipitation[52–54]. During the binding process, it has been found that certain OC functional groups have a higher tendency to be bound to Fe(III) (oxyhydr)oxides than others[37,55]. Depending on the initial OC composition, aromatic-, carboxylic-rich, and high molecular weight OC could be preferentially adsorbed or coprecipitated with Fe[37,56,57]. Consequently, OC classes which are rich in those components are likely preferentially bound in comparison to other classes which have a higher probability of remaining in solution. Binding of OC to Fe(III) (oxyhydr)oxides therefore leads to preferential

stabilization of OC, which could affect the bioavailability of the remaining dissolved OC pool[58] and thus emission of GHGs. However, this process has not yet been studied in permafrost peatlands and consequences for OC cycling across permafrost thaw are therefore unclear.
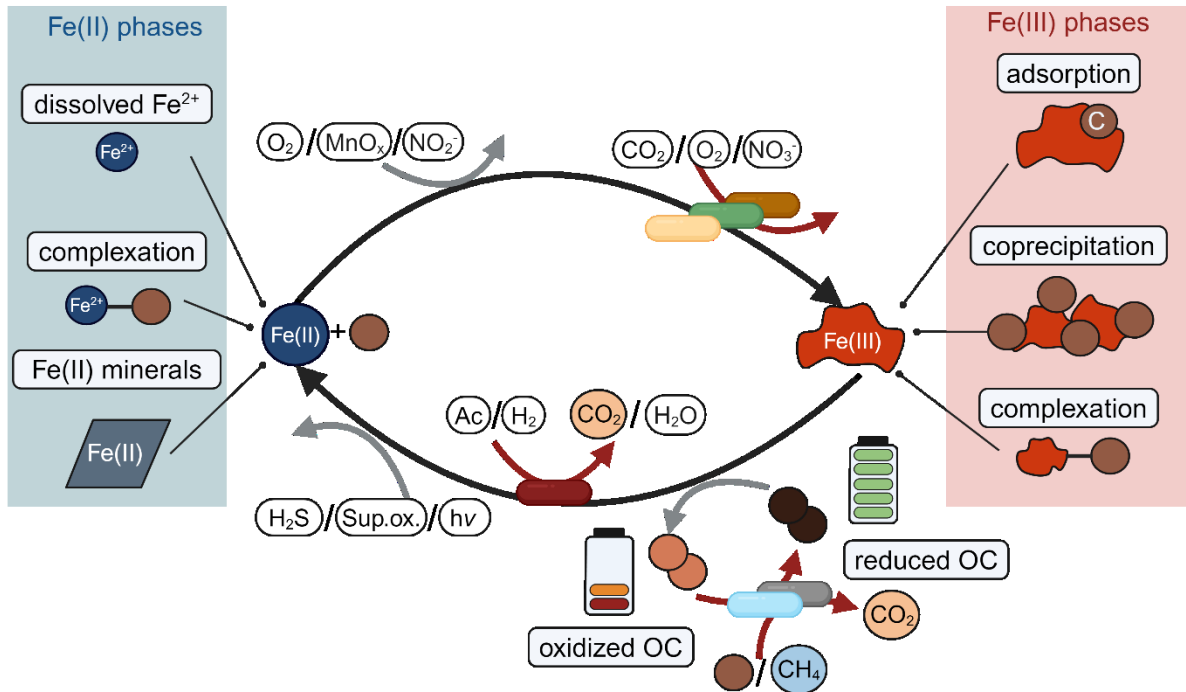

Figure 2. Schematic displaying relevant processes for coupled Fe-C cycling in permafrost soils. Blue and red boxes to the left and right show the binding environment of the two redox states of Fe: ferrous (Fe(II)) and ferric Fe (Fe(III)). Fe(II) can be present as dissolved Fe^{2+}, Fe(II)-OC complexes, and Fe(II) minerals (e.g. FeS). Fe(III) is typically present as poorly crystalline Fe(III) minerals, either with adsorbed or coprecipitated OC, or as poorly soluble Fe(III)-OC complexes. Fe(III) reduction and Fe(II) oxidation can be mediated by biotic (red arrows) and abiotic (grey arrows) processes. Reduction of Fe(III) can be abiotically facilitated by photoreduction (hv), hydrogen sulfide (H_2S), or superoxide (sup.ox.). Microbially-induced Fe(III) reduction can occur by oxidation of small OC molecules e.g. acetate (Ac) or by hydrogen (H_2) to CO_2 and water (H_2O), respectively. Microorganisms can also oxidize OC or CH_4 to CO_2, using oxidized OC as a terminal electron acceptor. The reduced OC then transfers electrons to Fe(III), functioning as an electron shuttle. The resulting Fe(II) phases can be oxidized to Fe(III) abiotically via oxygen (O_2), oxidized manganese species (MnO_x), or nitrite (NO_2^-). Microbial Fe(II) oxidation can be performed by phototrophic (using energy from light (hv) and C from CO_2), microaerophilic (with O_2), and nitrate (NO_3^-)-reducing Fe(II) oxidizers. Processes were summarized based on Kappler et al. (2021)[59] and Dong et al. (2023)[41]. The figure is made with BioRender.com.

During permafrost thaw, thawing of permafrost ice can lead to soil subsidence, causing waterlogging and anoxic conditions to develop. Under these conditions in subsequent permafrost thaw stages, Fe(III)-OC associations could be microbially reduced and dissolved, forming Fe(II) phases and dissolved OC. The release of OC under anoxic conditions will likely make it more bioavailable (in terms of CO_2 emissions) compared its Fe-bound state under oxic conditions[60,61]. Reduction of Fe(III)-OC associations could occur both abiotically and microbially in permafrost soils. Abiotic Fe(III) reduction is facilitated by hydrogen sulfide, superoxide species or reduced OC[59,62] (Figure 2). Microbial reduction of Fe(III)-OC associations could be performed by respiratory or fermentative Fe(III)-reducing microorganisms coupled to the oxidation of OC[41], ultimately producing CO_2. The activity of several other microorganisms can also lead to Fe(III) reduction as a side reaction due to electron shuttling by OC[63]. When OC or CH_4 is oxidized by microorganisms, the electrons may get stored in redox-active OC functional groups, such as phenol or hydroquinone groups[64,65], which are thereby reduced[41]. The reduced OC can now transfer electrons to Fe(III), after which the OC is present in its initial oxidized state, thus acting as an electron shuttle. Both dissolved organic matter[66,67] and particulate organic matter[62] have been shown to be involved in electron transfer reactions. Overall, reduction of Fe(III)-OC associations could occur in thawed, anoxic permafrost soils, enhancing OC oxidation and thus possibly increasing CO_2 emissions following permafrost thaw. However, the direct contribution of Fe(III)-OC associations to CO_2 emissions following permafrost thaw has not yet been quantified.

Reduction of Fe(III)-OC associations might also affect CH_4 emissions in future thawed permafrost peatlands. Previous field-based studies in wetlands or permafrost soils showed inhibition of methanogenesis due to Fe(III) reduction since Fe(III) is the more thermodynamically favorable electron acceptor compared to CO_2[68–70]. Net release of CH_4 might also be decreased due to Fe(III) functioning as an electron acceptor for anaerobic methane oxidation[71,72]. In contrast, Fe(III) reduction was also shown to enhance methanogenesis in some cases. Reduction of Fe(III) could promote methanogenesis due to the subsequent pH increase, which makes conditions more favorable for (acetoclastic) methanogens[73,74]. Some studies also showed that more crystalline Fe(III) minerals may act as electron shuttles for methanogens[75,76]. Another previously overlooked factor is the release of Fe-bound OC during reduction of Fe(III)-OC associations. The additional OC could enhance methanogenesis by increasing the activity of fermenting microorganisms, which provide substrates for methanogens[77]. The resulting net effect of Fe(III)-OC associations to GHG emissions across permafrost thaw is therefore unclear, making it necessary to comprehensively study this phenomenon across natural permafrost thaw gradients.

Stordalen Mire – using a space for time approach

Stordalen Mire is a peatland complex, 12 km east of Abisko (Sweden) at the edge of the discontinuous permafrost zone[78]. It is very heterogeneous in its landscape, consisting of hummock features underlain by permafrost (palsa), ombrotrophic *Sphagnum*-dominated bogs with a seasonally fluctuating active layer, and minerotrophic, permafrost-free fens (Figure 3). Average annual temperatures in the region have risen above 0°C since the year 2000[79], thereby inducing permafrost thaw. Parts of the intact, oxic permafrost palsa areas developed into partly anoxic bog and permanently anoxic fen areas[6,78], thus providing a natural permafrost thaw gradient. These changes have been well-monitored by continuous measurements of precipitation, air and soil temperatures, as well as active layer depth for over 60 years[79], and were eventually supplemented with the measurement of ecosystem-scale GHG fluxes[80,81]. The site therefore has several advantages to study permafrost thaw: First, it encompasses several stages of thaw (from palsa to bog to fen) that transition from one to the other within 15 ha[80]. By taking representative soil, water, and gas samples along this spatial gradient, we can therefore predict biogeochemical conditions of thawed permafrost soils in the future, thereby applying a space-for-time approach. Second, the wealth of context data in form of hydrological data, vegetation cover as well as organic matter and microbial community composition help to interpret the newly generated results. Several land-mark studies have been conducted at Stordalen Mire, including multi-omic approaches to study the diversity of methanogenic microorganisms[82,83], microbial organic matter degradation[84,85] as well as the initial characterization of Fe(III)-OC associations[46,86] across permafrost thaw. It therefore provides a suitable study site to investigate the role of Fe(III)-OC associations for potential OC binding and GHG release following thaw.

12

Figure 3. Photograph of Stordalen Mire, displaying the three permafrost thaw stages delineated by coloured lines: palsa (orange), bog (green), fen (blue). The white arrow follows the spatial gradient along permafrost thaw. The picture was taken in September 2022.

Knowledge gaps of iron-induced organic carbon cycling in thawing permafrost soils

Previous studies have characterized Fe(III)-OC associations across different permafrost thaw stages using field-based measurements and soil extractions[34,35,46,48]. These results offer snapshots of the current bound OC quantity and composition within Fe(III)-OC associations at the time of sampling as a net result of all biogeochemical processes in the soil. However, it is unknown what the Fe-bound OC quantity and composition is at the time of formation of Fe(III)-OC associations in each thaw stage. Since the OC composition shifts across the thaw gradient (e.g. from more aromatic compounds in bog to more lipid-like and lignin-like compounds in fen[87]), the OC functional groups able to interact with Fe(III) (oxyhydr)oxides also change. This could have effects on the bound OC quantity and preferential binding of OC to Fe(III) (oxyhydr)oxides which has implications for the bioavailability of the remaining dissolved OC pool. It is thus necessary to systematically investigate the potential binding capacity and preferential binding patterns of Fe(III) (oxyhydr)oxides across permafrost thaw (Figure 4). This knowledge will allow us to understand which OC compounds are potentially immobilized in permafrost soils. We will also gain understanding of the composition of OC compounds which will likely be released due to Fe(III) reduction in subsequent anoxic thaw stages.

There is field-based evidence that reductive dissolution of Fe(III)-OC associations and the following release of previously bound OC leads to an increase in GHG emissions across permafrost thaw[86]. Further, substantial parts of anaerobic respiration (40-63%) have been attributed to Fe(III) reduction in intact permafrost peatlands in Alaska[88]. Recent metagenomic studies also highlighted the increase in abundance of Fe-metabolizing microorganisms after permafrost thaw[89,90]. All these indicators point towards the importance of Fe-induced OC cycling during thaw, but the quantitative contributions to GHG emissions are not well understood (Figure 4). It is unknown to which degree Fe(III)-OC associations will be reduced under anoxic conditions and how the reduction will affect GHG emissions. Specifically, the contribution of Fe(III)-OC associations to CO_2 emissions during initial permafrost thaw is not clear.

In fully thawed, permanently anoxic permafrost soils, the majority of radiative forcing due to GHG emissions stems from CH_4[20]. It is currently not known how Fe(III)-OC associations affect net CH_4 release in anoxic permafrost soil. Previous evidence of the influence of Fe(III) on methanogenesis in peatland soils is based on the addition of Fe(III) as pure OC-free Fe(III) minerals[68,70], thus neglecting the influence that Fe-bound OC might have on CH_4 emissions. It is therefore unknown what role Fe(III)-OC associations could play for net CH_4 release in fully thawed permafrost soil (Figure 4).
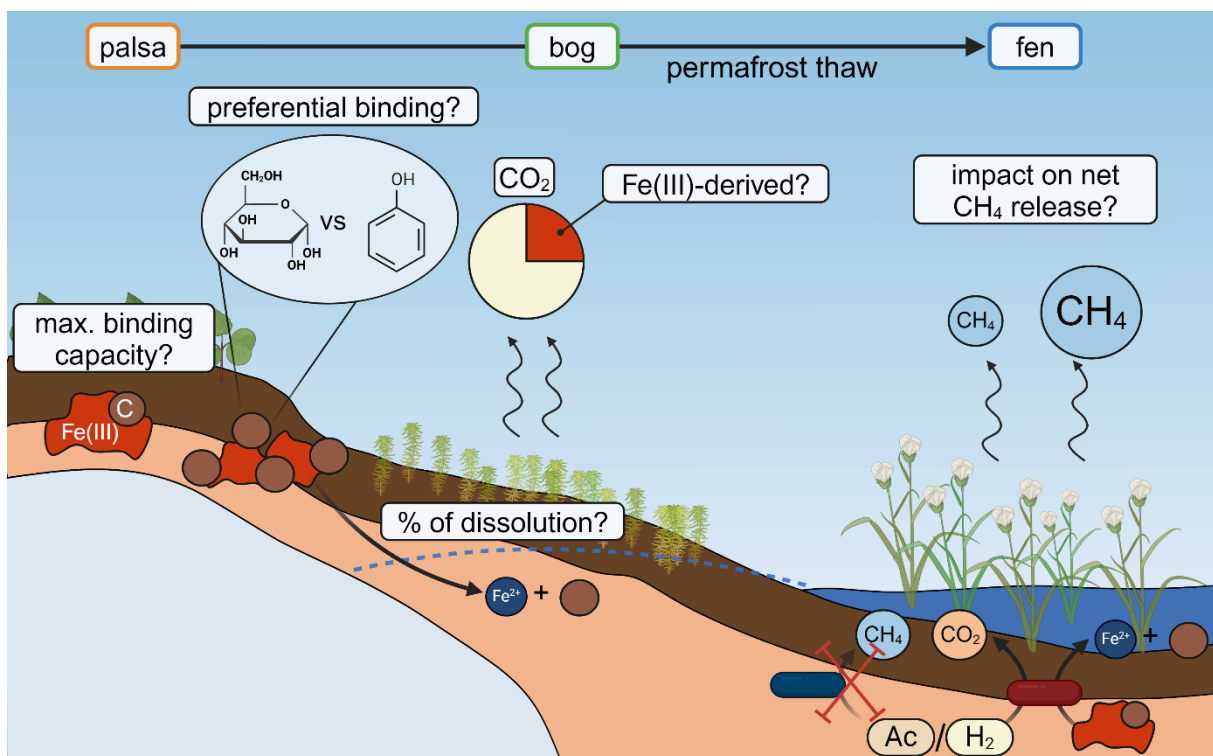
Figure 4. Schematic of knowledge gaps associated with Fe-OC cycling across permafrost thaw from palsa to bog and fen areas. Boxes with question marks display the knowledge gaps described in the section above. Abbreviations stand for: Fe(III): ferric iron, C: carbon, Fe^{2+}: ferrous iron, Ac: acetate, H_2: hydrogen, CH_4: methane, CO_2: carbon dioxide. Graphic is made with BioRender.com.

Objectives of this PhD work

Based on the outlined knowledge gaps, the objectives within this PhD work are the following:

(i)   Simulate the formation of Fe(III)-OC associations by adsorption and coprecipitation processes over a permafrost thaw gradient (**Chapter 2**), thereby

   a. Determining the maximum binding capacity of permafrost soil-derived OC from different thaw stages to Fe(III) (oxyhydr)oxides,

   b. Identifying the speciation of Fe in the formed Fe-OC associations, and

   c. Determining the OC compounds that are preferentially bound and assessing potential changes to the bioavailability of the remaining dissolved OC pool.

(ii)   Assess the fate of Fe(III)-OC associations across initial permafrost thaw, simulating abrupt permafrost thaw of palsa areas and seasonal waterlogging of bog areas (**Chapter 3**), including

   a. Determining the reduction extent of Fe(III)-OC associations after development of anoxic conditions,

   b. Quantifying the changes in GHG emissions due to reduction of Fe(III)-OC associations, and

   c. Identifying the changes in microbial community composition induced by reduction of Fe(III)-OC associations.

(iii)   Determine the role of Fe(III)-OC association for CH_4 release in fully thawed permafrost soils (**Chapter 4**), thereby

   a. Determining the reduction extent of Fe(III)-OC associations,

   b. Quantifying the net effect of Fe(III)-OC associations on CH_4 emissions and identifying the relevant processes affecting net CH_4 release, and

   c. Identifying the main microbial groups relevant to CH_4 cycling and how they are affected by addition of Fe(III)-OC associations.

References

1. Hugelius, G., Strauss, J., Zubrzycki, S., Harden, J. W., Schuur, E. A. G., Ping, C.-L., Schirrmeister, L., Grosse, G., Michaelson, G. J., Koven, C. D., O'Donnell, J. A., Elberling, B., Mishra, U., Camill, P., Yu, Z., Palmtag, J., & Kuhry, P. (2014). Estimated stocks of circumpolar permafrost carbon with quantified uncertainty ranges and identified data gaps. *Biogeosciences*, *11*(23), 6573–6593. https://doi.org/10.5194/bg-11-6573-2014

2. Schuur, E. A. G., McGuire, A. D., Schädel, C., Grosse, G., Harden, J. W., Hayes, D. J., Hugelius, G., Koven, C. D., Kuhry, P., Lawrence, D. M., Natali, S. M., Olefeldt, D., Romanovsky, V. E., Schaefer, K., Turetsky, M. R., Treat, C. C., & Vonk, J. E. (2015). Climate change and the permafrost carbon feedback. *Nature*, *520*(7546), 171–179. https://doi.org/10.1038/nature14338

3. Harris, S. A., French, H. M., Heginbottom, J. A., Johnston, G. H., Ladanyi, B., Sego, D. C., & van Everdingen, R. O. (1988). Glossary of permafrost and related ground-ice terms. In *Technical Memorandum (National Research Council of Canada. Associate Committee on Geotechnical Research): Bd. ACGR-TM-142*. National Research Council of Canada. Associate Committee on Geotechnical Research. Permafrost Subcommittee. https://doi.org/10.4224/20386561

4. Van Huissteden, J. (2020). *Thawing Permafrost: Permafrost Carbon in a Warming Arctic*. Springer International Publishing. https://doi.org/10.1007/978-3-030-31379-1

5. Davidson, E. A., & Janssens, I. A. (2006). Temperature sensitivity of soil carbon decomposition and feedbacks to climate change. *Nature*, *440*(7081), 165–173. https://doi.org/10.1038/nature04514

6. Varner, R. K., Crill, P. M., Frolking, S., McCalley, C. K., Burke, S. A., Chanton, J. P., Holmes, M. E., Saleska, S., & Palace, M. W. (2022). Permafrost thaw driven changes in hydrology and vegetation cover increase trace gas emissions and climate forcing in Stordalen Mire from 1970 to 2014. *Philosophical transactions. Series A, Mathematical, physical, and engineering sciences*, *380*(2215), 20210022. https://doi.org/10.1098/rsta.2021.0022

7. Voigt, C., Virkkala, A.-M., Hould Gosselin, G., Bennett, K. A., Black, T. A., Detto, M., Chevrier-Dion, C., Guggenberger, G., Hashmi, W., Kohl, L., Kou, D., Marquis, C., Marsh, P., Marushchak, M. E., Nesic, Z., Nykänen, H., Saarela, T., Sauheitl, L., Walker, B., … Sonnentag, O. (2023). Arctic soil methane sink increases with drier conditions and higher ecosystem respiration. *Nature Climate Change*, *13*(10), 1095–1104. https://doi.org/10.1038/s41558-023-01785-3

8. McGuire, A. D., Lawrence, D. M., Koven, C., Clein, J. S., Burke, E., Chen, G., Jafarov, E., MacDougall, A. H., Marchenko, S., Nicolsky, D., Peng, S., Rinke, A., Ciais, P., Gouttevin, I., Hayes, D. J., Ji, D., Krinner, G., Moore, J. C., Romanovsky, V., … Zhuang, Q. (2018). Dependence of the evolution of carbon dynamics in the northern permafrost region on the trajectory of climate change. *Proceedings of the National Academy of Sciences*, *115*(15), 3882–3887. https://doi.org/10.1073/pnas.1719903115

9. Wei, D., Qi, Y., Ma, Y., Wang, X., Ma, W., Gao, T., Huang, L., Zhao, H., Zhang, J., & Wang, X. (2021). Plant uptake of CO_2 outpaces losses from permafrost and plant respiration on the Tibetan Plateau. *Proceedings of the National Academy of Sciences*, *118*(33), e2015283118. https://doi.org/10.1073/pnas.2015283118

10. IPCC. (2013). Climate Change 2013: The Physical Science Basis. Contribution of Working Group I to the Fifth Assessment Report of the Intergovernmental Panel on Climate Change.

11. Rantanen, M., Karpechko, A. Yu., Lipponen, A., Nordling, K., Hyvärinen, O., Ruosteenoja, K., Vihma, T., & Laaksonen, A. (2022). The Arctic has warmed nearly four times faster than the globe since 1979. *Communications Earth & Environment*, *3*(1), 168. https://doi.org/10.1038/s43247-022-00498-3

12. Serreze, M. C., & Francis, J. A. (2006). The Arctic Amplification Debate. *Climatic Change*, *76*(3–4), 241–264. https://doi.org/10.1007/s10584-005-9017-y

13. Reyes, F. R., & Lougheed, V. L. (2015). Rapid Nutrient Release from Permafrost Thaw in Arctic Aquatic Ecosystems. *Arctic, Antarctic, and Alpine Research*, *47*(1), 35–48. https://doi.org/10.1657/AAAR0013-099

14. Natali, S. M., Schuur, E. A. G., Webb, E. E., Pries, C. E. H., & Crummer, K. G. (2014). Permafrost degradation stimulates carbon loss from experimentally warmed tundra. *Ecology*, *95*(3), 602–608. https://doi.org/10.1890/13-0602.1

15. Jansson, J. K., & Taş, N. (2014). The microbial ecology of permafrost. *Nature reviews. Microbiology*, *12*(6), 414–425. https://doi.org/10.1038/nrmicro3262

16. Ernakovich, J. G., Lynch, L. M., Brewer, P. E., Calderon, F. J., & Wallenstein, M. D. (2017). Redox and temperature-sensitive changes in microbial communities and soil chemistry dictate greenhouse gas loss from thawed permafrost. *Biogeochemistry*, *134*(1–2), 183–200. https://doi.org/10.1007/s10533-017-0354-5

17. Pokrovsky, O. S., Manasypov, R. M., Kopysov, S. G., Krickov, I. V., Shirokova, L. S., Loiko, S. V., Lim, A. G., Kolesnichenko, L. G., Vorobyev, S. N., & Kirpotin, S. N. (2020). Impact of Permafrost Thaw and Climate Warming on Riverine Export Fluxes of Carbon, Nutrients and Metals in Western Siberia. *Water*, *12*(6), 1817. https://doi.org/10.3390/w12061817

18. Mann, P. J., Strauss, J., Palmtag, J., Dowdy, K., Ogneva, O., Fuchs, M., Bedington, M., Torres, R., Polimene, L., Overduin, P., Mollenhauer, G., Grosse, G., Rachold, V., Sobczak, W. V., Spencer, R. G. M., & Juhls, B. (2022). Degrading permafrost river catchments and their impact on Arctic Ocean nearshore processes. *Ambio*, *51*(2), 439–455. https://doi.org/10.1007/s13280-021-01666-z

19. Schuur, E. A. G., Abbott, B. W., Commane, R., Ernakovich, J., Euskirchen, E., Hugelius, G., Grosse, G., Jones, M., Koven, C., Leshyk, V., Lawrence, D., Loranty, M. M., Mauritz, M., Olefeldt, D., Natali, S., Rodenhizer, H., Salmon, V., Schädel, C., Strauss, J., … Turetsky, M. (2022). Permafrost and Climate Change: Carbon Cycle Feedbacks From the Warming Arctic. *Annual Review of Environment and Resources*, *47*(1), 343–371. https://doi.org/10.1146/annurev-environ-012220-011847

20. Knoblauch, C., Beer, C., Liebner, S., Grigoriev, M. N., & Pfeiffer, E.-M. (2018). Methane production as key to the greenhouse gas budget of thawing permafrost. *Nature Climate Change*, *8*(4), 309–312. https://doi.org/10.1038/s41558-018-0095-z

21. Treat, C. C., Virkkala, A., Burke, E., Bruhwiler, L., Chatterjee, A., Fisher, J. B., Hashemi, J., Parmentier, F. W., Rogers, B. M., Westermann, S., Watts, J. D., Blanc-Betes, E., Fuchs, M., Kruse, S., Malhotra, A., Miner, K., Strauss, J., Armstrong, A., Epstein, H. E., … Hugelius, G. (2024). Permafrost Carbon: Progress on Understanding Stocks and Fluxes Across Northern Terrestrial Ecosystems. *Journal of Geophysical Research: Biogeosciences*, *129*(3), e2023JG007638. https://doi.org/10.1029/2023JG007638

22. Bintanja, R., & Andry, O. (2017). Towards a rain-dominated Arctic. *Nature Climate Change*, *7*(4), 263–267. https://doi.org/10.1038/nclimate3240

23. Turetsky, M. R., Abbott, B. W., Jones, M. C., Anthony, K. W., Olefeldt, D., Schuur, E. A. G., Grosse, G., Kuhry, P., Hugelius, G., Koven, C., Lawrence, D. M., Gibson, C., Sannel, A. B. K., & McGuire, A. D. (2020). Carbon release through abrupt permafrost thaw. *Nature Geoscience*, *13*(2), 138–143. https://doi.org/10.1038/s41561-019-0526-0

24. Schädel, C., Rogers, B. M., Lawrence, D. M., Koven, C. D., Brovkin, V., Burke, E. J., Genet, H., Huntzinger, D. N., Jafarov, E., McGuire, A. D., Riley, W. J., & Natali, S. M. (2024). Earth system models must include permafrost carbon processes. *Nature Climate Change*, *14*(2), 114–116. https://doi.org/10.1038/s41558-023-01909-9

25. Porras, R. C., Hicks Pries, C. E., Torn, M. S., & Nico, P. S. (2018). Synthetic iron (hydr)oxide-glucose associations in subsurface soil: Effects on decomposability of mineral associated carbon. *The Science of the total environment*, *613–614*, 342–351. https://doi.org/10.1016/j.scitotenv.2017.08.290

26. McGrath, C. R., Hicks Pries, C. E., Nguyen, N., Glazer, B., Lio, S., & Crow, S. E. (2022). Minerals limit the deep soil respiration response to warming in a tropical Andisol. *Biogeochemistry*, *161*(2), 85–99. https://doi.org/10.1007/s10533-022-00965-1

27. Mikutta, R., Mikutta, C., Kalbitz, K., Scheel, T., KAISER, K., & Jahn, R. (2007). Biodegradation of forest floor organic matter bound to minerals via different binding mechanisms. *Geochimica et Cosmochimica Acta*, *71*(10), 2569–2590. https://doi.org/10.1016/j.gca.2007.03.002

28. Dungait, J. A. J., Hopkins, D. W., Gregory, A. S., & Whitmore, A. P. (2012). Soil organic matter turnover is governed by accessibility not recalcitrance. *Global Change Biology*, *18*(6), 1781–1796. https://doi.org/10.1111/j.1365-2486.2012.02665.x

29. Martens, J., Mueller, C. W., Joshi, P., Rosinger, C., Maisch, M., Kappler, A., Bonkowski, M., Schwamborn, G., Schirrmeister, L., & Rethemeyer, J. (2023). Stabilization of mineral-associated organic carbon in Pleistocene permafrost. *Nature communications*, *14*(1), 2120. https://doi.org/10.1038/s41467-023-37766-5

30. Monhonval, A., Strauss, J., Thomas, M., Hirst, C., Titeux, H., Louis, J., Gilliot, A., Du Bois d'Aische, E., Pereira, B., Vandeuren, A., Grosse, G., Schirrmeister, L., Jongejans, L. L., Ulrich, M., & Opfergelt, S. (2022). Thermokarst processes increase the supply of stabilizing surfaces and elements (Fe, Mn, Al, and Ca) for mineral–organic carbon interactions. *Permafrost and Periglacial Processes*, *33*(4), 452–469. https://doi.org/10.1002/ppp.2162

31. Gentsch, N., Wild, B., Mikutta, R., Čapek, P., Diáková, K., Schrumpf, M., Turner, S., Minnich, C., Schaarschmidt, F., Shibistova, O., Schnecker, J., Urich, T., Gittel, A., Šantrůčková, H., Bárta, J., Lashchinskiy, N., Fuß, R., Richter, A., & Guggenberger, G. (2018). Temperature response of permafrost soil carbon is attenuated by mineral protection. *Global change biology*, *24*(8), 3401–3415. https://doi.org/10.1111/gcb.14316

32. Qin, S., Kou, D., Mao, C., Chen, Y., Chen, L., & Yang, Y. (2021). Temperature sensitivity of permafrost carbon release mediated by mineral and microbial properties. *Science Advances*, *7*(32), eabe3596. https://doi.org/10.1126/sciadv.abe3596

33. Gentsch, N., Mikutta, R., Alves, R. J. E., Barta, J., Čapek, P., Gittel, A., Hugelius, G., Kuhry, P., Lashchinskiy, N., Palmtag, J., Richter, A., Šantrůčková, H., Schnecker, J., Shibistova, O., Urich, T., Wild, B., & Guggenberger, G. (2015). Storage and transformation of organic matter fractions in cryoturbated permafrost soils across the Siberian Arctic. *Biogeosciences*, *12*(14), 4525–4542. https://doi.org/10.5194/bg-12-4525-2015

34. Liu, F., Qin, S., Fang, K., Chen, L., Peng, Y., Smith, P., & Yang, Y. (2022). Divergent changes in particulate and mineral-associated organic carbon upon permafrost thaw. *Nature communications*, *13*(1), 5073. https://doi.org/10.1038/s41467-022-32681-7

35. Thomas, M., Jongejans, L. L., Strauss, J., Vermylen, C., Calcus, S., Opel, T., Kizyakov, A., Wetterich, S., Grosse, G., & Opfergelt, S. (2024). A Third of Organic Carbon Is Mineral Bound in Permafrost Sediments Exposed by the World's Largest Thaw Slump,

Batagay, Siberia. *Permafrost and Periglacial Processes*, ppp.2230. https://doi.org/10.1002/ppp.2230

36. Kleber, M., Bourg, I. C., Coward, E. K., Hansel, C. M., Myneni, S. C. B., & Nunan, N. (2021). Dynamic interactions at the mineral–organic matter interface. *Nature Reviews Earth & Environment*, *2*(6), 402–421. https://doi.org/10.1038/s43017-021-00162-y

37. Chen, C., Dynes, J. J., Wang, J., & Sparks, D. L. (2014). Properties of Fe-organic matter associations via coprecipitation versus adsorption. *Environmental science & technology*, *48*(23), 13751–13759. https://doi.org/10.1021/es503669u

38. Roden, E. E., & Zachara, J. M. (1996). Microbial Reduction of Crystalline Iron(III) Oxides: Influence of Oxide Surface Area and Potential for Cell Growth. *Environmental Science & Technology*, *30*(5), 1618–1628. https://doi.org/10.1021/es9506216

39. Bhattacharyya, A., Schmidt, M. P., Stavitski, E., & Martínez, C. E. (2018). Iron speciation in peats: Chemical and spectroscopic evidence for the co-occurrence of ferric and ferrous iron in organic complexes and mineral precipitates. *Organic Geochemistry*, *115*, 124–137. https://doi.org/10.1016/j.orggeochem.2017.10.012

40. ThomasArrigo, L. K., & Kretzschmar, R. (2022). Iron speciation changes and mobilization of colloids during redox cycling in Fe-rich, Icelandic peat soils. *Geoderma*, *428*, 116217. https://doi.org/10.1016/j.geoderma.2022.116217

41. Dong, H., Zeng, Q., Sheng, Y., Chen, C., Yu, G., & Kappler, A. (2023). Coupled iron cycling and organic matter transformation across redox interfaces. *Nature Reviews Earth & Environment*, *4*(9), 659–673. https://doi.org/10.1038/s43017-023-00470-5

42. Chen, C., Dong, Y., & Thompson, A. (2023). Electron Transfer, Atom Exchange, and Transformation of Iron Minerals in Soils: The Influence of Soil Organic Matter. *Environmental Science & Technology*, *57*(29), 10696–10707. https://doi.org/10.1021/acs.est.3c01876

43. Lalonde, K., Mucci, A., Ouellet, A., & Gélinas, Y. (2012). Preservation of organic matter in sediments promoted by iron. *Nature*, *483*(7388), 198–200. https://doi.org/10.1038/nature10855

44. Zhao, B., Dou, A., Zhang, Z., Chen, Z., Sun, W., Feng, Y., Wang, X., & Wang, Q. (2023). Ecosystem-specific patterns and drivers of global reactive iron mineral-associated organic carbon. *Biogeosciences*, *20*(23), 4761–4774. https://doi.org/10.5194/bg-20-4761-2023

45. Lau, M. P., Hutchins, R. H. S., Tank, S. E., & A. Del Giorgio, P. (2024). The chemical succession in anoxic lake waters as source of molecular diversity of organic matter. *Scientific Reports*, *14*(1), 3831. https://doi.org/10.1038/s41598-024-54387-0

46. Patzner, M. S., Mueller, C. W., Malusova, M., Baur, M., Nikeleit, V., Scholten, T., Hoeschen, C., Byrne, J. M., Borch, T., Kappler, A., & Bryce, C. (2020). Iron mineral dissolution releases iron and associated organic carbon during permafrost thaw. *Nature communications*, *11*(1), 6329. https://doi.org/10.1038/s41467-020-20102-6

47. Patzner, M. S., Kainz, N., Lundin, E., Barczok, M., Smith, C., Herndon, E., Kinsman-Costello, L., Fischer, S., Straub, D., Kleindienst, S., Kappler, A., & Bryce, C. (2022). Seasonal Fluctuations in Iron Cycling in Thawing Permafrost Peatlands. *Environmental Science & Technology*, *56*(7), 4620–4631. https://doi.org/10.1021/acs.est.1c06937

48. Monhonval, A., Mauclet, E., Hirst, C., Bemelmans, N., Eekman, E., Schuur, E. A. G., & Opfergelt, S. (2023). Mineral organic carbon interactions in dry versus wet tundra soils. *Geoderma*, *436*, 116552. https://doi.org/10.1016/j.geoderma.2023.116552

49. Opfergelt, S. (2020). The next generation of climate model should account for the evolution of mineral-organic interactions with permafrost thaw. *Environmental Research Letters*, *15*(9), 091003. https://doi.org/10.1088/1748-9326/ab9a6d

50. Mu, C. C., Zhang, T. J., Zhao, Q., Guo, H., Zhong, W., Su, H., & Wu, Q. B. (2016). Soil organic carbon stabilization by iron in permafrost regions of the Qinghai-Tibet Plateau. *Geophysical Research Letters*, *43*(19), 10286–10294. https://doi.org/10.1002/2016GL070071

51. Joss, H., Patzner, M. S., Maisch, M., Mueller, C. W., Kappler, A., & Bryce, C. (2022). Cryoturbation impacts iron-organic carbon associations along a permafrost soil chronosequence in northern Alaska. *Geoderma*, *413*, 115738. https://doi.org/10.1016/j.geoderma.2022.115738

52. Peng, C., Bryce, C., Sundman, A., Borch, T., & Kappler, A. (2019). Organic Matter Complexation Promotes Fe(II) Oxidation by the Photoautotrophic Fe(II)-Oxidizer Rhodopseudomonas palustris TIE-1. *ACS Earth and Space Chemistry*, *3*(4), 531–536. https://doi.org/10.1021/acsearthspacechem.9b00024

53. Larese-Casanova, P., Haderlein, S. B., & Kappler, A. (2010). Biomineralization of lepidocrocite and goethite by nitrate-reducing Fe(II)-oxidizing bacteria: Effect of pH, bicarbonate, phosphate, and humic acids. *Geochimica et Cosmochimica Acta*, *74*(13), 3721–3734. https://doi.org/10.1016/j.gca.2010.03.037

54. Laufer, K., Nordhoff, M., Halama, M., Martinez, R. E., Obst, M., Nowak, M., Stryhanyuk, H., Richnow, H. H., & Kappler, A. (2017). Microaerophilic Fe(II)-Oxidizing Zetaproteobacteria Isolated from Low-Fe Marine Coastal Sediments: Physiology and Composition of Their Twisted Stalks. *Applied and Environmental Microbiology*, *83*(8), e03118-16. https://doi.org/10.1128/AEM.03118-16

55. Lv, J., Zhang, S., Wang, S., Luo, L., Cao, D., & Christie, P. (2016). Molecular-Scale Investigation with ESI-FT-ICR-MS on Fractionation of Dissolved Organic Matter Induced by Adsorption on Iron Oxyhydroxides. *Environmental science & technology*, *50*(5), 2328–2336. https://doi.org/10.1021/acs.est.5b04996

56. Zhu, X., Wang, K., Liu, Z., Wang, J., Wu, E., Yu, W., Zhu, X., Chu, C., & Chen, B. (2023). Probing Molecular-Level Dynamic Interactions of Dissolved Organic Matter with Iron Oxyhydroxide via a Coupled Microfluidic Reactor and an Online High-Resolution Mass Spectrometry System. *Environmental Science & Technology*, *57*(7), 2981–2991. https://doi.org/10.1021/acs.est.2c06816

57. Eusterhues, K., Rennert, T., Knicker, H., Kögel-Knabner, I., Totsche, K. U., & Schwertmann, U. (2011). Fractionation of organic matter due to reaction with ferrihydrite: Coprecipitation versus adsorption. *Environmental science & technology*, *45*(2), 527–533. https://doi.org/10.1021/es1023898

58. Li, Y., Lv, J., Cao, D., & Zhang, S. (2021). Interfacial Molecular Fractionation Induces Preferential Protection of Biorefractory Organic Matter by Ferrihydrite. *ACS Earth and Space Chemistry*, *5*(5), 1094–1101. https://doi.org/10.1021/acsearthspacechem.1c00019

59. Kappler, A., Bryce, C., Mansor, M., Lueder, U., Byrne, J. M., & Swanner, E. D. (2021). An evolving view on biogeochemical cycling of iron. *Nature reviews. Microbiology*. https://doi.org/10.1038/s41579-020-00502-7

60. Poggenburg, C., Mikutta, R., Schippers, A., Dohrmann, R., & Guggenberger, G. (2018). Impact of natural organic matter coatings on the microbial reduction of iron oxides. *Geochimica et Cosmochimica Acta*, *224*, 223–248. https://doi.org/10.1016/j.gca.2018.01.004

61. Eusterhues, K., Neidhardt, J., Hädrich, A., Küsel, K., & Totsche, K. U. (2014). Biodegradation of ferrihydrite-associated organic matter. *Biogeochemistry*, *119*(1–3), 45–50. https://doi.org/10.1007/s10533-013-9943-0

62. Roden, E. E., Kappler, A., Bauer, I., Jiang, J., Paul, A., Stoesser, R., Konishi, H., & Xu, H. (2010). Extracellular electron transfer through microbial reduction of solid-phase humic substances. *Nature Geoscience*, *3*(6), 417–421. https://doi.org/10.1038/ngeo870

63. Lovley, D. R., Fraga, J. L., Blunt-Harris, E. L., Hayes, L. A., Phillips, E. J. P., & Coates, J. D. (1998). Humic Substances as a Mediator for Microbially Catalyzed Metal Reduction. *Acta Hydrochimica et Hydrobiologica*, *26*(3), 152–157. https://doi.org/10.1002/(SICI)1521-401X(199805)26:3<152::AID-AHEH152>3.0.CO;2-D

64. Chen, J., Gu, B., Royer, R., & Burgos, W. (2003). The roles of natural organic matter in chemical and microbial reduction of ferric iron. *The Science of The Total Environment*, *307*(1–3), 167–178. https://doi.org/10.1016/S0048-9697(02)00538-7

65. Scott, D. T., McKnight, D. M., Blunt-Harris, E. L., Kolesar, S. E., & Lovley, D. R. (1998). Quinone Moieties Act as Electron Acceptors in the Reduction of Humic Substances by Humics-Reducing Microorganisms. *Environmental Science & Technology*, *32*(19), 2984–2989. https://doi.org/10.1021/es980272q

66. Bauer, I., & Kappler, A. (2009). Rates and Extent of Reduction of Fe(III) Compounds and O_2 by Humic Substances. *Environmental Science & Technology*, *43*(13), 4902–4908. https://doi.org/10.1021/es900179s

67. Lovley, D. R., Coates, J. D., Blunt-Harris, E. L., Phillips, E. J. P., & Woodward, J. C. (1996). Humic substances as electron acceptors for microbial respiration. *Nature*, *382*(6590), 445–448. https://doi.org/10.1038/382445a0

68. Miller, K. E., Lai, C.-T., Friedman, E. S., Angenent, L. T., & Lipson, D. A. (2015). Methane suppression by iron and humic acids in soils of the Arctic Coastal Plain. *Soil Biology and Biochemistry*, *83*, 176–183. https://doi.org/10.1016/j.soilbio.2015.01.022

69. Lipson, D. A., Zona, D., Raab, T. K., Bozzolo, F., Mauritz, M., & Oechel, W. C. (2012). Water-table height and microtopography control biogeochemical cycling in an Arctic coastal tundra ecosystem. *Biogeosciences*, *9*(1), 577–591. https://doi.org/10.5194/bg-9-577-2012

70. Reiche, M., Torburg, G., & Küsel, K. (2008). Competition of Fe(III) reduction and methanogenesis in an acidic fen. *FEMS microbiology ecology*, *65*(1), 88–101. https://doi.org/10.1111/j.1574-6941.2008.00523.x

71. Bar-Or, I., Elvert, M., Eckert, W., Kushmaro, A., Vigderovich, H., Zhu, Q., Ben-Dov, E., & Sivan, O. (2017). Iron-Coupled Anaerobic Oxidation of Methane Performed by a Mixed Bacterial-Archaeal Community Based on Poorly Reactive Minerals. *Environmental Science & Technology*, *51*(21), 12293–12301. https://doi.org/10.1021/acs.est.7b03126

72. Ettwig, K. F., Zhu, B., Speth, D., Keltjens, J. T., Jetten, M. S. M., & Kartal, B. (2016). Archaea catalyze iron-dependent anaerobic oxidation of methane. *Proceedings of the National Academy of Sciences*, *113*(45), 12792–12796. https://doi.org/10.1073/pnas.1609534113

73. Wagner, R., Zona, D., Oechel, W., & Lipson, D. (2017). Microbial community structure and soil p H correspond to methane production in A rctic A laska soils. *Environmental Microbiology*, *19*(8), 3398–3410. https://doi.org/10.1111/1462-2920.13854

74. Sulman, B. N., Yuan, F., O'Meara, T., Gu, B., Herndon, E. M., Zheng, J., Thornton, P. E., & Graham, D. E. (2022). Simulated Hydrological Dynamics and Coupled Iron Redox Cycling Impact Methane Production in an Arctic Soil. *Journal of Geophysical Research: Biogeosciences*, *127*(10), e2021JG006662. https://doi.org/10.1029/2021JG006662

75. Fu, L., Zhou, T., Wang, J., You, L., Lu, Y., Yu, L., & Zhou, S. (2019). NanoFe3O4 as Solid Electron Shuttles to Accelerate Acetotrophic Methanogenesis by Methanosarcina barkeri. *Frontiers in Microbiology*, *10*, 388. https://doi.org/10.3389/fmicb.2019.00388

76. Xiao, L., Wei, W., Luo, M., Xu, H., Feng, D., Yu, J., Huang, J., & Liu, F. (2019). A potential contribution of a Fe(III)-rich red clay horizon to methane release: Biogenetic magnetite-mediated methanogenesis. *CATENA*, *181*, 104081. https://doi.org/10.1016/j.catena.2019.104081

77. Drake, H. L., Horn, M. A., & Wüst, P. K. (2009). Intermediary ecosystem metabolism as a main driver of methanogenesis in acidic wetland soil. *Environmental Microbiology Reports*, *1*(5), 307–318. https://doi.org/10.1111/j.1758-2229.2009.00050.x

78. Christensen, T. R., Johansson, T., Åkerman, H. J., Mastepanov, M., Malmer, N., Friborg, T., Crill, P., & Svensson, B. H. (2004). Thawing sub-arctic permafrost: Effects on vegetation and methane emissions. *Geophysical Research Letters*, *31*(4), 2003GL018680. https://doi.org/10.1029/2003GL018680

79. Callaghan, T. V., Bergholm, F., Christensen, T. R., Jonasson, C., Kokfelt, U., & Johansson, M. (2010). A new climate era in the sub-Arctic: Accelerating climate changes and multiple impacts. *Geophysical Research Letters*, *37*(14), 2009GL042064. https://doi.org/10.1029/2009GL042064

80. Johansson, T., Malmer, N., Crill, P. M., Friborg, T., Åkerman, J. H., Mastepanov, M., & Christensen, T. R. (2006). Decadal vegetation changes in a northern peatland, greenhouse gas fluxes and net radiative forcing. *Global change biology*, *12*(12), 2352–2369. https://doi.org/10.1111/j.1365-2486.2006.01267.x

81. Olefeldt, D., Roulet, N. T., Bergeron, O., Crill, P., Bäckstrand, K., & Christensen, T. R. (2012). Net carbon accumulation of a high-latitude permafrost palsa mire similar to permafrost-free peatlands. *Geophysical Research Letters*, *39*(3), 2011GL050355. https://doi.org/10.1029/2011GL050355

82. Ellenbogen, J. B., Borton, M. A., McGivern, B. B., Cronin, D. R., Hoyt, D. W., Freire-Zapata, V., McCalley, C. K., Varner, R. K., Crill, P. M., Wehr, R. A., Chanton, J. P., Woodcroft, B. J., Tfaily, M. M., Tyson, G. W., Rich, V. I., & Wrighton, K. C. (2024). Methylotrophy in the Mire: Direct and indirect routes for methane production in thawing permafrost. *mSystems*, *9*(1), e00698-23. https://doi.org/10.1128/msystems.00698-23

83. McCalley, C. K., Woodcroft, B. J., Hodgkins, S. B., Wehr, R. A., Kim, E.-H., Mondav, R., Crill, P. M., Chanton, J. P., Rich, V. I., Tyson, G. W., & Saleska, S. R. (2014). Methane dynamics regulated by microbial community response to permafrost thaw. *Nature*, *514*(7523), 478–481. https://doi.org/10.1038/nature13798

84. Woodcroft, B. J., Singleton, C. M., Boyd, J. A., Evans, P. N., Emerson, J. B., Zayed, A. A. F., Hoelzle, R. D., Lamberton, T. O., McCalley, C. K., Hodgkins, S. B., Wilson, R. M., Purvine, S. O., Nicora, C. D., Li, C., Frolking, S., Chanton, J. P., Crill, P. M., Saleska, S. R., Rich, V. I., & Tyson, G. W. (2018). Genome-centric view of carbon processing in thawing permafrost. *Nature, 560*(7716), 49–54. https://doi.org/10.1038/s41586-018-0338-1

85. McGivern, B. B., Cronin, D. R., Ellenbogen, J. B., Borton, M. A., Knutson, E. L., Freire-Zapata, V., Bouranis, J. A., Bernhardt, L., Hernandez, A. I., Flynn, R. M., Woyda, R., Cory, A. B., Wilson, R. M., Chanton, J. P., Woodcroft, B. J., Ernakovich, J. G., Tfaily, M. M., Sullivan, M. B., Tyson, G. W., … Wrighton, K. C. (2024). Microbial polyphenol metabolism is part of the thawing permafrost carbon cycle. *Nature Microbiology*, *9*(6), 1454–1466. https://doi.org/10.1038/s41564-024-01691-0

86. Patzner, M. S., Logan, M., McKenna, A. M., Young, R. B., Zhou, Z., Joss, H., Mueller, C. W., Hoeschen, C., Scholten, T., Straub, D., Kleindienst, S., Borch, T., Kappler, A., & Bryce, C. (2022). Microbial iron cycling during palsa hillslope collapse promotes

greenhouse gas emissions before complete permafrost thaw. *Communications Earth & Environment*, *3*(1), 76. https://doi.org/10.1038/s43247-022-00407-8

87. Hodgkins, S. B., Tfaily, M. M., McCalley, C. K., Logan, T. A., Crill, P. M., Saleska, S. R., Rich, V. I., & Chanton, J. P. (2014). Changes in peat chemistry associated with permafrost thaw increase greenhouse gas production. *Proceedings of the National Academy of Sciences of the United States of America*, *111*(16), 5819–5824. https://doi.org/10.1073/pnas.1314641111

88. Lipson, D. A., Raab, T. K., Goria, D., & Zlamal, J. (2013). The contribution of Fe(III) and humic acid reduction to ecosystem respiration in drained thaw lake basins of the Arctic Coastal Plain. *Global Biogeochemical Cycles*, *27*(2), 399–409. https://doi.org/10.1002/gbc.20038

89. Romanowicz, K. J., Crump, B. C., & Kling, G. W. (2023). Genomic evidence that microbial carbon degradation is dominated by iron redox metabolism in thawing permafrost. *ISME Communications*, *3*(1), 124. https://doi.org/10.1038/s43705-023-00326-5

90. Li, Y., Xue, Y., Roy Chowdhury, T., Graham, D. E., Tringe, S. G., Jansson, J. K., & Taş, N. (2024). Genomic insights into redox-driven microbial processes for carbon decomposition in thawing Arctic soils and permafrost. *mSphere*, e00259-24. https://doi.org/10.1128/msphere.00259-24

Chapter 2: Author contributions

Preferential adsorption and coprecipitation of permafrost organic matter with poorly crystalline iron minerals

Eva Voggenreiter, Philippe Schmitt-Kopplin, Laurel ThomasArrigo, Casey Bryce, Andreas Kappler and Prachi Joshi

The study was conceptualized by A. Kappler, C. Bryce, P. Joshi and myself. A. Kappler acquired the funding. The methodology was designed by P. Schmitt-Kopplin, A. Kappler, P. Joshi and myself. I collected the samples and performed the experiments. The resulting data was formally analyzed by myself, P. Schmitt-Kopplin (regarding FT-ICR-MS data), L. ThomasArrigo and P. Joshi (regarding synchrotron spectra). Resources regarding access to synchrotron beamtime were provided by L. ThomasArrigo and P. Joshi. Visualization of the data and writing of the original draft of the manuscript was performed by me. Supervision was provided by P. Joshi and A. Kappler. All authors contributed to the review and editing of the final manuscript.

Chapter 2:

Preferential adsorption and coprecipitation of permafrost organic matter with poorly crystalline iron minerals

Eva Voggenreiter[1], Philippe Schmitt-Kopplin[2,3], Laurel ThomasArrigo[4], Casey Bryce[5], Andreas Kappler[1,6], Prachi Joshi[1]

[1]Geomicrobiology, Department of Geosciences, University of Tübingen, Schnarrenbergstrasse 94-96, 72076 Tübingen, Germany

[2]Analytical Biogeochemistry, Helmholtz Center Munich, Ingolstädter Landstrasse 1, 85764 Neuherberg, Germany

[3]Analytical Food Chemistry, Technical University of Munich, Maximus-von-Imhof-Forum 2, 85354 Freising

[4]Environmental Chemistry, University of Neuchâtel, Avenue de Bellevaux 51, CH-2000, Neuchâtel, Switzerland

[5]School of Earth Sciences, University of Bristol, Wills Memorial Building, Queens Road Bristol BS8 1RJ, United Kingdom

[6]Cluster of Excellence: EXC 2124: Controlling Microbes to Fight Infection, Schnarrenbergstrasse 94-96, 72076 Tübingen, Germany

Abstract

Future permafrost thaw will likely lead to substantial release of greenhouse gases due to thawing of previously unavailable organic carbon (OC). Accurate predictions of this release are limited by poor knowledge of the bioavailabity of mobilized OC during thaw. Organic carbon bioavailability decreases due to adsorption to, or coprecipitation with, poorly crystalline ferric iron (Fe(III)) (oxyhydr)oxide minerals but the maximum binding extent and binding selectivity of permafrost OC to these minerals is unknown. We therefore utilized water-extractable organic matter (WEOM) from soils across a permafrost thaw gradient to quantify adsorption and coprecipitation processes with poorly crystalline Fe(III) (oxyhydr)oxides. We found that the maximum adsorption capacity of WEOM from intact and partly thawed permafrost soils was similar (204 and 226 mg C g^{-1} ferrihydrite, respectively) but decreased to 81 mg C g^{-1} ferrihydrite for WEOM from the fully thawed site. In comparison, coprecipitation of WEOM from intact and partly thawed soils with Fe immobilized up to 925 and 1532 mg C g^{-1} Fe respectively due to formation of precipitated Fe(III)-OC phases. Analysis of the OC composition before and after adsorption/coprecipitation revealed that high molecular weight, oxygen-rich, carboxylic- and aromatic-rich OC was preferentially bound to Fe(III) minerals relative to low molecular weight, aliphatic-rich compounds which may be more bioavailable. This selective binding effect was stronger after adsorption than coprecipitation. Our results suggest that OC binding by Fe(III) (oxyhydr)oxides sharply decreases under fully thawed conditions and that small, aliphatic OC molecules that may be readily bioavailable are less protected across all thaw stages.

Graphical abstract
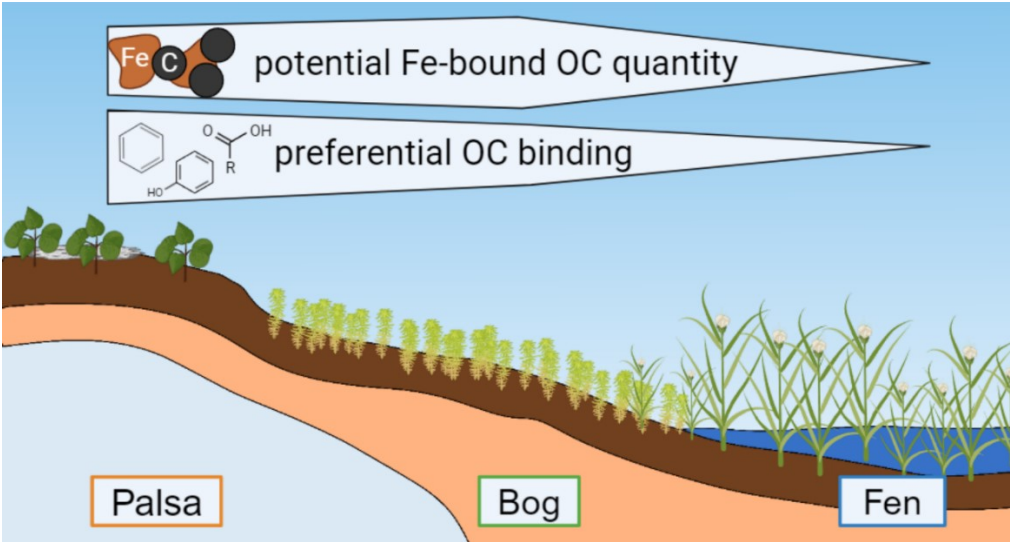
Environmental significance statement

Permafrost thaw leads to the release of organic carbon (OC), which may bind with ubiquitous ferric iron (Fe(III)) minerals. It is therefore important to understand the quantity and composition of Fe-bound OC in order to predict the (bio)availability of OC that is released. Here, we simulated adsorption and coprecipitation processes of OC along a permafrost thaw gradient with Fe(III) (oxyhydr)oxide minerals. We found that the quantity of Fe-bound OC decreases with permafrost thaw and observed preferential binding of less bioavailable OC by Fe(III) (oxyhydr)oxides. Our work therefore suggests that although these minerals bind OC in permafrost soil, the overall effect on protecting OC against microbial degradation is not as strong as previously thought as binding selects for less bioavailable OC.

Introduction

Permafrost soils are a major organic carbon (OC) stock, accounting for roughly one third of global soil OC (ca. 1300 Pg), yet only cover 15% of the global soil area[1,2]. It has been estimated that permafrost thaw will cause the release of 67-237 Pg C as greenhouse gases by 2100 under business-as-usual climate scenarios[2] due to microbial decomposition of OC that was previously not bioavailable. This microbially mediated release of OC as the greenhouse gases carbon dioxide (CO_2) or methane (CH_4) is still poorly constrained in timing and extent since it is influenced by a variety of biogeochemical factors[3–6]. One of the key factors that controls the release of CO_2 and CH_4 is the bioavailability of OC for microbial decomposition. This OC bioavailability is lowered by its association with mineral surfaces in the soil, possibly leading to lower greenhouse gas emissions[7,8].

An array of different minerals can interact with OC in soil, such as phyllosilicates, metal (oxyhydr)oxides, as well as metal sulfides[8]. Iron (Fe) (oxyhydr)oxides are especially known to bind a large quantity of OC in acidic soils[9] due to their high surface area[10] and thus play a larger role in permafrost peatland soils compared to other minerals, such as phyllosilicates[11]. This binding can occur through (i) adsorption of OC onto existing Fe(III) (oxyhydr)oxides, or (ii) abiotic (or in certain cases, microbially mediated) precipitation of Fe(III) (oxyhydr)oxides by oxidation of dissolved Fe(II) in the presence of OC (referred to as "coprecipitation")[12,13]. Adsorption takes place under both oxic and anoxic conditions while coprecipitation mainly occurs at redox interfaces when conditions transition from anoxic to oxic. Here, we refer to phases that are formed after either adsorption or coprecipitation as Fe-OC associations. The formation pathway of Fe-OC associations directly affects the properties of the Fe mineral. While adsorption of OC changes the surface properties of the mineral, coprecipitation with OC may affect Fe speciation and crystallinity of the resulting Fe-OC phase, which in turn may affect the reactivity of Fe[14–18].

During the binding process, different OC compounds may be selectively bound while others remain in solution. Past studies using forest-floor extracts, plant litter, or humic reference materials suggested that the initial OC composition might determine which OC compounds are preferentially bound. Depending on the starting composition, it has been found that high molecular weight, oxygen-rich, carboxyl-rich, and aromatic compounds[19–21] or in some cases carbohydrates[22] could be preferentially bound to Fe(III) (oxyhydr)oxides. The composition of dissolved OC (DOC) after binding thus differs compared to its initial state, which has consequences for its bioavailability[20] and its residence time in soils[23].

Recently, several studies have shown that substantial fractions of OC may be bound to minerals (30-82%) in permafrost environments, with the dominant mineral fraction as Fe(III)

(oxyhydr)oxides[12,24,25]. The amount of Fe-bound OC is relatively consistent across different sites: ca. 10-20% of soil OC in intact permafrost soils of Scandinavia, Alaska, and the Tibetan Plateau[24,26–28]. This suggests that part of the OC may remain unavailable due to binding with Fe minerals even with the increase in microbial activity due to permafrost thaw. However, our systematic understanding of the formation and composition of Fe-OC associations in permafrost soils and in subsequent thaw stages is limited. Along the thaw gradient, the soils undergo biogeochemical shifts due to changes in vegetation cover (higher abundance of sedges compared to shrubs and mosses)[29,30], soil pH (acidic to circumneutral)[31] and redox state (from oxic to anoxic)[32]. These changes affect the OC quantity and composition along the different thaw stages[29,33,34]. For instance, bog and fen peat contain more tannin-, lignin- and protein-like compounds compared to palsa peat[29]. Therefore, the amount of OC and the functional groups therein that react with Fe(III) (oxyhydr)oxides may differ over a thaw gradient. Extrapolating the results of adsorption and coprecipitation experiments from other ecosystems or OC reference compounds is difficult as the geochemical conditions (e.g., pH) and initial OC composition might differ substantially in permafrost systems[35,36]. Systematic studies are thus necessary to understand the change in OC composition due to binding with Fe(III) (oxyhydr)oxides, independent of changes due to other biogeochemical factors during thaw. Finally, field-based studies[37–39] only offer a snapshot of the net result of simultaneously occurring processes, making it difficult to disentangle effects of adsorption and coprecipitation alone. It is currently not known how much OC can potentially be bound by Fe(III) (oxyhydr)oxides via adsorption and coprecipitation along a permafrost thaw gradient, what impact these processes have on Fe mineralogy, and how they would influence preferential OC binding.

To address these knowledge gaps, the goal of this study was to systematically evaluate the quantity and selectivity of OC binding across permafrost thaw by simulating adsorption and coprecipitation, forming Fe-OC associations. The specific objectives were to (i) determine the maximum binding capacity of DOC from permafrost across different thaw stages to Fe(III) (oxyhydr)oxides by adsorption and coprecipitation, (ii) identify the speciation of Fe the formed Fe-OC associations, and (iii) evaluate changes in the chemical composition of OC due to binding to assess the potential changes in bioavailability. To achieve this, we utilized soils of a representative thawing permafrost peatland (Stordalen Mire, Sweden). We used *in situ* OC from soils of three distinct thaw stages, as previously defined by changes in vegetation and hydrology[30,40,41]. The thaw stages were classified as (i) palsa underlain by permafrost, (ii) partly thawed, seasonally anoxic bog, and (iii) fully thawed, permanently anoxic fen areas. We chose to use water-extractable organic matter (WEOM) from the mineral-poor organic horizon as representative OC fractions for the experiments for two reasons: First, WEOM is the OC

fraction which is most likely to enter the porewater and interact with Fe(III) (oxyhydr)oxides. Second, using WEOM allowed us to integrate all changes in OC composition due to vegetation, redox and pH condition shifts over the thaw gradient, thus being the most representative of environmental conditions.

Materials and Methods

Field site description and sampling

Our field site, Stordalen Mire, is a subarctic permafrost peatland complex close to Abisko, Sweden (68 22' N, 19 03' E). It is located in the discontinuous permafrost zone and consists of several sub-habitats: 1) raised palsas underlain by intact permafrost and vegetated by dwarf shrubs, bryophytes, and lichens, 2) *Sphagnum*-rich bogs with a higher active layer depth than palsas that experience seasonal water table fluctuations, and 3) fully inundated and anoxic fens, characterized by sedges (*Eriophorum vaginatum, Carex rostrata*)[30,42]. Along the thaw gradient, pH values of the porewater increase from acidic (pH 3.5 to 4.5) in palsa and bog soils to circumneutral (pH 5 to 6.5) in fen soils[31,43–45]. The porewater generally has a low ionic strength; most dissolved species are in the μM-range[31].

In order to extract soil organic matter (see below) for the adsorption and coprecipitation experiments, we sampled the organic horizon of each thaw stage in July 2021 (Figure S1). The soil surface, covered with plant roots or young *Sphagnum spp.* layers, was removed and the soil below was collected by grab sampling, filled in plastic (LDPE) bags, and stored at 4°C until further use. Soils in bog and fen areas were water-saturated and packed in the bags such that no headspace remained in order to limit oxygen exposure. Duplicate soil cores were collected per thaw stage at representative sites, based on the vegetation cover and pH values as described above, to compare solid phase OC composition to the WEOM. Cores were taken using a 50 cm long Humax corer as described previously[46].

WEOM extraction

All glassware used in the extraction and further experiments was acid washed (1 M HCl), rinsed three times with double-deionized water (DDI, Millipore, >18 MΩ cm^{-1}), and subsequently baked at 300°C for 8 h before use. WEOM was extracted from the organic horizon of each permafrost thaw stage by mixing field-moist soil with DDI water for 24 h on an overhead shaker at a 1:10 weight/volume (w/v) ratio. Since we aimed to simulate conditions under which ferrihydrite would likely react with dissolved OC in permafrost soils, we carried out extractions for adsorption experiments under oxic conditions. For coprecipitation experiments,

the extraction was done under anoxic conditions to simulate anoxic conditions in waterlogged soil layers. Afterwards, the suspensions were filled in glass serum bottles and centrifuged at 5250 rcf for 15 minutes. The supernatant was filtered sequentially through pre-rinsed 8 µm (Merck Millipore, MCE) and 0.22 µm (Merck Millipore, Steritop PES) filters. After filtration, extracts for the coprecipitation experiments were bubbled with N_2 gas (99.999%) for 1 h to make them anoxic again after filtration. All extracts were stored in the dark at 4°C until use (storage time was less than 24 h). Aliquots of all WEOM types were immediately freeze-dried after filtration, and the resulting solids were stored in the dark until analysis by Fourier-transform infrared spectroscopy (FTIR, details below). Initial DOC concentrations in the extracts of different soils and extraction conditions ranged from 9.8-23.5 mg C L^{-1} (Table S1). They were quantified as described later in section "Setup of adsorption experiments".

Ferrihydrite synthesis

Ferrihydrite was used in the adsorption experiments since it is a very common Fe(III) (oxyhydr)oxide mineral found in peatlands[47,48] and has been shown to present in soils of all thaw stages at Stordalen Mire[28]. It is also typically the most relevant to OC carbon binding in soils since it can bind the highest amounts of OC per g Fe due to its high specific surface area (>200 m^2 g^{-1})[49,50]. It was synthesized as reported previously[51]. Briefly, 40 g $Fe(NO_3)_3*9H_2O$ were dissolved in 500 mL DDI water and the pH was raised until 7.5 by addition of 1 M KOH under rapid stirring (800 rpm). The suspension was centrifuged (4250 rcf, 10 min) and washed with DDI water four times. Ferrihydrite was resuspended in 200 mL DDI water, stored at 4°C in the dark, and used within 6 weeks after synthesis. Mineral identity of ferrihydrite was confirmed by [57]Mössbauer spectroscopy and specific surface area was quantified after freeze-drying (further details in Text S1).

Setup of adsorption experiments

Adsorption experiments were carried out by adding aliquots of a ferrihydrite suspension (10.7 g L^{-1} Fh) to 20 mL of WEOM solution from palsa, bog, and fen soils inside closed 50 mL glass serum bottles. The WEOM was first adjusted to pH 4.5 (for palsa and bog WEOM) and pH 6 (for fen WEOM). For the adsorption isotherm of each WEOM type, the WEOM was diluted to different OC concentrations using a 3 mM NaCl solution as constant background ionic strength. The mass of added ferrihydrite was adjusted for each WEOM type, depending on its DOC concentration, to create the same initial molar C:Fe ratios across experiments (0.5 to 3.3, see Table S2). After addition of ferrihydrite, the pH of the suspension was adjusted again to pH 4.5 (for palsa and bog WEOM) and pH 6 (for fen WEOM) using 0.1 M HCl. The pH was

checked and re-adjusted 1 h later, if necessary. To quantify Fe concentrations in each replicate after adsorption, an aliquot (0.5 mL) of the suspension was acidified with 1 M HCl followed by total Fe quantification by the ferrozine assay[52]. A control setup using 3 mM NaCl solution with no added WEOM but added ferrihydrite was used to determine background concentrations of DOC. No DOC originating from the ferrihydrite was detected.

Suspensions were then capped and shaken horizontally at 60 rpm for 24 h in the dark. They were filtered afterwards using pre-rinsed 0.22 μm filters (Merck Millipore, PVDF) inside filter cups (25 mm diameter, Millipore). The filtrate was used to quantify remaining DOC (as non-purgeable OC) after acidification with 2 M HCl by a TOC analyzer (multi N/C 2100S, Analytik Jena AG, Germany). The bound OC content was calculated as in Text S2. The aromaticity of the filtrate was evaluated using specific ultraviolet spectroscopy at 254 nm ($SUVA_{254}$, details below). The molecular composition of the WEOM before and after adsorption in reactors with an initial C:Fe ratio of ~2 was analyzed by Fourier-transform ion cyclotron resonance mass spectrometry (FT-ICR-MS, details further below). This ratio was chosen since it was the highest common, initial ratio in all adsorption experiments. The solids of the same reactors (initial C:Fe ratio of ~2) per WEOM type were further analyzed for OC functional groups by FTIR spectroscopy and Fe mineralogy by Fe K-edge X-ray absorption spectroscopy (XAS) and ^{57}Fe Mössbauer spectroscopy. For solid phase analysis, the filter paper containing the ferrihydrite with adsorbed WEOM was washed twice with deionized water to remove loosely-bound ions. Then it was centrifuged (10055 rcf, 5 min) to release the particles from the paper surface. The supernatant was removed and samples were air-dried and stored at 4°C until analysis.

Setup of coprecipitation experiments

Coprecipitation was simulated by abiotic oxidation of dissolved, anoxic Fe(II) in the presence of palsa and bog WEOM at different initial C:Fe ratios (0.35 to 1.2). Note that these ratios slightly differ from the ones used in the adsorption experiment since a higher Fe(II) addition was necessary to produce a sufficient amount of Fe precipitates. Coprecipitation was not simulated with fen WEOM since this thaw stage is permanently water-logged and anoxic[53] with no redox fluctuations[38]; thus abiotic coprecipitation due to Fe(II) oxidation is unlikely to play a major role.

Ferrous iron was added at a concentration of 1.5 mM to different dilutions of anoxic WEOM. A stock Fe(II) solution (0.3 M) was prepared by dissolving iron(II) chloride tetrahydrate ($FeCl_2$*$4H_2O$, Sigma Aldrich, USA) in anoxic DDI water, after which the solution was sterile-filtered (0.22 μm, Merck Millipore, PVDF) and stored in a N_2-flushed, closed bottle in the dark.

The added Fe(II) concentration is in the upper range of dissolved Fe(II) concentrations found at Stordalen Mire[46].

The experiments were set up by adding the anoxic Fe(II) solution to 20 mL of anoxic WEOM solution inside an N_2-flushed bottle. Afterwards, vials were opened and a cotton stopper was placed on top to ensure a constant O_2 supply into the solution. The pH was measured at the start of the oxidation period and every 24 h thereafter, and adjusted back to pH 4.5 using 0.1 M NaOH if needed. The vials were shaken at 60 rpm on a horizontal shaker for 3 d in the dark. Afterwards, the same sampling procedure as described above for quantification of DOC, $SUVA_{254}$, and determination of molecular OC composition by FT-ICR-MS and FTIR was carried out. Additionally, aliquots of the solutions before oxidation and the resulting suspensions after 3 d of oxidation as well as of the filtrate were acidified with 1 M HCl and the total Fe concentration was quantified using the ferrozine assay. The total Fe concentration in the filtrate was subtracted from the concentration in suspension after 3 d of oxidation to calculate the amount of Fe that had precipitated. To collect enough solid material for XAS analysis, 2.5 mM Fe(II) were added to 200 mL of WEOM in a sacrificial setup (initial molar C:Fe ratio=0.6) and solids were collected after 3 d.

Fe *K*-edge X-ray absorption spectroscopy

Iron speciation in the Fe-OC associations was determined by Fe *K*-edge X-ray absorption spectroscopy at the SAMBA beamline at Synchrotron SOLEIL (Paris, France). Dried samples were homogenized with a mortar and pestle and pressed into pellets (7 mm diameter) with PVP (Polyvinylpyrrolidone K12, Carl Roth), before being sealed with Kapton® tape. At the beamline, transmission spectra were recorded in continuous scan mode at 20 K using a He(I) cryostat. An Si(220) monochromator was used and calibrated to the first derivative maximum of the *K*-edge absorption of an Fe(0) foil. Harmonic rejection was performed by two Si mirrors coated in Pd. Approximately 8-10 scans were collected per sample and merged to obtain the final spectra, used for analysis of Fe *K*-edge X-ray absorption near edge structure (XANES) and extended X-ray absorption fine structure (EXAFS). Iron oxidation state and speciation was determined through linear combination fit analysis (LCF) of XANES and EXAFS spectra, respectively, using Athena[54]. The Fe binding environment was further determined by shell fitting using Artemis[54]. Additional details of the XAS analyses are given in the SI (Text S3).

^{57}Fe Mössbauer spectroscopy was used to identify changes in the Fe mineralogy after adsorption of WEOM (initial C:Fe ratio = 2) of each WEOM type to complement XAS measurements. The minerals were collected using filtration and the filter paper with particles was sealed with Kapton® tape. Details of spectral collection and analysis are given in the SI (Text S1). Spectra were recorded at 6 K. Analysis of coprecipitates was not possible due to limited sample mass.

Organic carbon analysis

Specific UV absorption (SUVA254)

The change in the contribution of aromatic functional groups to DOC before and after adsorption or coprecipitation was analyzed using the specific UV absorption parameter at 254 nm (SUVA$_{254}$). Three spectra were recorded from 200 to 650 nm per experimental replicate using a UV-vis spectrophotometer (Specord 50 plus, Analytik Jena, Germany), averaged, and the mean absorption at 254 nm was blank-corrected and normalized to the measured DOC concentration.

Fourier-transform infrared spectroscopy

The adsorbed or coprecipitated WEOM in the solid phase was analyzed by Fourier-transform infrared spectroscopy (FTIR). Dried samples (1 mg) were diluted with KBr (Carl Roth, USA) and pressed into 250 mg pellets. Spectra were recorded from 370 to 4500 cm^{-1} with a resolution of 4 cm^{-1} using a Vertex 80v FTIR spectrometer (Bruker, USA). Thirty-two scans were recorded per sample, averaged, and normalized (min: 0, max:1) to obtain the final spectra.

Fourier-transform ion cyclotron resonance mass spectrometry

Ultrahigh resolution molecular composition of WEOM before and after adsorption or coprecipitation was analyzed by Fourier-transform ion cyclotron resonance mass spectrometry (FT-ICR-MS) using a 12 Tesla Bruker Solarix mass spectrometer (Bruker Daltonics, Bremen, Germany) in negative electrospray ionization mode at the Helmholtz Center Munich (Germany). Samples were prepared for analysis by solid phase (SPE) extraction of 5 mL sample using Bond Elut PPL cartridges (100 mg, 3 mL volume, Agilent Technologies, USA) and eluted in LC-MS grade methanol (Thermo-Scientific)[55]. It is known that SPE has a bias

towards specific OC classes[56] but we assume that this bias is similar for samples before and after binding for each WEOM type, respectively. Details of instrument parameters and calibration are provided in the SI (Text S4). Subsequent data analysis included a comparison of relative intensities of shared and initially present compounds in the spectra before and after adsorption or coprecipitation. All detected compounds were grouped in either "condensed aromatic", "aromatic" or "more aliphatic" classes based on the modified aromaticity index according to Koch & Dittmar (2006)[57]. The nominal oxidation state of organic carbon (NOSC) and standard free Gibbs energy of the oxidation half reaction (ΔG_{ox}^0) were calculated according to LaRowe & van Cappellen (2011)[58]. We used unweighted, average NOSC values across all detected formulae for a more conservative estimation since relative intensity-weighted NOSC values could skew the average due to a few very ionizable compounds[59].

Conceptual framework of bioavailability

We inferred changes in bioavailability of OC from its chemical composition, based on the SUVA$_{254}$, FTIR, and FT-ICR-MS results. Within this framework, OC classes like carbohydrates and proteins have a higher bioavailability since they are readily used by microorganisms due to the low energy investment compared to the utilization of lignin-derived or aromatic compounds[60]. Additionally, OC bound on minerals would also have a low bioavailability due to the physical protection by minerals[13] since the binding affinity to minerals often is higher than the affinity to the active site of exoenzymes[61].

Results and Discussion

Quantity of organic carbon bound during adsorption and coprecipitation

The mass of OC bound to ferrihydrite via adsorption generally increased with increasing DOC concentration before reaching a threshold value (Figure 1A). The maximum adsorption capacity, based on a Langmuir fit, of bog WEOM and palsa WEOM to ferrihydrite at pH 4.5 was 226±3 and 204±19 mg C g^{-1} Fh, while it was lower for fen WEOM at pH 6 (81±4 mg C g^{-1} Fh). Our results for palsa and bog WEOM were comparable to previous studies using water extracts from forest floor litter (196-250 mg C g^{-1})[19,22,62]. The resulting maximum C:Fe ratios in ferrihydrite with adsorbed palsa and bog WEOM (Table S3) were also comparable to permafrost OC bound on ferrihydrite-coated sand that were placed in the same thaw stages[38].
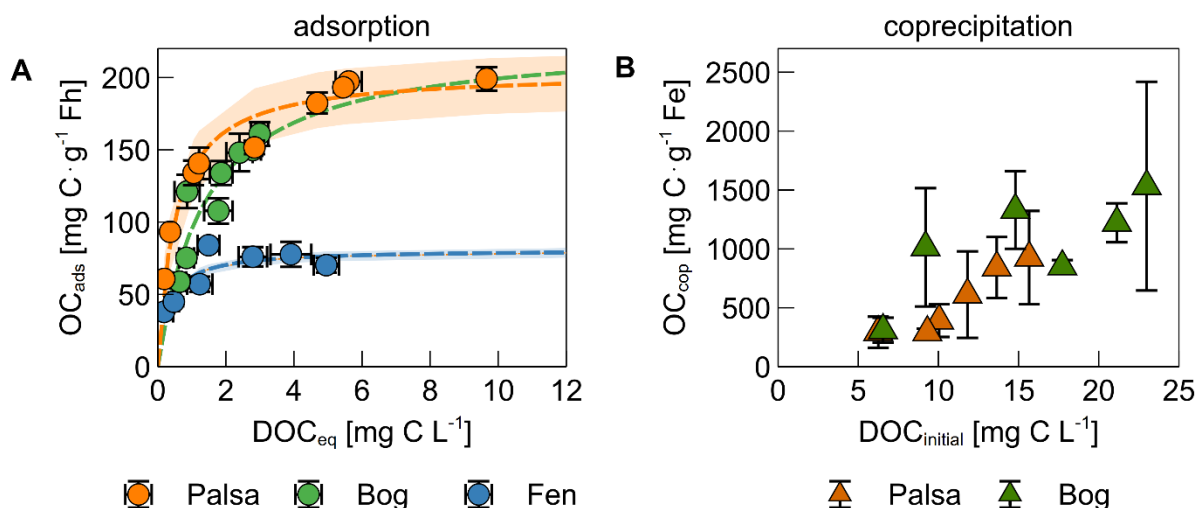
Figure 1. (A) Adsorption isotherm of water-extractable organic matter (WEOM) from different permafrost thaw stages on ferrihydrite (Fh). The mass of OC adsorbed (mg C g^{-1} Fh) is displayed against the equilibrium DOC concentration in solution after sorption. Data are denoted by circles and the Langmuir fit and 95% confidence interval is displayed as a dashed line and shaded area, respectively. The sorption experiments were performed at pH 4.5 for palsa, pH 4.5 for bog, and pH 6.0 for fen WEOM to represent environmentally relevant conditions. (B) Quantity of coprecipitated organic carbon (mg C g^{-1} Fe) as a function of the initial DOC (triangles). All data points and error bars represent the average and standard deviation of experimental triplicates. Note that the units and range of the y-axis are different for the two graphs.

The lower maximum adsorption capacity in case of fen WEOM may be due to several factors: (i) pH and (ii) WEOM composition. At lower pH, a higher proportion of ferrihydrite surface sites are protonated, causing a more positive surface charge[63,64]. As adsorption of OC to Fe(III) (oxyhydr)oxides is expected to be (mostly) electrostatic, negatively charged OC ions are therefore adsorbed to a higher degree to ferrihydrite at pH 4.5 than at pH 6[63]. However, we speculate that this change in pH cannot explain the full magnitude of decrease in adsorption capacity. The net surface charge of ferrihydrite from pH 4.5 to pH 6 decreases by 38-50%[65,66], suggesting that the change in surface charge is too small to explain the discrepancy between the quantity of adsorbed bog and fen WEOM. Another possible reason for the differences in WEOM sorption at pH 4.5 and pH 6 is the difference in composition between bog and fen WEOM. Fen WEOM is more microbially processed due to a higher microbial diversity and higher plant litter input, resulting in a higher abundance of lipid-, amino-sugar, and carbohydrate-like compounds[31,33]. In comparison, bog WEOM contains more aromatic-rich molecules[31,40,45]. Differences in OM composition have been shown to result in changes in adsorption capacities[67–69], which is discussed in further detail below. The presence of bridging

cations (Ca, Mg) could also increase the binding of OM to ferrihydrite[70], however, overall cation concentrations in WEOM from different thaw stages were low (<10 µM, Table S4). Note that we performed experiments with fen WEOM only at pH 6 in order to best represent environmental conditions.

Coprecipitation of palsa and bog WEOM with iron generally led to higher amounts of Fe-bound OC than adsorption (Figure 1B). The maximum masses of OC bound during coprecipitation with Fe were 925±397 and 1530±885 mg C g^{-1} Fe for palsa and bog WEOM, respectively. Resulting maximum C:Fe ratios were at least twice as high as previously reported for similar initial C:Fe ratios[19,22,71]. One reason for this might be the use of higher pH values (pH 6 or 7) in other studies[18,19,22,71,72], which leads to a lower binding capacity of the precipitated Fe due to lower surface charge of the formed Fe(III) oxyhydroxides. Second, many studies used dissolved Fe(III) as a reactant[14,19,22,73] during coprecipitation and increase the pH instead of oxidation of anoxic Fe(II) as in our study. The use of Fe(III) results in more precipitation of Fe relative to C at acidic pH values[74], due to the lower solubility of Fe(III) compared to Fe(II). This could lead to a lower content of bound OC, as illustrated by previously published values which are ca. 2 to 6 times lower at comparable initial C:Fe ratios and the same pH[73]. We expect that the OC binding capacities due to coprecipitation measured here are more applicable to redox interfaces in permafrost peatlands than values of other studies[19,22,71,73] as our experiments were done at environmentally relevant pH values and include Fe(II) oxidation.

After 3 days of oxidation, the percentage of oxidized and precipitated Fe was similar in experiments with palsa and bog WEOM (11±5% and 10±5%, respectively) and did not change based on the initial C:Fe ratio (Figure S2). Nierop et al. (2002)[74] reported similarly low Fe precipitation when Fe(II) was added to OC of peat water extracts. Complexation of Fe(II) by DOC and the low pH could possibly hinder oxidation to Fe(III)[75,76] and its subsequent precipitation. In contrast, coprecipitation led to removal of up to 44±8% DOC from solution in palsa WEOM and up to 72±1% in bog WEOM (Figure S2). For bog WEOM, the percentage of coprecipitated OC increased with the initial C:Fe ratio (Figure S2). This difference in share of coprecipitated OC is likely due to initial OC composition of palsa and bog WEOM (as discussed below). Coprecipitation in permafrost soils is thus able to remove much more OC from solution than adsorption, even with only a small percentage of Fe precipitating.

We acknowledge that there are also other minerals present along the thaw gradient which could bind OC, such as phyllosilicates or iron sulfide minerals[28]. However, previous studies showed that both minerals bind less OC per g mineral (FeS[77]: 55 mg C g^{-1}, phyllosilicates[78]: 5-12 mg C g^{-1}) at comparable initial C:Fe ratios than ferrihydrite by adsorption or during coprecipitation with dissolved Fe(II). Therefore, we expect that adsorption to, or

coprecipitation with poorly crystalline Fe(III) (oxyhydr)oxides plays a larger role in permafrost environments.

Fe speciation in formed Fe-OC associations

To determine Fe speciation in the solid phase, we used Fe *K*-edge X-ray absorption spectroscopy. We first did linear combination fitting (LCF) of the XANES region in order to determine the Fe oxidation state. All Fe in ferrihydrite with adsorbed WEOM and in post-coprecipitation mineral phases was Fe(III) (Figure S3, Table S5). Fitting results of EXAFS spectra showed that the post-adsorption phases consisted mostly of ferrihydrite and minor (<10%) fractions of lepidocrocite (Figure 2**Fehler! Verweisquelle konnte nicht gefunden werden.**). Additional Mössbauer spectra (Figure S5) of ferrihydrite with adsorbed WEOM at 6 K showed the presence of 2 sextets, with typical parameters (Table S8) for poorly crystalline ferrihydrite[79,80]. It is likely that the small fraction of lepidocrocite was not detected since parameters of lepidocrocite have been shown to overlap with those of ferrihydrite in Mössbauer spectra[81].

In contrast, the Fe phase after coprecipitation with palsa and bog WEOM consisted of approximately 40% Fe(III) bound directly to OC ("Fe(III)-OC phases") with the remaining fraction of Fe being ferrihydrite. This is consistent with observations by Schwertmann et al. (2005)[82], who detected poorly soluble Fe(III)-OC phases when oxidizing Fe(II) in the presence of DOC. The detected Fe(III)-OC phase was best fit using Fe(III)-citrate (which contains carboxylic groups) as a reference, aligning with past studies of Fe-OC phases in non-permafrost peatlands[47,83]. Since carboxylic groups are present in soils of all thaw stages[40] and carboxyl-richness of natural OM has recently been proposed to be a controlling factor in OC binding to Fe(III) (oxyhydr)oxides[84], it is likely that carboxyl groups are significantly involved in coprecipitation with Fe in permafrost soils.
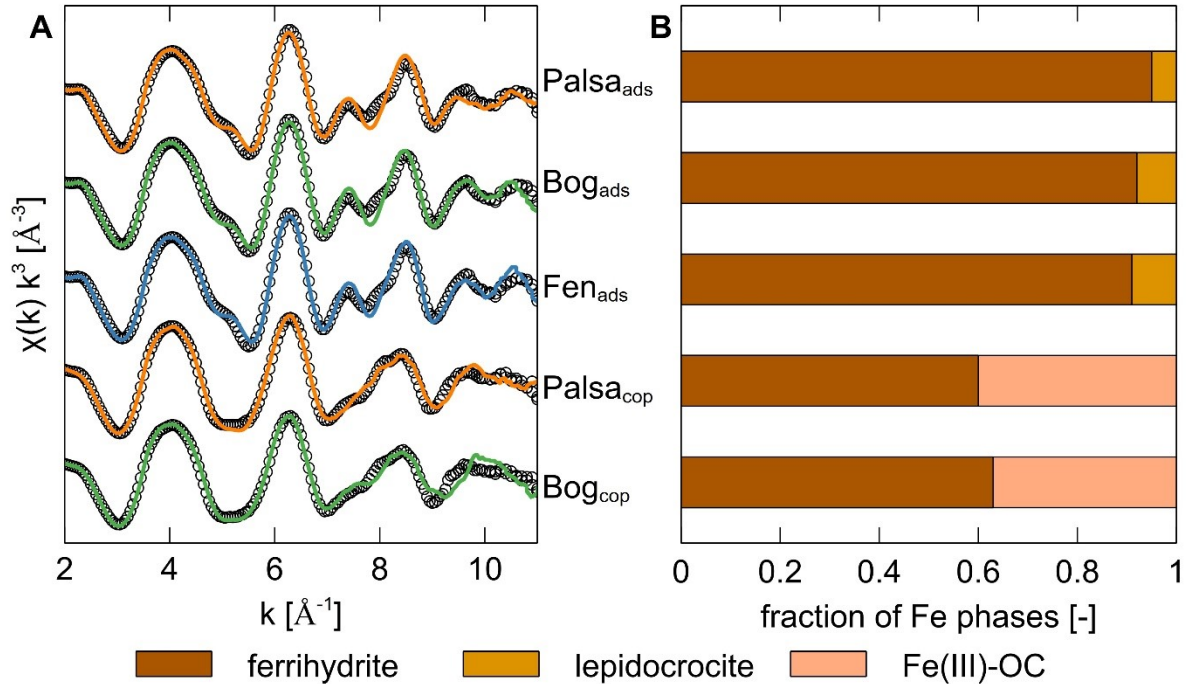
Figure 2. (A) Iron *K*-edge k^3-weighted EXAFS spectra and linear combination fits (2 to 11 Å^{-1}) of ferrihydrite with adsorbed WEOM (ads) from palsa, bog and fen, and Fe-OC coprecipitates (cop) synthesized with WEOM from palsa and bog. Experimental data is displayed as coloured lines and linear combination fits as black circles (see fit parameters in Table S6). (B) Bar plot showing relative abundances of different Fe phases in the post-adsorption and post-coprecipitation mineral phases. The same labelling as for graph (A) applies here. Fe(III)-OC was fit using Fe(III)-citrate as a reference.

Shell fitting analysis of the Fourier-transformed Fe *K*-edge EXAFS region (Figure S4, detailed results in Text S5) further suggested that formed coprecipitates were likely more poorly crystalline and/or had a lower particle size than ferrihydrite with adsorbed WEOM[85,86]. Within the coprecipitate set, the coprecipitates formed with palsa WEOM are likely more poorly crystalline than with bog WEOM, based on lower coordination numbers of both Fe-Fe paths (Table S7). A higher proportion of carboxylic groups, which are present in palsa peat compared to subsequent thaw stages[40], might have led to this lower crystallinity[84]. Thus, coprecipitation of OC in palsa and bog ecosystems likely causes formation of solid Fe(III)-OC phases and more poorly crystalline ferrihydrite, explaining the larger OC binding capacities of Fe-OC coprecipitates in contrast to adsorption by ferrihydrite.

40

Molecular fractionation of organic matter during adsorption and coprecipitation

Solid phase characterization using FTIR spectroscopy

The change in OC composition due to adsorption or coprecipitation was followed using FTIR spectroscopy of the initial WEOM and the solid phase after binding (Figure 3). The initial WEOM from all thaw stages contained common OC functional groups: (i) C-O groups in carbohydrates (1050 cm^{-1}), (ii) carboxylic groups, as apparent by peaks at 1400 cm^{-1}, 1630 cm^{-1} and 1720 cm^{-1} due to symmetric, asymmetric COO$^-$ and C=O stretches, respectively, and (iii) aromatic groups, visible as C=C stretches in aromatic rings (1630 cm^{-1})[19,87,88]. Note that we could not evaluate the aliphatic C band caused by CH stretches of -CH$_2$ groups (2840-2930 cm^{-1}) because of an overlay by the band produced from O-H stretching in water[87] (Figure S6). Relative peak heights of carboxylic and aromatic groups were higher than carbohydrates in palsa WEOM, whereas carbohydrates were relatively enriched in bog WEOM. This is in line with previous studies on changes of OC composition due to permafrost thaw at Stordalen Mire[29,40], in which carbohydrates often accumulate under the acidic and waterlogged conditions in bogs. Fen WEOM displayed weaker peaks of carbohydrate, carboxylic, and aromatic functional groups overall, compared to palsa and bog WEOM. We attribute this to higher overall microbial activity, leading to a depletion of labile carbohydrates in the water-extractable phase of the soil[31]. Overall, the initial WEOM composition was comparable to that of the solid peat from representative soil cores (Figure S7).
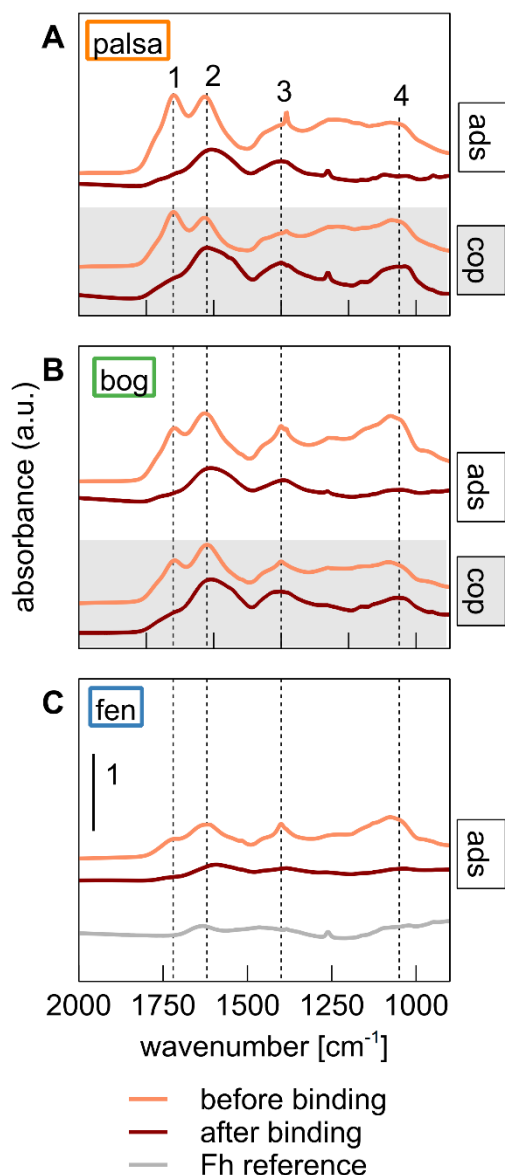
Figure 3. Normalized Fourier-transform infrared spectra of solids post-adsorption (ads) and post-coprecipitation (cop, both post-binding phases in maroon) in comparison to the original WEOM before binding (in orange) for (A) palsa, (B) bog, and (C) fen. The FTIR spectrum of ferrihydrite used for the adsorption experiments (grey) is given for reference. The scalebar in panel (C) applies for the other panels as well. Numbers and dashed lines stand for the following wavenumbers that are characteristic of the functional groups: 1 = 1720 cm^{-1} (C=O stretch in COOH), 2 = 1630 cm^{-1} (aromatic C=C stretch and/or asymmetric COO$^-$ stretch), 3 = 1400 cm^{-1} (symmetric COO$^-$ stretch), 4 = 1050 cm^{-1} (C-O stretch of carbohydrates)[19,87,88].

We observed preferential adsorption of certain organic functional groups to ferrihydrite for all WEOMs (Figure 3). The magnitude of this effect was higher for palsa and bog WEOM than for fen WEOM. For example, the main OC functional groups bound on ferrihydrite from palsa WEOM were carboxylic (1400 and 1630 cm^{-1}) and aromatic groups (1630 cm^{-1}). In

contrast, carbohydrates of palsa WEOM were adsorbed to a lower degree on ferrihydrite compared to carboxylic and aromatic groups. Preferential adsorption has been observed with plant litter or peat-derived OC in some previous studies with ferrihydrite and other Fe oxyhydroxides[19,20,89,90]. Coprecipitation led to less preferential binding of OC than adsorption for both palsa and bog WEOM, likely due to higher C:Fe ratios in the solid and more organic-organic interactions[21].

To assess the change in OC preferential binding semi-quantitatively and compare changes between WEOM types, we calculated peak ratios (PR) of aromatic C=C and COO$^-$ peaks to carbohydrate peaks before and after binding, respectively (Table S10). These ratios, also termed humification indices in the context of organic matter decomposition[87], are used to show the selective decrease or increase of a particular functional group. Peak ratios generally increased after binding. Selective binding of aromatic groups relative to carbohydrates was highest for adsorption with palsa and bog WEOM (based on increases in PR values of 128 and 151%, respectively) while PR after adsorption of fen WEOM increased only by 17%. Similarly, the carboxylic to carbohydrate PR increased by 157 and 100% after adsorption of palsa and bog WEOM on ferrihydrite, while the PR for fen WEOM increased only by 25%. Selective binding may be higher for palsa and bog WEOM since they contain more oxidized OC moieties (e.g., carboxylic groups) than fen WEOM that have been shown to display a higher adsorption affinity to Fe(III) (oxyhydr)oxides[69,90]. Coprecipitation of palsa WEOM with oxidized Fe(II) generally led to lower preferential binding of WEOM, with increases in PR by 50 and 33% for aromatic/carbohydrates and carboxylic/carbohydrates, respectively. Coprecipitation of bog WEOM induced almost no change in either PR. Taken together, OC binding to Fe(III) (oxyhydr)oxides in permafrost systems seems to be selective, favouring binding of carboxyl- and aromatic-rich OC moieties, especially during adsorption. However, this effect is lower under fully thawed conditions.

Aqueous phase characterization using FT-ICR-MS

Ultrahigh resolution mass spectrometry was used to evaluate the changes in OC composition in solution after adsorption and coprecipitation (see initial OC composition in Figure S9). For both sets of experiments, the remaining WEOM in solution after binding was enriched in compounds with a low O/C and high H/C ratio (Figure 4). Compounds with these formulae therefore remained in solution while more aromatic or unsaturated (low H/C ratio) and more oxygen-containing OC (high O/C ratio) compounds preferentially bound. Simultaneously, higher molecular weight molecules (with the same number of C atoms) were preferentially bound in all experiments (Figure S8).

We expect that high molecular weight compounds are bound to a higher extent since they are less soluble, more hydrophobic and contain more functional groups; hence they may partition into the solid phase. We also detected a decrease in the NOSC of OC in solution in all experiments (Table S11), meaning more oxidized OC compounds are preferentially bound. The change in NOSC was generally higher in adsorption compared to coprecipitation experiments, and highest after adsorption of bog WEOM to ferrihydrite (decrease from 0.02 to -0.20). These general trends are similar to selective binding of other terrestrial OC sources on Fe(III) (oxyhydr)oxides[20,21,90–92]. Moreover, direct observations of Fe-bound OC composition in thawing permafrost soils by Patzner et al. (2022)[46] also indicate the preferential binding of aromatic-rich and high molecular weight OC.

When comparing changes of different OC classes according to the modified aromaticity index, it was apparent that aromatic OC was preferentially adsorbed in all experiments (Figure 4F). Adsorption induced a higher preferential binding of aromatic moieties than coprecipitation for both palsa and bog WEOM, consistent with the FTIR spectroscopy results. Comparing within the adsorption experiments, the relative change in aromatic groups is similar with OC from all thaw stages (11-14% increase after adsorption). In contrast, preferential binding of aromatic OC by coprecipitation is slightly higher in bog WEOM (11%) than palsa WEOM (7%), contradictory to the trends detected by FTIR. We assume these discrepancies stem from the insensitivity of FTIR spectroscopy to detect small changes in bound OC functional groups and possibly from the sample preparation step SPE, which only extracts a subset of OC molecules[56].
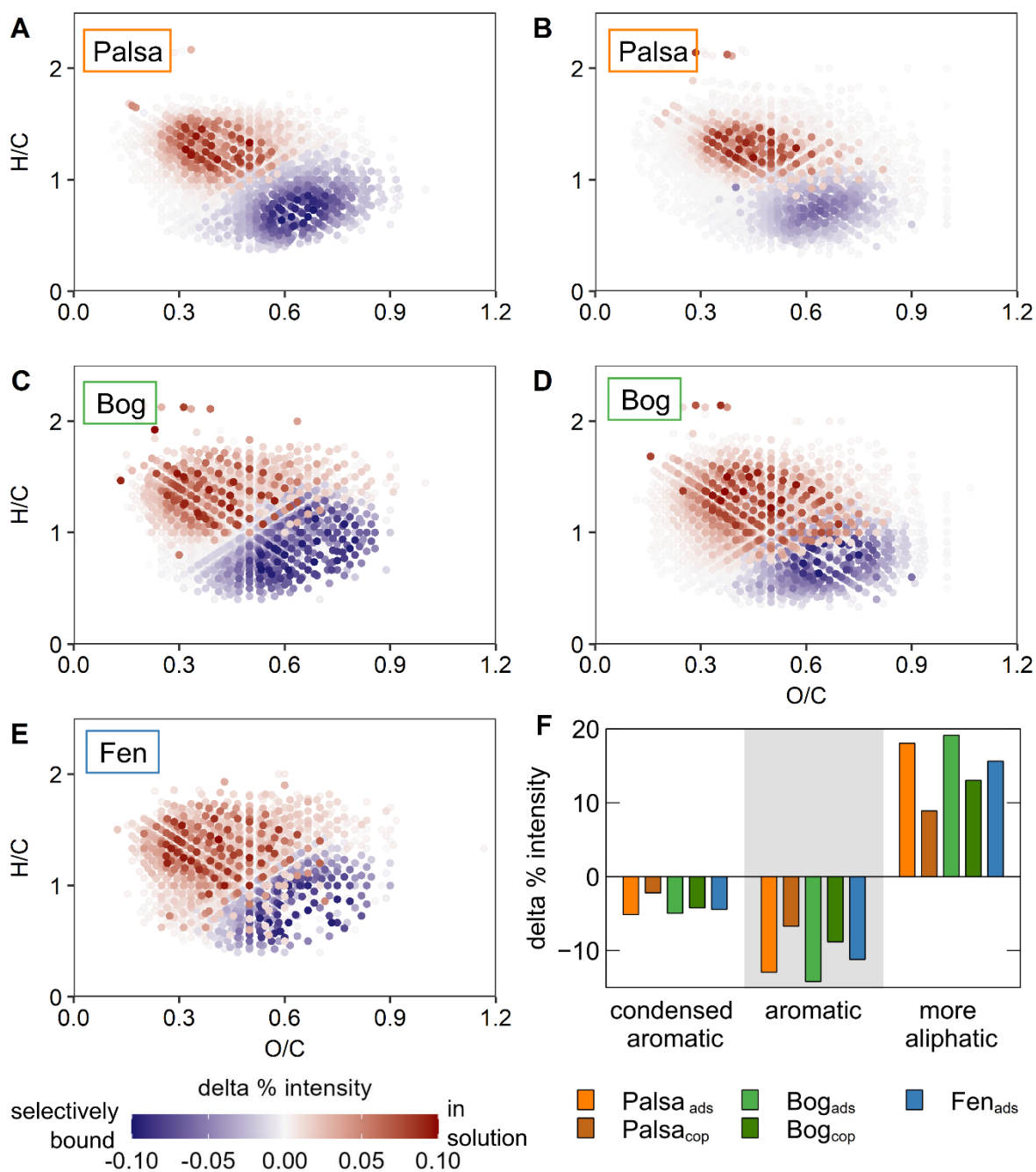
Figure 4. Van Krevelen diagrams showing changes in WEOM composition from palsa (A, B), bog (C, D) and fen (E) soils before and after adsorption (A, C, E) and coprecipitation (B, D). Organic compounds which are preferentially bound during adsorption or coprecipitation are displayed in blue and those retained in solution in red. (F) Change in molecular classes based on modified aromaticity index calculated for all experiments. Negative values indicate preferential adsorption while positive values mean compounds with formulae in those classes remained in solution.

To test changes in aromaticity over all initial C:Fe values, SUVA$_{254}$ was measured. Results also indicated that aromaticity in palsa and bog WEOM after adsorption decreased compared to the initial WEOM (Figure S10). With decreasing DOC concentration in equilibrium, this preferential adsorption of aromatic groups in palsa and bog WEOM increased, as already reported elsewhere[19,90]. However, fen WEOM showed increasing SUVA$_{254}$ values with increasing DOC in equilibrium, meaning aromatic groups preferentially adsorbed with increasing DOC concentration. Since fen WEOM is rich in complex carbohydrates and amino acids[31], we speculate that those OC groups could dominate at lower WEOM concentrations and are thus bound to the mineral surface in a higher proportion than aromatic groups. Support for the dependence of preferential binding on initial composition is also given by Eusterhues et al. (2011)[22] who found that different polysaccharides in a forest-floor extract preferentially adsorbed to ferrihydrite. SUVA$_{254}$ values after coprecipitation of palsa WEOM also decreased with decreasing equilibrium DOC concentration, while those after coprecipitation with bog WEOM stayed constant (Figure S10). This points toward a higher preferential binding effect for palsa WEOM compared to bog WEOM.

Effect of preferential binding of organic matter on bioavailability towards microbial decomposition

We considered different parameters to judge the effect of selective binding of WEOM on changes to the bioavailability of dissolved OC. We considered structure, represented by aromaticity and double bond equivalents in the FT-ICR-MS data and partially by FTIR spectra and SUVA values as well as molecular weight based on FT-ICR-MS data. Based on these parameters, we propose that more bioavailable OC is likely relatively enriched in solution after adsorption and coprecipitation. The preferential binding of aromatic and high molecular weight compounds would leave smaller, more aliphatic compounds in solution that are considered to be more labile towards microbial decomposition. This is supported by the work of Li et al. (2021)[20] who found that the extent of aerobic microbial degradation of ferrihydrite-bound OC, which was later again desorbed into the aqueous phase, was considerably lower than the original OC.

We also considered NOSC as an indicator for bioavailability. This parameter differed from our proposed trend. The average NOSC of OC in solution decreased after binding, implying that compounds that were energetically favorable towards decomposition were bound in the (formed) Fe-OC associations. Based on theoretical definitions, the remaining dissolved low-NOSC compounds are more difficult to degrade for microorganisms[93]. Possible reasons for this discrepancy are that NOSC is purely based on formula and not on structure or

molecular weight of OC molecules. Bioavailability can also be regarded similar to energy availability, which is the ratio of invested to returned energy during OC decomposition[60]. This emergent definition indicates that the total energy within an OC compound, which is proportional to its NOSC, may not be exactly related to what compound will be used energy efficiently by microorganisms[60]. Further research should therefore focus on how compounds of similar NOSC but different structure are respired by microorganisms. As we see limitations in the interpretation of NOSC for bioavailability in this context, we consider the other indicators (supported by the bioavailability experiments by Li et al. (2021)[20]) as more reliable. Therefore, the changes in OC composition after binding indicate that less bioavailable OC is selectively bound to Fe(III) oxyhydroxides in thawing permafrost soils, leaving easier degradable compounds in solution.

Conclusions

Our findings provide insights into the potential of Fe(III) (oxyhydr)oxides to bind porewater OC in (permafrost) peatlands. We found higher C:Fe ratios in Fe-OC associations formed by coprecipitation than by adsorption, even at relatively low initial C:Fe ratios. Given that very high C:Fe ratios (5-16 [g C g^{-1} Fe]) were observed in a variety of (permafrost) peatlands[26,28,94], coprecipitation as simulated in our study could be the major pathway for the formation of Fe-OC associations in palsa and bog ecosystems. It is feasible that the bound OC content is higher in a natural setting than in Fe-OC associations formed in batch experiments since DOC would be continuously supplied under natural conditions and reaction time scales are likely longer than 3 days. Coprecipitation thus likely plays a large role at trapping OC at redox interfaces, while adsorption, although binding less OC, is more relevant in upper, oxic soil layers.

Our results indicate that maximum adsorption capacities of OC drastically decreased from palsa and bog soils to fully thawed fen soils. This would mean that Fe(III) (oxyhydr)oxides provide less protection for OC in fully thawed, circumneutral permafrost conditions. Further, as more palsa soils transition to bogs or fens in the future, several processes could alter the binding of OC to poorly crystalline Fe(III) (oxyhydr)oxides. First, already existing Fe-OC coprecipitates could possibly further adsorb OC once they are formed. Second, under anoxic conditions in further thaw stages, the formed Fe-OC associations are likely to be microbially reduced and dissolved, releasing Fe^{2+} and OC into solution[46]. Based on the high quantities of bound OC to Fe minerals in palsa and bog soils, this would lead to a substantial OC release during transitions between thaw stages. The previously Fe-bound OC could then be used for anaerobic respiration, increasing CO_2 emissions and may ultimately also increase CH_4

emissions by supplying more dissolved OC. It is also possible that the released OC is partly bound by phyllosilicate or iron sulfide minerals, which are present in the fen soil[28]. Further, our observed preferential binding effects imply that Fe mineral protection of OC in permafrost soils is biased towards less bioavailable OC (albeit to a lower extent during coprecipitation than adsorption). This may affect OC cycling in primarily oxic soil horizons of permafrost soils since unbound, low-molecular weight compounds could partly be respired by microorganisms. Thus, Fe(III) (oxyhydr)oxides may limit DOC concentrations, especially in palsa and bog ecosystems, but may not substantially inhibit microbially mediated CO_2 emissions.

Acknowledgements

References

1. Hugelius G, Strauss J, Zubrzycki S, Harden JW, Schuur EAG, Ping C-L, et al. Estimated stocks of circumpolar permafrost carbon with quantified uncertainty ranges and identified data gaps. *Biogeosciences* 2014;**11**(23):6573–93.

2. Schuur EAG, McGuire AD, Schädel C, Grosse G, Harden JW, Hayes DJ, et al. Climate change and the permafrost carbon feedback. *Nature* 2015;**520**(7546):171–9.

3. Sihi D, Inglett PW, Gerber S, Inglett KS. Rate of warming affects temperature sensitivity of anaerobic peat decomposition and greenhouse gas production. *Glob Chang Biol* 2018;**24**(1):e259-e274.

4. Ernakovich JG, Lynch LM, Brewer PE, Calderon FJ, Wallenstein MD. Redox and temperature-sensitive changes in microbial communities and soil chemistry dictate greenhouse gas loss from thawed permafrost. *Biogeochemistry* 2017;**134**(1-2):183–200.

5. Couwenberg J, Thiele A, Tanneberger F, Augustin J, Bärisch S, Dubovik D, et al. Assessing greenhouse gas emissions from peatlands using vegetation as a proxy. *Hydrobiologia* 2011;**674**(1):67–89.

6. Woodcroft BJ, Singleton CM, Boyd JA, Evans PN, Emerson JB, Zayed AAF, et al. Genome-centric view of carbon processing in thawing permafrost. *Nature* 2018;**560**(7716):49–54.

7. Porras RC, Hicks Pries CE, Torn MS, Nico PS. Synthetic iron (hydr)oxide-glucose associations in subsurface soil: Effects on decomposability of mineral associated carbon. *Sci Total Environ* 2018;**613-614**:342–51.

8. Kleber M, Bourg IC, Coward EK, Hansel CM, Myneni SCB, Nunan N. Dynamic interactions at the mineral–organic matter interface. *Nat Rev Earth Environ* 2021.

9. Rasmussen C, Heckman K, Wieder WR, Keiluweit M, Lawrence CR, Berhe AA, et al. Beyond clay: towards an improved set of variables for predicting soil organic matter content. *Biogeochemistry* 2018;**137**(3):297–306.

10. Saidy AR, Smernik RJ, Baldock JA, Kaiser K, Sanderman J. The sorption of organic carbon onto differing clay minerals in the presence and absence of hydrous iron oxide. *Geoderma* 2013;**209-210**:15–21.

11. Zhu E, Liu Z, Wang S, Wang Y, Liu T, Feng X. Organic Carbon and Lignin Protection by Metal Oxides Versus Silicate Clay: Comparative Study Based on Wetland and Upland Soils. *J. Geophys. Res. Biogeosci.* 2023;**128**(7).

12. Gentsch N, Mikutta R, Shibistova O, Wild B, Schnecker J, Richter A, et al. Properties and bioavailability of particulate and mineral-associated organic matter in Arctic permafrost soils, Lower Kolyma Region, Russia. *Eur J Soil Sci* 2015;**66**(4):722–34.

13. Kleber M, Eusterhues K, Keiluweit M, Mikutta C, Mikutta R, Nico PS. Mineral–Organic Associations: Formation, Properties, and Relevance in Soil Environments. In: Elsevier; 2015, p. 1–140.

14. Eusterhues K, Wagner FE, Häusler W, Hanzlik M, Knicker H, Totsche KU, et al. Characterization of ferrihydrite-soil organic matter coprecipitates by X-ray diffraction and Mössbauer spectroscopy. *Environ. Sci. Technol.* 2008;**42**(21):7891–7.

15. Shimizu M, Zhou J, Schröder C, Obst M, Kappler A, Borch T. Dissimilatory reduction and transformation of ferrihydrite-humic acid coprecipitates. *Environ Sci Technol* 2013;**47**(23):13375–84.

16. Eusterhues K, Hädrich A, Neidhardt J, Küsel K, Keller TF, Jandt KD, et al. Reduction of ferrihydrite with adsorbed and coprecipitated organic matter: microbial reduction by

Geobacter bremensis vs. abiotic reduction by Na-dithionite. *Biogeosciences* 2014;**11**(18):4953–66.

17. Mikutta C. X-ray absorption spectroscopy study on the effect of hydroxybenzoic acids on the formation and structure of ferrihydrite. *Geochimica et Cosmochimica Acta* 2011;**75**(18):5122–39.

18. Angelico R, Ceglie A, He J-Z, Liu Y-R, Palumbo G, Colombo C. Particle size, charge and colloidal stability of humic acids coprecipitated with Ferrihydrite. *Chemosphere* 2014;**99**:239–47.

19. Chen C, Dynes JJ, Wang J, Sparks DL. Properties of Fe-organic matter associations via coprecipitation versus adsorption. *Environ Sci Technol* 2014;**48**(23):13751–9.

20. Li Y, Lv J, Cao D, Zhang S. Interfacial Molecular Fractionation Induces Preferential Protection of Biorefractory Organic Matter by Ferrihydrite. *ACS Earth Space Chem.* 2021.

21. Zhu X, Wang K, Liu Z, Wang J, Wu E, Yu W, et al. Probing Molecular-Level Dynamic Interactions of Dissolved Organic Matter with Iron Oxyhydroxide via a Coupled Microfluidic Reactor and an Online High-Resolution Mass Spectrometry System. *Environ. Sci. Technol.* 2023;**57**(7):2981–91.

22. Eusterhues K, Rennert T, Knicker H, Kögel-Knabner I, Totsche KU, Schwertmann U. Fractionation of organic matter due to reaction with ferrihydrite: coprecipitation versus adsorption. *Environ Sci Technol* 2011;**45**(2):527–33.

23. Coward EK, Ohno T, Plante AF. Adsorption and Molecular Fractionation of Dissolved Organic Matter on Iron-Bearing Mineral Matrices of Varying Crystallinity. *Environ Sci Technol* 2018;**52**(3):1036–44.

24. Liu F, Qin S, Fang K, Chen L, Peng Y, Smith P, et al. Divergent changes in particulate and mineral-associated organic carbon upon permafrost thaw. *Nat Commun* 2022;**13**(1):5073.

25. Martens J, Mueller CW, Joshi P, Rosinger C, Maisch M, Kappler A, et al. Stabilization of mineral-associated organic carbon in Pleistocene permafrost. *Nat Commun* 2023;**14**(1):2120.

26. Joss H, Patzner MS, Maisch M, Mueller CW, Kappler A, Bryce C. Cryoturbation impacts iron-organic carbon associations along a permafrost soil chronosequence in northern Alaska. *Geoderma* 2022;**413**:115738.

27. Mu CC, Zhang TJ, Zhao Q, Guo H, Zhong W, Su H, et al. Soil organic carbon stabilization by iron in permafrost regions of the Qinghai-Tibet Plateau. *Geophys. Res. Lett.* 2016;**43**(19):10,286-10,294.

28. Patzner MS, Mueller CW, Malusova M, Baur M, Nikeleit V, Scholten T, et al. Iron mineral dissolution releases iron and associated organic carbon during permafrost thaw. *Nat Commun* 2020;**11**(1):6329.

29. Wilson RM, Hough MA, Verbeke BA, Hodgkins SB, Chanton JP, Saleska SD, et al. Plant organic matter inputs exert a strong control on soil organic matter decomposition in a thawing permafrost peatland. *Sci Total Environ* 2022:152757.

30. Malmer N, Johansson T, Olsrud M, Christensen TR. Vegetation, climatic changes and net carbon sequestration in a North-Scandinavian subarctic mire over 30 years. *Glob Chang Biol* 2005;**0**(0):051006062331004-???

31. AminiTabrizi R, Wilson RM, Fudyma JD, Hodgkins SB, Heyman HM, Rich VI, et al. Controls on Soil Organic Matter Degradation and Subsequent Greenhouse Gas Emissions Across a Permafrost Thaw Gradient in Northern Sweden. *Front. Earth Sci.* 2020;**8**.

32. Perryman CR, McCalley CK, Malhotra A, Fahnestock MF, Kashi NN, Bryce JG, et al. Thaw Transitions and Redox Conditions Drive Methane Oxidation in a Permafrost Peatland. *J. Geophys. Res. Biogeosci.* 2020;**125**(3).

33. Hough M, McCabe S, Vining SR, Pickering Pedersen E, Wilson RM, Lawrence R, et al. Coupling plant litter quantity to a novel metric for litter quality explains C storage changes in a thawing permafrost peatland. *Glob Chang Biol* 2022;**28**(3):950–68.

34. Kane ES, Veverica TJ, Tfaily MM, Lilleskov EA, Meingast KM, Kolka RK, et al. Reduction-Oxidation Potential and Dissolved Organic Matter Composition in Northern Peat Soil: Interactive Controls of Water Table Position and Plant Functional Groups. *J. Geophys. Res. Biogeosci.* 2019;**124**(11):3600–17.

35. Guo Z, Wang Y, Wan Z, Zuo Y, He L, Li D, et al. Soil dissolved organic carbon in terrestrial ecosystems: Global budget, spatial distribution and controls. *Global Ecol. Biogeogr.* 2020;**29**(12):2159–75.

36. Heffernan L, Kothawala DN, Tranvik LJ. Review article: Terrestrial dissolved organic carbon in northern permafrost. *The Cryosphere* 2024;**18**(3):1443–65.

37. Monhonval A, Strauss J, Mauclet E, Hirst C, Bemelmans N, Grosse G, et al. Iron Redistribution Upon Thermokarst Processes in the Yedoma Domain. *Front. Earth Sci.* 2021;**9**.

38. Patzner MS, Kainz N, Lundin E, Barczok M, Smith C, Herndon E, et al. Seasonal Fluctuations in Iron Cycling in Thawing Permafrost Peatlands. *Environ. Sci. Technol.* 2022;**56**(7):4620–31.

39. Monhonval A, Mauclet E, Hirst C, Bemelmans N, Eekman E, Schuur EA, et al. Mineral organic carbon interactions in dry versus wet tundra soils. *Geoderma* 2023;**436**:116552.

40. Hodgkins SB, Tfaily MM, McCalley CK, Logan TA, Crill PM, Saleska SR, et al. Changes in peat chemistry associated with permafrost thaw increase greenhouse gas production. *Proc Natl Acad Sci U S A* 2014;**111**(16):5819–24.

41. Holmes ME, Crill PM, Burnett WC, McCalley CK, Wilson RM, Frolking S, et al. Carbon Accumulation, Flux, and Fate in Stordalen Mire, a Permafrost Peatland in Transition. *Global Biogeochem. Cycles* 2022;**36**(1).

42. Olefeldt D, Roulet NT, Bergeron O, Crill P, Bäckstrand K, Christensen TR. Net carbon accumulation of a high-latitude permafrost palsa mire similar to permafrost-free peatlands. *Geophys. Res. Lett.* 2012;**39**(3):n/a-n/a.

43. Lupascu M, Wadham JL, Hornibrook ERC, Pancost RD. Temperature Sensitivity of Methane Production in the Permafrost Active Layer at Stordalen, Sweden: A Comparison with Non-permafrost Northern Wetlands. *Arctic, Antarctic, and Alpine Research* 2012;**44**(4):469–82.

44. Mondav R, Woodcroft BJ, Kim E-H, McCalley CK, Hodgkins SB, Crill PM, et al. Discovery of a novel methanogen prevalent in thawing permafrost. *Nat Commun* 2014;**5**:3212.

45. Hodgkins SB, Tfaily MM, Podgorski DC, McCalley CK, Saleska SR, Crill PM, et al. Elemental composition and optical properties reveal changes in dissolved organic matter along a permafrost thaw chronosequence in a subarctic peatland. *Geochimica et Cosmochimica Acta* 2016;**187**:123–40.

46. Patzner MS, Logan M, McKenna AM, Young RB, Zhou Z, Joss H, et al. Microbial iron cycling during palsa hillslope collapse promotes greenhouse gas emissions before complete permafrost thaw. *Commun Earth Environ* 2022;**3**(1).

47. Bhattacharyya A, Schmidt MP, Stavitski E, Martínez CE. Iron speciation in peats: Chemical and spectroscopic evidence for the co-occurrence of ferric and ferrous iron in organic complexes and mineral precipitates. *Organic Geochemistry* 2018;**115**:124–37.

48. ThomasArrigo LK, Kretzschmar R. Iron speciation changes and mobilization of colloids during redox cycling in Fe-rich, Icelandic peat soils. *Geoderma* 2022;**428**:116217.

49. Roden EE, Zachara JM. Microbial Reduction of Crystalline Iron(III) Oxides: Influence of Oxide Surface Area and Potential for Cell Growth. *Environ. Sci. Technol.* 1996;**30**(5):1618–28.

50. Larsen O, Postma D. Kinetics of reductive bulk dissolution of lepidocrocite, ferrihydrite, and goethite. *Geochimica et Cosmochimica Acta* 2001;**65**(9):1367–79.

51. Schwertmann U, Cornell RM. *Iron Oxides in the Laboratory: Preparation and Characterization.* 2nd ed. Weinheim: Wiley-VCH; 2008.

52. Stookey LL. Ferrozine---a new spectrophotometric reagent for iron. *Anal. Chem.* 1970;**42**(7):779–81.

53. Olefeldt D, Roulet NT. Effects of permafrost and hydrology on the composition and transport of dissolved organic carbon in a subarctic peatland complex. *J. Geophys. Res.* 2012;**117**(G1).

54. Ravel B, Newville M. ATHENA and ARTEMIS Interactive Graphical Data Analysisusing IFEFFIT. *Phys. Scr.* 2005;**2005**(T115):1007.

55. Dittmar T, Koch B, Hertkorn N, Kattner G. A simple and efficient method for the solid-phase extraction of dissolved organic matter (SPE-DOM) from seawater. *Limnol. Oceanogr. Methods* 2008;**6**(6):230–5.

56. Chen M, Kim S, Park J-E, Jung H-J, Hur J. Structural and compositional changes of dissolved organic matter upon solid-phase extraction tracked by multiple analytical tools. *Anal Bioanal Chem* 2016;**408**(23):6249–58.

57. Koch BP, Dittmar T. From mass to structure: an aromaticity index for high-resolution mass data of natural organic matter. *Rapid Commun. Mass Spectrom.* 2006;**20**(5):926–32.

58. LaRowe DE, van Cappellen P. Degradation of natural organic matter: A thermodynamic analysis. *Geochimica et Cosmochimica Acta* 2011;**75**(8):2030–42.

59. Naughton HR, Keiluweit M, Tfaily MM, Dynes JJ, Regier T, Fendorf S. Development of energetic and enzymatic limitations on microbial carbon cycling in soils. *Biogeochemistry* 2021;**153**(2):191–213.

60. Gunina A, Kuzyakov Y. From energy to (soil organic) matter. *Glob Chang Biol* 2022;**28**(7):2169–82.

61. Dungait JAJ, Hopkins DW, Gregory AS, Whitmore AP. Soil organic matter turnover is governed by accessibility not recalcitrance. *Glob Chang Biol* 2012;**18**(6):1781–96.

62. Hu Z, McKenna AM, Wen K, Zhang B, Mao H, Goual L, et al. Controls of Mineral Solubility on Adsorption-Induced Molecular Fractionation of Dissolved Organic Matter Revealed by 21 T FT-ICR MS. *Environ. Sci. Technol.* 2024;**58**(5):2313–22.

63. Cornell RM, Schwertmann U. *The iron oxides*. 2nd ed. Weinheim: Wiley-VCH; 2003.

64. Tipping E. The adsorption of aquatic humic substances by iron oxides. *Geochimica et Cosmochimica Acta* 1981;**45**(2):191–9.

65. Jain A, Raven KP, Loeppert RH. Arsenite and Arsenate Adsorption on Ferrihydrite: Surface Charge Reduction and Net OH - Release Stoichiometry. *Environ. Sci. Technol.* 1999;**33**(8):1179–84.

66. Bompoti N, Chrysochoou M, Machesky M. Surface structure of ferrihydrite: Insights from modeling surface charge. *Chemical Geology* 2017;**464**:34–45.

67. Gu B, Schmitt J, Chen Z, Liang L, McCarthy JF. Adsorption and desorption of natural organic matter on iron oxide: mechanisms and models. *Environ. Sci. Technol.* 1994;**28**(1):38–46.

68. Gu B, Schmitt J, Chen Z, Liang L, McCarthy JF. Adsorption and desorption of different organic matter fractions on iron oxide. *Geochimica et Cosmochimica Acta* 1995;**59**(2):219–29.

69. McAdams BC, Hudson J, Arnold WA, Chin Y-P. Effects of aquatic dissolved organic matter redox state on adsorption to goethite. *Aquat Sci* 2023;**85**(1).

70. Sowers TD, Adhikari D, Wang J, Yang Y, Sparks DL. Spatial Associations and Chemical Composition of Organic Carbon Sequestered in Fe, Ca, and Organic Carbon Ternary Systems. *Environ. Sci. Technol.* 2018;**52**(12):6936–44.

71. Sodano M, Lerda C, Nisticò R, Martin M, Magnacca G, Celi L, et al. Dissolved organic carbon retention by coprecipitation during the oxidation of ferrous iron. *Geoderma* 2017;**307**:19–29.

72. Possinger AR, Zachman MJ, Dynes JJ, Regier TZ, Kourkoutis LF, Lehmann J. Co-precipitation induces changes to iron and carbon chemistry and spatial distribution at the nanometer scale. *Geochimica et Cosmochimica Acta* 2021;**314**:1–15.

73. Chen K-Y, Chen T-Y, Chan Y-T, Cheng C-Y, Tzou Y-M, Liu Y-T, et al. Stabilization of Natural Organic Matter by Short-Range-Order Iron Hydroxides. *Environ. Sci. Technol.* 2016;**50**(23):12612–20.

74. Nierop KGJ, Jansen B, Verstraten JM. Dissolved organic matter, aluminium and iron interactions: precipitation induced by metal/carbon ratio, pH and competition. *Science of The Total Environment* 2002;**300**(1-3):201–11.

75. Theis TL, Singer PC. Complexation of iron(II) by organic matter and its effect on iron(II) oxygenation. *Environ. Sci. Technol.* 1974;**8**(6):569–73.

76. Daugherty EE, Gilbert B, Nico PS, Borch T. Complexation and Redox Buffering of Iron(II) by Dissolved Organic Matter. *Environ. Sci. Technol.* 2017;**51**(19):11096–104.

77. Ma H, Wang P, Thompson A, Xie Q, Zhu M, Teng HH, et al. Secondary Mineral Formation and Carbon Dynamics during FeS Oxidation in the Presence of Dissolved Organic Matter. *Environ. Sci. Technol.* 2022;**56**(19):14120–32.

78. Young R, Avneri-Katz S, McKenna A, Chen H, Bahureksa W, Polubesova T, et al. Composition-Dependent Sorptive Fractionation of Anthropogenic Dissolved Organic Matter by Fe(III)-Montmorillonite. *Soil Syst.* 2018;**2**(1):14.

79. Byrne JM, Kappler A. A revised analysis of ferrihydrite at liquid helium temperature using Mössbauer spectroscopy. *American Mineralogist* 2022;**107**(8):1643–51.

80. Murad E, Cashion J. Mössbauer Spectroscopy of Environmental Materials and Their Industrial Utilization. New York, NY: Springer; 2011.

81. Murad E, Schwertmann U. The influence of crystallinity on the Mössbauer spectrum of lepidocrocite. *Mineral. mag.* 1984;**48**(349):507–11.

82. Schwertmann U, Wagner F, Knicker H. Ferrihydrite–Humic Associations. *Soil Science Society of America Journal* 2005;**69**(4):1009–15.

83. ThomasArrigo LK, Notini L, Shuster J, Nydegger T, Vontobel S, Fischer S, et al. Mineral characterization and composition of Fe-rich flocs from wetlands of Iceland: Implications for Fe, C and trace element export. *Sci Total Environ* 2022;**816**:151567.

84. Curti L, Moore OW, Babakhani P, Xiao K-Q, Woulds C, Bray AW, et al. Carboxyl-richness controls organic carbon preservation during coprecipitation with iron (oxyhydr)oxides in the natural environment. *Commun Earth Environ* 2021;**2**(1):1–13.

85. Mikutta C, Frommer J, Voegelin A, Kaegi R, Kretzschmar R. Effect of citrate on the local Fe coordination in ferrihydrite, arsenate binding, and ternary arsenate complex formation. *Geochimica et Cosmochimica Acta* 2010;**74**(19):5574–92.

86. Michel FM, Ehm L, Antao SM, Lee PL, Chupas PJ, Liu G, et al. The structure of ferrihydrite, a nanocrystalline material. *Science* 2007;**316**(5832):1726–9.

87. Niemeyer J, Chen Y, Bollag J-M. Characterization of Humic Acids, Composts, and Peat by Diffuse Reflectance Fourier-Transform Infrared Spectroscopy. *Soil Science Society of America Journal* 1992;**56**(1):135–40.

88. Tfaily MM, Cooper WT, Kostka JE, Chanton PR, Schadt CW, Hanson PJ, et al. Organic matter transformation in the peat column at Marcell Experimental Forest: Humification and vertical stratification. *J. Geophys. Res. Biogeosci.* 2014;**119**(4):661–75.

89. Kaiser K, Guggenberger G. Sorptive stabilization of organic matter by microporous goethite: sorption into small pores vs. surface complexation. *Eur J Soil Sci* 2007;**58**(1):45–59.

90. Lv J, Zhang S, Wang S, Luo L, Cao D, Christie P. Molecular-Scale Investigation with ESI-FT-ICR-MS on Fractionation of Dissolved Organic Matter Induced by Adsorption on Iron Oxyhydroxides. *Environ Sci Technol* 2016;**50**(5):2328–36.

91. Coward EK, Ohno T, Sparks DL. Direct Evidence for Temporal Molecular Fractionation of Dissolved Organic Matter at the Iron Oxyhydroxide Interface. *Environ Sci Technol* 2019;**53**(2):642–50.

92. Riedel T, Zak D, Biester H, Dittmar T. Iron traps terrestrially derived dissolved organic matter at redox interfaces. *Proc Natl Acad Sci U S A* 2013;**110**(25):10101–5.

93. Boye K, Noël V, Tfaily MM, Bone SE, Williams KH, Bargar JR, et al. Thermodynamically controlled preservation of organic carbon in floodplains. *Nat. Geosci.* 2017;**10**(6):415–9.

94. Huang X, Liu X, Liu J, Chen H. Iron-bound organic carbon and their determinants in peatlands of China. *Geoderma* 2021;**391**:114974.

95. Lagarec K, Rancourt DG. Extended Voigt-based analytic lineshape method for determining N-dimensional correlated hyperfine parameter distributions in Mössbauer spectroscopy. *Nuclear Instruments and Methods in Physics Research Section B: Beam Interactions with Materials and Atoms* 1997;**129**(2):266–80.

96. Brunauer S, Emmett PH, Teller E. Adsorption of Gases in Multimolecular Layers. *J. Am. Chem. Soc.* 1938;**60**(2):309–19.

97. Kaur N, Gräfe M, Singh B, Kennedy B. Simultaneous Incorporation of Cr, Zn, Cd, and Pb in the Goethite Structure. *Clays and Clay Minerals* 2009;**57**(2):234–50.

98. Waychunas G, Rea B, Fuller C, Davis J. Surface chemistry of ferrihydrite: Part 1. EXAFS studies of the geometry of coprecipitated and adsorbed arsenate. *Geochimica et Cosmochimica Acta* 1993;**57**(10):2251–69.

99. ThomasArrigo LK, Kaegi R, Kretzschmar R. Ferrihydrite Growth and Transformation in the Presence of Ferrous Iron and Model Organic Ligands. *Environ. Sci. Technol.* 2019;**53**(23):13636–47.

100. Mikutta C, Mikutta R, Bonneville S, Wagner F, Voegelin A, Christl I, et al. Synthetic coprecipitates of exopolysaccharides and ferrihydrite. Part I: Characterization. *Geochimica et Cosmochimica Acta* 2008;**72**(4):1111–27.

101. Karlsson T, Persson P. Coordination chemistry and hydrolysis of Fe(III) in a peat humic acid studied by X-ray absorption spectroscopy. *Geochimica et Cosmochimica Acta* 2010;**74**(1):30–40.

Supporting Information

Text S1. Ferrihydrite characterization

[57]Fe Mössbauer spectroscopy was used to confirm mineral identity. Samples were inserted into a closed-cycle exchange gas cryostat (Janis cryogenics) under a backflow of He. Spectra were collected at 6 K using a constant acceleration drive system (WissEL) in transmission mode with a [57]Co/Rh source. All spectra were calibrated against an α-[57]Fe foil that was measured at room temperature. Data analysis was performed using Recoil (University of Ottawa) and the extended Voigt Based Fitting routine[95]. The half width at half maximum was constrained to 0.138 mm s^{-1} during fitting.

Specific surface area was determined by Micromeritics Gemini VII surface area and porosity analyzer (Micromeritics Instrument Corporation, USA) on freeze-dried aliquots. For surface area analysis, freeze-dried samples were outgassed with N_2 for 24 h at 298 K to avoid mineral transformation[19] and N_2 adsorption was quantified at 77 K at partial pressure ranges from 0.05 to 0.3 p/p_0. Specific surface area was determined by the BET (Brunauer-Emmett-Teller) equation[96].

Text S2. Calculation of bound organic carbon amount and Langmuir isotherm fitting

To calculate the mass of OC bound to ferrihydrite, the dissolved OC concentration remaining in solution after adsorption (equilibrium DOC) was subtracted from the initial dissolved OC concentration of each dilution and normalized to the measured ferrihydrite content. The DOC concentration in DOC-free control was used for blank correction. The mass of bound OC in all the adsorption experiments was used to create Langmuir isotherms which enable to calculate the maximum adsorption capacity (q_{max}) of each WEOM type to ferrihydrite[63]:

$$q = q_{max} \frac{K_L \times c_{eq}}{1 + K_L \times c_{eq}} \qquad \textbf{Eq (1)}$$

The variable q stands for the amount of adsorbed OC [mg OC g[-1] Fh], K_L is the sorption coefficient [L mg^{-1} C] and c_{eq} is the equilibrium concentration of DOC in the aqueous phase [mg C L^{-1}]. Best fit parameters of K_L and q_{max} were obtained by minimizing the square difference of the q values based on experimental data and the initial model. A 95% confidence interval was calculated to assess the uncertainty of the model fit.

Text S3. Fe *K*-edge X-ray absorption spectroscopy (XAS)

Data processing included energy calibration of all sample spectra to the reference foil, pre-edge subtraction and post-edge normalization, as well as adjustment of the edge energy of each spectrum to the zero-crossing of the second-derivative of the X-ray absorption near-edge structure (XANES) region using Athena[54]. Linear combination fitting (LCF) of the XANES spectra was done from -20 to 30 eV (around the edge energy) with ferrihydrite and Fe(II)-citrate as references to determine Fe oxidation state. Fe speciation was determined by LCF of the k^3-weighted extended X-ray absorption fine structure (EXAFS) spectra in a *k* range from 2 to 11 Å^{-1}. The following references were included: ferrihydrite, lepidocrocite, Fe(III)-citrate and Fe(III)-catechol. The edge energy of all spectra and reference samples was set to 7128 eV. Components were constrained between 0 and 100% during LCF fitting, but no constraints were set for the sum of all components. Initial fractions of detected Fe phases were re-calculated to sum up to 100%. The Fe binding environment was further determined by shell fitting, using Artemis[54]. Therefore, the k^3-weighted EXAFS spectra were Fourier-transformed in a *k*-range from 2 to 12 Å^{-1} using the Kaiser-Bessel window function, width of 3 Å^{-1} and Rbkg of 1. Theoretical phase-shift and amplitude functions were calculated with FEFF v.6 based on the structure of goethite[97].

Text S4. Fourier-transform ion-cyclotron-resonance mass spectrometry (FT-ICR-MS)

Samples were injected undiluted into the electrospray chamber at 120 µL/h by a syringe pump. 500 scans were averaged per sample and spectra were internally calibrated using well-known constituents of NOM spanning m/z ratios from 255 to 949 with a mass error less than 0.5 ppm. Data processing was done using Compass Data Analysis (Bruker, Bremen, Germany) and formula assignment of peaks with a signal to noise ratio higher than 4 was performed by an in-house software of the Research Unit Analytical Biogeochemistry (Helmholtz Center Munich). Recovery of the solid phase extraction was checked by drying methanol extracts under constant N_2 flow. Samples were re-dissolved with DDI water and dissolved OC concentration was measured by a TOC analyzer (multi N/C 2100S, Analytik Jena AG, Germany). Recovery was 84 ± 28%. It is known that SPE has a bias towards specific OC classes but we assume that this bias is similar for samples before and after binding for each WEOM type.

Text S5. Shell fitting of Fourier-transformed Fe *K*-edge EXAFS

To elucidate changes in local coordination environment and crystal structure, we conducted shell fitting analysis on the Fourier-transformed Fe *K*-edge EXAFS region. All

spectra showed two dominant shells: one at ca. 1.99 Å, corresponding to a single scatter Fe-O path, and one feature ranging from 2.1 to 3.6 Å, which was fit with two single-scatter Fe-Fe paths (Figure S). The two Fe-Fe paths are defined as edge-sharing Fe-Fe$_1$ (R= 3.00-3.05 Å) and corner-sharing Fe-Fe$_2$ (R=3.41-3.47 Å). Their coordination numbers (CNs) varied depending on OC binding mechanism (adsorption vs coprecipitation) and type of used WEOM (Table S7). All samples of ferrihydrite with adsorbed WEOM had CNs that are typical for ferrihydrite[17,98,99], with 2.1-2.6 and 1.9 for Fe-Fe$_1$ and Fe-Fe$_2$, respectively. In contrast, CNs of Fe-Fe$_2$ were slightly lower in coprecipitates (0.6 for coprecipitates with palsa WEOM and 1.4 for coprecipitates with bog WEOM). A decrease in corner-sharing Fe-Fe paths due to increased OC content has been described before[99,100] and could indicate lower ferrihydrite particle size[85] and/or lower crystallinity due to impeded crystal growth in the crystallographic z-axis[86]. However, our CN values cannot be directly compared between adsorption and coprecipitation samples, since Debye-Waller parameters (σ^2) were differently defined in each set, according to the mean values of initially floated σ^2 of samples in each set. The values of σ^2 could be slightly different due to structural ordering differences[73,101]. Within the coprecipitate set, the ones formed with palsa WEOM are likely more poorly crystalline than with bog WEOM, based on CN values of Fe-Fe paths. A higher proportion of carboxylic groups could lead to a lower crystallinity[84].

Figure S1. Map of Stordalen Mire (Abisko, Sweden) with marked sampling points. Abbreviation OH stands for organic horizon (used for water extracts). Image from Google Earth, taken in August 2022.
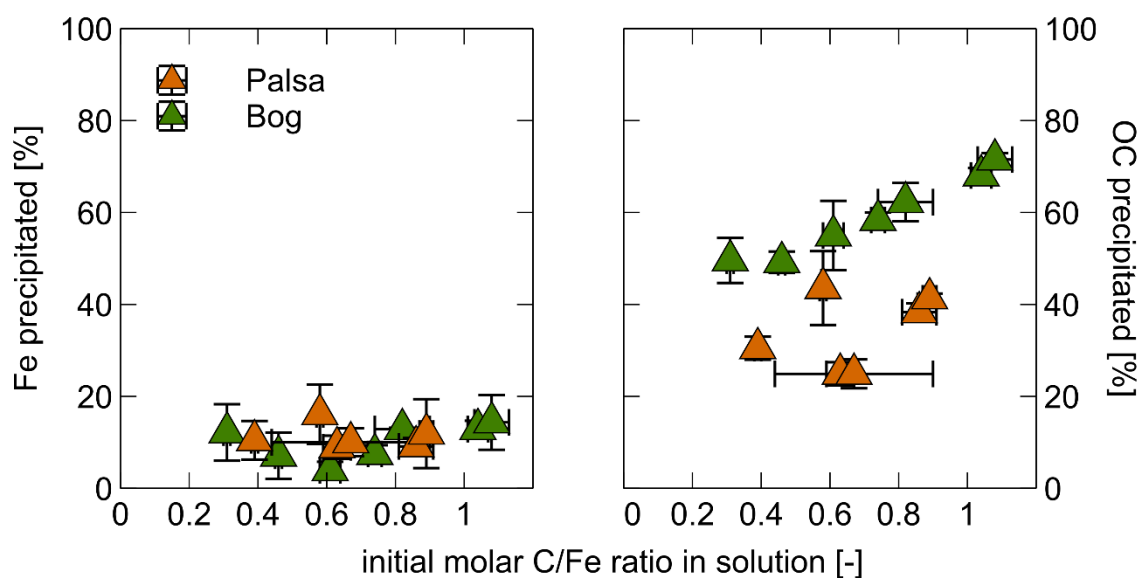

Figure S2. Percentage of precipitated Fe (left) and organic carbon (right) from WEOM of palsa and bog soils by coprecipitation as function of the initial molar C/Fe ratio [mol/mol]. All data points and error bars represent the average and standard deviation of experimental triplicates.
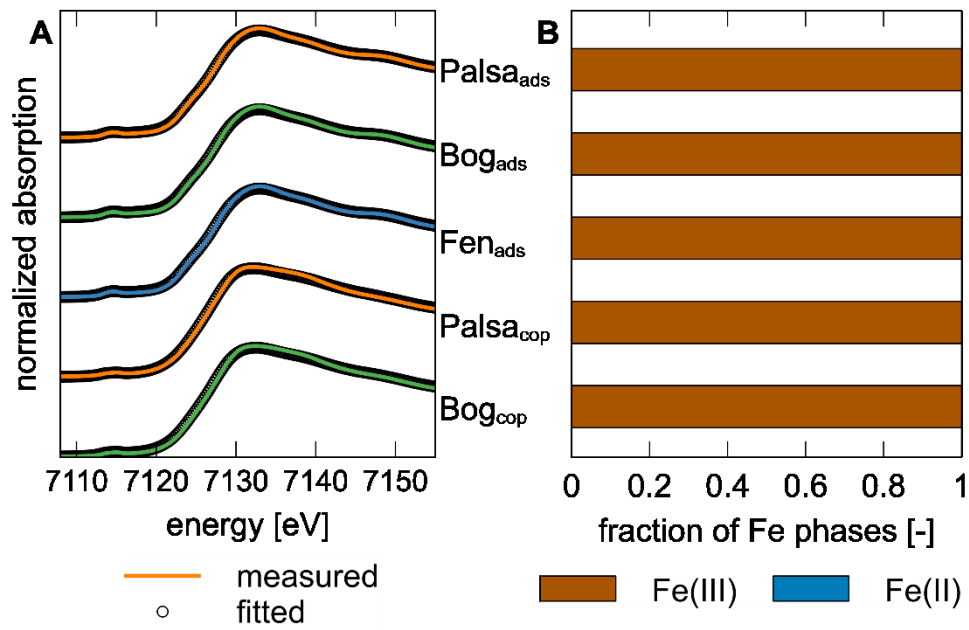
Figure S3. Linear combination fitting of Fe *K*-edge X-ray absorption near edge structure spectra of ferrihydrite with adsorbed WEOM (ads) of palsa, bog and fen soils, and Fe-OC coprecipitates (cop) synthesized with WEOM from palsa and bog soils (A). Speciation of Fe in Fe-OC associations. The same labelling as for graph (A) applies. All Fe was Fe(III) (B). Ferrihydrite and Fe(II)-citrate were used as reference spectra for Fe(III) and Fe(II), respectively.
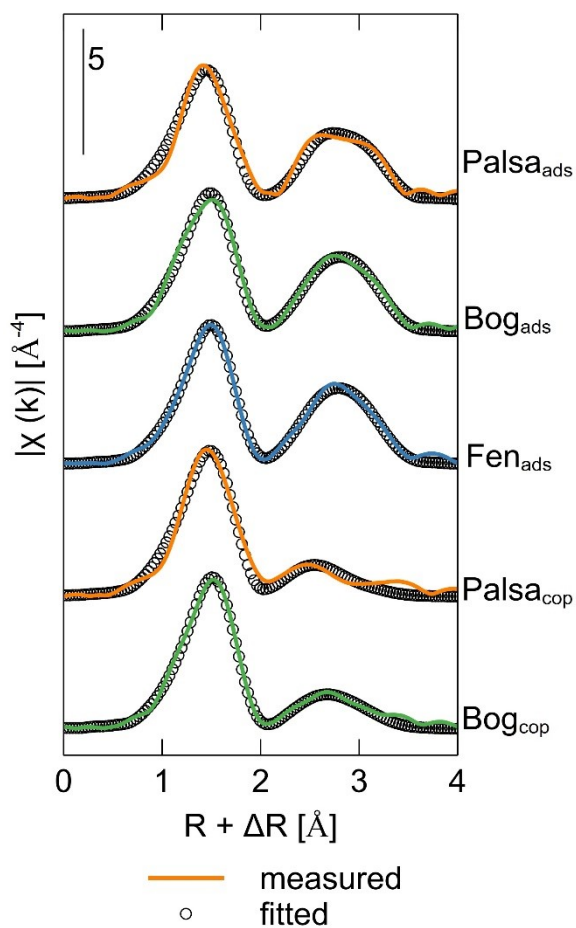
Figure S4. Fe *K*-edge Fourier-transform magnitudes of ferrihydrite with adsorbed WEOM (ads) of palsa, bog and fen, and Fe-OC coprecipitates (cop) synthesized with WEOM from palsa and bog soils. Solid lines show the measured data and open circles represent the fitted model. Fitting parameters are displayed in Table S7**Fehler! Verweisquelle konnte nicht gefunden werden.**.
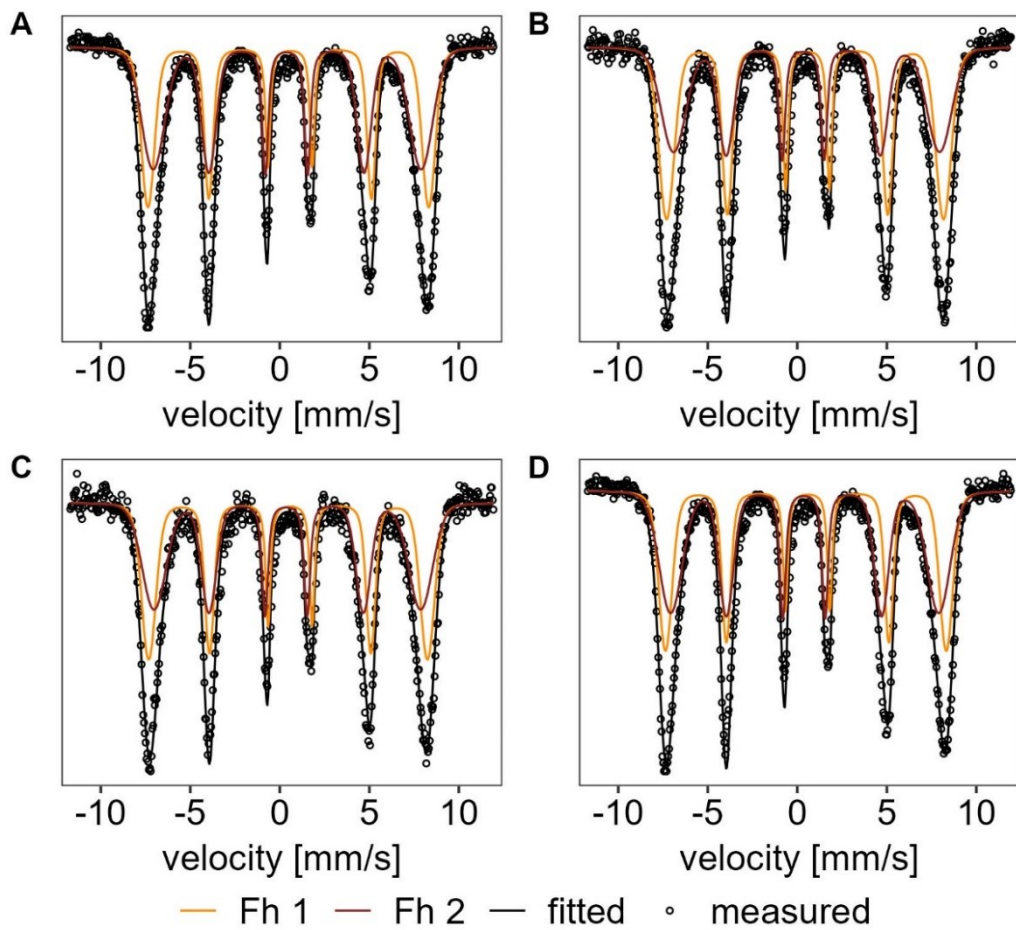
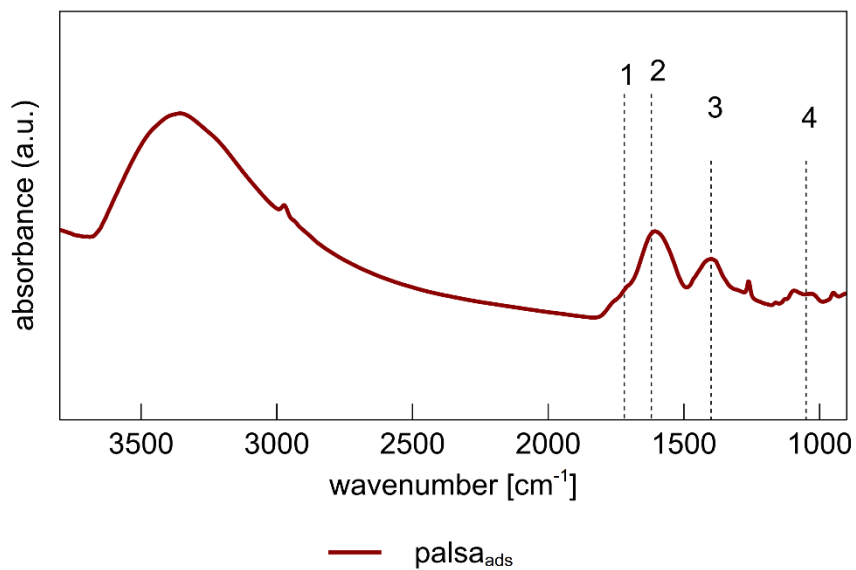**Figure S5**. Mössbauer spectra of initial ferrihydrite (A) and with adsorbed WEOM from palsa (B), bog (C) and fen (D), measured at 6 K.

Figure S6. Example of a FTIR spectra from 900-3700 cm^{-1} of solids post-adsorption using WEOM from palsa. Numbers stand for the FTIR bands that were interpreted in the main text: 1 = 1720 cm^{-1} (C=O stretch in COOH), 2 = 1630 cm^{-1} (aromatic C=C stretch and/or asymmetric COO$^-$ stretch), 3 = 1400 cm^{-1} (symmetric COO$^-$ stretch), 4 = 1050 cm^{-1} (C-O stretch of carbohydrates) according to the references given in Table S9.
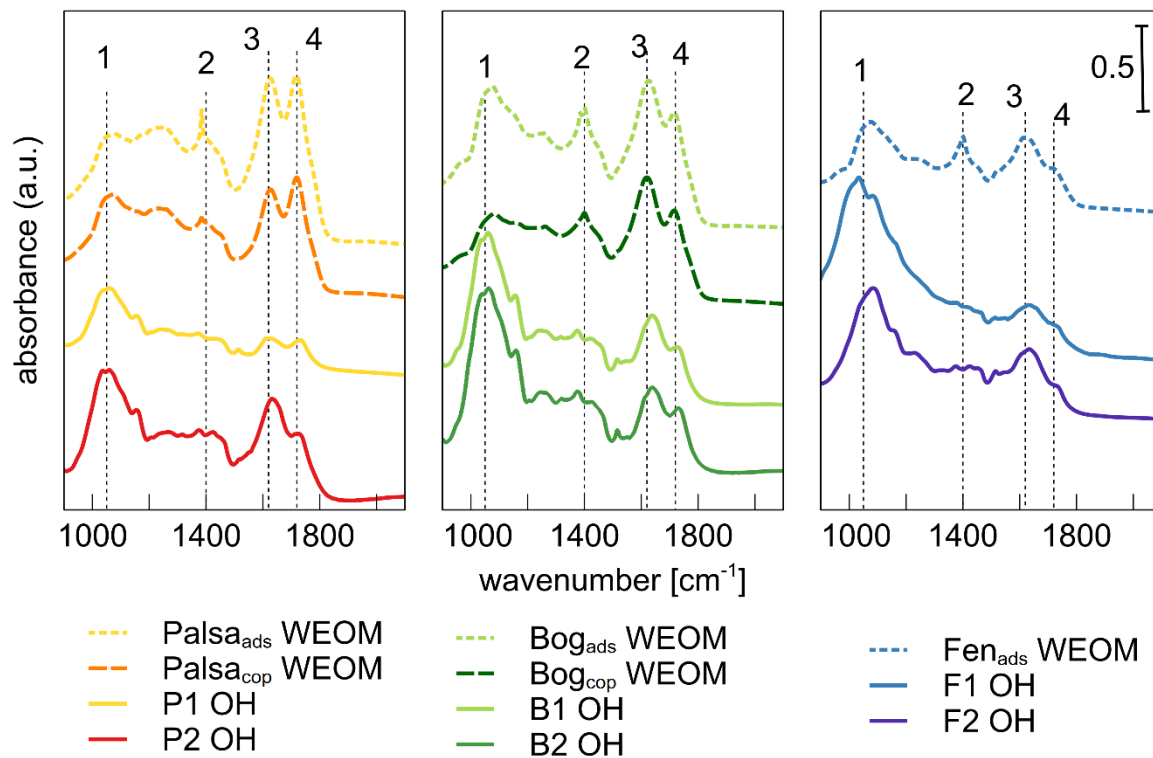
Figure S7. FTIR spectra of the initial WEOM of palsa, bog and fen soils used for adsorption with ferrihydrite (ads) and of palsa and bog soils used for coprecipitation with dissolved Fe(II) (cop) in comparison to solid phase OM from the same soil horizon (OH= organic horizon) of representative soil cores. Numbers stand for the following wavenumbers and functional groups: 1 = 1050 cm^{-1} (C-O stretch of carbohydrates), 2 = 1400 cm^{-1} (symmetric COO- stretch), 3 = 1630 cm^{-1} (aromatic C=C stretch and/or asymmetric COO- stretch), 4 = 1720 cm^{-1} (C=O stretch in COOH).
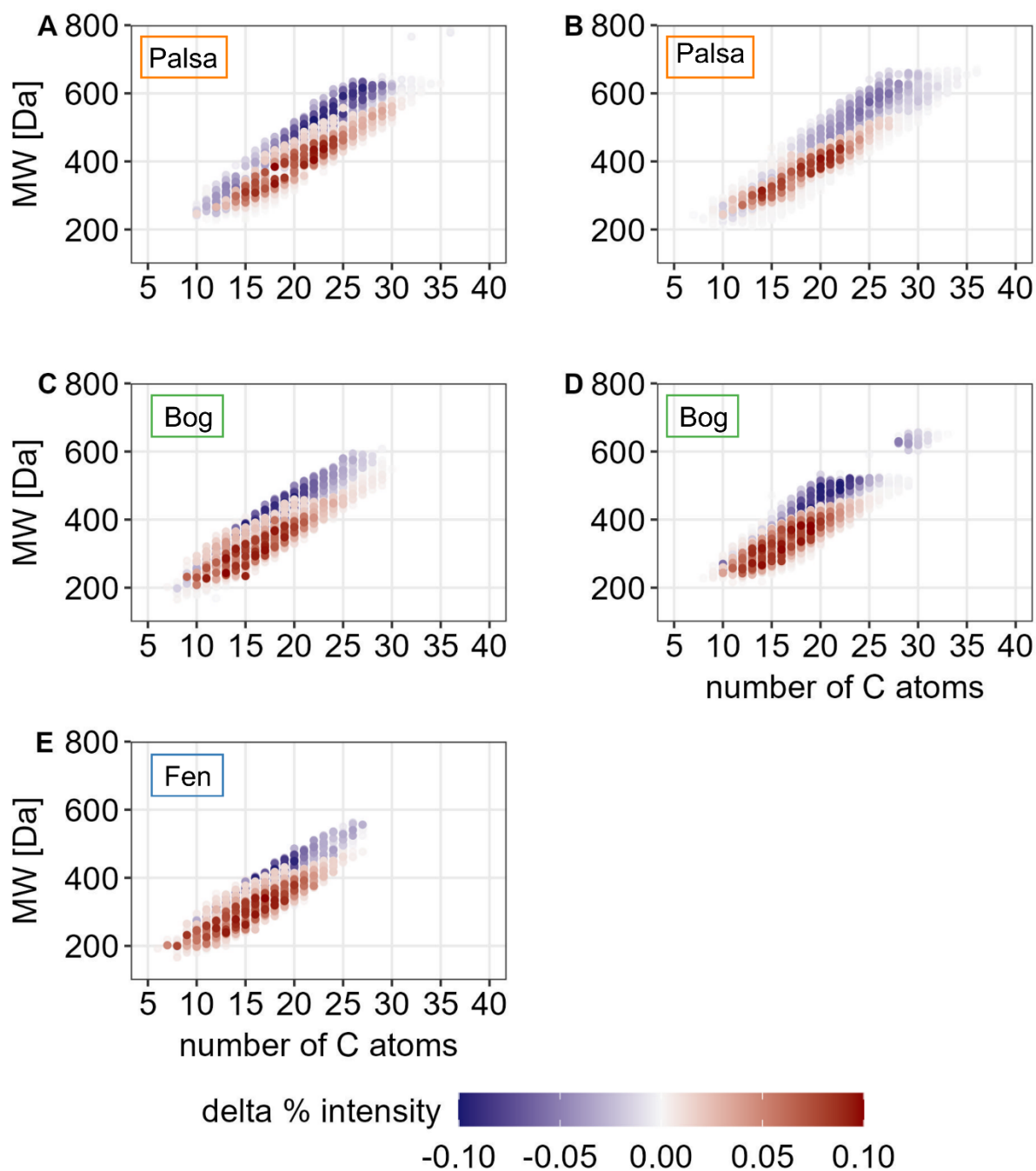
Figure S8. Molecular weight against number of C atoms in a detected molecule before and after adsorption of ferrihydrite with WEOM of palsa (A), bog (C), and fen (E), and coprecipitation of dissolved Fe(II) with WEOM (B, D) from palsa (B) and bog (D) soils. Organic matter compounds which are lost from the dissolved phase, i.e., preferentially bound during adsorption or coprecipitation, are displayed in blue and those retained in solution in red.
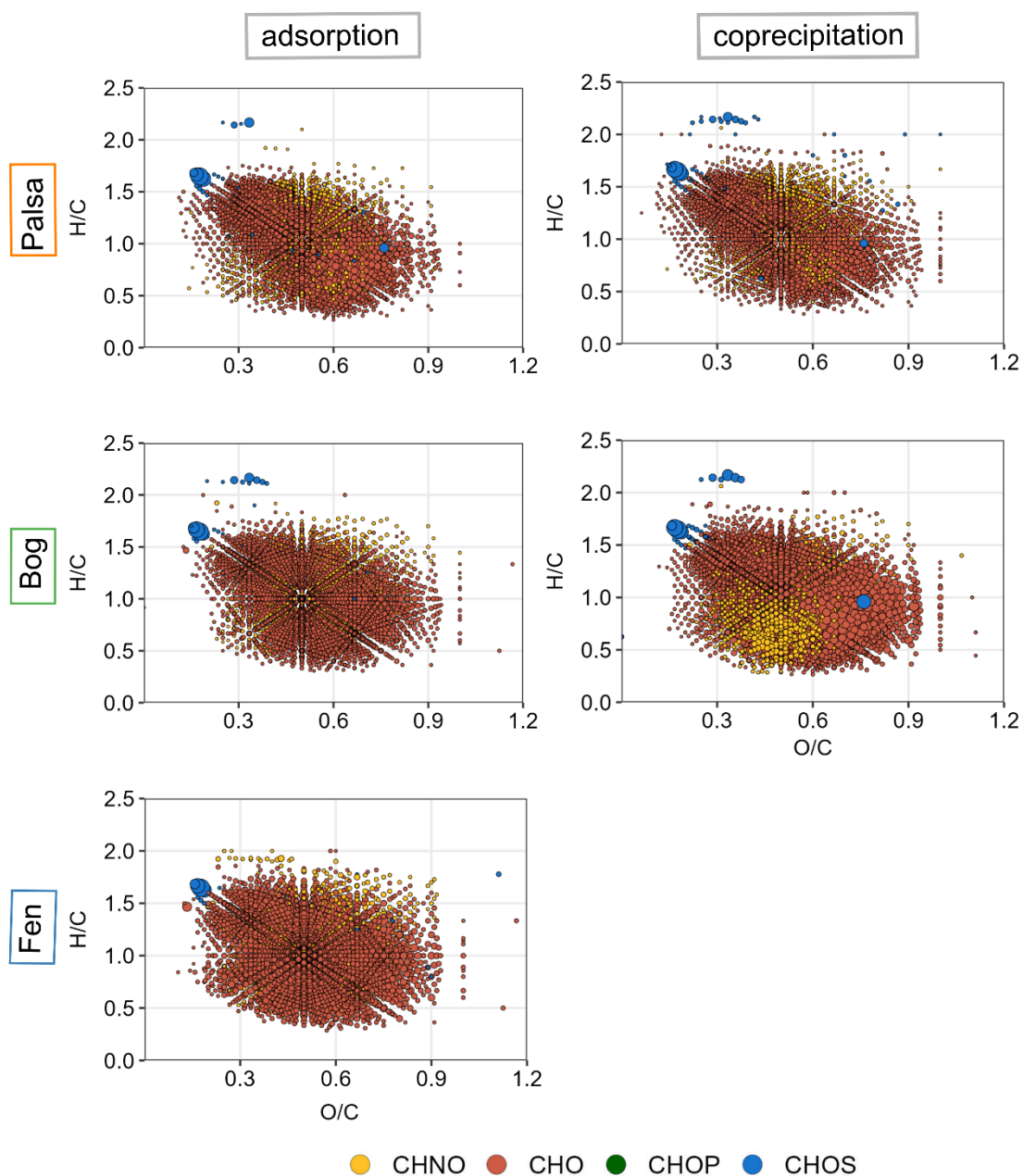
Figure S9. Initial composition of water-extractable organic matter from each experiment, displaying Van Krevelen diagrams (H/C against O/C) of each OC compound. The size of each circle represents the relative intensity of the given OC compound and the colour indicates the elemental composition.
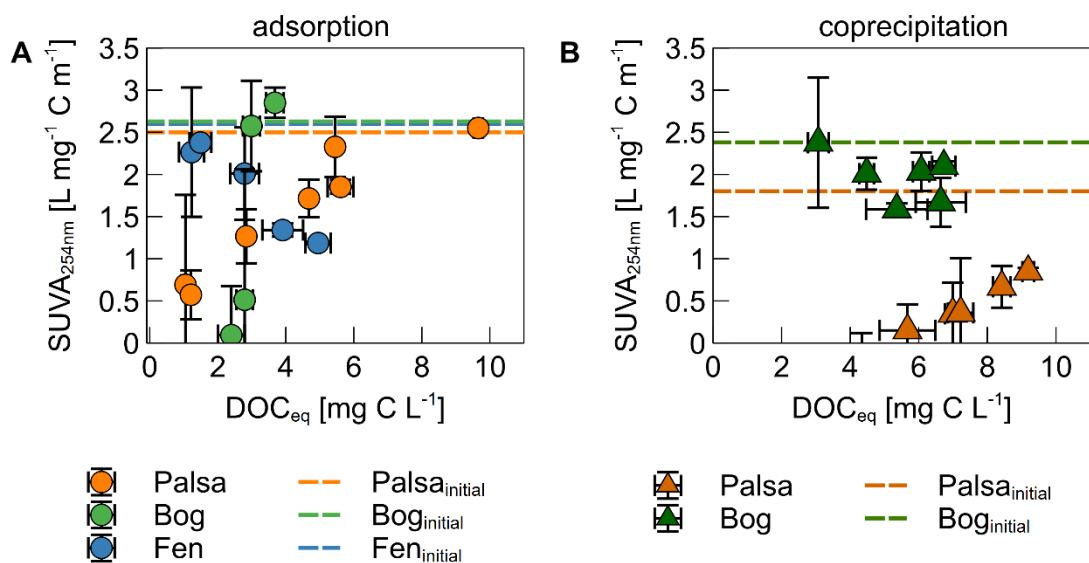
Figure S10. Specific ultraviolet absorption (SUVA₂₅₄) measured at 254 nm of WEOM from palsa, bog and fen soils after adsorption to ferrihydrite (A) or coprecipitation of dissolved Fe(II) with WEOM from palsa and bog soils (B) against the dissolved organic carbon in equilibrium. The SUVA value of the initial WEOM is displayed as a dotted line for each experiment. Some absolute absorption values were below detection limit (e.g. for bog adsorption experiment) and are thus not included in the graph. All data points and error bars represent the average and standard deviation of experimental triplicates, respectively.

Table S1. Overview of conducted adsorption and coprecipitation experiments, including the initial OC concentration in WEOM, pH of the experiment, resulting maximum OC binding capacity (q_{max}) and goodness of fit (R^2).

Experiment		thaw stage	Initial OC [mg C/L]	pH	q_{max} [mg C/ g Fh][a]	q_{max} [mg C/g Fe]	R^2
Adsorption ferrihydrite	with	Palsa	17.9	4.5	204	391[b]	0.96
		Bog	9.81	4.5	226	433[b]	0.80
		Fen	12.7	6.0	80.9	155[b]	0.78
Coprecipitation dissolved Fe(II)	with	Palsa	16.4	4.5		925[c]	n.a.
		Bog	23.5	4.5		1532[c]	n.a.

[a] estimated via Langmuir fitting
[b] re-calculated per g Fe for adsorption experiments
[c] based on highest measured C:Fe ratio in solid by coprecipitation

Table S2. Parameters of adsorption experiments including specific surface area (SSA) of ferrihydrite, initial molar C:Fe ratios in solution, added ferrihydrite concentrations and resulting mean bound OC content.

thaw stage	SSA of added ferrihydrite [m²/g]	initial C:Fe ratio [mol/mol]	added ferrihydrite [mg/L]	bound OC [mg C/g Fh]
Palsa	195	0.5	80.0	60.7
		0.8	80.0	93.3
		1.0	80.0	134.1
		1.2	80.0	140.7
		1.6	80.0	151.7
		1.9	80.0	182.4
		2.0	80.0	197.2
		2.1	80.0	193.2
		3.3	50.0[1]	199.1
Bog	203	0.5	50.0	58.7
		0.9	50.0	75.3
		1.1	50.0	121.1
		1.3	50.0	107.7
		1.6	50.0	134.0
		1.7	50.0	149.8
		1.8	50.0	148.0
		2.5	40.0[1]	161.0
Fen	195	0.5	70.0	37.92
		0.7	70.0	44.92
		1.0	70.0	57.10
		1.1	70.0	84.03
		1.4	70.0	76.01
		1.7	70.0	77.71
		1.8	70.0	70.24

[1]Ferrihydrite concentrations were decreased to attempt to reach the saturation threshold and better constrain the Langmuir fit.

Table S3. Maximum organic carbon to iron weight ratios (C:Fe) of formed Fe-OC associations with organic carbon from palsa, bog and fen soils in adsorption and coprecipitation laboratory experiments (this study) compared to field-based studies. Ratios represent previously published values of ferrihydrite-coated sand that was exposed over 2 months in permafrost soils and average ± standard deviation of dithionite-citrate-bicarbonate (DCB) extractions from soil cores across different sites.

thaw stage	C:Fe [g/g]			
	adsorption	coprecipitation	ferrihydrite sand[1] (Stordalen Mire)	DCB extractions (Stordalen Mire)[2,3]
Palsa	0.39 ± 0.04	0.93 ± 0.4		8.7 ± 3.6
Bog	0.44 ± 0.01	1.53 ± 0.9	0.28	7.3 ± 5.1
Fen	0.16 ± 0.01		0.73	0.0 ± 0.0

[1]Patzner et al, 2022a
[2]Patzner et al., 2020
[3]Patzner et al., 2022b

Table S4. Cation concentrations measured in the initial WEOM of each thaw stage, used for adsorption (ads) and coprecipitation (cop) experiments. Measurements were done using inductively coupled plasma mass spectrometry (ICP-MS, Agilent 7900, Agilent Technologies, USA) with Ar as carrier gas and in He mode for Al, K, Ca and no-gas mode for Mg.

WEOM	Mg [µM]	Al [µM]	K [µM]	Ca [µM]
Palsa_ads	0.6	1.3	2.5	3.5
Bog_ads	0.0	0.6	1.0	3.1
Fen_ads	0.0	0.3	7.4	0.1
Palsa_cop	0.0	0.2	4.1	1.5
Bog_cop	0.4	0.5	1.3	5.4

Table S5. Linear combination fit results for Fe K-edge XANES spectra of ferrihydrite with adsorbed WEOM (ads) of palsa, bog and fen, and Fe-OC coprecipitates (cop) synthesized with WEOM from palsa and bog soils. Ferrihydrite and Fe(II)-citrate were used as reference spectra for Fe(III) and Fe(II), respectively.

sample	Fe(III) [%]	Fe(II) [%]	NSSR[a] [%]	red. $X^{2,b}$ [%]
Palsa_ads	100	0	0.05	0.01
Bog_ads	100	0	0.10	0.02
Fen_ads	100	0	0.06	0.02
Palsa_cop	100	0	0.10	0.10
Bog_cop	100	0	0.15	0.15

[a] normalized sum of of squared residuals (residuals (100 $\sum_i$ (data$_i$-fit$_i$)^2/$\sum_i$ data^2)
[b] measure of fit accuracy ((N_{idp} /N_{pts}) $\sum_i$ ((data$_i$-fit$_i$)/ε_i)^2(N_{idp}-N_{var})$^{-1}$)). N_{idp} /N_{pts} and N_{var} are the number of independent points in the model fit (37.5), the total number of data points (250) and the number of fit variables (2), respectively.

Table S6. Linear combination fit results for Fe K-edge EXAFS spectra of ferrihydrite with adsorbed WEOM (ads) of palsa, bog and fen, and Fe-OC coprecipitates (cop) synthesized with WEOM from palsa and bog soils.

sample	ferrihydrite [%]	lepidocrocite [%]	Fe(III)-OM [%]	NSSR[a] [%]	red. $X^{2,b}$ [-]
Palsa_ads	95	5	0	3.0	0.08
Bog_ads	92	8	0	2.7	0.20
Fen_ads	91	9	0	2.5	0.07
Palsa_cop	63	0	37	6.0	0.10
Bog_cop	64	0	36	1.6	0.28

[a] normalized sum of of squared residuals (residuals (100 $\sum_i$ (data$_i$-fit$_i$)^2/$\sum_i$ data^2)
[b] measure of fit accuracy ((N_{idp} /N_{pts}) $\sum_i$ ((data$_i$-fit$_i$)/ε_i)^2(N_{idp}-N_{var})$^{-1}$)). N_{idp} /N_{pts} and N_{var} are the number of independent points in the model fit (18.2), the total number of data points (181) and the number of fit variables (2-4), respectively.

Table S7. Shell-fit parameters determined from Fourier-transformed Fe *K*-edge EXAFS spectra of ferrihydrite with adsorbed WEOM (ads) of palsa, bog and fen, and Fe-OC coprecipitates (cop) synthesized with WEOM from palsa and bog soils.

sample	ΔE_0[a] [eV]	Fe-O			Fe-Fe$_1$		Fe-Fe$_2$		NSSR[e] [%]	red. $X^{2,f}$
		CN[b]	R[c] [Å]	$\sigma^{2,d}$	CN	R [Å]	CN	R [Å]		
Palsa$_{ads}$	-5.12 ± 1.78	5.5	1.97	0.012	2.1	3.03	1.9	3.44	2.0	468
Bog$_{ads}$	-3.07 ± 1.27	5.4	1.98	0.011	2.5	3.05	1.9	3.45	1.1	516
Fen$_{ads}$	-3.18 ± 1.15	4.9	1.98	0.010	2.6	3.05	1.9	3.44	0.9	282
Palsa$_{cop}$	-4.39 ± 1.52	6.3	2.00	0.012	2.0	3.00	0.6	3.47	2.1	70
Bog$_{cop}$	-3.00 ± 0.88	5.4	2.00	0.010	2.3	3.05	1.4	3.41	0.7	397

[a]Energy shift parameter
[b]path degeneracy (coordination number)
[c]mean half path length
[d]Debye-Waller parameter
[e]normalized sum of squared residuals ($100 \sum_i (data_i-fit_i)^2/\sum_i data^2$)
[f]measure of fit accuracy ($(N_{idp} /N_{pts}) \sum_i ((data_i-fit_i)/\varepsilon_i)^2(N_{idp}-N_{var})^{-1}$)). N_{idp} ,N_{pts} and N_{var} are the number of independent points in the model fit (16.3), the total number of data points (329) and the number of fit variables (8), respectively.
note: The passive amplitude reduction factor was set to 0.9 for all models and the Debye-Waller parameters were defined as constants within the ferrihydrite with adsorbed WEOM samples and the coprecipitate samples for the Fe-Fe$_1$ (0.012 and 0.017, respectively) and Fe-Fe$_2$ path (0.008 and 0.014, respectively). The Debye-Waller parameters were similar to other published values[73,83]. We tried to include a multiple Fe-O-O scattering path, as reported elsewhere[17,83], but this did not change the fitting parameters or goodness of the fit. We also attempted to include an Fe-C path in the coprecipitate spectra, as has been previously fit in Fe-OC coprecipitates with peat OC[73], but the additional path did not match the spectra or significantly improve the fit (F-test).

Table S8. Mössbauer parameters of the initial ferrihydrite and after adsorption with WEOM from different permafrost thaw stages. Abbreviations stand for: CS = center shift, QS = quadrupole split, H = hyperfine field, X^2 = goodness of fit parameter. The half width at half maximum was constrained to 0.138 mm s^{-1} during fitting.

Sample	Initial C:Fe [molar]	T [K]	Site	CS [mm/s]	QS [mm/s]	H [T]	Relative area [%]	X^2 [-]
Fh_initial	0	77	Fh	0.45	0.91		100.0	1.04
		6	Fh1	0.55	-0.04	48.95	48.3	2.38
			Fh2	0.34	0.05	47.82	51.7	
Fh_Palsa_ads	2.1	6	Fh1	0.50	-0.07	47.96	51.3	1.12
			Fh2	0.42	0.09	46.07	48.7	
Fh_Bog_ads	1.8	6	Fh1	0.52	-0.06	48.27	48.4	1.04
			Fh2	0.39	0.03	46.18	51.6	
Fh_Fen_ads	1.8	6	Fh1	0.53	-0.05	48.62	44.7	1.95
			Fh2	0.39	0.02	46.42	55.3	

Table S9. Assignment of peaks in FTIR spectra (Chen et al. (2014)[19], Tfaily et al. (2014)[88], Niemeyer et al. (1992)[87] and references therein).

wavenumber [cm^{-1}]	assignment
1030, 1050, 1170	C-O and C-OH stretches of carbohydrates
1400	symmetric COO- stretch
1630	aromatic C=C stretch and/or asymmetric COO- stretch
1720	C=O stretch in COOH

Table S10. Peak ratios (PR) of initial WEOM of palsa, bog and fen soils (before binding) and of WEOM bound to ferrihydrite or in Fe-OC coprecipitates (after binding). Values are based on peak height after normalization of FTIR spectra.

type of PR		adsorption			coprecipitation	
		palsa	bog	fen	palsa	bog
1630 cm^{-1}/1050 cm^{-1} (aromatic C=C/ C-O in carbohydrates)	before binding	1.5	1.1	0.9	1.0	1.3
	after binding	3.4	2.7	1.0	1.6	1.2
	% change	128.3	151.0	17.8	50.3	-4.7
1400 cm^{-1}/1050 cm^{-1} (COO$^-$ stretch/ C-O in carbohydrates)	before binding	1.0	0.9	0.8	0.8	0.8
	after binding	2.5	1.8	1.0	1.1	0.8
	% change	156.6	100.5	25.7	32.9	3.0

Table S11. Number of total assigned formulae, N-containing and S-containing formulae as well as (relative intensity weighted,) average parameters across all assigned molecular formulae of measured samples by FT-ICR-MS. Samples include dissolved WEOM from palsa, bog and fen before binding and after binding (by adsorption to ferrihydrite or coprecipitation with dissolved Fe(II)). Abbreviations stand for DBE/C_w= weighted double bond equivalent per number of C atoms in a detected molecule, NOSC= non-weighted nominal oxidation state of organic carbon, $NOSC_w$ = weighted nominal oxidation state of organic carbon, ΔG_{ox}^0= standard molar Gibbs free energy of oxidation half reaction (calculated from unweighted NOSC values), $modAI_w$= weighted modified aromaticity index according to Koch & Dittmar (2006).

| | | adsorption | | | coprecipitation | |
		Palsa	Bog	Fen	Palsa	Bog
Total number of assigned formulae	before binding	3304	3099	3003	3475	3594
	after binding	3253	3045	1918	3667	3650
Number of N-containing molecular formulae	before binding	1118	840	816	1079	1246
	after binding	1152	1125	594	1174	1376
Number of S-containing molecular formulae	before binding	69	60	143	60	66
	after binding	103	217	145	217	179
Molecular mass$_w$ [Da]	before binding	449	376	359	431	428
	after binding	405	333	318	404	353
DBE/C_w	before binding	0.55	0.54	0.56	0.50	0.58
	after binding	0.46	0.42	0.47	0.45	0.50
NOSC	before binding	0.04	0.05	0.02	-0.05	0.07
	after binding	-0.08	-0.22	-0.20	-0.10	-0.07
NOSC$_w$	before binding	-0.01	-0.01	0.02	-0.16	0.14
	after binding	-0.31	-0.45	-0.32	-0.31	-0.16
ΔG_{ox}^0 [kJ mol^{-1} C^{-1}]	before binding	59.3	58.8	59.6	61.6	58.3
	after binding	62.6	66.6	65.9	63.3	62.3
modAI$_w$	before binding	0.39	0.36	0.40	0.33	0.41
	after binding	0.30	0.23	0.30	0.28	0.32

Chapter 3: Author contributions

Reduction of iron-organic carbon associations shifts net greenhouse gas release after initial permafrost thaw

Eva Voggenreiter, Laurel ThomasArrigo, Joachim Kilian, Daniel Straub, Maike Friedel, Mark Stahl, Andreas Kappler, Prachi Joshi

The study was conceptualized by A. Kappler, P. Joshi and myself. A. Kappler acquired the funding. The experiments were designed by A. Kappler, P. Joshi and myself. I performed the experiments. D. Straub and myself formally analyzed the 16S rRNA amplicon sequencing data. M. Friedel collected samples from the field campaign and formally analyzed geochemical parameters. The GC-MS data was acquired by J. Kilian and analyzed by J. Kilian and M. Stahl and myself. L. ThomasArrigo, P. Joshi and myself analyzed the synchrotron spectra. Visualization of the data and writing of the original draft of the manuscript was performed by myself. Supervision was provided by P. Joshi and A. Kappler. All authors contributed to the review and editing of the final manuscript.

Chapter 3:

Reduction of iron-organic carbon associations shifts net greenhouse gas release after initial permafrost thaw

Eva Voggenreiter[1], Laurel ThomasArrigo[2], Joachim Kilian[3], Daniel Straub[4], Maike Friedel[1], Mark Stahl[3], Andreas Kappler[1,5], Prachi Joshi[1,*]

[1] Geomicrobiology, Department of Geosciences, University Tuebingen, Schnarrenbergstrasse 94-96, 72076 Tuebingen, Germany

[2] Environmental Chemistry, University of Neuchâtel, Avenue de Bellevaux 51, CH-2000, Neuchâtel, Switzerland

[3] Center for Plant Molecular Biology, University of Tuebingen, Auf d. Morgenstelle 32, 72076 Tuebingen, Germany

[4] Quantitative Biology Center (QBiC), University of Tuebingen, Auf d. Morgenstelle 10, 72076 Tuebingen, Germany

[5] Cluster of Excellence: EXC 2124: Controlling Microbes to Fight Infection, Tuebingen, Germany

Abstract

In thawing permafrost soils, associations between organic carbon (OC) and ferric iron (Fe(III)) (oxyhydr)oxide minerals may stabilize OC in recently thawed soil layers, thus limiting the microbially mediated release of greenhouse gases (GHGs) such as carbon dioxide (CO_2) and methane (CH_4). Conversely, the development of anoxic conditions during thaw could lead to the microbial reductive dissolution of these Fe(III)-OC associations, resulting in a mobilization of the associated OC with unknown consequences for GHG release. In this study, we investigated the role of Fe(III)-OC associations in soil GHG release during the collapse of previously oxic permafrost soils ("palsa") and the inundation of seasonally anoxic soils ("bog") at Stordalen Mire (Abisko, Sweden). We performed anoxic microcosm experiments using these two soils with the addition of ^{57}Fe-labeled Fe(III)-OC coprecipitates, as well as a field-based experiment, in which we incubated ^{NA}Fe(III)-OC coprecipitates under *in situ* conditions. Results showed that Fe(III)-OC coprecipitates were only stable under oxic conditions in the palsa soil during the field-based experiment, but were fully microbially reduced after 42 days in the microcosm experiments in both soils. Rapid reductive dissolution of 15 and 11% of coprecipitates in palsa and bog soils, respectively, occurred within 1 day. Emissions of GHGs were differently affected for the two soils: In case of the palsa soil, cumulative CO_2 emissions increased by 43±16% after addition of the Fe(III)-OC coprecipitate compared to a no-coprecipitate treatment, due to microbial Fe(III) reduction coupled to OC oxidation and likely additional OC input due to the release of Fe-bound OC. For the bog soil, CH_4 emissions were temporarily suppressed, likely due to inhibition of methanogenesis by Fe(III) reduction of added coprecipitates, as detected by a decrease in *mcrA* gene copies. In conclusion, our findings demonstrate that Fe(III)-OC associations do not provide protection for OC in the case of anoxic conditions after permafrost thaw, with resulting GHG emissions controlled by previous redox status and microbial community.

Graphical abstract
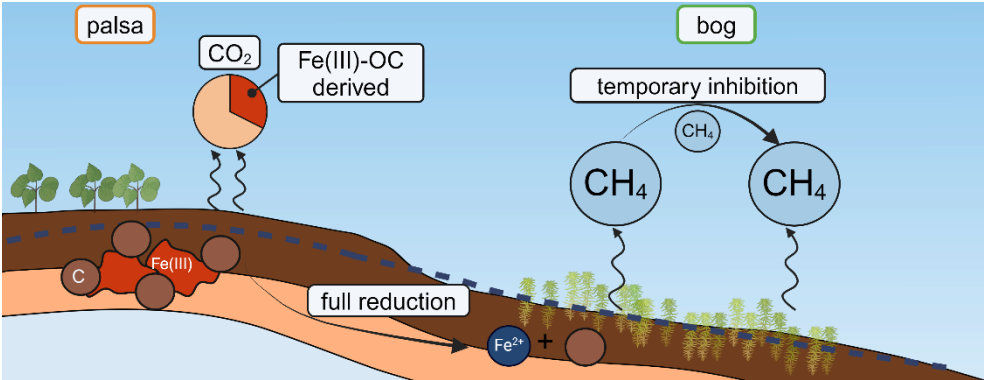
Introduction

Thawing permafrost soils are predicted to be an increasing source of the greenhouse gases (GHGs) carbon dioxide (CO_2) and methane (CH_4) due to higher bioavailability of organic carbon (OC) and higher soil temperatures in the future[1]. Predicted quantities of emitted OC are uncertain, with estimates varying between 37-149 Pg CO_2 and 1090-5050 Tg CH_4 by the year 2100[2]. While most of the mass of emitted OC will stem from CO_2, the majority (up to 70%) of the radiative forcing will come from the emission of CH_4, due to its higher global warming potential (28x over an 100 year timescale)[3,4]. The high variability of projected GHG emissions are due to the multifaceted responses of permafrost areas to thaw, based on their hydrologic conditions[5,6], soil geochemistry[7,8] and microbial community composition[9,10]. The presence of soil minerals, which can bind and presumably stabilize OC against microbial decomposition, is a particularly important factor during permafrost thaw [11–14].

The fraction of mineral-bound OC in permafrost soils ranges from 33-74% of total OC[15–18]. The variation of the mineral-bound OC fraction is partly due to different minerals displaying a range of binding capacities for OC, with the redox-active ferric iron (Fe(III)) (oxyhydr)oxides contributing to the highest estimates on a mass basis[19,20]. Interactions of OC with Fe(III) (oxyhydr)oxides can occur due to adsorption with an already existing mineral, by coprecipitation of dissolved Fe and OC at oxic-anoxic redox transitions, or by occlusion of OC within the mineral structure[21], forming Fe(III)-OC associations. Field-based evidence has shown that relatively older OC is stored in mineral fractions of permafrost soils, dominated by Fe(III) (oxyhydr)oxides[15,17], displaying their ability to sequester OC over long time frames. Some studies also showcased the preservation or *de novo* formation of Fe(III)-OC associations after permafrost thaw, implying that Fe-bound OC would lead to a lower permafrost-carbon feedback by decreasing future GHG emissions[14,16,22,23]. In the case of Yedoma permafrost deposits, lower basal respiration of thawed sediment layers was directly correlated with higher amounts of poorly crystalline Fe(III) (oxyhydr)oxides[17], indicating how Fe(III) (oxyhydr)oxides can limit OC degradation .

However, the stabilizing function of Fe(III)-OC associations is brought into question if permafrost thaw leads to the development of anoxic conditions due to soil subsidence and waterlogging in lowland permafrost areas[24–27]. Anoxic conditions could lead to microbial reductive dissolution of Fe(III) (oxyhydr)oxides, thus releasing the previously bound OC to the aqueous phase[28,29]. Previous work in humid soils may provide insight into the stability of Fe(III)-OC associations under anoxic conditions and following GHG emissions. For example, emissions of CO_2[30] as well as of CH_4 increased[31] after dissolution of Fe minerals, indicating that anoxia might negate Fe-mediated OC protection. Still, Fe(III)-OC associations seem to persist in many wetland environments[32,33], especially *Sphagnum*-dominated wetlands[34], which

typically experience anoxic conditions. Complementarily, it has been demonstrated that Fe(III)-OC associations were reduced to a lower extent than OC-free Fe(III) (oxyhydr)oxides using the pure *Geobacter* cultures in lab studies due to higher particle sizes and limited microbial access to Fe(III)[35,36]. It is thus unclear what the future fate of Fe(III)-OC associations will be after permafrost thaw.

Based on the uncertainty regarding the availability of Fe(III)-OC associations towards reduction in thawing permafrost soils, the quantitative contribution to GHG emissions during thaw is unclear. Previous estimates of the contribution of Fe(III) reduction to anaerobic respiration in permafrost soils are based on field measurements of poorly crystalline Fe(III) content and net CO_2 fluxes across thaw transitions[37,38] or after injections of dissolved Fe(III) into the soil[39]. Resulting contributions of Fe(III) reduction to total CO_2 emissions ranged from 22 to 63%[37,38], showing that Fe(III) reduction is an important contributor to anaerobic respiration in these soils. However, no conclusions about the direct role of Fe(III)-OC associations on CO_2 release can be drawn based on these measurements. Further, it is unknown how the reduction of Fe(III)-OC associations in thawing permafrost soils would affect net CH_4 release. Previous studies demonstrated the suppression of methanogenesis due to Fe(III) reduction since Fe(III) is a more thermodynamically favorable electron acceptor[40–42]. In contrast, methanogenesis and Fe(III) reduction seemed to occur simultaneously in Alaskan permafrost soils[43,44]. The release of OC from Fe(III)-OC associations could also increase CH_4 emissions by supplying new OC compounds for fermenting microorganisms which provide the substrates (fatty acids, H_2) for methanogenesis[45].

Knowledge of the net effects of Fe(III)-OC associations on GHG emissions during permafrost thaw is therefore limited. In this study, we aimed to (i) determine the reduction extent of Fe(III)-OC associations upon permafrost thaw, (ii) quantify the changes in GHG emissions due to reduction of Fe(III)-OC associations and their contribution to net GHG release, and (iii) evaluate the changes of microbial community composition due to addition of Fe(III)-OC associations. In order to achieve this, we synthesized [57]Fe-enriched Fe(III)-OC coprecipitates, representative of Fe(III)-OC associations, using extracted natural organic matter from a permafrost thaw gradient at Stordalen Mire (Abisko, Sweden). The Fe(III)-OC coprecipitates were then exposed to anoxic conditions in a microcosm experiment containing an anoxic soil slurry from the same site. We performed the experiment using soils of two different permafrost thaw stages. We used intact, oxic permafrost soils ("palsa") and inundated them in order to simulate rapid permafrost thaw, as well as partly thawed permafrost soils ("bog") to simulate the anoxic stage of natural seasonal water table fluctuations.

Material and Methods

Field site description and sampling

Stordalen Mire is a well-characterized permafrost peatland complex, located at the edge of the discontinuous permafrost zone near Abisko, Sweden (68 22' N, 19 03' E). It consists of several subhabitats: intact permafrost areas (palsas) covered by dwarf shrubs, bryophytes and lichens, semi-wet bogs dominated by *Sphagnum* spp. mosses, and permanently waterlogged fens covered by sedges (*Eriophorum vaginatum, Carex rostrata*)[46]. Mean annual air temperature in Abisko increased from -0.9°C during 1957-1971 [46] to 0.7°C during 2005-2019[47] leading to thawing of permafrost ice underneath palsas and conversion to bog and fen areas[48].

Soil and porewater samples were collected in July 2022. Collected subsoils (30 cm depth) from palsa and bog areas were used as inoculum for the microcosm experiment. The upper soil (2-10 cm depth) was collected and used for extraction of soil organic matter for the Fe(III)-OC coprecipitate synthesis. Both soils were retrieved by bulk sampling and stored in sterilized plastic bags (LDPE). The bog soils, which were fully water saturated, were filled into the bags such that no headspace remained and abiotic oxidation was minimized. Back in Tübingen, the soils were stored in gas-tight, N_2-flushed mason jars at 4°C until use. An aliquot of the soils used for the microcosm experiment was dried (60°C) inside an anoxic glovebox (MBraun Unilab Workstation, 100% N_2 atmosphere) for initial analysis of Fe speciation by selective extractions (Text S1, Figure S1) and Fe *K*-edge X-ray absorption spectroscopy (XAS). Total organic carbon content was determined by elemental analysis (SoliTOC Cube, Elementar, Germany). A soil standard was used for calibration (Soil Standard OAS, Cat No B2152, Elemental Microanalysis Limited). Porewater was sampled over different depths (5-43 cm) at at four different locations per thaw stage in order to compare *in situ* concentrations of aqueous Fe and OC concentrations to results from the microcosm experiments. We used MacroRhizon® samplers (60 cm length, 0.15 µm pore size, Rhizosphere Research, Netherlands) and stored porewater in sterilized serum vials with an N_2 headspace after sampling.

Synthesis of (^{57}Fe-enriched) Fe(III)-OC coprecipitates

A water extraction was used to extract soil organic matter from the upper soils of palsa and bog for the synthesis of Fe(III)-OC coprecipitates. The detailed procedure can be found in Text S2. The final dissolved organic carbon (DOC) concentrations in the extracts were 18 and 11 mg C L^{-1} for palsa and bog soil, respectively. The coprecipitates used in the microcosm experiments were prepared from an isotopically labeled ^{57}Fe-enriched $FeCl_3$ solution, which made it possible to differentiate added Fe(III)-OC coprecipitates from the native Fe pool. The

enriched [57]Fe(III) solution (150 mM) was prepared as described previously[49,50] and subsequently mixed with an equimolar $^{NA}FeCl_3$ (FeCl$_3$x6H$_2$O, Sigma-Aldrich) solution in a ratio of 1:10, to create a 10% [57]Fe-enriched Fe(III)Cl$_3$ solution. The coprecipitates used in the field experiment were synthesized using $^{NA}Fe(III)Cl_3$.

The synthesis involved mixing 1.5 L of water-extractable organic matter (WEOM) from each thaw stage with the [57]Fe-enriched FeCl$_3$ solution to create an initial molar C:Fe ratio of 1. A NaCl solution (3 mM) was added to keep the ionic strength constant. The pH was raised by adding 50 mM NaOH dropwise until pH 4.5 under constant stirring (800 rpm). The low pH was chosen since soil pH and porewater pH in palsa and bog soils are between pH 3.5-5.5 (Figure S2a). The suspensions were left to stand for 2 h, after which the pH was readjusted to pH 4.5. Afterwards, the suspensions were washed by filling them in pre-soaked dialysis membranes (14 kDa, Sigma-Aldrich) in DDI water. The water was exchanged several times until conductivity was <20 µS cm^{-1}. The washed suspensions were centrifuged, and the solids were resuspended in 50 mL DDI water. The pH was adjusted to pH 4.5 and the solution was bubbled with N$_2$ (99.999%) for 15 min to make it anoxic. The Fe speciation was characterized by [57]Fe Mössbauer spectroscopy (Figure S3) and Fe *K*-edge XAS (Figure S4, Figure S5).

Microcosm experiment to analyze the role of Fe(III)-OC coprecipitate addition for greenhouse gas fluxes

Setup of microcosm experiment

The subsoils used in the microcosm experiment were homogenized by wet sieving with a sterilized 2 mm sieve. Moist palsa soil (5.5 g dry weight) was then added to six 250 mL Schott bottles and moist bog soil (8 g dry weight) was added to six 250 mL serum bottles under sterile conditions. The bottles were then closed with sterilized butyl rubber stoppers. The headspace in each bottle was exchanged by applying vacuum for 5 min and flushing with N$_2$ gas for 5 min (3 cycles). Artificial, anoxic porewater solution (composition in Table S1) was added within an anoxic glovebox to the bottles to reach a final soil-solution ratio of 0.23 and 0.88 mg dry soil mL^{-1} for palsa and bog soil, respectively. All bottles were incubated under anoxic conditions at room temperature in the dark for 30 days prior to the addition of [57]Fe-enriched Fe(III)-OC coprecipitates. At this point, coprecipitates that were synthesized using palsa WEOM were added to three of the bottles containing palsa soil, and those synthesized with bog WEOM were added to three bottles containing bog soil. The amount of added [57]Fe-enriched Fe(III)-OC coprecipitates was adjusted to the amount of native Fe minerals in each bottle, increasing the total 6 M HCl-extractable Fe by 50% (see Figure S6d).

In a control experiment, we tested the importance of abiotic reduction of added Fe(III)-OC coprecipitates by the native DOC within the soil. For that purpose, we added the same concentration of Fe(III)-OC coprecipitates to sterile filtered (0.22 μm, PES, Carl Roth) aqueous phase from the no-coprecipitate treatments of palsa and bog soil, collected at the end of the experiment. A new batch of the coprecipitates was prepared for this control experiment in order to have similar storage times as in the main experiment. In the case of the palsa soil, the filtered aqueous phase was diluted with artificial porewater solution in order to have the same concentration of DOC as on day 0 of the main experiment. For bog soil, this was not possible since the DOC had decreased over time, thus the aqueous phase was left undiluted. The speciation of aqueous Fe and concentration of aqueous ^{57}Fe and DOC were quantified over 48 h as specified in section Geochemical analyses.

Gas sampling of microcosm experiment

Sampling of the microcosms included measuring GHG fluxes and geochemical sampling inside the glovebox. To measure GHG fluxes, the rubber stoppers of the bottles were pierced with two needles, each attached to a three-way valve. The headspace of all bottles was flushed with moistened N_2 for 10 min via a gas distribution setup. After 10 min, the flow of N_2 gas was stopped and the gases were left to accumulate. A 2 mL sample was taken from the headspace and transferred to a He-flushed 12 mL Exetainer® vial (Labco, UK) after 0, 30 and 60 min. The individual and cumulative gas fluxes were calculated based on the increase in gas concentration (see Text S3).

Aqueous and solid phase sampling of the microcosm experiment

The geochemical sampling was carried out in an anoxic glovebox. An aliquot of the suspension (1 mL before addition of Fe(III)-OC coprecipitates, 1.5 mL during the main experiment) was taken out. The suspension was centrifuged (10055 rcf, 5 min) and the supernatant was taken off. The supernatant was used to quantify DOC concentration and aqueous Fe speciation after acidification with anoxic 1 M HCl. The soil pellet was dried at 60°C in anoxic conditions overnight and weighed to estimate the dry mass in each sample. The poorly crystalline Fe mineral fraction was quantified by adding 1.5 mL anoxic 0.5 M HCl to the soil[51,52]. After 24 h, the extraction solution and remaining solid were separated by centrifugation (10055 rcf, 5 min) and the supernatant was diluted in 1 M HCl for measurement of Fe speciation and ^{57}Fe concentration.

At certain time points (right after addition of coprecipitates: day 0, after 8 d and 42 d) an additional 15 mL of suspension was taken out of the bottles. An aliquot (4 mL) was centrifuged in the glovebox, the supernatant was transferred to a new tube and immediately frozen (-20°C) for measurement of microbial metabolites by gas chromatography mass spectrometry (GC-MS). The soil pellet was frozen (-20°C) and subsequently freeze-dried under anoxic conditions for analysis by Fe K-edge XAS. A separate aliquot of 1 mL was used to measure pH (InLab Easy BNC, Mettler Toledo, Germany) outside the glovebox. The remaining 10 mL were transferred to 15 mL centrifuge tubes (polypropylene, RNase- and DNase-free, Biologix) and centrifuged outside the glovebox (17200 rcf, 5 min). The supernatant was taken off under sterile conditions and the remaining soil pellet was immediately frozen (-80°C) for later extraction of DNA and RNA and subsequent molecular biological analysis.

Geochemical analysis

Dissolved OC concentrations were measured (as non-purgeable OC) after acidification with 2 M HCl by a TOC analyzer (multi N/C 2100S, Analytik Jena AG, Germany). Aqueous and solid (0.5 M HCl-extractable) Fe speciation and total Fe concentration were quantified using the ferrozine assay[53]. We only interpreted changes of total Fe concentrations from the solids and not its speciation since abiotic reduction of Fe(III) by OC under acidic conditions[54] lead to an underestimation of the Fe(III) content. Gas samples were measured by a gas chromatograph (TraceGC1300, ThermoFisher Scientific, USA; modified by S+HA analytics), equipped with two column configurations (first configuration: 30 m long, 0.53 mm ID TGBondQ column and 30 m long, 0.53 mm ID Molsieve column; second configuration: 30 m long, 0.53 mm ID TGBondQ column and a 30 m long 0.25 mm ID TGBondQ+ column; all ThermoFisher Scientific) which are each connected to a Pulse Discharged Detector. Gas concentrations were quantified with external calibrations of standards of pure CH_4 and CO_2 (99.5% CH_4, 99.9% CO_2, Westfalen) in He-flushed Exetainer® vials in a range of 0.05-500 ppm.

Concentrations of ^{57}Fe in aqueous and 0.5 M HCl-extracted solid samples were quantified by inductively coupled plasma mass spectrometry (ICP-MS, Agilent 7900, Agilent Technologies, USA) with Ar as carrier gas and in He mode after dilution in 1% HNO_3 (analytical grade, Carl Roth). Contribution of ^{57}Fe-enriched Fe-OC coprecipitates to the aqueous and solid (0.5 M HCl-extractable) Fe pool were calculated (Text S4). The concentration of microbial metabolites, such as small sugars, organic acids, and amino acids were quantified using targeted GC-MS (Shimadzu GC/MS TQ 8040, Japan). A full list of measured metabolites is given in Table S2. Metabolites were analyzed either by headspace injection or as liquid samples after derivatization and addition of octanol or ^{13}C-glucose as internal standard,

respectively. More details are given in Text S5. Concentrations were quantified with an 8-point external calibration containing standards of all targeted analytes, ranging from 20 to 10^7 pmol.

Solid phase Fe characterization

Iron speciation in the solid was also investigated by Fe K-edge XAS at Synchrotron SOLEIL (SAMBA beamline, Paris, France) and Synchrotron ELETTRA (XAFS beamline, Trieste, Italy). For this purpose, the initial ^{57}Fe-enriched coprecipitates were air-dried prior to homogenization with a mortar and pestle. The dried solids were pressed into pellets (7 mm diameter) with PVP (Polyvinylpyrrolidone K12, Carl Roth) and sealed with Kapton® tape. Freeze-dried samples of solids from the microcosms were processed in the same way in a glovebox after anoxic freeze drying.

At both beamlines, transmission spectra were recorded at 77 K using a N_2(l) cryostat. At SOLEIL, a Si(220) monochromator was used and calibrated to the first derivative maximum of the K-edge absorption of an Fe(0) foil. Harmonic rejection was performed by two Si mirrors coated in Pd. Between 8 and 14 scans per sample were collected in continuous scan mode and merged. At ELETTRA, a Si(111) monochromator was calibrated to the first derivative maximum of the K-edge absorption spectrum of an Fe(0) foil. Higher beam harmonics were decreased by detuning the monochromator by 30%. Two to three scans were collected per sample and merged. The final spectra were used for analysis of Fe K-edge X-ray absorption near edge structure (XANES) to estimate Fe oxidation state and extended X-ray absorption fine structure (EXAFS) to determine Fe speciation. All data processing and analysis were done in Athena software[55] with detailed description included in Text S6. The initial synthesized ^{57}Fe-enriched Fe(III)-OC coprecipitates were analyzed using ^{57}Fe Mössbauer spectroscopy to determine Fe speciation. Details on the measurement and data analysis are given in Text S7.

Molecular biology analysis

Total DNA and RNA of soil samples from the microcosm experiment were extracted in experimental triplicate using the RNeasy PowerSoil® Total RNA Kit with DNA Elution (Qiagen, Germany). Details on protocol adjustments, quality control steps and transformation of RNA to cDNA are given in Text S8. Bacterial and archaeal 16S rRNA genes were amplified from DNA and cDNA using the universal primers 515f[56] and 806r[57] fused to Illumina adapters. Library preparation steps (Nextera, Illumina) and sequencing were performed using Illumina MiSeq sequencing system (Illumina, USA) at the Institute for Medical Microbiology and Hygiene of the University of Tübingen. Data processing, including quality control, reconstruction of

sequences and taxonomic annotation (Text S8) was done using nf-core/ampliseq version 2.8.0[58,59] of the nf-core collection of workflows[60]. Fe(III)-reducing, Fe(II)-oxidizing as well as methanotrophic and methanogenic microorganisms were identified, as listed elsewhere[38]. To evaluate which microbial taxa were significantly affected by addition of Fe(III)-OC coprecipitates, we used the multivariate analysis of composition of microbiomes (ANCOM). We compared the relative abundance of all ASVs in DNA- and RNA-based datasets after 8 and 42 days of the coprecipitate-added treatment to the no-coprecipitate control, since we expected only minimal changes at day 0.

Quantitative PCR (qPCR) was performed on DNA and cDNA samples to quantify changes in total bacterial and archaeal 16S rRNA (gene) copies as well as for methyl-coenzyme M reductase subunit alpha (*mcrA*), a functional gene relevant for CH_4 production[61,62]. The used primer sequences, plasmid standards, dilution factors of samples and details of the temperature programs are summarized in Table S3. The assays were performed using SybrGreen® Supermix (Bio-Rad Laboratories, USA) on the C1000 Touch thermal cycler (CFX96TM real time system, Bio-Rad Laboratories). Sample dilutions (10-1000x) were necessary since presence of complex OC compounds lead to inhibition of the fluorescence signal in samples with no dilution[63]. Copy numbers were determined in analytical triplicate of each experimental replicate. Data analysis was performed in Bio-Rad CFX Maestro 1.1 software, vs. 4.1 (Bio-Rad, 2017).

Field experiment to determine the *in situ* reduction extent of Fe(III)-OC coprecipitates and effect on greenhouse gas fluxes

Construction of peepers and experiment setup

We performed a field experiment in order to determine the *in situ* reduction extent of [NA]Fe(III)-OC coprecipitates in palsa and bog soils and quantify the effect on net greenhouse gas emissions over a thaw season. For this purpose, passive porewater samplers ("peepers", 20 cm length, 10x 1 cm high cells, containing each 12 mL) were used to incubate synthesized [NA]Fe(III)-OC coprecipitates in the peeper cells under ambient conditions at Stordalen Mire. Three peepers were each placed in palsa and bog areas in July 2022, on plots with similar vegetation and ca. 1 m apart from each other (Figure S7). Cells of the peepers were filled with anoxic, deionized water through attached butyl rubber tubing immediately before installation in the soil. The peepers were equilibrated for 4 d in the soil, after which an anoxic suspension of 55.8 mg L^{-1} Fe in [NA]Fe(III)-OC coprecipitates was added via the tubing to two of the peepers in each thaw stage. The suspension was added into every second cell in the following depths from the soil surface: 4-5 cm, 8-9 cm, 12-13 cm, 16-17 cm, 20-21 cm. We chose a membrane

with 8 µm pore size in the peeper in order to facilitate microbial access to the $^{NA}Fe(III)$-OC coprecipitates. We tested if synthesized coprecipitates would pass the membrane due to their size by placing a piece of the membrane inside filter cups (25mm, Millipore) and filtering through 1 mL of coprecipitate suspension. The filtrate was acidified with 1 M HCl and total Fe concentration was measured by the ferrozine assay. Results showed that 92 and 94% of palsa and bog coprecipitates, respectively, were retained by the filter.

Additionally, we monitored the water table depth and soil temperature at palsa and bog areas in 15 min intervals with groundwater dataloggers (MicroDiver, Schlumberger Water Services). The dataloggers were placed inside hollow, plastic tubes with cuts at the bottom which were inserted into the soil between the peepers in both thaw stages. The measured absolute pressure was corrected using a barometric pressure reading based of a datalogger (Baro-Diver) left at the Abisko Research station during the duration of the field experiment (ca. 10 km from the site).

Sampling and analysis of field-based experiment

Greenhouse gas emissions were measured using static, non-flow gas chambers, as described previously[64], with the following adjustments: (i) the chambers were wrapped in aluminum foil to exclude photosynthetic processes and (ii) incubation time was 20 min and samples were taken every 5 min by a gas-tight 50 mL syringe. A volume of 18 mL gas was injected into pre-evacuated 12 mL Exetainer® vials. Gas fluxes were measured in triplicate, once in July (2, 20 and 21 h after addition of coprecipitates) and at the end of the summer season (September, after 53 d). One peeper containing the $^{NA}Fe(III)$-OC coprecipitates and one containing only deionized water were selected for the gas measurements. Between measurements, the gas chamber was removed and put to the side to let the plot equilibrate back to ambient conditions for at least 40 min. Gas concentrations of CO_2 and CH_4 were measured back in Tübingen (see section Geochemical analyses).

The equilibrated porewater and/or remaining ^{NA}Fe-OC coprecipitate suspension in the peepers were sampled after 53 days in September 2022. A N_2-filled 20 mL syringe was attached to one side of the butyl tubing of each cell, while another N_2-flushed, empty syringe was attached to the outlet side. The outlet-syringe was pulled to capture the anoxic solution in the peepers and the inlet syringe was simultaneously pushed to avoid underpressure and flow of new porewater into the peeper cell. The contents of the syringe were distributed in the following way: 7 mL were transferred to an N_2-flushed, gas tight 50 mL serum vial and stored at 4°C until measurement of dissolved and solid Fe speciation. An aliquot of 3 mL was added to a He-filled 11 mL headspace vial to measure dissolved porewater gases (CO_2, CH_4). For

that purpose, the vials were vigorously shaken for 2 min after which 3 mL of the headspace gas was transferred to a He-flushed, 12 mL Exetainer® vial. The remaining volume (1-2 mL) was filtered (0.22 μm, PES, Carl Roth; pre-rinsed with 50 mL DDI) and frozen (-20°C) until measurement of DOC. Samples for measurement of aqueous and solid Fe speciation were prepared in an anoxic glovebox. An aliquot of 1 mL was filtered (0.22 μm, PES, Carl Roth) and stabilized with 1 mL of 2 M HCl to quantify aqueous Fe speciation. Total Fe in initial suspensions was determined by dissolving 0.8 mL unfiltered sample in 0.8 mL 2 M HCl. The solid Fe content and speciation was calculated by subtraction of total - aqueous concentrations. Cells of the peepers placed in the palsa area were empty after the thaw season due to too low porewater volume in the soil. In order to analyze the Fe speciation of the [NA]Fe(III)-OC coprecipitates, the membrane in front of each peeper cell with attached coprecipitates was cut out and added to 1.5 mL of 1 M HCl in an anoxic glovebox. Results were blank-corrected by extracting a membrane part which was not in contact with the coprecipitates. Analytical methods for determination of Fe speciation and concentration, dissolved porewater gases and DOC concentration are described in section Geochemical analysis.

Statistics

Mean and standard deviations were calculated for each variable analyzed in triplicate. When differences between treatments with added Fe(III)-OC coprecipitates and the no-coprecipitate controls were calculated, the mean values were used for calculation and the errors (standard deviation) were propagated. Datasets involving GHG fluxes, concentrations of microbial metabolites, relative abundances of taxa on the phyla level of the microbial community and qPCR-based copy numbers were compared between the coprecipitate-added and no-coprecipitate treatments using a two-way ANOVA, followed by Tukey HSD tests. If datasets were non-parametric, they were log transformed unless otherwise stated. All statistical analyses were performed in R vs. 4.3.3[65].

Results and Discussion

Rapid increase in aqueous Fe concentration is originating from reductive dissolution of Fe(III)-OC coprecipitates

Aqueous Fe^{2+} concentrations in microcosms were quantified in order to track the potential reductive dissolution of added ^{57}Fe-enriched Fe(III)-OC coprecipitates. Before the addition of Fe(III)-OC coprecipitates, both soils exhibited an increase in aqueous Fe^{2+} concentrations over time which plateaued at 1.11 ± 0.06 mM Fe^{2+} after 30 days in the palsa soil and at 1.09 ± 0.08 mM Fe^{2+} after 14 days in the bog soil (Figure S6a). This shows that native Fe(III) (oxyhydr)oxides were reductively dissolved over time as anoxic conditions established in the incubation. The initial aqueous Fe^{2+} concentrations at the start of the experiment (0.16 ± 0.02 and 0.58 ± 0.09 mM Fe^{2+} in the palsa and bog reactors, respectively) were consistent with the concentrations measured in the porewater taken from the field site (Figure S2b). In the field, we observed increasing Fe^{2+} concentrations with depth, consistent with likely decreasing redox potentials.

After addition of coprecipitates into the microcosms, there was an increase in aqueous Fe^{2+} concentrations in coprecipitate-amended treatments compared to the no-coprecipitate controls (ΔFe_{aq}). After one day, ΔFe_{aq} was 0.13 ± 0.09 mM in palsa soil and 0.33 ± 0.02 mM Fe in bog soil (Figure 1a). This difference stayed constant for the duration of the experiment, fluctuating around 0.15 ± 0.03 and 0.35 ± 0.04 mM for palsa and bog soil, respectively. Based on ΔFe_{aq} between the two treatments, $15\pm4\%$ and $11\pm1\%$ of added Fe(III) in coprecipitates were dissolved in palsa and bog soil, respectively. To directly quantify aqueous Fe from Fe(III)-OC coprecipitates, we used the measured ^{57}Fe concentrations (Figure 1b). This dataset also showed an increase in aqueous Fe from coprecipitates in coprecipitate-amended treatments of 0.31 ± 0.05 and 0.32 ± 0.02 mM for palsa and bog soil, respectively, after one day. This proves that there was a rapid reductive dissolution of added Fe(III)-OC coprecipitates in both soils. The dissolution of coprecipitates based on the ^{57}Fe dataset was 31% and 10% for palsa and bog coprecipitates. These results therefore agree well with ΔFe_{aq} in case for the bog soil, but not for the palsa soil. It is likely that this was a consequence of partial abiotic isotope exchange (see below).
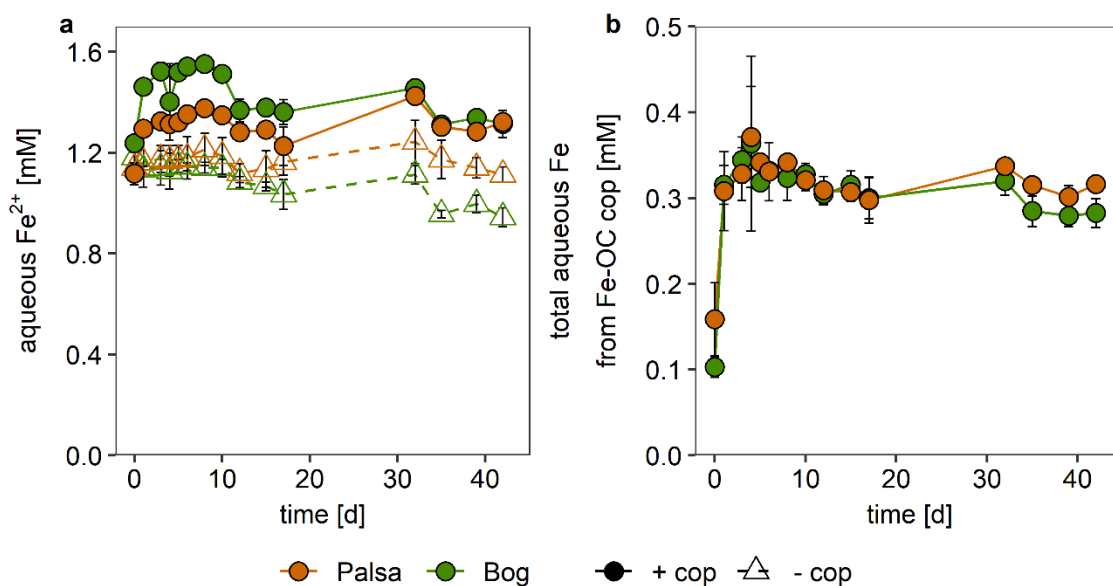
Figure 1. Concentrations of aqueous Fe over time. Measured concentrations of aqueous Fe^{2+} in treatments with Fe(III)-OC coprecipitate addition ("+ cop", filled circles) and the no-coprecipitate control ("- cop", open triangles) of palsa and bog soils (a). Calculated concentrations of aqueous Fe stemming from Fe(III)-OC coprecipitates based on the fraction of ^{57}Fe (b). All data points and error bars represent the average and standard deviation of experimental triplicates.

Based on the aqueous ^{57}Fe concentrations, all of the reductive dissolution of added Fe(III)-OC coprecipitates occurred within one day and did not change further along the incubation. We considered the following reasons for this: First, it is possible that there was abiotic reduction of coprecipitates due to complexation with DOC at the low pH (palsa: pH 3.4-3.8, bog: pH 4.2-4.7, Figure S6i) in the microcosms. Especially aromatic and (poly-)phenolic organic carbon functional groups are known to reduce Fe(III) abiotically at low pH conditions[54]. We tested this possibility with an abiotic experiment in which the same concentration of coprecipitates was added to sterile-filtered aqueous phase from the control treatment. We did not observe any increase in aqueous Fe^{2+} concentrations over 48 h, indicating that no abiotic Fe(III) reduction of coprecipitates due to the native DOC occurred. Instead, coprecipitate-added treatments of palsa and bog soils showed an immediate decrease of aqueous Fe^{2+} compared to the reactors with without addition of coprecipitates (6 and 8% respectively, Figure S8). After 48 h, there was no further change in aqueous Fe^{2+} or total Fe in any of the reactors. The decrease is therefore attributable to sorption of aqueous Fe^{2+} onto the coprecipitate surface[66–68].

This experiment also enabled us to test whether there was abiotic isotope exchange between the $^{57}Fe(III)$ in coprecipitates and the aqueous $^{56}Fe^{2+}$ by evaluating changes in the

fraction of aqueous ^{57}Fe. The fraction of aqueous ^{57}Fe increased by 1.86±0.02% and 1.21±0.03% after 48 h in the coprecipitate-added setup of palsa and bog reactors, respectively, compared to the no-coprecipitate control (Figure S8). The change in aqueous ^{57}Fe fraction is therefore smaller than in the main experiment (2.23±0.19% and 2.37±0.17% in palsa and bog reactors, respectively). Coupled with the fact that aqueous Fe^{2+} concentrations did not increase in the abiotic experiment, this dataset therefore shows that abiotic isotope exchange cannot explain the full increase of aqueous ^{57}Fe that we observed within two days in the main experiment.

The second possibility is that the microbial community was well-adapted to the reduction of Fe(III)-OC associations, leading to the initially fast response in terms of the reductive dissolution of added coprecipitates. We found several taxa which are known as respiratory (*Geobacter*, *Pseudomonas, Anaeromyxobacter*) and fermentative (*Clostridiales*) Fe(III)-reducers[69–72], which could play a role even while their total relative abundance did not exceed 1% (Figure S9). Other yet-unidentified Fe(III)-reducing microorganisms, possibly within the phyla *Acidobacteriota* or *Firmicutes*[73–76] could have also contributed to Fe(III) reduction of the coprecipitates.

We also considered a third possibility that soil-derived, reduced particulate organic matter (POM) could have transferred electrons to the Fe(III)-OC coprecipitates, either abiotically, as shown with dissolved, redox-active DOC[77] or biotically by microorganisms using the POM as an electron shuttle[78]. Assuming that POM can transfer 0.08 mmol e$^-$ g^{-1} POM in its reduced state, as estimated in Swedish non-permafrost peatlands[79,80], the available POM in our experiments could theoretically reduce 0.13 and 0.20 mmol Fe(III) in palsa and bog reactors, respectively (Table S4). As the actual amount of reduced Fe from added Fe(III)-OC coprecipitates was only 0.08 and 0.04 mmol after one day of incubation in palsa and bog soils, respectively, POM could have played a role in reducing Fe(III) in added coprecipitates. Overall, we therefore conclude that the rapid increase in aqueous Fe^{2+} originates from the microbially-induced reduction of added coprecipitates with a possible contribution of abiotic electron transfer from reduced POM to Fe(III).

Dissolution of Fe-OC coprecipitates forms intermediate Fe(III)-OC phases

We determined changes in solid phase Fe speciation over time by using Fe *K*-edge XAS. Based on the mass of added total Fe (estimated from 0.5 M HCl extraction, Figure S6d), the addition of Fe(III)-OC coprecipitates, all of which was initially Fe(III) (Figure S4), contributed to 30% of total Fe in the coprecipitate-added reactors. The fraction of oxidized Fe (Fe(III)/total Fe) in the solid phase based on XANES fitting decreased over time in the microcosm experiment in both soils (Figure 2a). At day 0, the fraction of Fe(III) in both soils without added

coprecipitates was similar (20 and 18% in palsa and bog soil, respectively). In the coprecipitate-added treatments, the fraction was higher by 8 and 13% than in the no-coprecipitate control for palsa and bog soil, respectively. This indicates that a large proportion of coprecipitates was already reduced shortly after addition to the reactors (49 and 37% of palsa and bog coprecipitates, respectively) before the sample for analysis by XAS (within 4 h) was taken. It is unlikely that we did not capture this fraction of coprecipitates due to a sampling bias, since the 0.5 M HCl extracted solids in the coprecipitate-added treatments displayed the expected total content of Fe (50% more Fe compared to initial Fe content, Figure S6d). After one day of incubation, the fraction of Fe(III) in coprecipitate-added treatments decreased further. The difference in fraction of oxidized Fe between the coprecipitate-added and no-coprecipitate control treatment therefore decreased to 3 and 2% for palsa and bog soil, respectively. In the palsa soil, the Fe oxidation state in both treatments continued to decrease until the end of the experiment (42 days), after which no Fe(III) was present in the coprecipitate-amended treatment and 7% Fe(III) was in the no-coprecipitate control. In the bog soil, the percentage of oxidized Fe slightly increased in both treatments after 8 days, after which it decreased again to 10 and 13% for the coprecipitate-added and no-coprecipitate treatment, respectively, at the end of the experiment (42 days). Overall, the results therefore show that Fe(III)-OC coprecipitates were fully reduced for both soils after 42 days since the fraction of oxidized Fe was lower in the coprecipitate-added treatment compared to the respective no-coprecipitate control.

The reduction of both added coprecipitates and native Fe(III) minerals occurred faster in palsa soil than in bog soil. The reason might be higher DOC concentrations in palsa than in bog soil (Figure S6g), specifically higher concentrations of substrates commonly serving as electron donor for Fe(III) reduction[81], like acetate or glucose (Figure S10)[69,82]. The high DOC concentrations could have also led to more electron shuttling between the Fe(III)-OC coprecipitates and Fe(III)-reducers[83,84]. Another reason might be the increased standard electron potential of the Fe^{3+}/Fe^{2+} redox couple at decreased pH values[85,86].
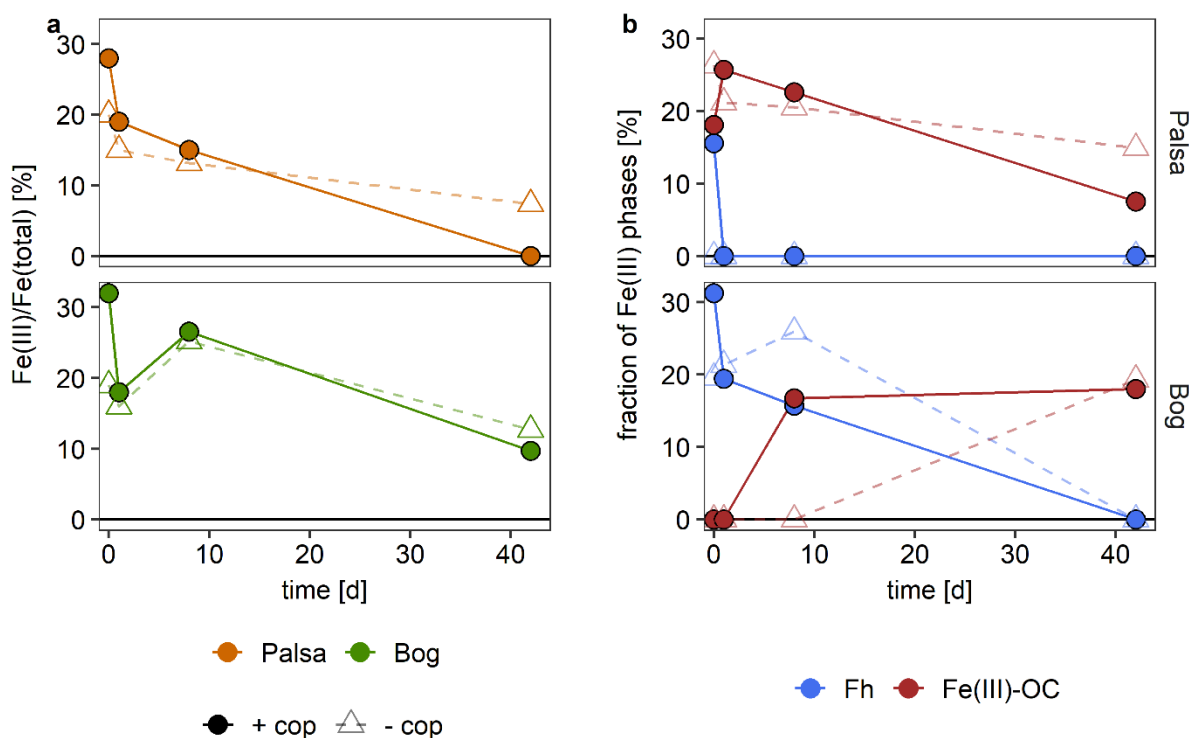
Figure 2. Solid phase Fe speciation of palsa (upper panel) and bog soil (lower panel) in microcosm experiment with addition of ^{57}Fe-enriched Fe(III)-OC coprecipitates (+ cop, filled circles) and without (- cop, open triangles). The Fe(III)/Fe(total) ratio based on linear combination fitting of Fe K-edge XANES region for soil is displayed over time (a). The fraction of Fe(III)-containing phases, ferrihydrite (Fh) and Fe(III)-OC phases (Fe(III)-OC), based on linear combination fitting of k^3-weighted Fe K-edge EXAFS spectra is shown over time (b).

The relative abundances of the two identified Fe(III) phases, ferrihydrite and Fe(III) directly bound to OC (Fe(III)-OC), varied over time (Figure 2b). We detected a higher percentage of ferrihydrite in the coprecipitate-added treatments compared to the no-coprecipitate controls at day 0 for both soils (16 compared to 0% and 31 compared to 20% for palsa and bog soil, respectively). The fraction of ferrihydrite in the coprecipitate-added treatment decreased in both soils and reached 0% after 1 day in palsa soil and after 42 days in the bog soil. Concurrently, the percentage of Fe(III)-OC (initially) increased in the coprecipitate-added treatment of both soils. In the palsa soil, the fraction of Fe(III)-OC increased from 18 to 26% after 1 day, before decreasing to 8% after 42 days. In the bog soil, Fe(III)-OC increased from 0 to 17% after 8 days and stayed constant for the remaining experiment duration. While Fe(III) phases decreased, the percentage of Fe(II) bound to OC (Fe(II)-OC) increased in all treatments (Table 1).

These trends suggest that the added coprecipitates (in form of ferrihydrite) were intermediately transformed to poorly-soluble Fe(III)-OC phases. We speculate that part of the

reduced Fe from coprecipitates might have been bound to POM and subsequently oxidized by reduced redox-active POM functional groups (e.g. quinones), as was previously shown under anoxic conditions[87]. This process could have occurred faster in the palsa soil (1 day) than in the bog soil (> 10 days) due to the lower pH values which make quinone reduction more thermodynamically favorable[88]. However, the direct processes responsible for Fe(III)-OC formation in a ternary system of aqueous Fe^{2+}, Fe(III) (oxyhydr)oxides and POM under anoxic conditions deserve further study. The Fe(III)-OC phase is likely subsequently microbially reduced over time, forming Fe(II)-OC phases. For the bog treatment, we did not observe a reduction of Fe(III)-OC phase within the time span of the experiment, since the coprecipitates in form of ferrihydrite were reduced at a lower rate and just depleted at the end of the experiment. The same trends regarding the fraction of ferrihydrite and Fe(III)-OC were visible in the no-coprecipitate controls of both soils, due to reduction of native Fe(III) phases.

Table 1. Linear combination fitting results for k^3-weighted Fe K-edge EXAFS spectra of the initial synthesized [57]Fe-enriched Fe-OC coprecipitates and the initial soils, as well as the samples from the microcosm experiment with added coprecipitates ("+cop") and without ("-cop") at day 0, after 1, 8 and 42 days of incubation. The references of Fe(III)-citrate and Fe(III)-catechol were classified as Fe(III)-OC while Fe(II)-citrate, Fe(II)-catechol and Fe(II)-EDTA were all classified as Fe(II)-OC.

	sample	Fh[a] [%]	Lp[b] [%]	Fe(III)-OC [%]	Fe(II)-OC [%]	NSSR[c] [%]	red. $\chi^{2,d}$ [%]
Palsa	[57]FeOC_initial	93	7	0	0	2.3	11.3
	soil initial	29	0	32	39	2.5	10.5
	mix "[57]FeOC"+"-cop_0"[e]	24	2	20	55	n.a.	n.a.
	+cop_0	16	0	18	66	2.6	7.6
	+cop_1	0	0	26	74	1.7	5.7
	+cop_8	0	0	23	77	1.6	5.2
	+cop_42	0	0	8	93	1.6	6.8
	-cop_0	0	0	26	74	1.8	5.8
	-cop_1	0	0	21	79	2.0	7.1
	-cop_8	0	0	21	80	1.8	6.2
	-cop_42	0	0	15	85	1.8	6.2
Bog	[57]FeOC_initial	93	7	0	0	1.8	9.2
	soil initial	29	0	23	49	4.3	16.1
	mix "[57]FeOC"+"-cop_0"[e]	41	2	0	56	n.a.	n.a.
	+cop_0	31	0	0	69	2.4	7.1
	+cop_1	19	0	0	81	4.0	12.9
	+cop_8	16	0	17	68	1.8	6.3
	+cop_42	0	0	18	82	1.4	4.9
	-cop_0	20	0	0	80	5.2	16.2
	-cop_1	21	0	0	79	2.0	5.7
	-cop_8	26	0	0	74	2.5	7.6
	-cop_42	0	0	19	81	1.9	6.4

[a]ferrihydrite
[b]lepidocrocite
[c]normalized sum of of squared residuals (residuals ($100 \sum_i (data_i-fit_i)^2/\sum_i data^2$)
[d]measure of fit accuracy (($N_{idp}/N_{pts}) \sum_i ((data_i-fit_i)/\varepsilon_i)^2(N_{idp}-N_{var})^{-1}$)). N_{idp}/N_{pts} and N_{var} are the number of independent points in the model fit (18.1), the total number of data points (181) and the number of fit variables (2-7), respectively.
[e]represents the theoretical Fe speciation according to mixing of the initially synthesized Fe(III)-OC coprecipitates and the non-amended control at day 0 (soil_0)

Greenhouse gas emissions in palsa soils are dominated by increased CO_2 emissions due to Fe(III)-OC coprecipitate reduction

The release of GHGs was differently affected by coprecipitate addition depending on the soil type. In palsa soils, cumulative CO_2 emissions significantly increased in the coprecipitate-

added treatment compared to the no-coprecipitate control by 43±16% (733±80 compared to 511±15 µmol CO_2 g^{-1} soil, ANOVA, $p<0.01$) after 42 days (Figure 3a). After 3 days, the fluxes of the coprecipitate-added palsa treatment were higher than the respective control and showed the largest difference after 10 and 12 days (ANOVA, $p<0.05$, Figure S11). The difference in cumulative CO_2 emissions is likely due to microbial Fe(III) reduction. We calculated how much CO_2 would be produced directly from the reduction of Fe(III) based on thermodynamic assumptions (4 mol Fe reduced per 1 mol CO_2 produced)[37,89]. We found that 15-30% of the increase in CO_2 emissions relative to the no-coprecipitate control may be attributable directly to Fe(III) reduction of the coprecipitates. Further, if all added coprecipitated OC would be released and mineralized, that would explain, on average, 66% of the increase in CO_2 emissions between the treatments. However, as the addition of coprecipitated OC only contributed to 0.1% of total OC and 7% of DOC in the palsa reactors, it is questionable whether there would have been a preferential mineralization of the previously Fe-bound OC. It is also possible that the release of Fe-bound OC stimulated further reduction of native Fe(III) minerals or induced priming effects so that the native OC pool was mineralized to a higher extent. Recent work by ThomasArrigo et al. (2023)[90] and Wang et al. (2024)[91] support the latter argument, since they found that the release of previously Fe-coprecipitated glucuronic acid/glucose led to higher respiration of native OC in anoxic soils.
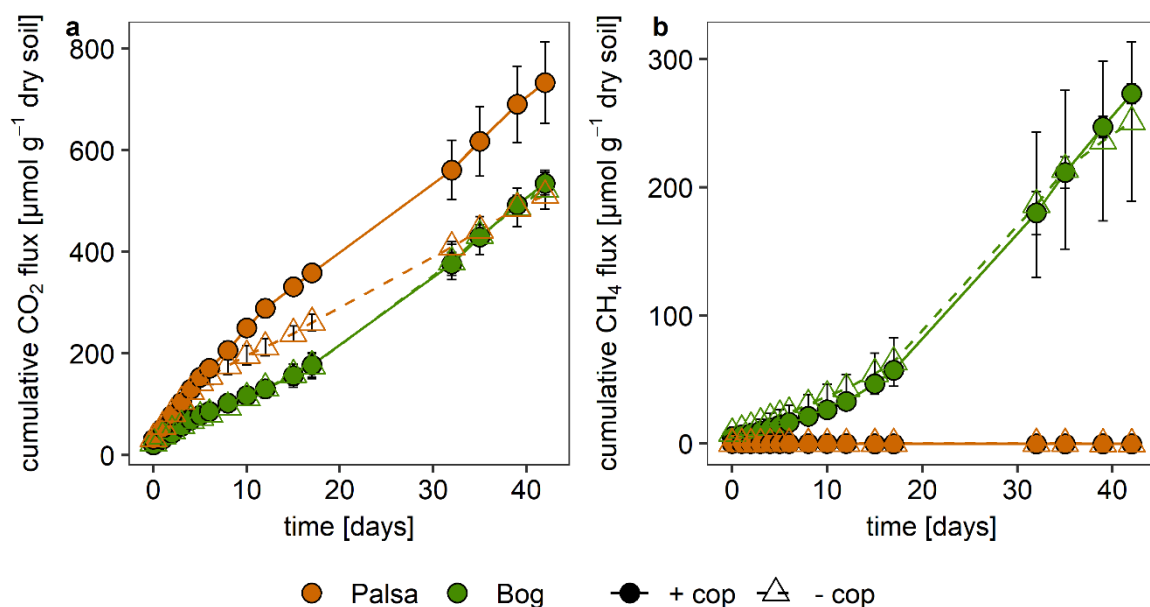
Figure 3. Cumulative greenhouse gas emissions of CO_2 (a) and CH_4 (b) in microcosm experiments of palsa and bog soils with addition of ^{57}Fe-enriched Fe(III)-OC coprecipitates ("+ cop") and in a no-coprecipitate control ("- cop") over time. All data points and error bars represent the average and standard deviation of experimental triplicates respectively.

Emissions of CH_4 were below the detection limit in both treatment for the palsa soil during the entire experiment duration (Figure 3b). This is in line with the absence of identified methanogens in the palsa soil based on the 16S rRNA amplicon sequencing data (Figure S12) and the RNA-based *mcrA* gene copy numbers, which were below the detection limit (Figure 4). The DNA-based *mcrA* copy numbers in the palsa soil were ca. 100 times lower than for the bog soil and did not change between the coprecipitate-added and the no-coprecipitate control (Figure S13). In comparison, a few aerobic methanotrophs were detected (*Roseiarcus*, *Methylocapsa*, *Rhodoblastus*) and their relative abundance decreased over time regardless of the treatment ($0.68\pm0.05\%$ at day 0 compared to $0.26\pm0.06\%$, Figure S12).
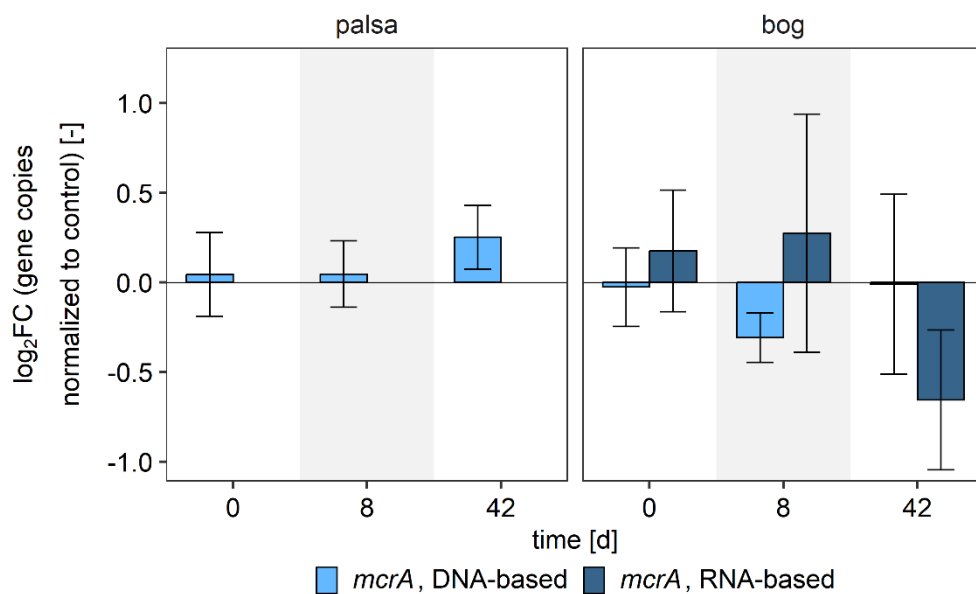
Figure 4. Change in gene copy numbers of the *mcrA* gene in microcosm experiment of palsa and bog soils with added ^{57}Fe-enriched Fe(III)-OC coprecipitates based on quantitative PCR results. Results are displayed as the log_2 fold change (FC) of the mean copy numbers of "+ cop" treatment to the mean of the no-coprecipitate control [copies$_{+cop}$ g^{-1} dry soil/ copies$_{-cop}$ g^{-1} dry soil] for DNA- and RNA-based analysis per time point. Absolute gene copy numbers are displayed in Figure S13. Data bars and error bars represent the mean and 95% confidence interval of experimental triplicates, respectively.

Our results are thus similar to previous metagenomic studies which mentioned the low to negligible activity of methanogens in palsa soil[92,93]. Still, we did expect to measure CH_4 emissions after a certain time lag in palsa reactors due to the establishment of anoxic conditions and since field-based flux measurements showed high net CH_4 emission after initial palsa collapse[38]. The fact that our results therefore differ from field measurements might mean that (i) longer anoxic periods are necessary to establish methanogenic conditions or (ii) CH_4 release during palsa collapse in the field likely stems from the contact with bog methanogen

communities. Support for the latter argument are given by Knoblauch et al. (2018)[94] who found no CH_4 emissions from a Siberian permafrost soil layer with no detectable *mcrA* gene copies after 7 years of incubation, until they added an inoculum from another soil layer which contained active methanogens.

Reduction of Fe(III)-OC coprecipitates in bog soils induces no change on net CO_2 release and temporarily inhibits CH_4 emissions

Within the bog reactors, cumulative CO_2 emissions did not differ between the two treatments (535±22 compared to 523±38 µmol CO_2 g^{-1} soil in coprecipitate-added and control treatment, respectively) after 42 days. Also, individual fluxes between the two treatments were not significantly different at any timepoint. This was surprising since the reduction of added Fe within the Fe(III)-OC coprecipitates should have produced an additional 100 µM CO_2 g^{-1} soil within the incubation, based on the stoichiometry mentioned in section 3.3. Therefore, there likely was a counteracting effect on CO_2 release. It is possible that the activity of microorganisms was suppressed by the addition of certain *Sphagnum*-derived phenolic compounds that were initially coprecipitated with Fe. In a previous study, Cory et al. (2022)[95] demonstrated that the inactivation of soluble phenolics in incubations with bog soil led to an increase in CO_2 emissions by 62%, indicating that soluble phenolics can suppress microbial respiration. Since phenolic compounds are abundant in bog porewaters[96,97] and likely also in bog WEOM, they were likely bound to Fe(III) (oxyhydr)oxides during the coprecipitation synthesis[98]. It has also been suggested that release of Fe-bound OC in non-permafrost *Sphagnum* peatlands decreased β-glucosidase activity[99], which is a central enzyme for carbon degradation[100].

In contrast, continued CH_4 emissions were detected in both treatments of the bog soil and cumulative emissions at the end of the experiment did not differ from each other (273±7.6 compared to 251±62 µmol CH_4 g^{-1} soil for coprecipitate-added and no-coprecipitate treatment, respectively). In the beginning of the experiment, cumulative CH_4 emissions were slightly lower from day 0 to day 12 in the coprecipitate-added treatment compared to the no-coprecipitate control (15±8.9 compared to 22±12 µmol CH_4 g^{-1} soil, Kruskal-Wallis test, p=0.18). This might indicate suppression of methanogenesis due to Fe(III) reduction of the added Fe(III)-OC coprecipitates. However, once the majority of Fe(III)-OC coprecipitates were reduced (after 10 days), CH_4 emissions increased again, reaching the same cumulative CH_4 emission as in the no-coprecipitate treatment.

The trends in DNA-based *mcrA* gene copies are in line with the temporary suppression of CH_4 emissions between 0 and 12 days. The DNA-based *mcrA* copy numbers were lower in

the coprecipitate-added treatment after 8 days compared to the no-coprecipitate control (log$_2$ fold change (FC): -0.31±0.14, Figure 4) while copy numbers did not differ based on treatment after 42 days (log$_2$ FC: -0.01±0.50). We also found slightly lower abundance and potential activity of methanogen taxa (including *Bathyarchaeia*, *Methanosarcina*, *Methanobacterium* and *Methanomassillicoccales*) in the coprecipitate-added treatment compared to the no-coprecipitate control after 8 days (Figure S12), highlighting the inhibition of methanogen communities. The genus *Methanosarcina*, which can use a diverse set of substrates[101,102], made up the majority of the abundance and potential activity of identified methanogens. The RNA-based *mcrA* copy numbers did not match with our hypothesis that temporary inhibition of methanogenesis occurred. Copy numbers did not differ significantly from the no-coprecipitate control after 8 days and instead were slightly lower after 42 days (log$_2$ FC: -0.64±0.39). We speculate that the difference between the DNA- and RNA-based *mcrA* values might be due to varying activity of methanogen taxa compared to their abundance. Some methanogens are hypothesized to be more vulnerable to competition effects with Fe(III)-reducing microorganisms (acetoclastic and hydrogenotrophic methanogens) than others (methylotrophic methanogens) [102,103]. Indeed, Ellenbogen et al. (2024)[92] found that methylotrophic methanogens can make up 7-54% of the total methanogen activity in bog soil and that members of the order *Methanosarcinales* are capable of using methoxylated compounds for methanogenesis. In any case, it was apparent that the addition of Fe(III)-OC coprecipitates temporarily decreased CH$_4$ emissions due to suppression of methanogenesis.

Fermenting and organic carbon-degrading microorganisms are stimulated by Fe(III)-OC coprecipitate addition

Changes in microbial community composition and potential activity upon addition of Fe(III)-OC coprecipitates were monitored using 16S rRNA (gene) amplicon sequencing and quantification of the bacterial and archaeal 16S rRNA gene over the course of the microcosm experiment. Community composition differed between the two soils and changed over time. Within the palsa soil, the community was dominated by the phyla *Acidobacteriota, Actinobacteriota, Proteobacteria* and *Firmicutes.* The RNA-based relative abundance of the phylum *Acidobacteriota* increased over time for both treatments (44±3% at day 0 compared to 62±6% at day 42, Figure 5a). The presence of this phylum is typical in permafrost soils[10,75,104] since it encompasses a wide array of taxa capable of complex polysaccharide degradation as well as several fermentation pathways[104]. Its increasing relative abundance over time could signal the increase of fermenting bacteria due to anoxia. After 42 days of incubation, there was a significantly higher relative abundance of *Firmicutes* in the coprecipitate-added palsa treatment, compared to the respective no-coprecipitate control (14±3% compared to 7±3%,

two-way ANOVA, p<0.01) which points towards a higher activity of fermenting microorganisms in this treatment[105]. Since fermentation produces low-molecular weight OC compound, such fatty acids, which are often further mineralized to CO_2, *Firmicutes* could have indirectly contributed to the higher CO_2 emissions in the coprecipitate-added treatment. Additionally, ANCOM revealed that the abundance of *Sphingomonas* spp. was significantly upregulated in the coprecipitate-added treatment of DNA- and RNA-based samples after 8 and 42 days compared to the no-coprecipitate control. This genus is ubiquitous in soils and known for degradation of a wide range of OC compounds[106], including aromatic compounds[107,108]. We therefore speculate that *Sphingomonas* could have been involved in decomposition of the aromatic-rich OC that was released from palsa coprecipitates, since these moieties are found to preferentially bind to Fe(III) (oxyhydr)oxides[109–111].
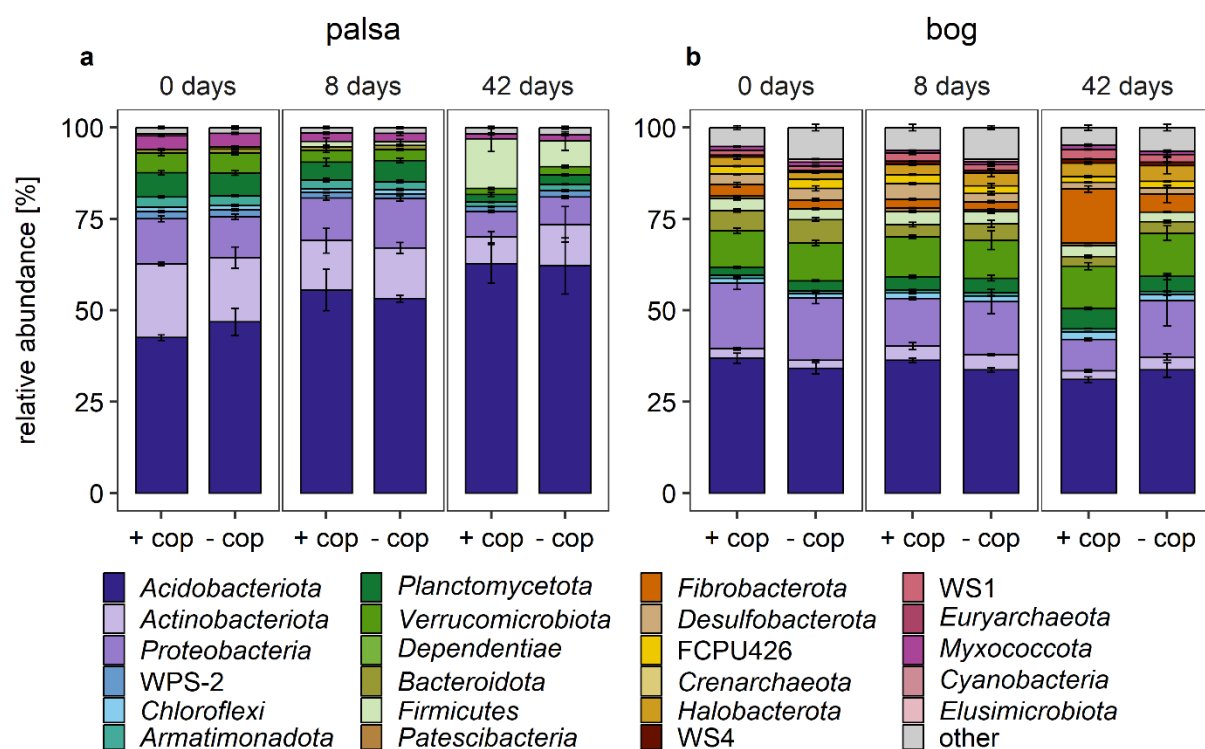
Figure 5. Shifts in the likely active (RNA-based) microbial community of palsa (a) and bog (b) soil in microcosm experiment with addition of ^{57}Fe-enriched Fe(III)-OC coprecipitates ("+ cop") and in a no-coprecipitate control ("- cop") over time. Taxa are displayed at the phylum level and those with a relative abundance below 0.5% were categorized as "other". Data and error bars represent average and standard deviation of experimental triplicates. The DNA-based dataset shows similar trends and is displayed in Figure S14.

Based on qPCR results, RNA-based gene copy numbers of bacterial and archaeal 16S rRNA gene were higher in the coprecipitate-added palsa soil directly after addition of

coprecipitates at day 0 compared to the no-coprecipitate control ($\log_2$ FC: 1.44±0.58 and 1.29±0.69, respectively, Figure S15). DNA- and RNA-based copy numbers of bacterial and archaeal 16S gene did not differ from the no-coprecipitate control after 8 days and were slightly elevated after 42 days. This could also signal a potential priming effect, induced by the release of previously Fe-bound OC, as discussed above.

The microbial community in the bog soil was more diverse than in the palsa soil, based on the number of phyla present. The dominant phylum was *Acidobacteria*, similar to the palsa soils, but its relative abundance did not change over time; instead, it remained constant at 34±2% (Figure 5b). It was also notable that the relative abundance of *Fibrobacterota*, a taxa generally known for containing (hemi-)cellulose-degraders[112,113], significantly increased in the coprecipitate-added bog treatment compared to the respective no-coprecipitate control after 42 days (15±1% compared to 5±2%, two-way ANOVA, p<0.001). This could hint at a higher OC degradation potential. Upregulated taxa due to coprecipitate addition based on ANCOM also included *Sphingomonas*, as well as *Geobacteraceae* (full list given in Figure S16). The genus *Sphingomonas* could be upregulated due to the release of Fe-bound OC as discussed above. The family *Geobacteraceae* includes well-known respiratory Fe(III)-reducers, such as *Geobacter*[69,71], which were likely more abundant due to the higher supply of Fe(III) in form of coprecipitates. Copy numbers of the bacterial and archaeal 16S gene in the coprecipitate-added bog treatment did not differ from the no-coprecipitate control over time (Figure S15), contrary to the palsa treatments. This result is consistent with the lack of difference in cumulative CO_2 emissions between the two treatments.

In situ redox conditions impact greenhouse gas emissions and Fe reduction extent in the field experiment

Within the field experiment, we determined the *in situ* reduction extent of Fe(III)-OC coprecipitates and resulting changes in net greenhouse gas emissions in the two thaw stages. For that purpose, we incubated the synthesized [NA]Fe(III)-OC coprecipitates inside peepers during the thaw season of 2022 (July to September). After 53 days, we recovered 20±7% and 10±4% of initially added solid Fe (55.8 mg L^{-1}) within the coprecipitate-added peepers in palsa and bog areas, respectively. The Fe oxidation state of these remaining solids was 99 and 23% Fe(III) in palsa and bog areas, respectively (Figure 6). The low recovery of coprecipitates within the palsa peeper was likely due to attachment of the particles to the inner or bottom part of the cells, which were not captured during our anoxic HCl extraction of the membrane. Results therefore show that added coprecipitates were not reduced within in the still oxic palsa soils. In comparison, 77% of recovered coprecipitates in the anoxic bog soils were reduced and it is likely that some Fe was dissolved during the reduction and therefore not recovered in our analysis. Taking this loss of Fe into account together with the solid phase Fe(II) content, the

102

overall reduction would be equal to 90±4%. There was no trend over depth regarding the Fe speciation within either the palsa or bog peepers (Figure S17). The no-coprecipitate added peeper in the bog area also contained 0.8-2.2 mg Fe L^{-1}, all of which was Fe(II). Dissolved species (Fe^{2+}, DOC, CO_2, CH_4) did not differ between the two setups in bog (Figure S18).

Greenhouse gas emissions differed based on season and thaw stage (Figure S19). We therefore displayed the differences in net CO_2 and CH_4 emissions between the coprecipitate-added and control plots per measurement time for each thaw stage. For the coprecipitate-added palsa plot, net CO_2 emissions (under dark conditions) did not change relative to the control plot over time (0.35±0.38 in July compared to 0.32±0.19 µmol m^{-2} s^{-1} in September, Figure 6a). This is in line with the oxic soil conditions based on water table height (Figure S20), leading to persistent Fe(III)-OC coprecipitates and thus no change in CO_2 emissions between the coprecipitate-added and respective control plot. Emissions from the coprecipitate added plot in bog soil changed drastically. Differences in CO_2 emissions of the coprecipitate-added to the control plot decreased from -0.01±0.29 in July to -0.87±0.40 µmol m^{-2} s^{-1} in September (Figure 6b). This result was thus similar to our microcosm experiment, in the sense that CO_2 emissions did not increase due to reductive dissolution of Fe(III)-OC coprecipitates. We conclude that similar processes as in the microcosm experiment could play a role, which could be enhanced under *in situ* conditions due to lower temperatures in the field than in the lab experiment, and therefore overall lower microbial respiration[114]. Net emissions of CH_4 relative to the control plot also decreased from July to September (0.27±0.08 to -0.07±0.04 µmol m^{-2} s^{-1}) which could show the inhibition of methanogenesis, similarly to the microcosm experiment. Since not all added Fe(III)-OC coprecipitates were reduced yet, the inhibition of methanogenesis was likely still ongoing. Both the microcosm and field-based experiment therefore show that Fe(III)-OC coprecipitates are able to be fully reduced within across several weeks if anoxic conditions are formed, therefore influencing the greenhouse gas budget of thawing permafrost soils.
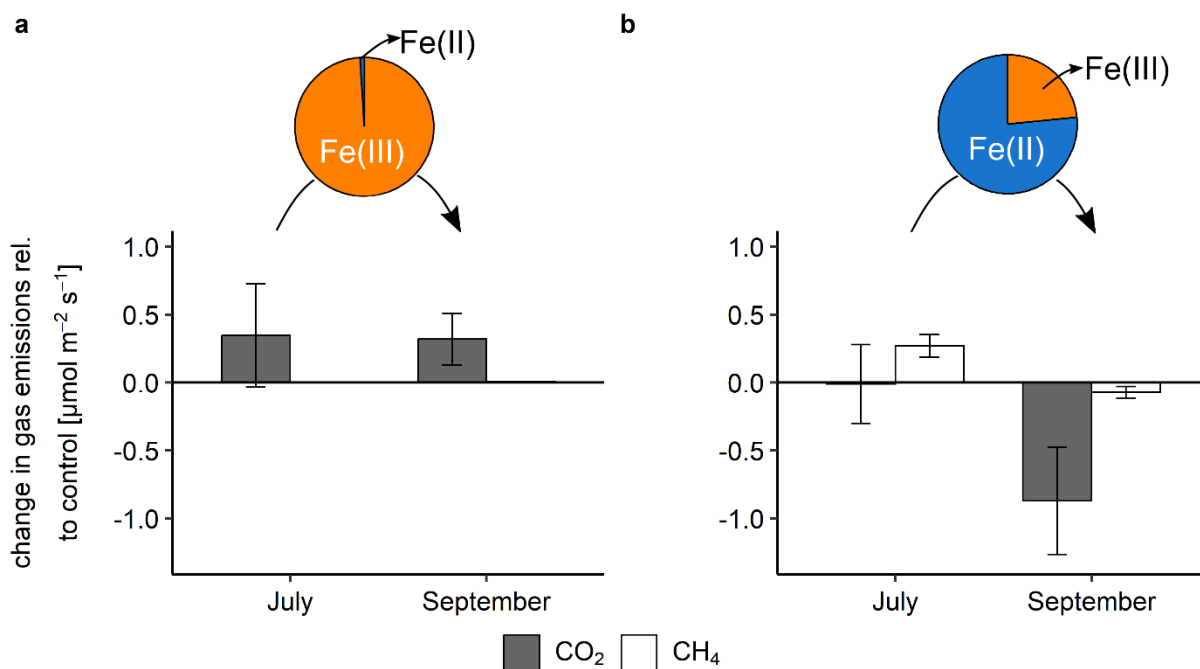
Figure 6. Redox state of recovered ^{NA}Fe(III)-OC coprecipitates and resulting changes in greenhouse gas emissions in (a) palsa and (b) bog soil of the field experiment. The Fe speciation in the solid after incubation over the thaw season is displayed in the pie diagram (average over all depths and two peepers, n=10) for both soils. Change in CO_2 and CH_4 emissions 2-24 h after addition of ^{NA}Fe(III)-OC coprecipitates (July) and after 53 days (September) are shown relative to a control plot in which only deionized water was added. Absolute flux data is provided in Figure S19. Data bars and error bars represent the average and standard deviation of triplicate flux measurements of one "+ cop" plot and one control plot.

Conclusion

Our work demonstrates that mineral-bound OC in the form of Fe(III)-OC associations is not protected after permafrost thaw followed by the onset of anoxic conditions. The added Fe(III)-OC coprecipitates were fully reduced within several weeks in collapsed palsa soils within the microcosm experiment. The reduction increased CO_2 emissions by 43±16% compared to the non-amended control, due to the use of Fe(III) as an additional electron acceptor and likely by releasing Fe-bound OC to the aqueous phase and priming the use of native DOC. As a result, excess emitted CO_2 was three times higher than expected based on the reduction of added Fe(III) alone. This implies that Fe-rich, low-land permafrost areas will likely see an increase in CO_2 emissions upon thaw-induced anoxia. Based on previously published data on Fe stocks in permafrost soils (52 to 638 g Fe m^{-2} in the upper 30 cm)[29,37,114] and a constant stoichiometry of reduced Fe to produced CO_2 (4:1), 23 to 286 Tg C could be released globally as CO_2 upon the dissolution of Fe(III)-OC associations in low-land tundra or

boreal ecosystems[115,116]. Our data even suggests that the ratio of reduced Fe to produced CO_2 after initial permafrost thaw is closer to 1:1, meaning that more CO_2 than expected based on Fe(III) reduction alone could be released.

The added Fe(III)-OC coprecipitates were also (almost) fully reduced in the naturally anoxic bog soils in both experiments. Contrary to expectations, there was no clear increase in CO_2 emissions in the microcosm experiment, such that we could not assess the direct contribution of Fe(III)-OC coprecipitates to CO_2 release. This suggests that counteracting processes, possibly due to the unique OC composition in *Sphagnum*-dominated bogs played a role. Once permafrost soils have transitioned into anoxic bog-like wetlands, the reduction of Fe(III)-OC associations might therefore not lead to excess CO_2 release. The underlying processes for this observation are still unclear and deserve further research. Regarding CH_4 emissions, it was apparent that the reduction of Fe(III)-OC coprecipitates temporarily decreased emissions in the bog soil, as long as coprecipitates were still present. Since bog soils often experience periodic water table fluctuations[117,118], the content of Fe(III)-OC associations could be replenished by abiotic coprecipitation of dissolved Fe and OC, leading to initial suppression of methanogenesis during anoxic periods. Further, the formation of Fe(III)-OC phases after coprecipitate dissolution, likely complexed to POM, could explain the high C:Fe ratios found in *Sphagnum*-dominated wetlands[34] and increase the persistence of Fe(III) under anoxic conditions. Together, our results therefore show that Fe(III)-OC associations are no stable C sink during anoxic conditions in thawing permafrost soils, thereby affecting the GHG balance in diverging ways depending on the soil biogeochemical conditions.

References

1. Schuur, E. A. G., McGuire, A. D., Schädel, C., Grosse, G., Harden, J. W., Hayes, D. J., Hugelius, G., Koven, C. D., Kuhry, P., Lawrence, D. M., Natali, S. M., Olefeldt, D., Romanovsky, V. E., Schaefer, K., Turetsky, M. R., Treat, C. C., & Vonk, J. E. (2015). Climate change and the permafrost carbon feedback. *Nature*, *520*(7546), 171–179. https://doi.org/10.1038/nature14338

2. Schuur, E. A. G., Abbott, B. W., Commane, R., Ernakovich, J., Euskirchen, E., Hugelius, G., Grosse, G., Jones, M., Koven, C., Leshyk, V., Lawrence, D., Loranty, M. M., Mauritz, M., Olefeldt, D., Natali, S., Rodenhizer, H., Salmon, V., Schädel, C., Strauss, J., … Turetsky, M. (2022). Permafrost and Climate Change: Carbon Cycle Feedbacks From the Warming Arctic. *Annual Review of Environment and Resources*, *47*(1), 343–371. https://doi.org/10.1146/annurev-environ-012220-011847

3. Turetsky, M. R., Abbott, B. W., Jones, M. C., Anthony, K. W., Olefeldt, D., Schuur, E. A. G., Grosse, G., Kuhry, P., Hugelius, G., Koven, C., Lawrence, D. M., Gibson, C., Sannel, A. B. K., & McGuire, A. D. (2020). Carbon release through abrupt permafrost thaw. *Nature Geoscience*, *13*(2), 138–143. https://doi.org/10.1038/s41561-019-0526-0

4. Walter Anthony, K., Schneider Von Deimling, T., Nitze, I., Frolking, S., Emond, A., Daanen, R., Anthony, P., Lindgren, P., Jones, B., & Grosse, G. (2018). 21st-century modeled permafrost carbon emissions accelerated by abrupt thaw beneath lakes. *Nature Communications*, *9*(1), 3262. https://doi.org/10.1038/s41467-018-05738-9

5. Andresen, C. G., Lawrence, D. M., Wilson, C. J., McGuire, A. D., Koven, C., Schaefer, K., Jafarov, E., Peng, S., Chen, X., Gouttevin, I., Burke, E., Chadburn, S., Ji, D., Chen, G., Hayes, D., & Zhang, W. (2020). Soil moisture and hydrology projections of the permafrost region – a model intercomparison. *The Cryosphere*, *14*(2), 445–459. https://doi.org/10.5194/tc-14-445-2020

6. Sim, T. G., Swindles, G. T., Morris, P. J., Baird, A. J., Cooper, C. L., Gallego-Sala, A. V., Charman, D. J., Roland, T. P., Borken, W., Mullan, D. J., Aquino-López, M. A., & Gałka, M. (2021). Divergent responses of permafrost peatlands to recent climate change. *Environmental Research Letters*, *16*(3), 034001. https://doi.org/10.1088/1748-9326/abe00b

7. Ernakovich, J. G., Lynch, L. M., Brewer, P. E., Calderon, F. J., & Wallenstein, M. D. (2017). Redox and temperature-sensitive changes in microbial communities and soil chemistry dictate greenhouse gas loss from thawed permafrost. *Biogeochemistry*, *134*(1–2), 183–200. https://doi.org/10.1007/s10533-017-0354-5

8. Gray, N. D., McCann, C. M., Christgen, B., Ahammad, S. Z., Roberts, J. A., & Graham, D. W. (2014). Soil geochemistry confines microbial abundances across an arctic landscape; implications for net carbon exchange with the atmosphere. *Biogeochemistry*, *120*(1–3), 307–317. https://doi.org/10.1007/s10533-014-9997-7

9. Graham, D. E., Wallenstein, M. D., Vishnivetskaya, T. A., Waldrop, M. P., Phelps, T. J., Pfiffner, S. M., Onstott, T. C., Whyte, L. G., Rivkina, E. M., Gilichinsky, D. A., Elias, D. A., Mackelprang, R., VerBerkmoes, N. C., Hettich, R. L., Wagner, D., Wullschleger, S. D., & Jansson, J. K. (2012). Microbes in thawing permafrost: The unknown variable in the climate change equation. *The ISME journal*, *6*(4), 709–712. https://doi.org/10.1038/ismej.2011.163

10. Waldrop, M. P., Chabot, C. L., Liebner, S., Holm, S., Snyder, M. W., Dillon, M., Dudgeon, S. R., Douglas, T. A., Leewis, M.-C., Walter Anthony, K. M., McFarland, J. W., Arp, C. D., Bondurant, A. C., Taş, N., & Mackelprang, R. (2023). Permafrost microbial communities and functional genes are structured by latitudinal and soil geochemical gradients. *The ISME Journal*, *17*(8), 1224–1235. https://doi.org/10.1038/s41396-023-01429-6

11. Gentsch, N., Wild, B., Mikutta, R., Čapek, P., Diáková, K., Schrumpf, M., Turner, S., Minnich, C., Schaarschmidt, F., Shibistova, O., Schnecker, J., Urich, T., Gittel, A., Šantrůčková, H., Bárta, J., Lashchinskiy, N., Fuß, R., Richter, A., & Guggenberger, G. (2018). Temperature response of permafrost soil carbon is attenuated by mineral protection. *Global change biology*, *24*(8), 3401–3415. https://doi.org/10.1111/gcb.14316

12. Lim, A. G., Loiko, S. V., & Pokrovsky, O. S. (2022). Sizable pool of labile organic carbon in peat and mineral soils of permafrost peatlands, western Siberia. *Geoderma*, *409*, 115601. https://doi.org/10.1016/j.geoderma.2021.115601

13. Monhonval, A., Mauclet, E., Hirst, C., Bemelmans, N., Eekman, E., Schuur, E. A. G., & Opfergelt, S. (2023). Mineral organic carbon interactions in dry versus wet tundra soils. *Geoderma*, *436*, 116552. https://doi.org/10.1016/j.geoderma.2023.116552

14. Monhonval, A., Strauss, J., Thomas, M., Hirst, C., Titeux, H., Louis, J., Gilliot, A., Du Bois d'Aische, E., Pereira, B., Vandeuren, A., Grosse, G., Schirrmeister, L., Jongejans, L. L., Ulrich, M., & Opfergelt, S. (2022). Thermokarst processes increase the supply of stabilizing surfaces and elements (Fe, Mn, Al, and Ca) for mineral–organic carbon interactions. *Permafrost and Periglacial Processes*, *33*(4), 452–469. https://doi.org/10.1002/ppp.2162

15. Gentsch, N., Mikutta, R., Shibistova, O., Wild, B., Schnecker, J., Richter, A., Urich, T., Gittel, A., Šantrůčková, H., Bárta, J., Lashchinskiy, N., Mueller, C. W., Fuß, R., & Guggenberger, G. (2015). Properties and bioavailability of particulate and mineral-associated organic matter in Arctic permafrost soils, Lower Kolyma Region, Russia. *European Journal of Soil Science*, *66*(4), 722–734. https://doi.org/10.1111/ejss.12269

16. Liu, F., Qin, S., Fang, K., Chen, L., Peng, Y., Smith, P., & Yang, Y. (2022). Divergent changes in particulate and mineral-associated organic carbon upon permafrost thaw. *Nature communications*, *13*(1), 5073. https://doi.org/10.1038/s41467-022-32681-7

17. Martens, J., Mueller, C. W., Joshi, P., Rosinger, C., Maisch, M., Kappler, A., Bonkowski, M., Schwamborn, G., Schirrmeister, L., & Rethemeyer, J. (2023). Stabilization of mineral-associated organic carbon in Pleistocene permafrost. *Nature communications*, *14*(1), 2120. https://doi.org/10.1038/s41467-023-37766-5

18. Thomas, M., Jongejans, L. L., Strauss, J., Vermylen, C., Calcus, S., Opel, T., Kizyakov, A., Wetterich, S., Grosse, G., & Opfergelt, S. (2024). A Third of Organic Carbon Is Mineral Bound in Permafrost Sediments Exposed by the World's Largest Thaw Slump, Batagay, Siberia. *Permafrost and Periglacial Processes*, ppp.2230. https://doi.org/10.1002/ppp.2230

19. Hu, Z., McKenna, A. M., Wen, K., Zhang, B., Mao, H., Goual, L., Feng, X., & Zhu, M. (2024). Controls of Mineral Solubility on Adsorption-Induced Molecular Fractionation of Dissolved Organic Matter Revealed by 21 T FT-ICR MS. *Environmental Science & Technology*, *58*(5), 2313–2322. https://doi.org/10.1021/acs.est.3c08123

20. Zhu, E., Liu, Z., Wang, S., Wang, Y., Liu, T., & Feng, X. (2023). Organic Carbon and Lignin Protection by Metal Oxides Versus Silicate Clay: Comparative Study Based on Wetland and Upland Soils. *Journal of Geophysical Research: Biogeosciences*, *128*(7), e2023JG007474. https://doi.org/10.1029/2023JG007474

21. Kleber, M., Eusterhues, K., Keiluweit, M., Mikutta, C., Mikutta, R., & Nico, P. S. (2015). *Mineral–Organic Associations: Formation, Properties, and Relevance in Soil Environments* (S. 1–140). Elsevier. https://doi.org/10.1016/bs.agron.2014.10.005

22. Monhonval, A., Hirst, C., Strauss, J., Schuur, E. A. G., & Opfergelt, S. (2023). Strontium isotopes trace the dissolution and precipitation of mineral organic carbon interactions in thawing permafrost. *Geoderma*, *433*, 116456. https://doi.org/10.1016/j.geoderma.2023.116456

23. Thomas, M., Monhonval, A., Hirst, C., Bröder, L., Zolkos, S., Vonk, J. E., Tank, S. E., Keskitalo, K. H., Shakil, S., Kokelj, S. V., Van Der Sluijs, J., & Opfergelt, S. (2023). Evidence for preservation of organic carbon interacting with iron in material displaced from retrogressive thaw slumps: Case study in Peel Plateau, western Canadian Arctic. *Geoderma*, *433*, 116443. https://doi.org/10.1016/j.geoderma.2023.116443

24. Farquharson, L. M., Romanovsky, V. E., Cable, W. L., Walker, D. A., Kokelj, S. V., & Nicolsky, D. (2019). Climate Change Drives Widespread and Rapid Thermokarst Development in Very Cold Permafrost in the Canadian High Arctic. *Geophysical Research Letters*, *46*(12), 6681–6689. https://doi.org/10.1029/2019GL082187

25. Jorgenson, M. T., Harden, J., Kanevskiy, M., O'Donnell, J., Wickland, K., Ewing, S., Manies, K., Zhuang, Q., Shur, Y., Striegl, R., & Koch, J. (2013). Reorganization of vegetation, hydrology and soil carbon after permafrost degradation across heterogeneous boreal landscapes. *Environmental Research Letters*, *8*(3), 035017. https://doi.org/10.1088/1748-9326/8/3/035017

26. Varner, R. K., Crill, P. M., Frolking, S., McCalley, C. K., Burke, S. A., Chanton, J. P., Holmes, M. E., Saleska, S., & Palace, M. W. (2022). Permafrost thaw driven changes in hydrology and vegetation cover increase trace gas emissions and climate forcing in Stordalen Mire from 1970 to 2014. *Philosophical transactions. Series A, Mathematical, physical, and engineering sciences*, *380*(2215), 20210022. https://doi.org/10.1098/rsta.2021.0022

27. Woo, M., & Young, K. L. (2006). High Arctic wetlands: Their occurrence, hydrological characteristics and sustainability. *Journal of Hydrology*, *320*(3–4), 432–450. https://doi.org/10.1016/j.jhydrol.2005.07.025

28. Barreto, M. S. C., Wani, R. P., Goranov, A. I., Sowers, T. D., Fischel, M., Douglas, T. A., Hatcher, P. G., & Sparks, D. L. (2024). Carbon Fate, Iron Dissolution, and Molecular Characterization of Dissolved Organic Matter in Thawed Yedoma Permafrost under Varying Redox Conditions. *Environmental Science & Technology*, acs.est.3c08219. https://doi.org/10.1021/acs.est.3c08219

29. Patzner, M. S., Mueller, C. W., Malusova, M., Baur, M., Nikeleit, V., Scholten, T., Hoeschen, C., Byrne, J. M., Borch, T., Kappler, A., & Bryce, C. (2020). Iron mineral dissolution releases iron and associated organic carbon during permafrost thaw. *Nature communications*, *11*(1), 6329. https://doi.org/10.1038/s41467-020-20102-6

30. Chen, C., Hall, S. J., Coward, E., & Thompson, A. (2020). Iron-mediated organic matter decomposition in humid soils can counteract protection. *Nature communications*, *11*(1), 2255. https://doi.org/10.1038/s41467-020-16071-5

31. Huang, W., & Hall, S. J. (2017). Elevated moisture stimulates carbon loss from mineral soils by releasing protected organic matter. *Nature Communications*, *8*(1), 1774. https://doi.org/10.1038/s41467-017-01998-z

32. Sun, F.-S., Ma, C., Yu, G.-H., Kuzyakov, Y., Lang, Y.-C., Fu, P.-Q., Guo, L.-J., Teng, H. H., & Liu, C.-Q. (2023). Organic carbon preservation in wetlands: Iron oxide protection vs. thermodynamic limitation. *Water Research*, *241*, 120133. https://doi.org/10.1016/j.watres.2023.120133

33. Zhao, B., Dou, A., Zhang, Z., Chen, Z., Sun, W., Feng, Y., Wang, X., & Wang, Q. (2023). Ecosystem-specific patterns and drivers of global reactive iron mineral-associated organic carbon. *Biogeosciences*, *20*(23), 4761–4774. https://doi.org/10.5194/bg-20-4761-2023

34. Zhao, Y., Liu, C., Li, X., Ma, L., Zhai, G., & Feng, X. (2023). Sphagnum increases soil's sequestration capacity of mineral-associated organic carbon via activating metal oxides. *Nature Communications*, *14*(1), 5052. https://doi.org/10.1038/s41467-023-40863-0

35. Eusterhues, K., Hädrich, A., Neidhardt, J., Küsel, K., Keller, T. F., Jandt, K. D., & Totsche, K. U. (2014). Reduction of ferrihydrite with adsorbed and coprecipitated organic matter: Microbial reduction by Geobacter bremensis vs. Abiotic reduction by Na-dithionite. *Biogeosciences*, *11*(18), 4953–4966. https://doi.org/10.5194/bg-11-4953-2014

36. Poggenburg, C., Mikutta, R., Schippers, A., Dohrmann, R., & Guggenberger, G. (2018). Impact of natural organic matter coatings on the microbial reduction of iron oxides. *Geochimica et Cosmochimica Acta*, *224*, 223–248. https://doi.org/10.1016/j.gca.2018.01.004

37. Lipson, D. A., Raab, T. K., Goria, D., & Zlamal, J. (2013). The contribution of Fe(III) and humic acid reduction to ecosystem respiration in drained thaw lake basins of the Arctic Coastal Plain. *Global Biogeochemical Cycles*, *27*(2), 399–409. https://doi.org/10.1002/gbc.20038

38. Patzner, M. S., Logan, M., McKenna, A. M., Young, R. B., Zhou, Z., Joss, H., Mueller, C. W., Hoeschen, C., Scholten, T., Straub, D., Kleindienst, S., Borch, T., Kappler, A., & Bryce, C. (2022). Microbial iron cycling during palsa hillslope collapse promotes greenhouse gas emissions before complete permafrost thaw. *Communications Earth & Environment*, *3*(1). https://doi.org/10.1038/s43247-022-00407-8

39. Lipson, D. A., Jha, M., Raab, T. K., & Oechel, W. C. (2010). Reduction of iron (III) and humic substances plays a major role in anaerobic respiration in an Arctic peat soil. *Journal of Geophysical Research*, *115*. https://doi.org/10.1029/2009JG001147

40. Lipson, D. A., Zona, D., Raab, T. K., Bozzolo, F., Mauritz, M., & Oechel, W. C. (2012). Water-table height and microtopography control biogeochemical cycling in an Arctic coastal tundra ecosystem. *Biogeosciences*, *9*(1), 577–591. https://doi.org/10.5194/bg-9-577-2012

41. Miller, K. E., Lai, C.-T., Friedman, E. S., Angenent, L. T., & Lipson, D. A. (2015). Methane suppression by iron and humic acids in soils of the Arctic Coastal Plain. *Soil Biology and Biochemistry*, *83*, 176–183. https://doi.org/10.1016/j.soilbio.2015.01.022

42. Reiche, M., Torburg, G., & Küsel, K. (2008). Competition of Fe(III) reduction and methanogenesis in an acidic fen. *FEMS microbiology ecology*, *65*(1), 88–101. https://doi.org/10.1111/j.1574-6941.2008.00523.x

43. Herndon, E. M., Yang, Z., Bargar, J., Janot, N., Regier, T. Z., Graham, D. E., Wullschleger, S. D., Gu, B., & Liang, L. (2015). Geochemical drivers of organic matter decomposition in arctic tundra soils. *Biogeochemistry*, *126*(3), 397–414. https://doi.org/10.1007/s10533-015-0165-5

44. Yang, Z., Wullschleger, S. D., Liang, L., Graham, D. E., & Gu, B. (2016). Effects of warming on the degradation and production of low-molecular-weight labile organic carbon in an Arctic tundra soil. *Soil Biology and Biochemistry*, *95*, 202–211. https://doi.org/10.1016/j.soilbio.2015.12.022

45. Drake, H. L., Horn, M. A., & Wüst, P. K. (2009). Intermediary ecosystem metabolism as a main driver of methanogenesis in acidic wetland soil. *Environmental Microbiology Reports*, *1*(5), 307–318. https://doi.org/10.1111/j.1758-2229.2009.00050.x

46. Malmer, N., Johansson, T., Olsrud, M., & Christensen, T. R. (2005). Vegetation, climatic changes and net carbon sequestration in a North-Scandinavian subarctic mire over 30 years. *Global change biology*, *0*(0), 051006062331004-. https://doi.org/10.1111/j.1365-2486.2005.01042.x

47. Swedish Meteorological and Hydrological Institute. (2020, Februar 1). *Air temperature, Abisko Station*. https://www.smhi.se/data/meteorologi/ladda-ner-meteorologiska-observationer#stationid=188800,param=airtemperatureInstant,stations=core

48. Johansson, T., Malmer, N., Crill, P. M., Friborg, T., Åkerman, J. H., Mastepanov, M., & Christensen, T. R. (2006). Decadal vegetation changes in a northern peatland, greenhouse gas fluxes and net radiative forcing. *Global change biology*, *12*(12), 2352–2369. https://doi.org/10.1111/j.1365-2486.2006.01267.x

49. Notini, L., ThomasArrigo, L. K., Kaegi, R., & Kretzschmar, R. (2022). Coexisting Goethite Promotes Fe(II)-Catalyzed Transformation of Ferrihydrite to Goethite. *Environmental Science & Technology*, *56*(17), 12723–12733. https://doi.org/10.1021/acs.est.2c03925

50. ThomasArrigo, L. K., Byrne, J. M., Kappler, A., & Kretzschmar, R. (2018). Impact of Organic Matter on Iron(II)-Catalyzed Mineral Transformations in Ferrihydrite-Organic Matter Coprecipitates. *Environmental science & technology*, *52*(21), 12316–12326. https://doi.org/10.1021/acs.est.8b03206

51. Heron, Gorm., Crouzet, Catherine., Bourg, A. C. M., & Christensen, T. H. (1994). Speciation of Fe(II) and Fe(III) in Contaminated Aquifer Sediments Using Chemical Extraction Techniques. *Environmental Science & Technology*, *28*(9), 1698–1705. https://doi.org/10.1021/es00058a023

52. Kostka, J. E., & Luther, G. W. (1994). Partitioning and speciation of solid phase iron in saltmarsh sediments. *Geochimica et Cosmochimica Acta*, *58*(7), 1701–1710. https://doi.org/10.1016/0016-7037(94)90531-2

53. Stookey, L. L. (1970). Ferrozine—A new spectrophotometric reagent for iron. *Analytical Chemistry*, *42*(7), 779–781. https://doi.org/10.1021/ac60289a016

54. Chen, J., Gu, B., Royer, R., & Burgos, W. (2003). The roles of natural organic matter in chemical and microbial reduction of ferric iron. *The Science of The Total Environment*, *307*(1–3), 167–178. https://doi.org/10.1016/S0048-9697(02)00538-7

55. Ravel, B., & Newville, M. (2005). ATHENA and ARTEMIS Interactive Graphical Data Analysisusing IFEFFIT. *Physica Scripta*, *2005*(T115), 1007. https://doi.org/10.1238/Physica.Topical.115a01007

56. Parada, A. E., Needham, D. M., & Fuhrman, J. A. (2016). Every base matters: Assessing small subunit rRNA primers for marine microbiomes with mock communities, time series and global field samples. *Environmental Microbiology*, *18*(5), 1403–1414. https://doi.org/10.1111/1462-2920.13023

57. Apprill, A., McNally, S., Parsons, R., & Weber, L. (2015). Minor revision to V4 region SSU rRNA 806R gene primer greatly increases detection of SAR11 bacterioplankton. *Aquatic Microbial Ecology*, *75*(2), 129–137. https://doi.org/10.3354/ame01753

58. Straub, D., Tångrot, J., Peltzer, A., Lundin, D., emnilsson, nf-core bot, Sateesh_Peri, Adam Bennett, John Sundh, DiegoBrambilla, Asaf Peer, Till E, Lokeshwaran Manoharan, Maxime U Garcia, Sam Minot, PhilPalmer, Harshil Patel, Venkat Malladi, Matthew, … Kevin Menden. (2024). *nf-core/ampliseq: Ampliseq Version 2.8.0* (Version 2.8.0) [Software]. [object Object]. https://doi.org/10.5281/ZENODO.1493841

59. Straub, D., Blackwell, N., Langarica-Fuentes, A., Peltzer, A., Nahnsen, S., & Kleindienst, S. (2020). Interpretations of Environmental Microbial Community Studies Are Biased by the Selected 16S rRNA (Gene) Amplicon Sequencing Pipeline. *Frontiers in Microbiology*, *11*, 550420. https://doi.org/10.3389/fmicb.2020.550420

60. Ewels, P. A., Peltzer, A., Fillinger, S., Patel, H., Alneberg, J., Wilm, A., Garcia, M. U., Di Tommaso, P., & Nahnsen, S. (2020). The nf-core framework for community-curated bioinformatics pipelines. *Nature Biotechnology*, *38*(3), 276–278. https://doi.org/10.1038/s41587-020-0439-x

61. Friedrich, M. W. (2005). Methyl-Coenzyme M Reductase Genes: Unique Functional Markers for Methanogenic and Anaerobic Methane-Oxidizing Archaea. In *Methods in*

Enzymology (Bd. 397, S. 428–442). Elsevier. https://doi.org/10.1016/S0076-6879(05)97026-2

62. Juottonen, H., Galand, P. E., & Yrjälä, K. (2006). Detection of methanogenic Archaea in peat: Comparison of PCR primers targeting the mcrA gene. *Research in Microbiology*, *157*(10), 914–921. https://doi.org/10.1016/j.resmic.2006.08.006

63. Winkel, M., Mitzscherling, J., Overduin, P. P., Horn, F., Winterfeld, M., Rijkers, R., Grigoriev, M. N., Knoblauch, C., Mangelsdorf, K., Wagner, D., & Liebner, S. (2018). Anaerobic methanotrophic communities thrive in deep submarine permafrost. *Scientific Reports*, *8*(1), 1291. https://doi.org/10.1038/s41598-018-19505-9

64. Liebner, S., Ganzert, L., Kiss, A., Yang, S., Wagner, D., & Svenning, M. M. (2015). Shifts in methanogenic community composition and methane fluxes along the degradation of discontinuous permafrost. *Frontiers in Microbiology*, *6*. https://doi.org/10.3389/fmicb.2015.00356

65. R Core Team. (2024). *R: A language and environment for statistical computing* (Vienna, Austria). R Foundation for Statistical Computing. https://www.R-project.org/

66. Pedersen, H. D., Postma, D., Jakobsen, R., & Larsen, O. (2005). Fast transformation of iron oxyhydroxides by the catalytic action of aqueous Fe(II). *Geochimica et Cosmochimica Acta*, *69*(16), 3967–3977. https://doi.org/10.1016/j.gca.2005.03.016

67. ThomasArrigo, L. K., Mikutta, C., Byrne, J., Kappler, A., & Kretzschmar, R. (2017). Iron(II)-Catalyzed Iron Atom Exchange and Mineralogical Changes in Iron-rich Organic Freshwater Flocs: An Iron Isotope Tracer Study. *Environmental Science & Technology*, *51*(12), 6897–6907. https://doi.org/10.1021/acs.est.7b01495

68. Williams, A. G. B., & Scherer, M. M. (2004). Spectroscopic Evidence for Fe(II)−Fe(III) Electron Transfer at the Iron Oxide−Water Interface. *Environmental Science & Technology*, *38*(18), 4782–4790. https://doi.org/10.1021/es049373g

69. Coates, J. D., Phillips, E. J., Lonergan, D. J., Jenter, H., & Lovley, D. R. (1996). Isolation of Geobacter species from diverse sedimentary environments. *Applied and Environmental Microbiology*, *62*(5), 1531–1536. https://doi.org/10.1128/aem.62.5.1531-1536.1996

70. Li, L., Qu, Z., Wang, B., & Qu, D. (2017). Dynamics of the abundance and structure of metabolically active Clostridium community in response to glucose additions in flooded paddy soils: Closely correlated with hydrogen production and Fe(III) reduction. *Journal of Soils and Sediments*, *17*(6), 1727–1740. https://doi.org/10.1007/s11368-016-1637-5

71. Lovley, D. R., Holmes, D. E., & Nevin, K. P. (2004). Dissimilatory Fe(III) and Mn(IV) reduction. In *Advances in microbial physiology* (S. 212–286).

72. Treude, N., Rosencrantz, D., Liesack, W., & Schnell, S. (2003). Strain FAc12, a dissimilatory iron-reducing member of the Anaeromyxobacter subgroup of Myxococcales. *FEMS Microbiology Ecology*, *44*(2), 261–269. https://doi.org/10.1016/S0168-6496(03)00048-5

73. Blöthe, M., Akob, D. M., Kostka, J. E., Göschel, K., Drake, H. L., & Küsel, K. (2008). pH Gradient-Induced Heterogeneity of Fe(III)-Reducing Microorganisms in Coal Mining-Associated Lake Sediments. *Applied and Environmental Microbiology*, *74*(4), 1019–1029. https://doi.org/10.1128/AEM.01194-07

74. Glodowska, M., Schneider, M., Eiche, E., Kontny, A., Neumann, T., Straub, D., Berg, M., Prommer, H., Bostick, B. C., Nghiem, A. A., Kleindienst, S., & Kappler, A. (2021). Fermentation, methanotrophy and methanogenesis influence sedimentary Fe and As dynamics in As-affected aquifers in Vietnam. *Science of The Total Environment*, *779*, 146501. https://doi.org/10.1016/j.scitotenv.2021.146501

75. Hultman, J., Waldrop, M. P., Mackelprang, R., David, M. M., McFarland, J., Blazewicz, S. J., Harden, J., Turetsky, M. R., McGuire, A. D., Shah, M. B., VerBerkmoes, N. C., Lee, L. H., Mavrommatis, K., & Jansson, J. K. (2015). Multi-omics of permafrost, active layer and thermokarst bog soil microbiomes. *Nature*, *521*(7551), 208–212. https://doi.org/10.1038/nature14238

76. Li, H., Peng, J., Weber, K. A., & Zhu, Y. (2011). Phylogenetic diversity of Fe(III)-reducing microorganisms in rice paddy soil: Enrichment cultures with different short-chain fatty acids as electron donors. *Journal of Soils and Sediments*, *11*(7), 1234–1242. https://doi.org/10.1007/s11368-011-0371-2

77. Bauer, I., & Kappler, A. (2009). Rates and Extent of Reduction of Fe(III) Compounds and O_2 by Humic Substances. *Environmental Science & Technology*, *43*(13), 4902–4908. https://doi.org/10.1021/es900179s

78. Roden, E. E., Kappler, A., Bauer, I., Jiang, J., Paul, A., Stoesser, R., Konishi, H., & Xu, H. (2010). Extracellular electron transfer through microbial reduction of solid-phase humic substances. *Nature Geoscience*, *3*(6), 417–421. https://doi.org/10.1038/ngeo870

79. Joshi, P., Schroth, M. H., & Sander, M. (2021). Redox Properties of Peat Particulate Organic Matter: Quantification of Electron Accepting Capacities and Assessment of Electron Transfer Reversibility. *Journal of Geophysical Research: Biogeosciences*, *126*(8), e2021JG006329. https://doi.org/10.1029/2021JG006329

80. Obradović, N., Schmitz, R. A., Haffter, F., Meier, D. V., Lever, M. A., Schroth, M. H., & Sander, M. (2024). Peat Particulate Organic Matter Accepts Electrons During In Situ Incubation in the Anoxic Subsurface of Ombrotrophic Bogs. *Journal of Geophysical Research: Biogeosciences*, *129*(9), e2024JG008223. https://doi.org/10.1029/2024JG008223

81. Dong, H., Zeng, Q., Sheng, Y., Chen, C., Yu, G., & Kappler, A. (2023). Coupled iron cycling and organic matter transformation across redox interfaces. *Nature Reviews Earth & Environment*, *4*(9), 659–673. https://doi.org/10.1038/s43017-023-00470-5

82. Küsel, K., Dorsch, T., Acker, G., & Stackebrandt, E. (1999). Microbial Reduction of Fe(III) in Acidic Sediments: Isolation of *Acidiphilium cryptum* JF-5 Capable of Coupling the Reduction of Fe(III) to the Oxidation of Glucose. *Applied and Environmental Microbiology*, *65*(8), 3633–3640. https://doi.org/10.1128/AEM.65.8.3633-3640.1999

83. Klüpfel, L., Piepenbrock, A., Kappler, A., & Sander, M. (2014). Humic substances as fully regenerable electron acceptors in recurrently anoxic environments. *Nature Geoscience*, *7*(3), 195–200. https://doi.org/10.1038/ngeo2084

84. Scott, D. T., McKnight, D. M., Blunt-Harris, E. L., Kolesar, S. E., & Lovley, D. R. (1998). Quinone Moieties Act as Electron Acceptors in the Reduction of Humic Substances by Humics-Reducing Microorganisms. *Environmental Science & Technology*, *32*(19), 2984–2989. https://doi.org/10.1021/es980272q

85. Gorski, C. A., Edwards, R., Sander, M., Hofstetter, T. B., & Stewart, S. M. (2016). Thermodynamic Characterization of Iron Oxide–Aqueous Fe^{2+} Redox Couples. *Environmental Science & Technology*, *50*(16), 8538–8547. https://doi.org/10.1021/acs.est.6b02661

86. Kappler, A., Bryce, C., Mansor, M., Lueder, U., Byrne, J. M., & Swanner, E. D. (2021). An evolving view on biogeochemical cycling of iron. *Nature reviews. Microbiology*. https://doi.org/10.1038/s41579-020-00502-7

87. Joshi, P., ThomasArrigo, L. K., Sawwa, D., Sauter, L., & Kappler, A. (2024). Complexation by Particulate Organic Matter Alters Iron Redox Behavior. *ACS Earth and Space Chemistry*, *8*(2), 310–322. https://doi.org/10.1021/acsearthspacechem.3c00288

88. Uchimiya, M., & Stone, A. T. (2009). Reversible redox chemistry of quinones: Impact on biogeochemical cycles. *Chemosphere*, *77*(4), 451–458. https://doi.org/10.1016/j.chemosphere.2009.07.025

89. Küsel, K., Blöthe, M., Schulz, D., Reiche, M., & Drake, H. L. (2008). Microbial reduction of iron and porewater biogeochemistry in acidic peatlands. *Biogeosciences*, *5*(6), 1537–1549. https://doi.org/10.5194/bg-5-1537-2008

90. ThomasArrigo, L. K., Vontobel, S., Notini, L., & Nydegger, T. (2023). Coprecipitation with Ferrihydrite Inhibits Mineralization of Glucuronic Acid in an Anoxic Soil. *Environmental Science & Technology*, *57*(25), 9204–9213. https://doi.org/10.1021/acs.est.3c01336

91. Wang, S., Gao, W., Ma, Z., Zhu, Z., Luo, Y., Wei, L., Yuan, H., Chen, S., Ying, C., Mason-Jones, K., Kuzyakov, Y., & Ge, T. (2024). Iron mineral type controls organic matter stability and priming in paddy soil under anaerobic conditions. *Soil Biology and Biochemistry*, 109518. https://doi.org/10.1016/j.soilbio.2024.109518

92. Ellenbogen, J. B., Borton, M. A., McGivern, B. B., Cronin, D. R., Hoyt, D. W., Freire-Zapata, V., McCalley, C. K., Varner, R. K., Crill, P. M., Wehr, R. A., Chanton, J. P., Woodcroft, B. J., Tfaily, M. M., Tyson, G. W., Rich, V. I., & Wrighton, K. C. (2024). Methylotrophy in the Mire: Direct and indirect routes for methane production in thawing permafrost. *mSystems*, *9*(1), e00698-23. https://doi.org/10.1128/msystems.00698-23

93. McCalley, C. K., Woodcroft, B. J., Hodgkins, S. B., Wehr, R. A., Kim, E.-H., Mondav, R., Crill, P. M., Chanton, J. P., Rich, V. I., Tyson, G. W., & Saleska, S. R. (2014). Methane dynamics regulated by microbial community response to permafrost thaw. *Nature*, *514*(7523), 478–481. https://doi.org/10.1038/nature13798

94. Knoblauch, C., Beer, C., Liebner, S., Grigoriev, M. N., & Pfeiffer, E.-M. (2018). Methane production as key to the greenhouse gas budget of thawing permafrost. *Nature Climate Change*, *8*(4), 309–312. https://doi.org/10.1038/s41558-018-0095-z

95. Cory, A. B., Chanton, J. P., Spencer, R. G. M., Ogles, O. C., Rich, V. I., McCalley, C. K., IsoGenie Project Coordinators, EMERGE 2021 Field Team, & Wilson, R. M. (2022). Quantifying the inhibitory impact of soluble phenolics on anaerobic carbon mineralization in a thawing permafrost peatland. *PLOS ONE*, *17*(2), e0252743. https://doi.org/10.1371/journal.pone.0252743

96. AminiTabrizi, R., Wilson, R. M., Fudyma, J. D., Hodgkins, S. B., Heyman, H. M., Rich, V. I., Saleska, S. R., Chanton, J. P., & Tfaily, M. M. (2020). Controls on Soil Organic Matter Degradation and Subsequent Greenhouse Gas Emissions Across a Permafrost Thaw Gradient in Northern Sweden. *Frontiers in Earth Science*, *8*, 557961. https://doi.org/10.3389/feart.2020.557961

97. Freeman, C., Ostle, N. J., Fenner, N., & Kang, H. (2004). A regulatory role for phenol oxidase during decomposition in peatlands. *Soil Biology and Biochemistry*, *36*(10), 1663–1667. https://doi.org/10.1016/j.soilbio.2004.07.012

98. Chen, K.-Y., Chen, T.-Y., Chan, Y.-T., Cheng, C.-Y., Tzou, Y.-M., Liu, Y.-T., & Teah, H.-Y. (2016). Stabilization of Natural Organic Matter by Short-Range-Order Iron Hydroxides. *Environmental Science & Technology*, *50*(23), 12612–12620. https://doi.org/10.1021/acs.est.6b02793

99. Wang, Y., Liu, X., Zhang, X., Dai, G., Wang, Z., & Feng, X. (2022). Evaluating wetland soil carbon stability related to iron transformation during redox oscillations. *Geoderma*, *428*, 116222. https://doi.org/10.1016/j.geoderma.2022.116222

100. Ketudat Cairns, J. R., & Esen, A. (2010). β-Glucosidases. *Cellular and Molecular Life Sciences*, *67*(20), 3389–3405. https://doi.org/10.1007/s00018-010-0399-2

101. Kurth, J. M., Op Den Camp, H. J. M., & Welte, C. U. (2020). Several ways one goal—Methanogenesis from unconventional substrates. *Applied Microbiology and Biotechnology*, *104*(16), 6839–6854. https://doi.org/10.1007/s00253-020-10724-7

102. Liu, Y., & Whitman, W. B. (2008). Metabolic, Phylogenetic, and Ecological Diversity of the Methanogenic Archaea. *Annals of the New York Academy of Sciences*, *1125*(1), 171–189. https://doi.org/10.1196/annals.1419.019

103. Jørgensen, B. B. (2006). Bacteria and Marine Biogeochemistry. In H. D. Schulz & M. Zabel (Hrsg.), *Marine Geochemistry* (S. 169–206). Springer-Verlag. https://doi.org/10.1007/3-540-32144-6_5

104. Woodcroft, B. J., Singleton, C. M., Boyd, J. A., Evans, P. N., Emerson, J. B., Zayed, A. A. F., Hoelzle, R. D., Lamberton, T. O., McCalley, C. K., Hodgkins, S. B., Wilson, R. M., Purvine, S. O., Nicora, C. D., Li, C., Frolking, S., Chanton, J. P., Crill, P. M., Saleska, S. R., Rich, V. I., & Tyson, G. W. (2018). Genome-centric view of carbon processing in thawing permafrost. *Nature*, *560*(7716), 49–54. https://doi.org/10.1038/s41586-018-0338-1

105. Li, Y., Xue, Y., Roy Chowdhury, T., Graham, D. E., Tringe, S. G., Jansson, J. K., & Taş, N. (2024). Genomic insights into redox-driven microbial processes for carbon decomposition in thawing Arctic soils and permafrost. *mSphere*, e00259-24. https://doi.org/10.1128/msphere.00259-24

106. Sood, U., Hira, P., Singh, P., Singh, D. N., & Lal, R. (2021). *Sphingomonas*. In W. B. Whitman (Hrsg.), *Bergey's Manual of Systematics of Archaea and Bacteria* (1. Aufl., S. 1–84). Wiley. https://doi.org/10.1002/9781118960608.gbm00924.pub2

107. Kim, E., Aversano, P. J., Romine, M. F., Schneider, R. P., & Zylstra, G. J. (1996). Homology between genes for aromatic hydrocarbon degradation in surface and deep-subsurface Sphingomonas strains. *Applied and Environmental Microbiology*, *62*(4), 1467–1470. https://doi.org/10.1128/aem.62.4.1467-1470.1996

108. Zylstra, G. J., & Kim, E. (1997). Aromatic hydrocarbon degradation by Sphingomonas yanoikuyae B1. *Journal of Industrial Microbiology and Biotechnology*, *19*(5–6), 408–414. https://doi.org/10.1038/sj.jim.2900475

109. Chen, C., Dynes, J. J., Wang, J., & Sparks, D. L. (2014). Properties of Fe-organic matter associations via coprecipitation versus adsorption. *Environmental science & technology*, *48*(23), 13751–13759. https://doi.org/10.1021/es503669u

110. Voggenreiter, E., Schmitt-Kopplin, P., ThomasArrigo, L., Bryce, C., Kappler, A., & Joshi, P. (2024). Emerging investigator series: Preferential adsorption and coprecipitation of permafrost organic matter with poorly crystalline iron minerals. *Environmental Science: Processes & Impacts*, 10.1039.D4EM00241E. https://doi.org/10.1039/D4EM00241E

111. Zhu, X., Wang, K., Liu, Z., Wang, J., Wu, E., Yu, W., Zhu, X., Chu, C., & Chen, B. (2023). Probing Molecular-Level Dynamic Interactions of Dissolved Organic Matter with Iron Oxyhydroxide via a Coupled Microfluidic Reactor and an Online High-Resolution Mass Spectrometry System. *Environmental Science & Technology*, *57*(7), 2981–2991. https://doi.org/10.1021/acs.est.2c06816

112. Ransom-Jones, E., Jones, D. L., McCarthy, A. J., & McDonald, J. E. (2012). The Fibrobacteres: An Important Phylum of Cellulose-Degrading Bacteria. *Microbial Ecology*, *63*(2), 267–281. https://doi.org/10.1007/s00248-011-9998-1

113. Weimer, P. J. (2022). Degradation of Cellulose and Hemicellulose by Ruminal Microorganisms. *Microorganisms*, *10*(12), 2345. https://doi.org/10.3390/microorganisms10122345

114. Karhu, K., Auffret, M. D., Dungait, J. A. J., Hopkins, D. W., Prosser, J. I., Singh, B. K., Subke, J.-A., Wookey, P. A., Ågren, G. I., Sebastià, M.-T., Gouriveau, F., Bergkvist, G.,

Meir, P., Nottingham, A. T., Salinas, N., & Hartley, I. P. (2014). Temperature sensitivity of soil respiration rates enhanced by microbial community response. *Nature*, *513*(7516), 81–84. https://doi.org/10.1038/nature13604

115. Mu, C. C., Zhang, T. J., Zhao, Q., Guo, H., Zhong, W., Su, H., & Wu, Q. B. (2016). Soil organic carbon stabilization by iron in permafrost regions of the Qinghai-Tibet Plateau. *Geophysical Research Letters*, *43*(19), 10286–10294. https://doi.org/10.1002/2016GL070071

116. Hugelius, G., Strauss, J., Zubrzycki, S., Harden, J. W., Schuur, E. A. G., Ping, C.-L., Schirrmeister, L., Grosse, G., Michaelson, G. J., Koven, C. D., O'Donnell, J. A., Elberling, B., Mishra, U., Camill, P., Yu, Z., Palmtag, J., & Kuhry, P. (2014). Estimated stocks of circumpolar permafrost carbon with quantified uncertainty ranges and identified data gaps. *Biogeosciences*, *11*(23), 6573–6593. https://doi.org/10.5194/bg-11-6573-2014

117. Nitzbon, J., Schneider Von Deimling, T., Aliyeva, M., Chadburn, S. E., Grosse, G., Laboor, S., Lee, H., Lohmann, G., Steinert, N. J., Stuenzi, S. M., Werner, M., Westermann, S., & Langer, M. (2024). No respite from permafrost-thaw impacts in the absence of a global tipping point. *Nature Climate Change*, *14*(6), 573–585. https://doi.org/10.1038/s41558-024-02011-4

118. Breeuwer, A., Robroek, B. J. M., Limpens, J., Heijmans, M. M. P. D., Schouten, M. G. C., & Berendse, F. (2009). Decreased summer water table depth affects peatland vegetation. *Basic and Applied Ecology*, *10*(4), 330–339. https://doi.org/10.1016/j.baae.2008.05.005

119. Olefeldt, D., Roulet, N. T., Bergeron, O., Crill, P., Bäckstrand, K., & Christensen, T. R. (2012). Net carbon accumulation of a high-latitude permafrost palsa mire similar to permafrost-free peatlands. *Geophysical Research Letters*, *39*(3). https://doi.org/10.1029/2011GL050355

120. Raiswell, R., Canfield, D. E., & Berner, R. A. (1994). A comparison of iron extraction methods for the determination of degree of pyritisation and the recognition of iron-limited pyrite formation. *Chemical Geology*, *111*(1–4), 101–110. https://doi.org/10.1016/0009-2541(94)90084-1

121. Minh, D. D., Macdonald, B., Warneke, S., & White, I. (2018). Fluxes of greenhouse gases from incubated soils using different lid-closure times. *Soil Research*, *56*(1), 39. https://doi.org/10.1071/SR17050

122. Notini, L., Schulz, K., Kubeneck, L. J., Grigg, A. R. C., Rothwell, K. A., Fantappiè, G., ThomasArrigo, L. K., & Kretzschmar, R. (2023). A New Approach for Investigating Iron Mineral Transformations in Soils and Sediments Using ^{57}Fe-Labeled Minerals and ^{57}Fe Mössbauer Spectroscopy. *Environmental Science & Technology*, *57*(27), 10008–10018. https://doi.org/10.1021/acs.est.3c00434

123. Lagarec, K., & Rancourt, D. G. (1997). Extended Voigt-based analytic lineshape method for determining N-dimensional correlated hyperfine parameter distributions in Mössbauer spectroscopy. *Nuclear Instruments and Methods in Physics Research Section B: Beam Interactions with Materials and Atoms*, *129*(2), 266–280. https://doi.org/10.1016/s0168-583x(97)00284-x

124. Otte, J. M., Blackwell, N., Soos, V., Rughöft, S., Maisch, M., Kappler, A., Kleindienst, S., & Schmidt, C. (2018). Sterilization impacts on marine sediment—Are we able to inactivate microorganisms in environmental samples? *FEMS Microbiology Ecology*, *94*(12). https://doi.org/10.1093/femsec/fiy189

125. Martin, M. (2011). Cutadapt removes adapter sequences from high-throughput sequencing reads. *EMBnet.journal*, *17*(1), 10. https://doi.org/10.14806/ej.17.1.200

126. Callahan, B. J., McMurdie, P. J., Rosen, M. J., Han, A. W., Johnson, A. J. A., & Holmes, S. P. (2016). DADA2: High-resolution sample inference from Illumina amplicon data. *Nature Methods*, *13*(7), 581–583. https://doi.org/10.1038/nmeth.3869

127. Quast, C., Pruesse, E., Yilmaz, P., Gerken, J., Schweer, T., Yarza, P., Peplies, J., & Glöckner, F. O. (2012). The SILVA ribosomal RNA gene database project: Improved data processing and web-based tools. *Nucleic Acids Research*, *41*(D1), D590–D596. https://doi.org/10.1093/nar/gks1219

128. Bolyen, E., Rideout, J. R., Dillon, M. R., Bokulich, N. A., Abnet, C. C., Al-Ghalith, G. A., Alexander, H., Alm, E. J., Arumugam, M., Asnicar, F., Bai, Y., Bisanz, J. E., Bittinger, K., Brejnrod, A., Brislawn, C. J., Brown, C. T., Callahan, B. J., Caraballo-Rodríguez, A. M., Chase, J., … Caporaso, J. G. (2019). Reproducible, interactive, scalable and extensible microbiome data science using QIIME 2. *Nature Biotechnology*, *37*(8), 852–857. https://doi.org/10.1038/s41587-019-0209-9

129. Straub, K., Kappler, A., & Schink, B. (2005). Enrichment and Isolation of Ferric-Iron- and Humic-Acid-Reducing Bacteria. In *Methods in Enzymology* (Bd. 397, S. 58–77). Elsevier. https://doi.org/10.1016/S0076-6879(05)97004-3

130. Muyzer, G., Teske, A., Wirsen, C. O., & Jannasch, H. W. (1995). Phylogenetic relationships ofThiomicrospira species and their identification in deep-sea hydrothermal vent samples by denaturing gradient gel electrophoresis of 16S rDNA fragments. *Archives of Microbiology*, *164*(3), 165–172. https://doi.org/10.1007/BF02529967

131. Nadkarni, M. A., Martin, F. E., Jacques, N. A., & Hunter, N. (2002). Determination of bacterial load by real-time PCR using a broad-range (universal) probe and primers set. *Microbiology*, *148*(1), 257–266. https://doi.org/10.1099/00221287-148-1-257

132. Großkopf, R., Janssen, P. H., & Liesack, W. (1998). Diversity and Structure of the Methanogenic Community in Anoxic Rice Paddy Soil Microcosms as Examined by Cultivation and Direct 16S rRNA Gene Sequence Retrieval. *Applied and Environmental Microbiology*, *64*(3), 960–969. https://doi.org/10.1128/AEM.64.3.960-969.1998

133. Stahl, D., & Amann, R. (1991). Development and application of nucleic acid probes in bacterial systematics. In *Nucleic acid techniques in bacterial systematics* (S. 205–248). John Wiley & Sons Ltd.

134. Hales, B. A., Edwards, C., Ritchie, D. A., Hall, G., Pickup, R. W., & Saunders, J. R. (1996). Isolation and identification of methanogen-specific DNA from blanket bog peat by PCR amplification and sequence analysis. *Applied and Environmental Microbiology*, *62*(2), 668–675. https://doi.org/10.1128/aem.62.2.668-675.1996

135. Mueller, C. W., Rethemeyer, J., Kao-Kniffin, J., Löppmann, S., Hinkel, K. M., & G. Bockheim, J. (2015). Large amounts of labile organic carbon in permafrost soils of northern A laska. *Global Change Biology*, *21*(7), 2804–2817. https://doi.org/10.1111/gcb.12876

Supporting Information

Text S1. Selective Fe mineral extractions of subsoils used for the microcosm experiment

Selective Fe extractions were performed to quantify the content and speciation of different Fe pools in the subsoils of palsa and bog used for the microcosm experiment. A 0.5 M HCl extraction, targeting poorly crystalline Fe(III) (oxyhydr)oxide minerals, adsorbed Fe(II), FeS and partially $FeCO_3$[51,52] and a 6 M HCl extraction, targeting more crystalline phases (goethite, magnetite and partially Fe in phyllosilicates[51,119]) were performed in experimental triplicate. The dry soil (300 mg) was added into 1 M HCl-washed 20 mL glass vials in an anoxic glovebox (MBraun Unilab Workstation, 100% N_2 atmosphere) and 14 mL of anoxic extractant solution was added. The vials were closed with butyl rubber stoppers and crimped with aluminum caps, after which they were put on a rolling shaker (60 rpm) in the dark for 24 h. The samples were brought back to the glovebox and centrifuged (10,055 rcf, 5 min) after transferring them to 2 mL Eppendorf tubes. Samples were diluted in 1 M HCl and Fe speciation was measured by the ferrozine assay[53].

Text S2. Isolation of water-extractable organic matter (WEOM)

Field-moist soil of the upper soil layers of palsa and bog areas was added to double-deionized water (DDI, Millipore, >18 MΩ cm^{-1}) at a 1:10 weight/volume (w/v) ratio for 24 h on an overhead shaker in the dark. Resulting suspensions were centrifuged in pre-baked glass serum bottles (5250 rcf, 15 min) and the supernatant was sequentially filtered through pre-rinsed 8 µm (Merck Millipore, MCE) and 0.22 µm (Merck Millipore, Steritop PES) filters. The final water-extractable organic matter (WEOM) was stored at 4°C (<24 h until use).

Text S3. Calculation of greenhouse gas flux

The gas fluxes of carbon dioxide (CO_2) and methane (CH_4) were calculated according to Equation (1), as in Minh et al. (2018)[121]:

$$R = \Delta c \ \frac{p \times V_{HS}}{R \times T \times m_{soil}} \qquad\qquad Eq\ (1)$$

where R is the flux (µmol d^{-1} g^{-1} dry soil), Δc is the slope of the measured gas concentrations over time (ppm d^{-1}), p is the pressure (101325 Pa), V_{HS} is the headspace volume in the incubation bottle (m^3), R is the ideal gas constant (8.31 J mol^{-1} K^{-1}), T is the temperature (293 K) and m_{soil} is the mass of dry soil left in the incubation bottle (g dry weight). The V_{HS} and m_{soil} were changed after each sampling, due to output of sampled suspension.

The cumulative gas flux was calculated based on a simple interpolation:

$$R_{cum,n} = \Delta t_{n-k} \times \frac{1}{2} \times (R_k + R_n) + R_{cum,k} \qquad\qquad Eq\ (2)$$

where $R_{cum,n}$ is the cumulative flux at a given timepoint n (µmol g^{-1} dry soil), Δt_{k-n} is the timeframe between timepoint n and the prior timepoint k (d), R_k and R_n are the fluxes on timepoint k and n (µmol d^{-1} g^{-1} dry soil), respectively, and $R_{cum,k}$ is the cumulative flux at timepoint k (µmol g^{-1} dry soil). The first cumulative flux at timepoint 0 was calculated by including a measurement which was done one day prior (before addition of Fe(III)-OC coprecipitates).

Text S4. Calculation of aqueous and solid (0.5 M HCl extractable) Fe from ^{57}Fe-enriched Fe-OC coprecipitates

The share of aqueous and solid Fe originating directly from added coprecipitates was calculated based on the isotope signature, as described in Notini et al. (2023)[122]. We know that the fraction of ^{57}Fe to ^{56}Fe+^{57}Fe ($f^{57}Fe_{+cop}$), which is measured by ICP-MS, can also be described as

$$f^{57}Fe_{+cop} = \frac{f^{57}Fe_{Fe-oc} \times f_{Fe-oc} + f^{57}Fe_{soil} \times (100 - f_{Fe-oc})}{100} \qquad Eq\ (3)$$

, in which $f^{57}Fe_{Fe-OC}$ is the known fraction of ^{57}Fe to ^{56}Fe+^{57}Fe in the labelled coprecipitates (9.8 and 10.4% for palsa and bog coprecipitates, respectively), fFe_{Fe-OC} is the fraction of aqueous Fe coming from coprecipitates [%] and $f^{57}Fe_{soil}$ is the measured fraction of ^{57}Fe to ^{56}Fe+^{57}Fe in the no-coprecipitate control setup. By re-arranging for fFe_{Fe-OC}, we get:

$$\mathfrak{f}_{Fe-OC} = \frac{100 \times (\mathfrak{f}^{57}Fe_{+cop} - \mathfrak{f}^{57}Fe_{soil})}{\mathfrak{f}^{57}Fe_{Fe-OC} - \mathfrak{f}^{57}Fe_{soil}} \qquad \text{Eq (4)}$$

We then multiply the fraction with the absolute concentration of total aqueous Fe measured by the ferrozine assay ($c(Fe_{aq})$, [mM]) to get the amount of aqueous Fe derived from the reductive dissolution of ^{57}Fe-enriched Fe-OC coprecipitates c_{Fe-OC} [mM], which is displayed in Figure 1b:

$$c_{Fe-OC} = c(Fe_{aq}) \times \mathfrak{f}_{Fe-OC} \qquad \text{Eq (5)}$$

Text S5. Quantification of microbial metabolites by gas chromatography coupled to mass spectrometry (GC-MS)

The concentration of metabolites was measured using GC-MS (Shimadzu GC/MS TQ 8040, Japan) operated in Electron Ionisation mode (EI). Metabolites were measured either by headspace injection (MS acquisition mode: Scan) or as a liquid sample after derivatization (MS acquisition mode: MRM). For derivatization, samples were thawed on ice and 3000 pmol ^{13}C-glucose was added as an internal standard to 250 µL sample prior to freeze-drying. The solids were re-dissolved with 50 µL methoxamine (20 mg mL^{-1} pyridine), ultrasonicated for 10 min and subsequently incubated at 30° C for 90 min. Next, 70 µL N-methyl-N-(trimethylsilyl)-trifluor-acetamid (MSTFA) was added and samples were incubated at 40°C for 60 min, after which they were kept at room temperature for 2 h. A volume of 1 µL was used for injection in splitted mode on a Restek SH-Rxi-5SIL MS column (30 m; film 0.25 µm; diameter 0.25 mm). The injection port was heated to 280°C. For chromatographic separation a He flow rate of 1.1 mL min^{-1} and a temperature increase of 10°C min^{-1} from 100 to 320°C were employed. For the measurement via the headspace method, 250 µL of thawed sample together with 2500 pmol octanol as internal standard were added into glass vials with closed lids. A volume of 1 ml of headspace gas was injected onto the column Stabilwax-DA from Restek. The He flow rate was 1.1 mL min^{-1} and the column temperature increased by 10°C min^{-1} from 40 to 240°C. Concentrations were quantified with a 8-point external calibration containing standards of all targeted analytes, ranging from 20 to max. 10^7 pmol per 250 µL.

Text S6. Data analysis of Fe *K*-edge X-ray absorption spectra

Data processing included energy calibration, pre-edge subtraction, and post-edge normalization done in Athena[55]. The Fe redox state was estimated by linear combination fitting (LCF) of the XANES region from -20 to +30 eV around the edge energy. References for XANES spectra included ferrihydrite (representative for Fe(III)) and Fe(II)-citrate (representative for

Fe(II)). Speciation of Fe was examined by LCF of the k^3-weighted EXAFS region in a k range from 2 to 11 Å-1. The edge energy of all samples and references was set to 7128 eV. The following reference compounds were selected: ferrihydrite, lepidocrocite, Fe(III)-citrate, Fe(III)-catechol, Fe(II)-citrate, Fe(II)-EDTA, Fe(II)-catechol, Fe(II)-mercaptoethanol. Components were constrained between 0 and 100% during fitting, but no constraints were set on the sum of components. Initial fractions of detected Fe phases were re-calculated to sum up to 100% and fractions below 5% were disgarded.

Text S7. Data analysis of 57Fe Mössbauer spectra

^{57}Fe-enriched Fe(III)-OC coprecipitates were analyzed by ^{57}Fe Mössbauer spectrsocopy. Samples were collected by filtration (0.45 μm nitrocellulose, Millipore) after the washing procedure. The filter paper with contained solids was fixed between Kapton® tape and frozen (-20°C). Samples were inserted into a closed-cycle exchange gas cryostat (Janis cryogenics) under a gasflow of He to minimize air exposure. Spectra were collected at 30 and 6 K. Spectra were taken using a constant acceleration drive system (WissEL) in transmission mode with a ^{57}Co/Rh source. All spectra were calibrated against a 7 μm thick α-^{57}Fe foil that was measured at room temperature. Data analysis was performed using Recoil (University of Ottawa) and the Voigt based fitting routine[123] was used. The half width at half maximum was constrained to 0.116 mm s^{-1} during fitting.

Text S8. DNA and RNA extraction procedure and 16S rRNA (gene) amplicon sequencing

Total DNA and RNA of soil samples from the microcosm experiment were extracted in experimental triplicate using the RNeasy PowerSoil® Total RNA Kit with DNA Elution (Qiagen, Germany). The following adjustments were made to the manufacturer's instructions: 1-1.5 g of soil (wet weight) was added to the bead tube; 10 min bead-beating; all centrifugation steps (of 15 mL tubes) at 7000 rcf at 4°C; incubation time at -20°C for 1.5 h; final pellets were dried on a clean bench and resuspended in 50 µL RNase or DNase-free water. The quality of the extracted RNA and DNA was examined using Nanodrop (NanoDrop 1000, Thermo Scientific, USA) and concentrations were quantified using Qubit® 2.0 Fluorometer with RNA and DNA HS kits (Life Technologies, USA). Remaining DNA in the RNA samples was digested and the RNA was reverse transcribed using commercial kits (Invitrogen, Life Technologies, USA) as described in Otte et al. (2018)[124]. Complete digestion of DNA and transcription of RNA to cDNA was confirmed using agarose gel electrophoresis after polymerase chain reaction (PCR) with primers specific for the 16S rRNA gene of bacteria (341f, 907r).

Library preparation steps (Nextera, Illumina) and sequencing were performed using Illumina MiSeq sequencing system (Illumina, USA) at the Institute for Medical Microbiology and Hygiene (MGM) of the University of Tübingen. In total 12,854,425 paired-end reads with length 250 bp were obtained for 72 out of 108 samples (6,325 to 215,979 read pairs per sample, in average 119,022, only one sample below 40,000 read pairs). Data processing, including quality control, reconstruction of sequences and taxonomic annotation was done using nf-core/ampliseq version 2.8.0[58,59] of the nf-core collection of workflows[60]. Primers were trimmed using Cutadapt v3.4[125] and untrimmed sequences were discarded. Less than 37.6% of sequences were discarded per sample and 83.9% of sequences passed the filtering on average. Adapter and primer-free sequences were pooled with DADA2 v1.28[126] to eliminate PhiX contamination, trim reads (forward reads at 231 bp and reverse reads at 207 bp), discard reads with >2 expected errors, correct errors, merge read pairs, and remove PCR chimeras. Ultimately, 13476 amplicon sequencing variants (ASVs) were obtained across all samples. Between 67.97% and 81.11% reads per sample (average 77.50%) were retained. ASVs with length lower than 240 or above 270 bp were removed (143 of 13476). Taxonomic classification was performed by DADA2 and the database 'Silva 138.1 prokaryotic SSU'[127]. Of 13333 ASVs, 90 ASVs designated as mitochondria or chloroplasts were removed within QIIME2 version 2023.7.[128]. Finally, 13,243 amplicon sequencing variants (ASVs) with between 4,071 and 148,556 counts (average 78,255) per sample were obtained.
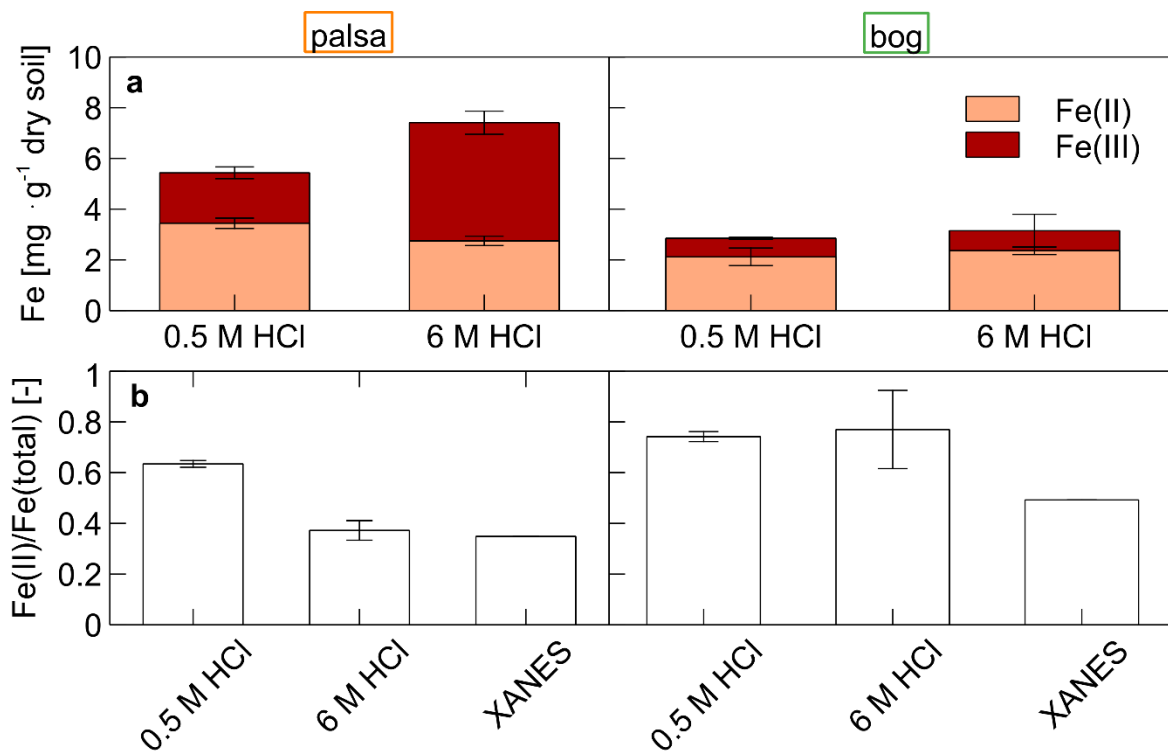
Figure S1. Fe content and speciation of initial palsa and bog soils used for the microcosm experiments. (a) Contents and speciation of Fe based on selective extractions targeting the poorly crystalline (0.5 M HCl-extractable) and more crystalline (6 M HCl-extractable) Fe pool. (b) Fe(II) to Fe(total) ratio for both soils based on selective extractions and linear combination fitting Fe *K*-edge X-ray absorption near edge structure (XANES). Data bars and error bars represent mean and standard deviation of experimental triplicates.
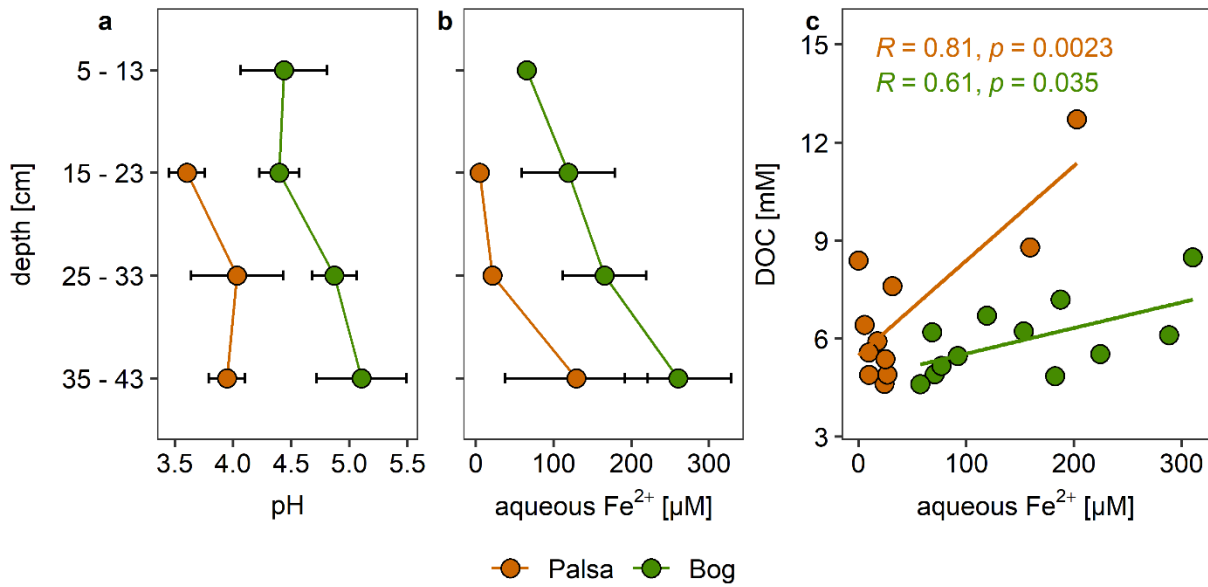
Figure S2. Geochemical parameters over depth in palsa and bog porewater. Subplots display porewater pH (a) and aqueous Fe^{2+} concentration (b) as well as a correlation of dissolved organic carbon (DOC) against aqueous Fe^{2+} concentrations. Lines show fitted Pearson correlation with given R and p value. The depth axis of subplot (a) is also applicable to (b). Data points and error bars show average and standard deviation of 3-5 samples per depth taken in July 2022.
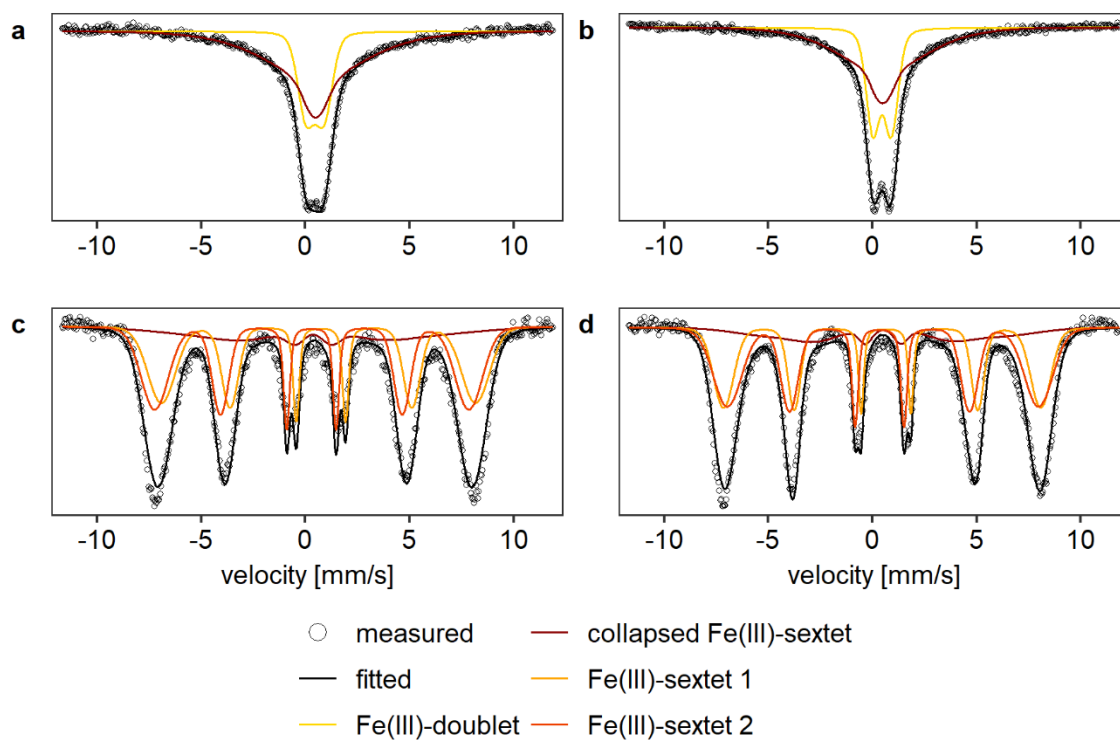
Figure S3. [57]Fe Mössbauer spectra of initial synthesized [57]Fe-enriched Fe(III)-OC coprecipitates using palsa (a, c) and bog (b, d) water-extractable organic matter. Spectra were taken at 30 K (a, b) and 6 K (c, d). Measured data is displayed as open dots and initial components and the overall fit as lines. The fitting parameters are shown in Table S6.
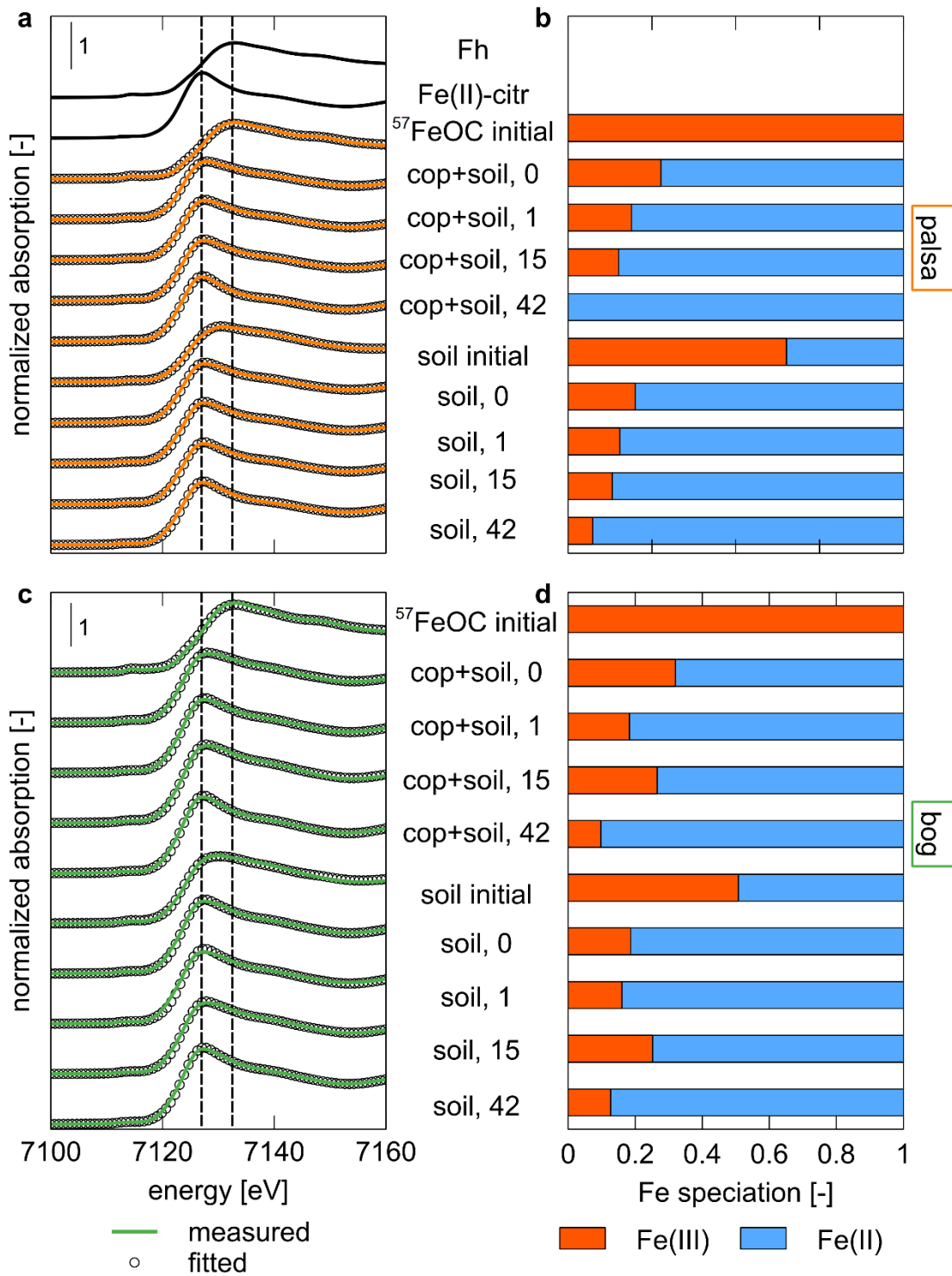
Figure S4. (a,c) Linear combination fitting of Fe *K*-edge X-ray absorption near edge structure (XANES) and (b,d) resulting Fe speciation relating to the microcosm experiment using (a,b) palsa and (c,d) bog soil. Results of initial ^{57}Fe-enriched Fe-OC coprecipitates, initial palsa and bog soils and samples with addition of ^{57}Fe-enriched Fe(III)-OC coprecipitates ("cop+soil") and no-coprecipitate controls ("soil") after 0, 1, 15 and 42 days are displayed. Solid lines show the measured spectra and open dots show the fits. The labels in the middle also apply to the bar

graph. References of ferrihydrite (Fh) and Fe(II)-citrate (Fe(II)-citr) were used as representatives for Fe(III) and Fe(II). Fitting parameters are given in Table S5.
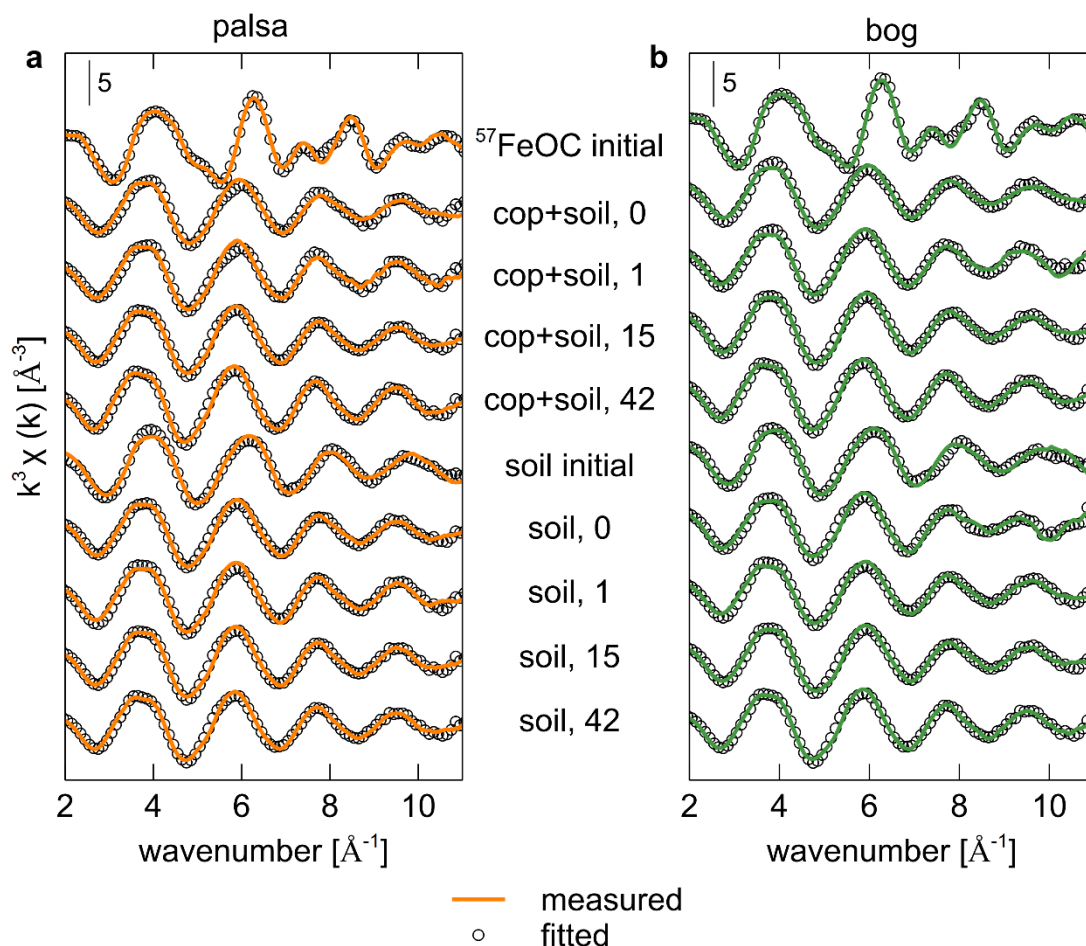
Figure S5. Linear combination fitting of k^3-weighted Fe K-edge extended X-ray absorption fine structure (EXAFS) relating to the microcosm experiment using (a) palsa and (b) bog soil. Results of initial ^{57}Fe -enriched Fe-OC coprecipitates, initial palsa and bog soils and samples with addition of ^{57}Fe-enriched Fe(III)-OC coprecipitates ("cop+soil") and no-coprecipitate controls ("soil") after 0, 1, 15 and 42 days are displayed. Solid lines show the measured spectra and open dots show the fits. Fitting results and parameters are given in the main text.
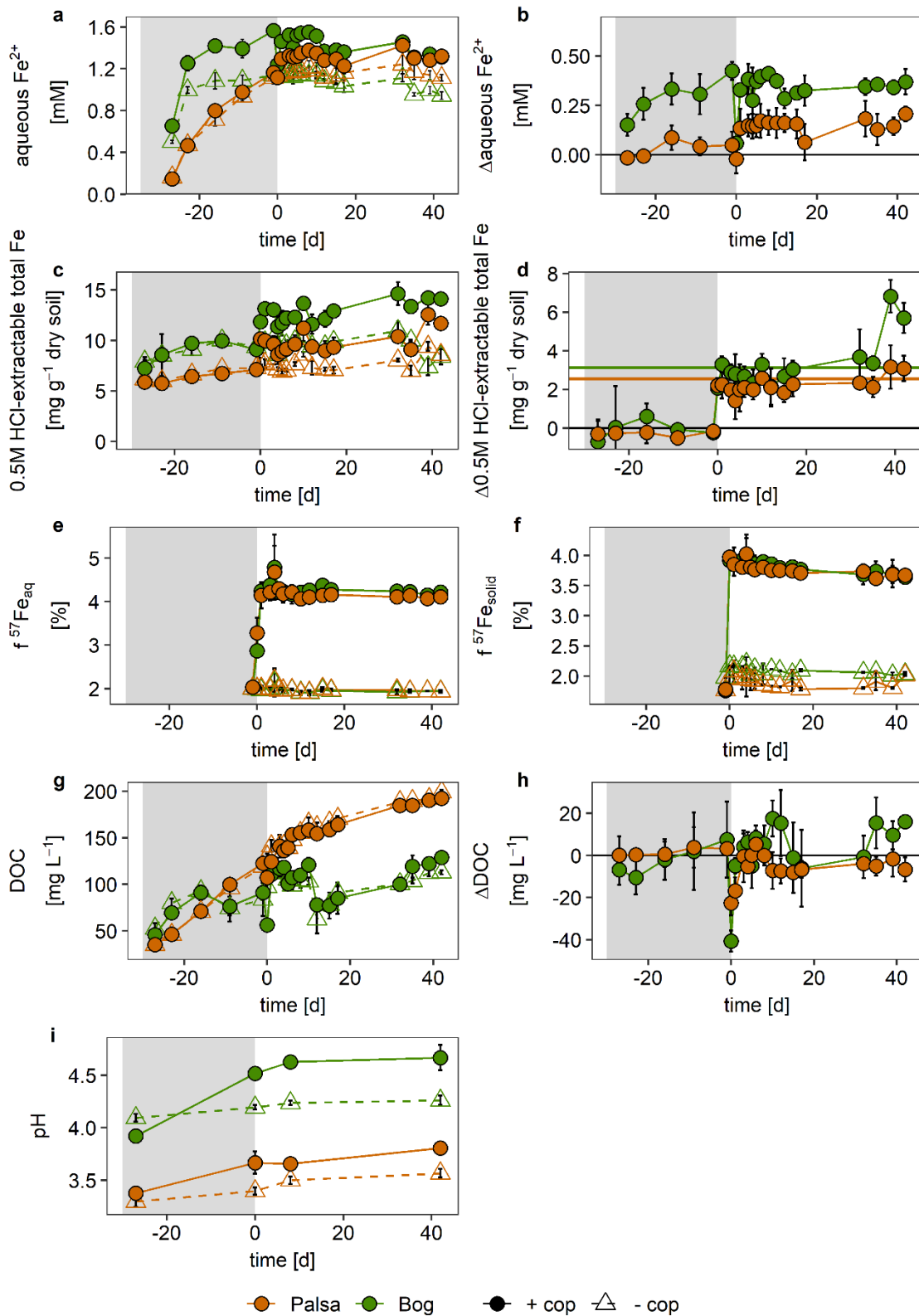
**Figure S6**. Different geochemical parameters (aqueous Fe, 0.5 M HCl-extractable total Fe, fraction of aqueous and solid ^{57}Fe, pH, and dissolved organic carbon concentration (DOC)) within the microcoms experiments using palsa and bog soil with added ^{57}Fe-enriched Fe(III)-OC coprecipitates (+ cop) and without (- cop). Left panels show the absolute data over time

and right panels show the difference between the + cop setup and the – cop setup (in case of aqueous Fe^{2+}, 0.5 M HCl-extractable Fe and DOC) over time. Solid, horizontal lines in panel d show the calculated addition of ^{57}Fe-enriched Fe(III)-OC coprecipitates which is equal to 50% relative to the native 6 M HCl-extractable Fe pool. The grey shaded area represents the incubation time before coprecipitates were added. Data points and error bars represent average and standard deviation of experimental triplicates.
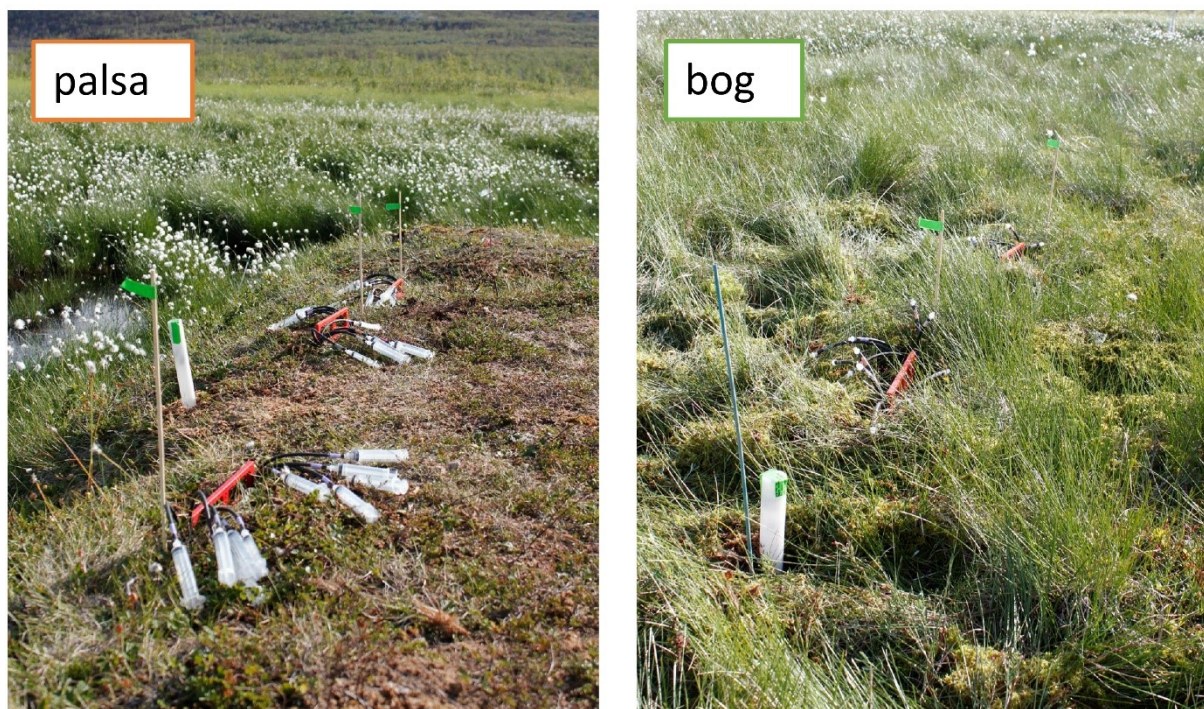
Figure S7. Photographs of setup of the field experiment involving three peepers and one water table datalogger (inside white plastic tube) in palsa and bog area. Photographs were taken in July 2022.
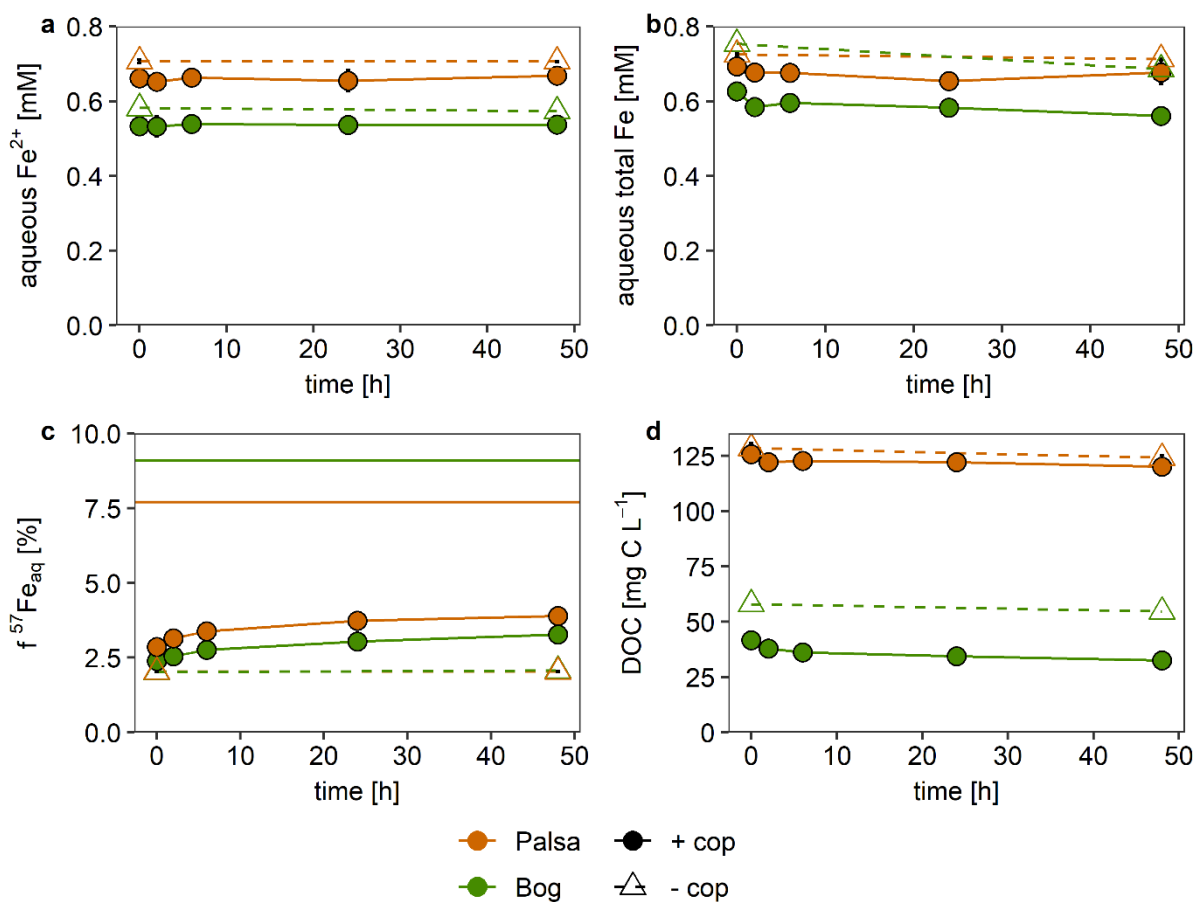
Figure S8. Results of the abiotic control setup of palsa- and bog-derived porewater with added ^{57}Fe-enriched Fe(III)-OC coprecipitates (+ cop) and without (- cop). Panels show the concentrations of aqueous Fe^{2+} (a), total Fe (b), the fraction of aqueous ^{57}Fe (c) and the DOC concentration (d) over time. Solid lines in panel (c) show the theoretical fraction of ^{57}Fe if complete isotopic exchange were to occur. Data points and error bars represent average and standard deviation of experimental triplicates in case of the coprecipitate-added setup and experimental duplicates for the no-coprecipitate palsa setup. Only one replicate was possible for the no-coprecipitate bog setup due to limiting sample volume.

130
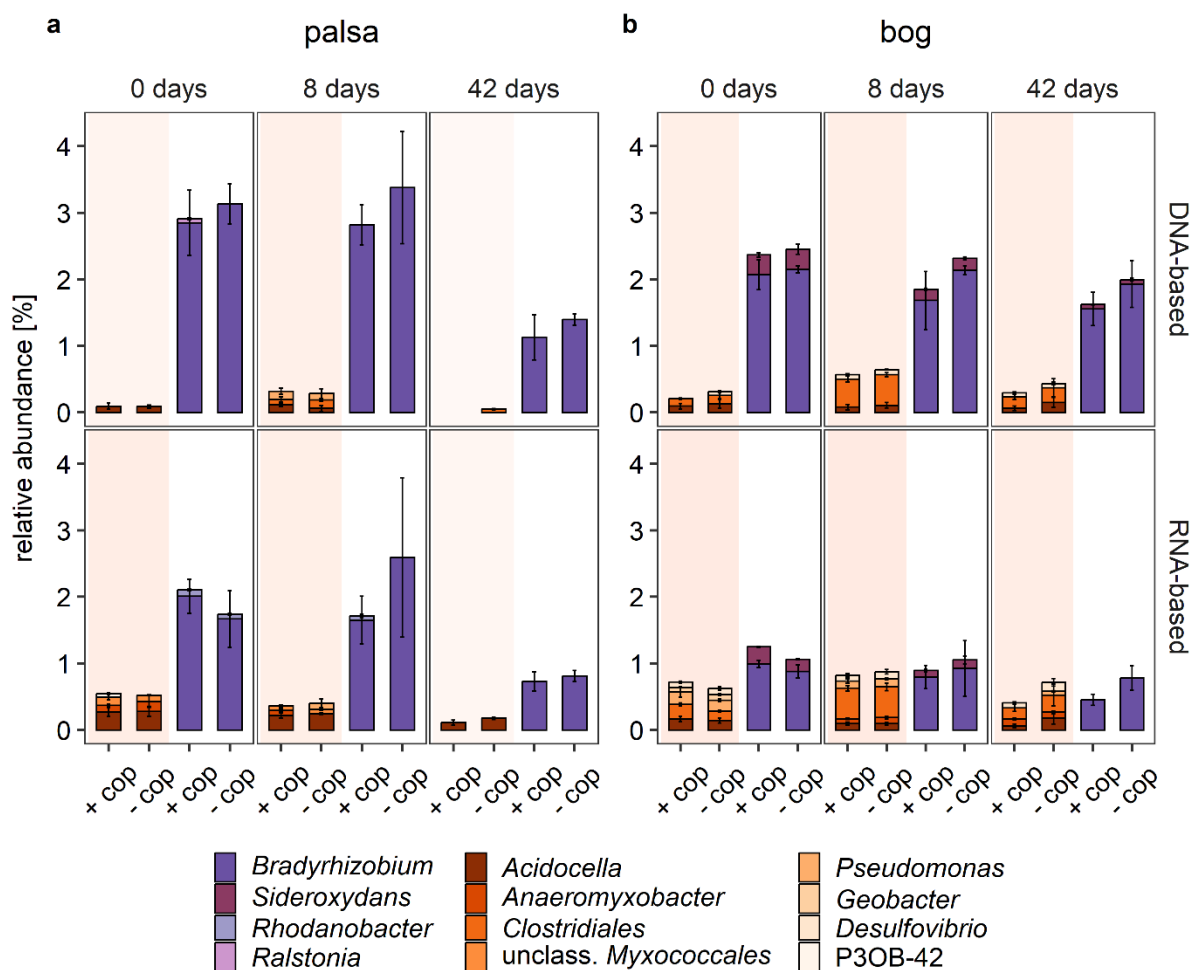
Figure S9. Relative abundances of present (DNA-based) and likely active (RNA-based) identified Fe(III)-reducing (orange colors) and Fe(II)-oxidizing (purple colours) microorganisms per timepoint (0, 8, 42 days) and setup (with added Fe(III)-OC coprecipitates: "+ cop", no-coprecipitate control: "- cop") in the microcosm experiment using (a) palsa and (b) bog soil. Results are based on 16S rRNA (gene) amplicon sequencing and taxa with a relative abundance >0.05% are displayed. Taxa are labelled at the genus-level, except for *Clostridiales* and unclassified *Myxococcales* for which no genus could be identified. Data bars and error bars display the mean and standard deviation of experimental triplicates.
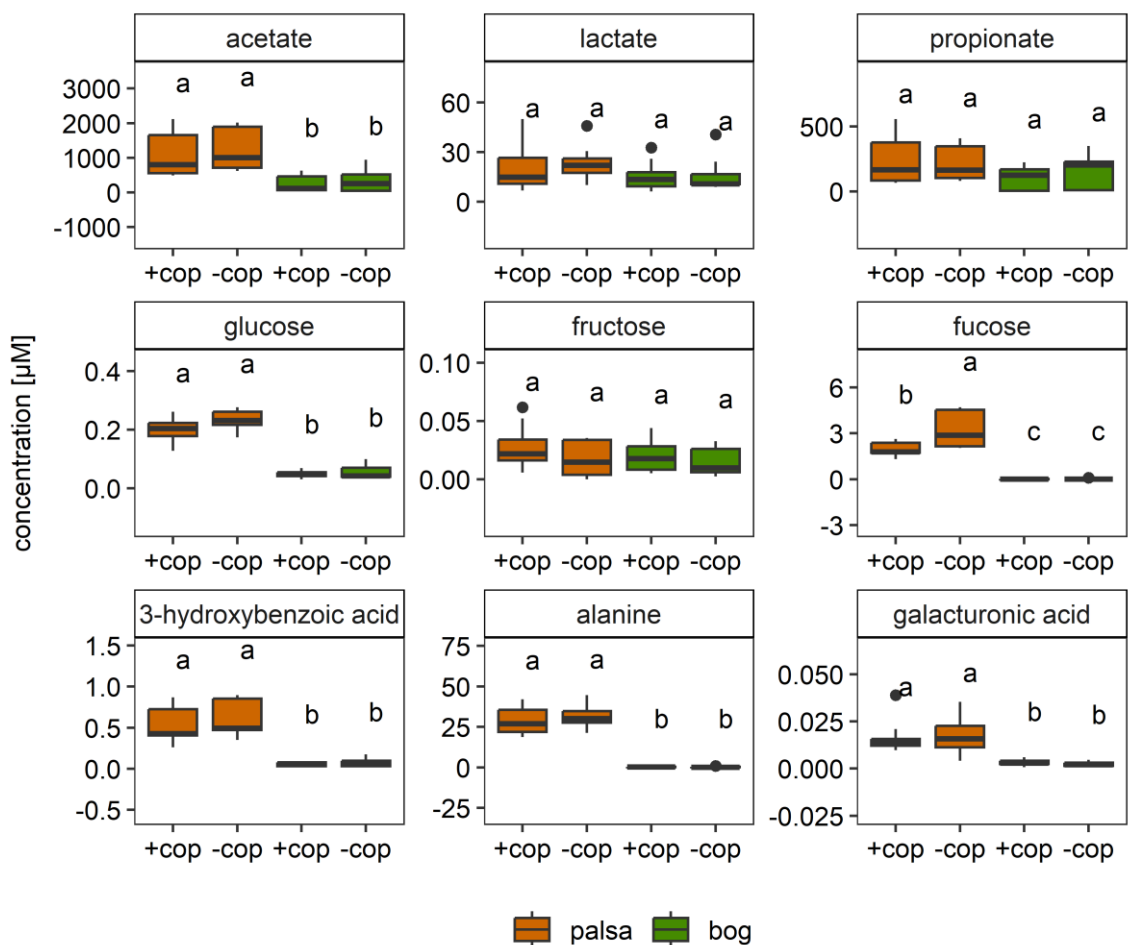
Figure S10. Concentrations of selected metabolites in the microcoms experiments using palsa and bog soil with added ^{57}Fe-enriched Fe(III)-OC coprecipitates (+ cop) and without (- cop). Note that the y-axis differs per subplot in order to display changes between the setups better. Concentrations per setup over time are summarized, such that each boxplot displays the distribution of concentrations of 9 replicates. Letters above the boxplots denote significant differences in concentration of each metabolite.
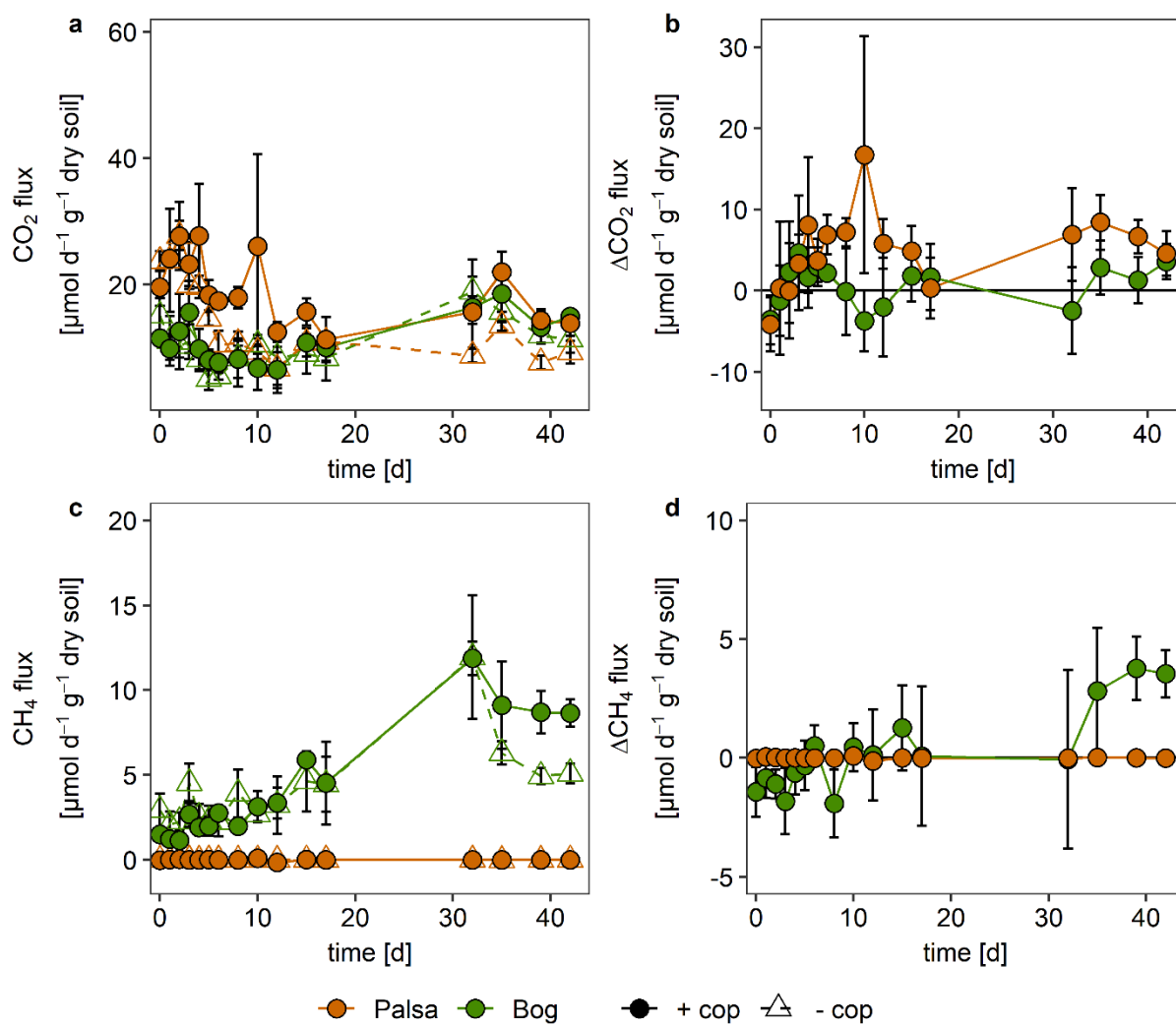
Figure S11. Measured gas fluxes of CO_2 and CH_4 per timepoint in the microcoms experiments using palsa and bog soil with added ^{57}Fe-enriched Fe(III)-OC coprecipitates (+ cop) and without (- cop). Left panels show the absolute data over time and right panels show the difference between the + cop setup and the – cop setup over time. Data points and error bars represent average and standard deviation of experimental triplicates.
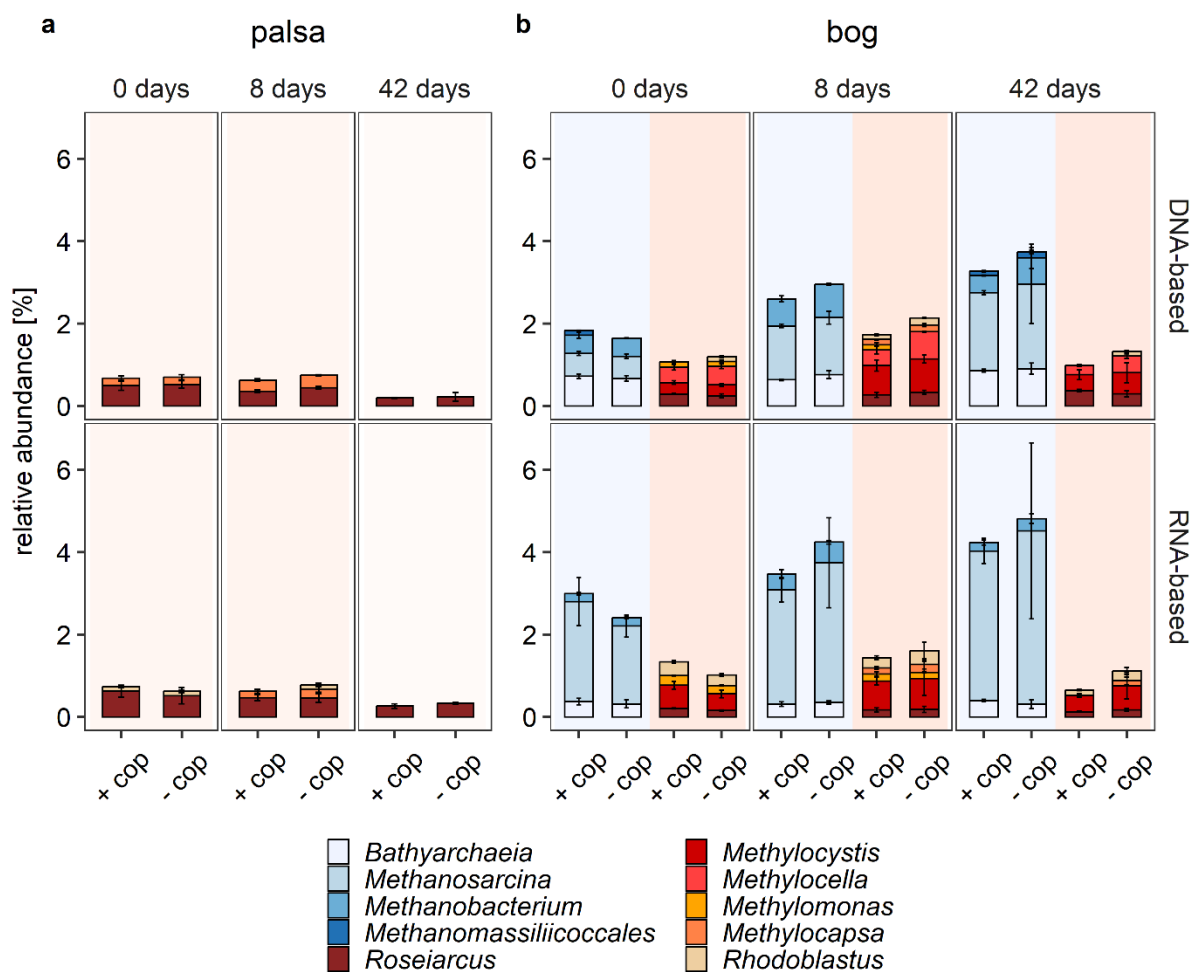
Figure S12. Relative abundances of present (DNA-based) and likely active (RNA-based) identified methanogens (blue colors) and methanotrophs (red colours) per timepoint (0, 8, 42 days) and setup (with added Fe(III)-OC coprecipitates: "+ cop", no-coprecipitate control: "-cop") in the microcosm experiment using (a) palsa and (b) bog soil. Results are based on 16S rRNA (gene) amplicon sequencing and taxa with a relative abundance >0.1% are displayed. Taxa are labelled at the genus-level, except for *Bathyarchaeia* and *Methanomassiliicoccales* for which no genus could be identified. No methanogens were detected in the palsa soil. Data bars and error bars display the mean and standard deviation of experimental triplicates.
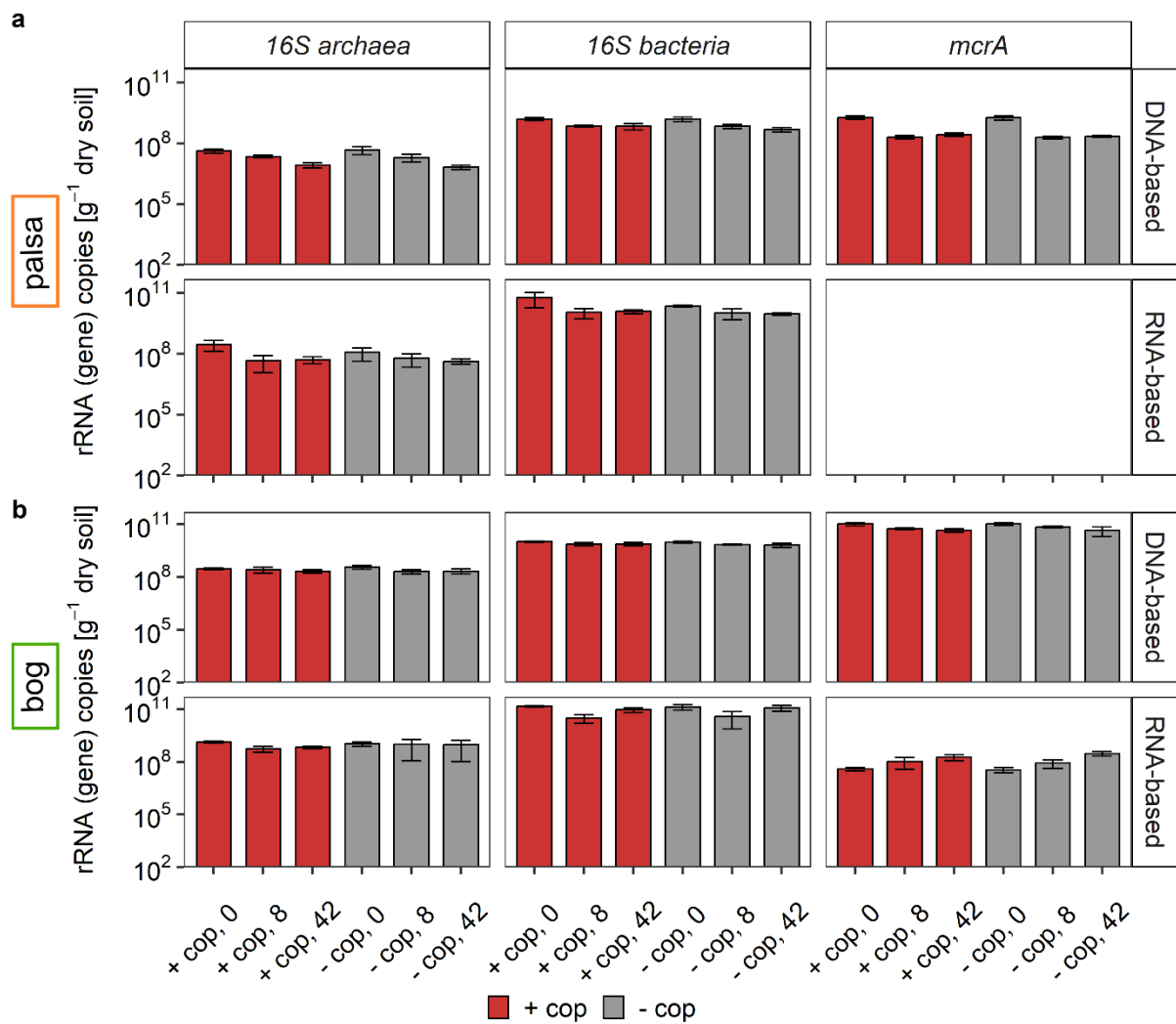
Figure S13. Absolute DNA- and RNA-based gene copy numbers [g^{-1} dry soil] determined by quantitative PCR assays with samples from the microcosm experiment using (a) palsa and (b) bog soil. The archaeal and bacterial *16S rRNA* as well as *mcrA* gene were quantified in samples with addition of ^{57}Fe-enriched Fe(III)-OC coprecipitates ("+ cop") and without ("-cop") after 0, 8 and 42 days. Data bars and error bars display the mean and standard deviation of experimental triplicates.
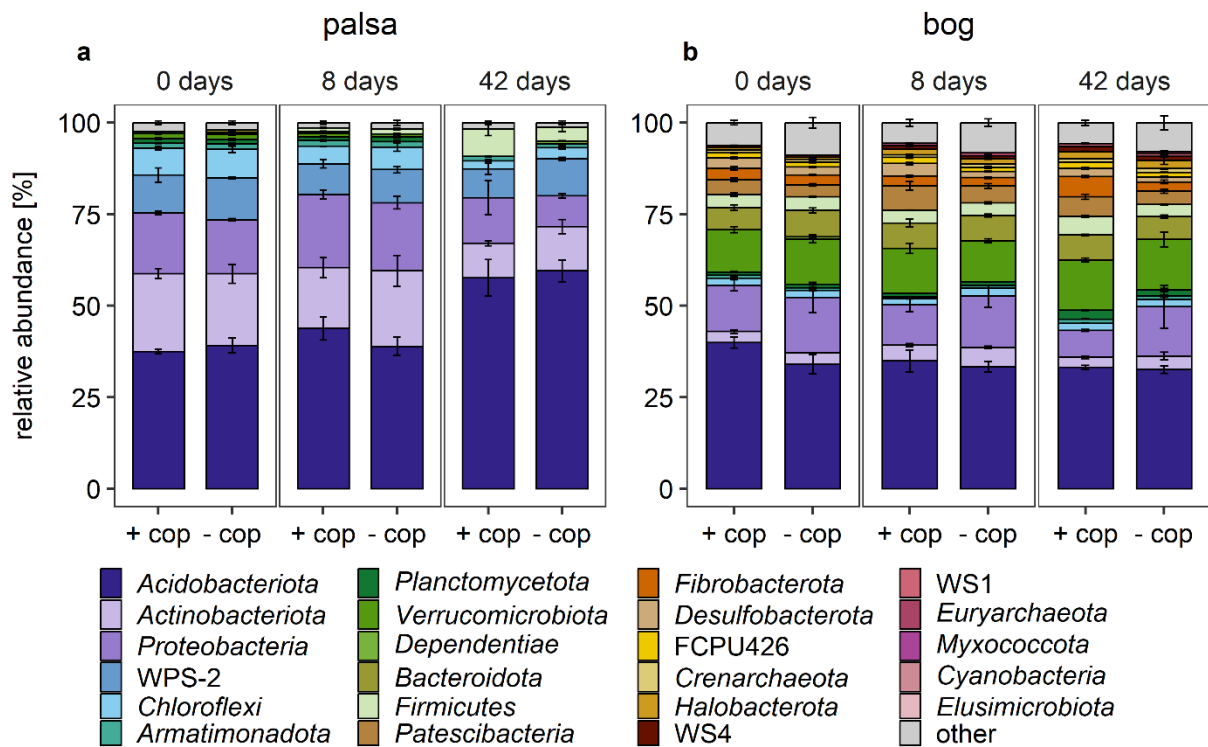
Figure S14. Relative abundance presend (DNA-based) microbial taxa of (a) palsa and (b) bog soil in microcosm experiment with addition of ^{57}Fe-enriched Fe(III)-OC coprecipitates ("+ cop") and in a no-coprecipitate control ("- cop") over time. Taxa are displayed at the phylum level and those with a relative abundance below 0.5% were categorized as "others". Data and error bars represent average and standard deviation of experimental triplicates.
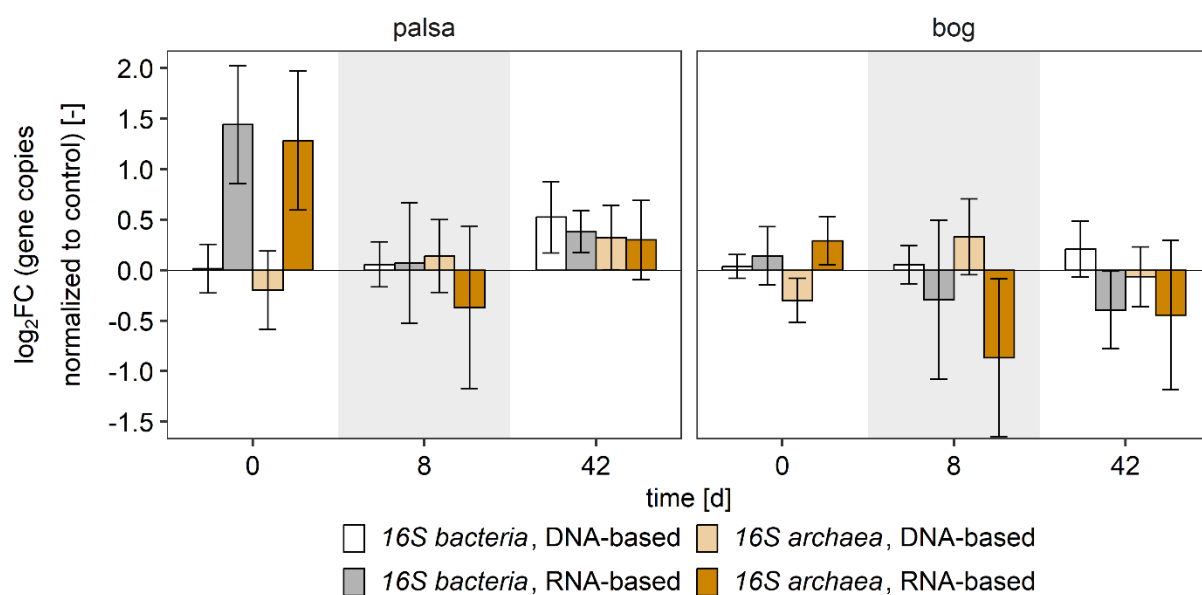
Figure S15. Change in gene copy numbers of the bacterial and archaeal 16S rRNA gene in microcosm experiment of palsa and bog soils with added ^{57}Fe-enriched Fe(III)-OC coprecipitates based on quantitative PCR results. Results are displayed as the $\log_2$ fold change (FC) of the mean copy numbers of "+ cop" treatment to the mean of the no-coprecipitate control [copies$_{+cop}$ g^{-1} dry soil/ copies$_{-cop}$ g^{-1} dry soil] for DNA- and RNA-based analysis per time point. Absolute gene copy numbers are displayed in Figure S13. Data bars and error bars represent the mean and 95% confidence interval of experimental triplicates, respectively.
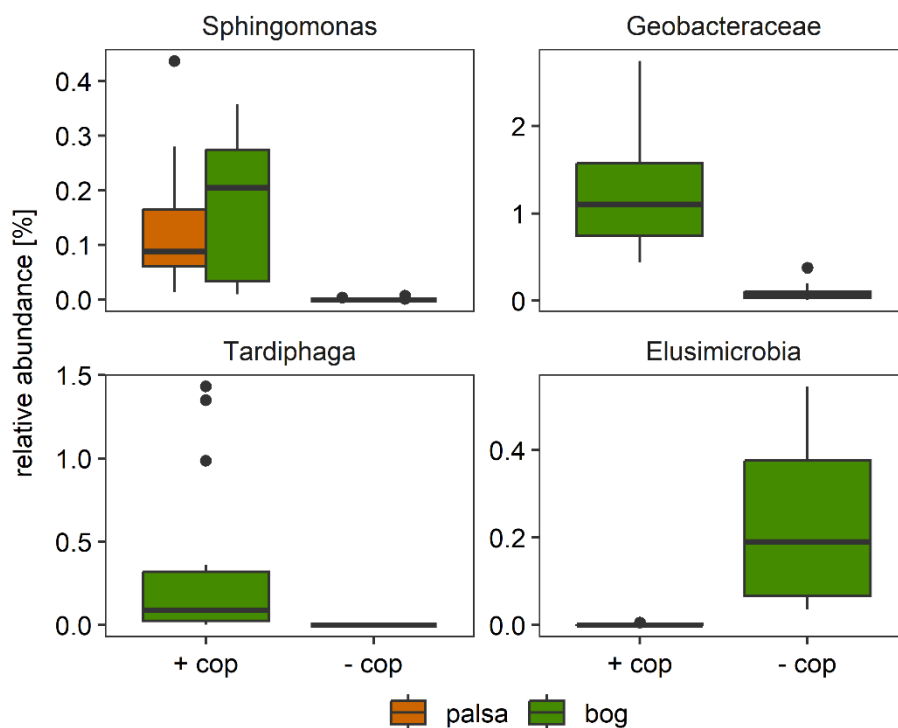
Figure S16. Relative abundance of identified Amplicon Sequence Variants (ASVs) which changed significantly microcosm experiment using palsa and bog soil with addition of ^{57}Fe-enriched Fe(III)-OC coprecipitates ("+ cop") and in no-coprecipitate controls ("- cop"). Data from DNA- and RNA-based 16S rRNA amplicon sequencing datasets after 8 and 42 days were used, such that each boxplot consists of 12 replicates.
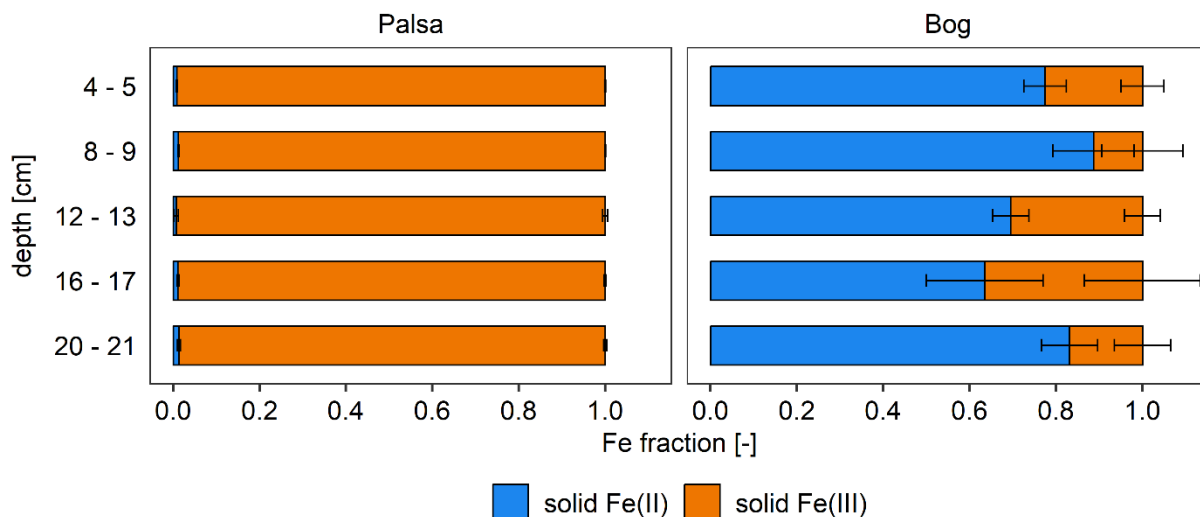
Figure S17. Fe speciation of recovered solids in peepers with added ^{NA}Fe(III)-OC coprecipitates over depth. Data and error bars show the mean and range of experimental duplicates.
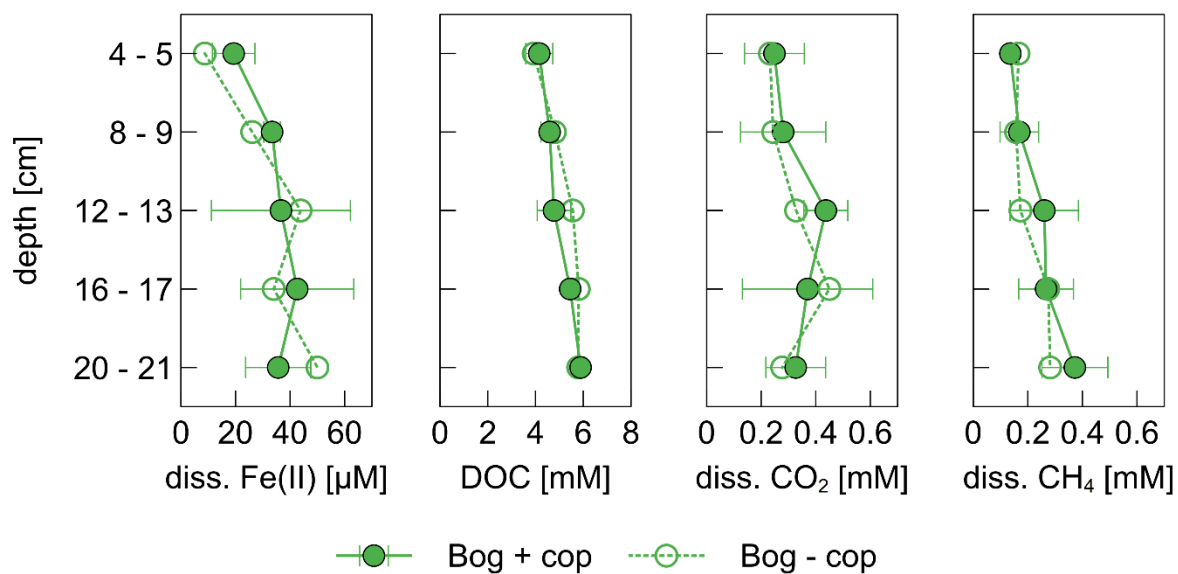
Figure S18. Dissolved species measured in the porewater of peepers of the field experiment. Peepers filled with synthesized ^{NA}Fe(III)-OC coprecipitates (Bog +cop) and the controls filled with deionized water (Bog -cop) were sampled after 53 days of incubation from July to September 2022. Data points and errorbars display the mean and range of experimental duplicates in case of the +cop data and results from the single replicate in case of the control. No data is available for peepers placed in palsa area due to the too low porewater volume in the soil.
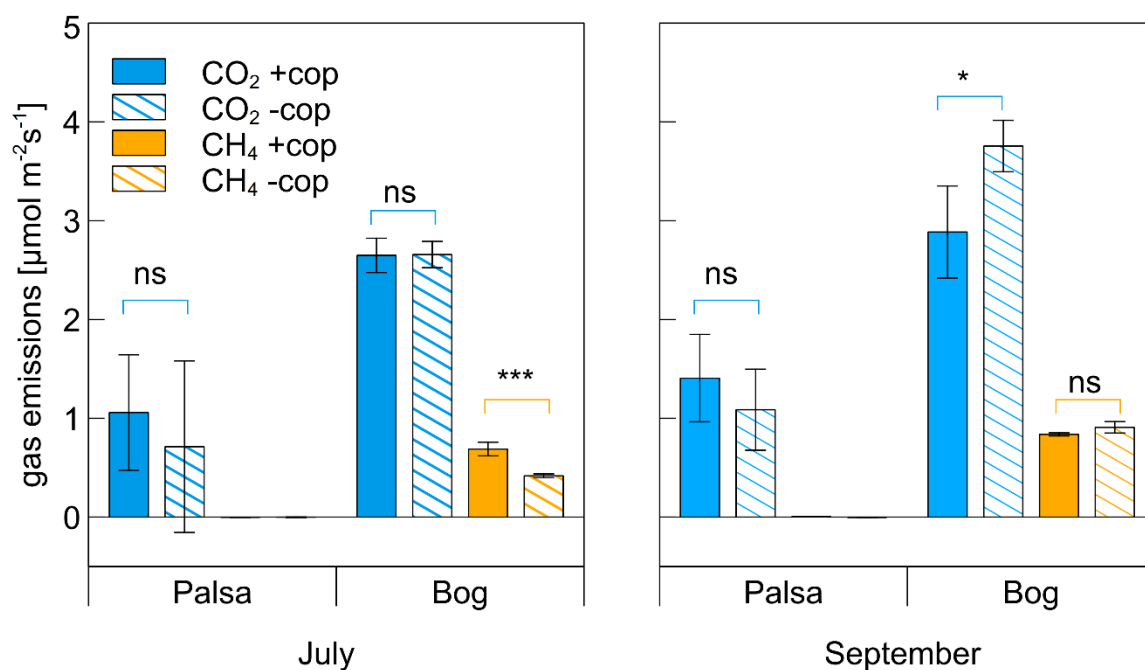
Figure S19. Absolute greenhouse gas emissions (CO_2 and CH_4) measured on top of the peepers filled with $^{NA}Fe(III)$-OC coprecipitates (+cop) and the controls filled with deionized water (-cop) in July (0-24h after addition of coprecipitates) and September (53 days after addition of coprecipitates). Data and error bars represent the mean and standard deviation of triplicate measurements of gas fluxes on top of one coprecipitate-added plot and one control plot. Symbols above the bars denote the level of significant difference between the two setups at a given time (one-way ANOVA, Tukey's HSD test): $p > 0.1$ – not significant (ns), $p \leq 0.1$ -*, $p \leq 0.05$ - **, $p \leq 0.001$ - ***.
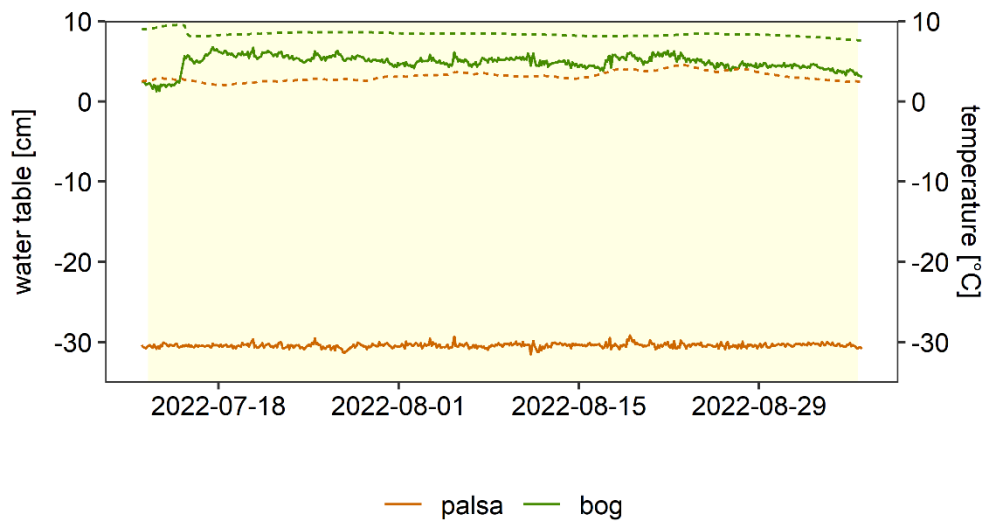
Figure S20. Measured water table depth relative to soil surface (solid lines) and soil temperature at 35 and 41 cm depth (dashed lines) in palsa and bog area, respectively, during the field experiment. The yellow shaded area shows the duration of the field experiment.

Table S1. Composition of artificial porewater used in the microcosm experiment, modified from a mineral medium[129]. The concentration of $CaCl_2$ was increased to keep the ionic strength constant.

Salt	Final concentration in bottles [mM]
KH_2PO_4	0.04
NH_4Cl	0.06
$MgSO_4 \times 7H_2O$	0.02
$CaCl_2 \times 2H_2O$	2.00

Table S2. Measured metabolites in microcoms experiments using palsa and bog soil with added ^{57}Fe-enriched Fe(III)-OC coprecipitates. Metabolites which were detected at least on one timepoint during the incubation in all experimental triplicates are marked with an "x".

metabolite	chemical class	detected in samples? palsa	bog	Injection method
alanine	amino acid	x	x	liquid
glutamic acid	amino acid	x	x	liquid
glycine	amino acid	x	x	liquid
histidine	amino acid	x		liquid
lysine	amino acid	x	x	liquid
methionine	amino acid	x		liquid
phenylalanine	amino acid	x	x	liquid
proline	amino acid	x	x	liquid
serine	amino acid	x	x	liquid
threonine	amino acid	x	x	liquid
tyrosine	amino acid	x	x	liquid
valine	amino acid	x	x	liquid
methanol	alcohol	x	x	headspace
acetic acid	organic acid	x	x	headspace
propionic acid	organic acid	x	x	headspace
butyric acid	organic acid	x	x	headspace
pentanoic acid	organic acid	x	x	headspace
citric acid	organic acid			liquid
fumaric acid	organic acid	x	x	liquid
lactic acid	organic acid	x	x	liquid
pyruvic acid	organic acid	x	x	liquid
succinic acid	organic acid	x	x	liquid
tartaric acid	organic acid	x	x	liquid
valeric acid	organic acid	x	x	headspace
3-hydroxybenzoic acid	phenol derivative	x	x	liquid
4-hydroxybenzoic acid	phenol derivative	x		liquid
hydroquinone	phenol derivative	x	x	liquid
galacitol	sugar alcohol	x		liquid
inositol	sugar alcohol	x	x	liquid
galacturonic acid	sugar acid	x	x	liquid
fructose	sugar	x	x	liquid
fucose	sugar	x	x	liquid
glucose	sugar	x	x	liquid
mannose	sugar	x	x	liquid
sucrose	sugar	x	x	liquid
xylose	sugar	x	x	liquid

Table S3. Overview of the used quantitative PCR assays, including primer pairs and their sequences, the thermal program, used dilution factors of samples and references.

Assay	Primer	Thermal program	Dilution factor	References
16S rRNA gene bacteria	341f	95°C - 3′; (95°C - 10′′; 55°C - 30′′) x 40; 60-95°C by 0.5°C - 5′′	DNA: 1000, RNA: 100 (palsa), 10 (bog)	Muyzer et al. (1995)[130]
	797r			Nadkarni et al. (2002)[131]
16S rRNA gene archaea	Ar109f	95°C - 3′; (95°C - 10′′; 52°C - 45′′; 72°C - 30′′) x 40; 60-95°C by 0.5°C - 5′′	DNA: 1000, RNA: 100 (palsa), 10 (bog)	Großkopf et al. (1998)[132]
	Ar915r			Stahl & Amann (1991)[133]
mcrA	ME1f	95°C - 5′; (95°C - 30′′; 48°C - 45′′) x 6; (95°C - 30′′; 55°C - 45′′; 72°C - 30′) x 40; 65-95°C by 0.5°C - 5′′	DNA: 100, RNA: 100 (palsa), 10 (bog)	Hales et al. (1996)[134]
	ME1r			

Table S4. Calculation of possible abiotic reduction of Fe(III)-OC coprecipitates by reduced particulate organic matter (POM) in the microcosm experiments.

	palsa		bog	
Added Fe [mM]		1.00		3.16
Volume bottles [L]		0.25		0.14
Soil [g dry weight]		5.5		8
Added Fe [mM/g soil]	1 mM / 5.5 g=	0.18	3.16 mM/ 8g=	0.39
EAC of POM [mmol e-/g POM]		0.08[a]		0.08[a]
soil OC content [g OC/g soil]		0.43		0.47
fraction of POM in soil [g POM/g OC]		0.72[b]		0.72[b]
mass POM in bottles [g POM]	5.5 g*0.72*0.43=	1.69	8 g*0.72*0.47=	2.68
EAC of POM in bottles [mmol e-]	0.08 mmol e$^-$/g POM *1.69 g=	0.13	0.08 mmol e$^-$/g POM *2.68 g=	0.20
possible reduced Fe(III) from POM [mmol Fe]		0.13		0.20
actual reduced Fe after 1 day [mM Fe]		0.31		0.32
actual reduced Fe after 1 day [mmol Fe]	0.31 mM * 0.25 L=	0.08	0.32 mM * 0.14 L=	0.04
Ratio of electrons provided by POM to actually reduced Fe after 1 day [-]	0.13 mmol/ 0.08 mmol=	1.65	0.20 mmol/0.04 mmol =	4.54

[a]electron accepting capacity (EAC) according to Joshi et al. (2021)[79] and Obradović (2024)[80]
[b]according to personal communication with Marie Mollenkopf, similar to values in Mueller et al. (2015)[135]

Table S5. Linear combination fitting results of Fe K-edge XANES spectra of the initial synthesized ^{57}Fe-enriched Fe(III)-OC coprecipitates and the initial soils, as well as the samples from the microcosm experiment with added coprecipitates ("cop+soil") and without ("soil") at t_0, after 1, 8 and 42 days of incubation. The references of Fe(II)-citrate and ferrihydrite were used as representatives for Fe(II) and Fe(III).

	sample	Fe(III) [%]	Fe(II) [%]	NSSR[a] [%]	red. $\chi^{2,b}$ [%]
Palsa	^{57}FeOC_initial	100	0	0.15	0.04
	cop+soil_0	28	72	0.05	0.01
	cop+soil_1	19	81	0.04	0.01
	cop+soil_8	15	85	0.06	0.02
	cop+soil_42	0	100	0.07	0.02
	soil initial	65	35	0.22	0.06
	soil_0	20	80	0.06	0.02
	soil_1	15	85	0.07	0.02
	soil_8	13	87	0.09	0.02
	soil_42	7	93	0.09	0.02
Bog	^{57}FeOC_initial	100	0	0.16	0.04
	cop+soil_0	32	68	0.05	0.01
	cop+soil_1	18	82	0.06	0.02
	cop+soil_8	27	73	0.07	0.02
	cop+soil_42	10	90	0.07	0.02
	soil initial	51	49	0.11	0.03
	soil_0	19	81	0.08	0.02
	soil_1	16	84	0.31	0.08
	soil_8	25	75	0.07	0.02
	soil_42	13	87	0.08	0.02

[a] normalized sum of of squared residuals (residuals ($100 \sum_i (data_i-fit_i)^2/\sum_i data^2$)
[b] measure of fit accuracy (($N_{idp}/N_{pts}) \sum_i ((data_i-fit_i)/\varepsilon_i)^2 (N_{idp}-N_{var})^{-1}$)). N_{idp}/N_{pts} and N_{var} are the number of independent points in the model fit (37.5), the total number of data points (250) and the number of fit variables (2), respectively.

Table S6. Fitting parameters of Mössbauer spectra of initial [57]Fe-enriched Fe(III)-OC coprecipitates.

sample	T [K]	site	CS[a] [mm s^{-1}]	QS or ε[b] [mm s^{-1}]	H[c] [T]	sd(H) [T]	Rel. area [%]	χ^2,d
[57]Fe-OC initial palsa	30	Fe(III) doublet	0.47	0.94			33	0.91
		Fe(III) collapsed	0.50	0.00	16.18	12.22	66	
	6	Fe(III) sextet 1	0.69	-0.05	46.8	3.8	42	
		Fe(III) sextet 2	0.29	0.01	46.8	3.7	45	2.43
		Fe(III) collapsed	0.45	0.07	32.7	14.4	13	
[57]Fe-OC initial bog	30	Fe(III) doublet	0.48	0.87			40	1.29
		Fe(III) collapsed	0.50	0.00	13.70	9.90	60	
	6	Fe(III) sextet 1	0.56	-0.09	47.4	2.6	36	
		Fe(III) sextet 2	0.42	0.07	46.2	4.0	51	2.57
		Fe(III) collapsed	0.59	0.07	33.3	11.3	13	

[a]center shift
[b]quadrupole split in paramagnetic state or quadrupole shift
[c]hyper fine field
[d]goodness of fit parameter

Chapter 4: Author contributions

Suppression of Methanogenesis by Microbial Reduction of Iron-Organic Carbon Associations in Fully Thawed Permafrost Soil

Eva Voggenreiter, Laurel ThomasArrigo, Martina Bottaro, Joachim Kilian, Daniel Straub, Fin Ring-Hrubesh, Casey Bryce, Mark Stahl, Andreas Kappler, Prachi Joshi

The study was conceptualized by A. Kappler, P. Joshi and myself. A. Kappler acquired the funding. The experiments were designed by A. Kappler, P. Joshi and myself. F. Ring-Hrubesh and C. Bryce contributed towards the experiment design regarding the field experiment. I performed the experiments. M. Bottaro measured the samples for ICP-MS and contributed to the data analysis. D. Straub and myself formally analyzed the 16S rRNA amplicon sequencing data. The GC-MS data was acquired by J. Kilian and formally analyzed by J. Kilian and M. Stahl and myself. L. ThomasArrigo, P. Joshi and myself analyzed the synchrotron spectra. Visualization of the data and writing of the original draft of the manuscript was performed by myself. Supervision was provided by P. Joshi and A. Kappler. All authors contributed to the review and editing of the final manuscript.

Chapter 4:

Suppression of Methanogenesis by Microbial Reduction of Iron-Organic Carbon Associations in Fully Thawed Permafrost Soil

Eva Voggenreiter[1], Laurel ThomasArrigo[2], Martina Bottaro[1], Joachim Kilian[3], Daniel Straub[4], Fin Ring-Hrubesh[5], Casey Bryce[5], Mark Stahl[3], Andreas Kappler[1,6], Prachi Joshi[1]

[1]Geomicrobiology, Department of Geosciences, University Tuebingen, Schnarrenbergstrasse 94-96, 72076 Tuebingen, Germany

[2]Environmental Chemistry, University of Neuchâtel, Avenue de Bellevaux 51, CH-2000, Neuchâtel, Switzerland

[3]Center for Plant Molecular Biology, University of Tuebingen, Auf d. Morgenstelle 32, 72076 Tuebingen, Germany

[4]Quantitative Biology Center (QBiC), University of Tuebingen, Auf d. Morgenstelle 10, 72076 Tuebingen, Germany

[5]School of Earth Sciences, University of Bristol, Wills Memorial Building, Queens Road Bristol BS8 1RJ, United Kingdom

[6]Cluster of Excellence: EXC 2124: Controlling Microbes to Fight Infection, Tuebingen, Germany

Abstract

Global methane (CH_4) emissions from thawing permafrost peatlands are expected to increase substantially in the future. Net emission of CH_4 depends on the presence of more favourable terminal electron acceptors for microbial respiration, such as ferric iron (Fe(III)). In soils with high OC content, Fe(III) is often coprecipitated with organic carbon (OC). The presence of Fe(III)-OC coprecipitates could either suppress CH_4 emissions due to inhibition of methanogenesis and stimulation of anaerobic methane oxidation coupled to Fe(III) reduction, or enhance emissions by providing additional OC. Here, we investigated the role of Fe(III)-OC coprecipitates in net CH_4 release in a fully thawed, waterlogged permafrost peatland (Stordalen Mire, Abisko, Sweden). We synthesized Fe(III)-OC coprecipitates using natural organic matter from the field site and added them to waterlogged soil in a microcosm experiment and *in situ*, and followed Fe speciation and changes in greenhouse gas emissions over time. Fe(III)-OC coprecipitates were partially reduced (22%) within 42 days in the microcosm experiment, while almost full reduction (92±4%) occurred *in situ* within 53 days. This led to a decrease in CH_4 emissions by 94% and 40% in microcosm and field experiment, respectively, compared to no-coprecipitate controls. A decrease in both RNA-based *mcrA* copy numbers and relative abundance of detected methanogens indicated that methanogenesis was mainly inhibited by the addition of the coprecipitates due to microbial Fe(III) reduction. In conclusion, Fe(III)-OC coprecipitates temporarily suppress net CH_4 emissions in fully thawed permafrost soils, and might play a similar role in mitigating CH_4 release in other (periodically) flooded soils.

Introduction

Methane (CH_4) is a potent greenhouse gas that is emitted globally at a rate of 576 Tg CH_4 y^{-1}, with a large portion (148 Tg y^{-1}) originating from periodically or permanently anoxic soils[1]. It is predicted that soil methane emissions will increase by 89% (SSP 2) until the year 2200 compared to 2010[2]. Permafrost peatlands play an especially large role in CH_4 release, since these soils contain a large organic carbon (OC) stock of which a substantial fraction represents labile, previously unavailable (frozen) OC[3,4]. In low-lying permafrost peatlands in which drainage of thawed permafrost is impeded or which are hydrologically connected to other water bodies, soil inundation and thermokarst formation is predicted[5–8]. As these soils are saturated with water, anoxic conditions are expected to develop and may lead to increasing CH_4 emissions, promoted further by increasing temperatures[9–11]. The net release of CH_4 depends on the balance of CH_4 production by methanogens and CH_4 oxidation by methanotrophs[12], which are affected by varying biogeochemical parameters. The key parameter in this release is the availability of terminal electron acceptors that are more thermodynamically favorable than CO_2, such as nitrate, sulfate, or ferric iron (Fe(III)) minerals[13,14].

The net effect of the presence of Fe(III) minerals on CH_4 release can vary. First, many studies reported inhibition of methanogenesis when Fe(III) reduction occurred[15–18]. The main reason for inhibition is that Fe(III) reduction outcompetes methanogenesis thermodynamically, implying that methanogenesis will proceed only once Fe(III) is depleted[12,19]. Second, Fe(III)-reducing microorganisms and methanogens compete for the same substrates, such as acetate and hydrogen (H_2), which Fe(III)-reducers can use at far lower concentrations than methanogens[20]. Fe(III) might also play a role within anaerobic oxidation of CH_4 by functioning as an electron acceptor[21,22], thus decreasing net CH_4 release. In contrast, there is also evidence that Fe(III) reduction can promote methanogenesis. One theoretical argument is that the pH increase induced by Fe(III) reduction could make conditions more favourable for (acetoclastic) methanogenesis[23,24]. Additionally, there is evidence from culture-based[25,26] and soil-based[27] studies that more crystalline Fe(III) minerals can serve as electron shuttles for methanogens.

In contrast to pure Fe(III) minerals and dissolved Fe(III), much less is known about the influence of organic matter-bound Fe(III) on net CH_4 release. Poorly crystalline, high surface area Fe(III) minerals, such as ferrihydrite, are often associated with organic matter through adsorption or coprecipitation[28], forming Fe(III)-OC associations. In permafrost peatland soils with high OC content, binding through coprecipitation is thought to be the dominant process based on OC:Fe ratios of selective extractions[29–31]. Fe(III)-OC coprecipitates may play a inhibitory or promotive role regarding CH_4 release. Once conditions turn anoxic, Fe(III)

reduction may occur, releasing Fe^{2+} and the previously bound OC to the aqueous phase. Since Fe(III)-OC coprecipitates are less crystalline than OC-free Fe(III) minerals, they might be more available for microbial reduction[32,33] and lead to stronger suppression of methanogenesis. On the other hand, the released OC could function as a substrate for fermenting microorganisms, providing more substrates for methanogenesis (fatty acids, H_2)[34]. High OC loadings in Fe(III)-OC coprecipitates could also inhibit microbial access to Fe[35], decreasing the extent of Fe(III) reduction and thus the competition with methanogenesis. The C and Fe cycles in anoxic soils are thus closely interlinked through the processes of Fe(III) reduction, fermentation, and methanogenesis.

Thawing permafrost soils provide a suitable ecosystem to study this linkage. An increasing number of studies reported that Fe-bound OC accounts for a significant fraction of total soil OC (up to 20%) in intact permafrost[29,36,37]. At the onset of thaw, these Fe(III)-OC associations are (partially) reductively dissolved. Often, CH_4 emissions are detected simultaneously[15,38,39]. However, the role of Fe(III)-OC associations in net CH_4 release is still unclear. Current knowledge based on field observations only provides correlations between Fe cycling and CH_4 release, but direct experimental evidence is lacking. Therefore, the objectives of this study were (i) to determine the reduction extent of Fe(III)-OC associations over several weeks in a fully thawed permafrost soil, (ii) to quantify the net effect of Fe(III) reduction of Fe(III)-OC associations on CH_4 release, and (iii) to identify main microbial groups relevant to CH_4 cycling due to addition of Fe(III)-OC associations. To achieve this, we incubated synthesized Fe(III)-OC coprecipitates together with soil from a fully thawed permafrost peatland (Stordalen Mire, Abisko, Sweden) within a microcosm experiment and an *in situ* field experiment. In the microcosm experiment, we aimed to gain a mechanistic understanding of the processes underlying CH_4 release with Fe(III)-OC coprecipitate addition. Within the field experiment, our aim was to estimate the overall net effect of Fe(III)-OC coprecipitate addition on CH_4 release under relevant environmental conditions. We used a combination of isotope specific techniques as well as spectroscopic and molecular biology methods to track the reduction of Fe(III)-OC coprecipitates, emission of CH_4 and carbon dioxide (CO_2), and changes in the abundance and activity of relevant methane-cycling microorganisms.

Materials and Methods

Field site description and sampling

Stordalen Mire is a thawing permafrost peatland, located near Abisko, Sweden (68 22' N, 19 03' E). It is situated in the discontinuous permafrost zone and consists of intact

permafrost areas (palsa hills) covered by dwarf shrubs, bryophytes and lichens, semi-wet bogs dominated by *Sphagnum ssp.* mosses, fully inundated fens covered by sedges (*Eriophorum vaginatum, Carex rostrata*), as well as numerous thaw ponds[40,41].

The fen soil was sampled in July 2022 at two depths that differed in organic matter content. The upper organic-rich soil (38% soil OC) was sampled from 2-10 cm depth below the soil surface and used to extract soil organic matter for synthesis of (^{57}Fe-enriched) Fe-OC coprecipitate (see 0). The organic-poor (2.51% soil OC), mineral-rich soil was sampled at 30 cm depth and used for the lab-based microcosm experiment. The soils were collected by grab sampling and stored in sterilized plastic bags (LDPE). Both layers were watersaturated and the soil was filled into the bags so that no headspace was remaining. Soils were stored at 4°C after collection and kept under cool conditions during transport. Back in Tübingen, the soils were stored in gas-tight, N_2-flushed mason jars at 4°C until use. A subsample of the mineral soil was dried inside an anoxic glovebox (MBraun Unilab Workstation, 100% N_2 atmosphere) at 60°C for general soil characterization. We determined the mineralogy by X-ray diffractometry (XRD), soil OC content by elemental analysis, and total Fe content by X-ray fluorescence (XRF) as well as Fe speciation by Fe *K*-edge X-ray absorption spectroscopy (XAS). More details are given in Text S1. Fe content and speciation in poorly crystalline and highly crystalline Fe pools were analysed after anoxic 0.5 M and 6 M HCl extractions (Figure S1).

Synthesis of (^{57}Fe-enriched) Fe(III)-OC coprecipitates

To synthesize Fe(III)-OC coprecipitates, soil organic matter from the fen organic horizon was extracted. Field-moist soil was added to double-deionized water (DDI, Millipore, >18 MΩ cm^{-1}) at a 1:10 weight/volume (w/v) ratio for 24 h on an overhead shaker in the dark. Afterwards, the suspensions were centrifuged in pre-baked glass serum bottles (5250 rcf, 15 min) and the supernatant was sequentially filtered through pre-rinsed 8 μm (Merck Millipore, MCE) and 0.22 μm (Merck Millipore, Steritop PES) filters. The resulting water-extractable organic matter (WEOM) was stored at 4°C for less than 24 h until use. The dissolved organic carbon (DOC) concentration was 24 mg C L^{-1}.

The coprecipitates used in the microcosm experiment were prepared from a ^{57}Fe-enriched (10%) $FeCl_3$ solution (details in Text S2), which enabled a differentiation of the added Fe minerals from the native Fe pool and improved the analysis by ^{57}Fe-specific Mössbauer spectroscopy. Both ^{NA}Fe- and ^{57}Fe-enriched Fe-OC coprecipitates were synthesized by mixing 1.5 L of WEOM with 20 mL of the respective $FeCl_3$ solution (initial C:Fe ratio=1), after which NaOH solution was added until pH 6. The final suspension was bubbled with N_2 (99.999%) for 15 min to make it anoxic. Fe speciation was analysed by the ferrozine assay [42] after dissolution

in 1 M HCl, and mineral identity was determined by ^{57}Fe Mössbauer spectroscopy (Figure S2) and Fe *K*-edge XAS (Figure S3).

Microcosm experiment to elucidate the net effect of Fe(III)-OC coprecipitate addition on greenhouse gas fluxes

Setup of microcosm experiment

Prior to using the mineral soil in the microcosm experiment, it was homogenized by wet sieving with a sterilized 2 mm sieve. Subsequently, field moist soil (12 g dry weight) was added to six 250 mL serum bottles under sterile conditions. The bottles were then closed with sterilized butyl rubber stoppers and crimped with aluminum caps. The headspace in the bottles was exchanged by applying vacuum for 5 min and flushing with N_2 gas for 5 min (3 cycles). The bottles were then transferred to an anoxic glovebox and sterile, anoxic, artificial porewater solution (composition in Table S1) was added: 135 mL for control setups and 100 mL for setups in which Fe(III)-OC coprecipitates were later added, to reach a final ratio of 85 mg dry soil mL^{-1} for both setups. All bottles were incubated under anoxic conditions at room temperature in the dark for 35 days prior to the addition of ^{57}Fe-enriched Fe(III)-OC coprecipitates. This initial incubation served to establish anoxic conditions in the soil, to avoid the first pulse of greenhouse gases due to rewetting[43], and to reduce all easily reduceable native Fe(III) minerals. Geochemical sampling was done once each week to monitor Fe(III) reduction (see below). The amount of added synthesized ^{57}Fe-enriched coprecipitates constituted an increase in total 6 M HCl-extractable Fe by 50% (Figure S4).

To test the occurance of abiotic isotopic exchange to between aqueous ^{56}Fe^{2+} and ^{57}Fe(III) in coprecipitates, we performed an additional control experiment. We added the same concentration of Fe(III)-OC coprecipitates to filtered (0.22 µm, PES, Carl Roth) solution from the control microcosms. The Fe(III)-OC coprecipitates were prepared as a new batch in order to have the same storage time as for the main experiment. The filtered porewater was diluted to have the same DOC concentration as on t_0 of the main experiment. The aqueous Fe concentration and speciation as well as fraction of ^{57}Fe was then quantified over 48 h.

Sampling of microcosm experiment

Analysis of the microcosms included measuring greenhouse gas (GHG) fluxes and sampling for geochemical changes. To measure GHG fluxes, the rubber stopper of the bottles was pierced with 2 needles with three-way valves attached. After 10 min of flushing the bottles with moistened N_2 gas, the flow was stopped, and the gases were left to accumulate for 60

154

min. A 2 mL sample was taken from the headspace and transferred to a He-flushed 12 mL Exetainer® vial (Labco, UK) after 0, 30, and 60 min (more details in Text S3). The individual and cumulative gas fluxes were calculated based on the increase in gas concentration, given in Text S4.

The bottles were then transferred to the glovebox for geochemical sampling. An aliquot of the suspension (1 mL before coprecipitate addition, 1.5 mL afterwards) was taken. The sample was centrifuged (10055 rcf, 5 min) and the supernatant was collected. The supernatant was used to quantify DOC concentration and aqueous Fe speciation after acidification with anoxic 1 M HCl. The soil pellet was dried at 60°C anoxically overnight and weighed to estimate the dry mass in each sample. To target the poorly crystalline Fe mineral fraction, 1.5 mL anoxic 0.5 M HCl was added and left to equilibrate with the soil for 24 h[44,45]. The extraction solution and remaining solid were separated by centrifugation (10055 rcf, 5 min) and the supernatant was diluted in 1 M HCl for analysis of Fe speciation and ^{57}Fe concentration. At certain time points (right after addition of coprecipitates, after 8, 15, and 42 d) an additional 15 mL of suspension was taken from the bottles. An aliquot (4 mL) was centrifuged in the glovebox, the supernatant was transferred to a new tube and immediately frozen (-20°C) for measurement of microbial metabolites by gas chromatography mass spectrometry (GC-MS). The soil pellet was frozen (-20°C) and subsequently freeze-dried under anoxic conditions for analysis by ^{57}Fe Mössbauer spectroscopy. An aliquot of 1 mL was used to measure pH (InLab Easy BNC, Mettler Toledo, Germany) outside the glovebox. The remaining 10 mL were transferred to 15 mL centrifuge tubes (polypropylene, RNase- and DNase-free, Biologix) and centrifuged outside the glovebox (17200 rcf, 5 min). The supernatant was taken off under sterile conditions and the remaining soil pellet was immediately frozen (-80°C) for later extraction of DNA and RNA and subsequent molecular biological analysis (see section Molecular biology analysis).

Geochemical analyses

Aqueous and solid (0.5 M HCl-extractable) Fe speciation and total Fe concentration were quantified using the ferrozine assay[42]. DOC concentration was measured (as non-purgeable OC) after acidification with 2 M HCl by a TOC analyzer (multi N/C 2100S, Analytik Jena AG, Germany). Gas samples were measured by a gas chromatograph (TraceGC1300, ThermoFisher Scientific, USA; modified by S+HA analytics), equipped with 2 column configurations (first configuration: 30 m long, 0.53 mm ID TGBondQ column and 30 m long, 0.53 mm ID Molsieve column; second configuration: 30 m long, 0.53 mm ID TGBondQ column and a 30 m long 0.25 mm ID TGBondQ+ column; all ThermoFisher Scientific) which are each connected to a Pulse Discharged Detector. Gas concentrations were quantified with

calibrations of standards of pure CH_4, N_2O, and CO_2 (99.5% CH_4, 99.9% CO_2, 99.999% N_2O, Westfalen, Germany) in He-flushed Exetainer® vials in a range of 0.05-500 ppm. N_2O was always below detection limit in the microcosm experiment and did not significantly increase during measurements in the field experiment. Concentrations of ^{57}Fe in aqueous and 0.5 M HCl-extracted solid samples were quantified by inductively coupled plasma mass spectrometry (ICP-MS, Agilent 7900, Agilent Technologies, USA) with Ar as carrier gas and in He mode after dilution in 1% HNO_3 (analytical grade, Carl Roth). Contribution of ^{57}Fe-enriched Fe(III)-OC coprecipitates to the aqueous and solid (0.5 M HCl-extractable) Fe pool were calculated (Text S5) and raw data ($f(^{57}Fe)$) is given in Figure S4 and S5. All results and statistical analyses were evaluated and performed, respectively, in R vs. 4.3.3[46].

Solid phase Fe characterization

^{57}Fe Mössbauer spectroscopy was used to analyse Fe speciation of the initial synthesized ^{57}Fe-enriched coprecipitates and in the solids from the microcosm experiment. Initial coprecipitates were collected by filtration (0.45 μm, nitrocellulose, Millipore). The filter paper with solids was fixed between Kapton® tape and frozen (-20°C). Anoxically freeze-dried samples from the microcosms (after centrifugation, as specified in section "Sampling of microcosm experiment" above) were ground with mortar and pestle in a glovebox and 60-80 mg were placed in 1 cm^2 Plexiglas holders. Samples at the beginning and end of the incubation were selected for analysis. Samples were inserted into a closed-cycle exchange gas cryostat (Janis cryogenics) under a gasflow of He to minimize air exposure (see Text S6). Spectra were collected at 30 and 6 K for initial ^{57}Fe-enriched Fe(III)-OC coprecipitates and at 77 and 6 K for microcosm samples.

Iron speciation of the initial soil and synthesized ^{57}Fe-enriched coprecipitates was also investigated by Fe *K*-edge XAS at Synchrotron SOLEIL (SAMBA beamline, Paris, France). Oxidation state of Fe was determined by fitting of the Fe *K*-edge X-ray absorption near edge structure (XANES) while fitting of the extended X-ray absorption fine structure (EXAFS) was used to determine the Fe speciation. For this purpose, the initial ^{57}Fe-enriched coprecipitates were air-dried prior to homogenization with a mortar and pestle. The dried solids were each pressed into pellets (7 mm diameter) with PVP (Polyvinylpyrrolidone K12, Carl Roth), before being sealed with Kapton® tape. More details on synchrotron spectra acquisition and data analysis can be found in Text S6.

Molecular biology analysis

Total DNA and RNA of soil samples from the microcosm experiment were extracted in experimental triplicate using the RNeasy PowerSoil® Total RNA Kit with DNA Elution (Qiagen, Germany). Details on protocol adjustments and quality controls are listed in Text S7. Remaining DNA in the RNA samples was digested and the RNA was reverse transcribed using commercial kits (Invitrogen, Life Technologies, USA) as described in Otte et al. (2018)[47]. Bacterial and archaeal 16S rRNA (gene) amplicon sequencing on both DNA and cDNA samples was done using the universal primers 515f[48] and 806r[49] fused to Illumina adapters. Library preparation steps (Nextera, Illumina) and sequencing were performed using Illumina MiSeq sequencing system (Illumina, USA) at the Institute for Medical Microbiology and Hygiene of the University of Tübingen. Data processing, including quality control, reconstruction of sequences, and taxonomic annotation (Text S7) was done using nf-core/ampliseq version 2.8.0[50,51] of the nf-core collection of workflows[52]. Methanogenic, methanotrophic, and Fe(III)-reducing taxa were identified, as listed in Patzner et al. (2022)[39] and references therein.

Quantitative PCR (qPCR) was performed on DNA and cDNA samples to quantify changes in total bacterial and archaeal 16S rRNA (gene) copies and in functional genes relevant for CH_4 cycling. Specifically, we targeted the methyl-coenzyme M reductase subunit alpha (*mcrA*) gene, used as a marker gene for methanogens[53,54], and particulate methane monooxygenase (*pmoA*) gene, used to assess the abundance of methanotrophs[55,56]. The used primer sequences, plasmid standards, dilution factors of samples, and details of the temperature programs are given in Table S2. The assays were performed using SybrGreen® Supermix (Bio-Rad Laboratories, USA) on the C1000 Touch thermal cycler (CFX96TM real time system, Bio-Rad Laboratories). Sample dilutions (10-1000x) were necessary since the presence of complex OC compounds led to inhibition of the fluorescence signal in samples without dilution[63]. Appropiate sample dilutions were tested (see Figure S6). Copy numbers were determined in analytical triplicates of each experimental replicate. Data analysis was performed in Bio-Rad CFX Maestro 1.1 software, vs. 4.1 (Bio-Rad, 2017).

Analysis of microbial metabolites

The concentration of microbial metabolites, including small sugars, organic acids, and amino acids were quantified using targeted GC-MS (Shimadzu GC/MS TQ 8040, Japan). Some of the selected metabolites are important substrates or products of methanogenesis, Fe(III) reduction or fermentation pathways. A full list of measured metabolites is given in Table S3. Metabolites were measured either by headspace injection or as liquid samples after

derivatization and addition of octanole or ^{13}C-glucose as internal standard, respectively. More details are given in Text S8. Concentrations were quantified with a 8-point external calibration containing standards of all targeted analytes, ranging from 20 to max. 10^7 pmol.

Field experiment to determine in situ effect of Fe(III)-OC coprecipitates on greenhouse gas fluxes in fully thawed fens

Construction of peepers and experiment setup

We performed a field experiment to determine the *in situ* reduction extent of ^{NA}Fe(III)-OC coprecipitates and the effect on net soil greenhouse gas emissions over a summer season. For this purpose, passive porewater samplers ("peepers", 20 cm length, 10 x 1 cm high cells, each of 12 mL volume) were constructed in house according to Bowes & Hornibrook (2006)[64] after Hesslein (1976)[65]. Peepers are traditionally used to passively sample the porewater in waterlogged soils or sediments, often at the sediment-water interface[65,66]. Here, we employed them to incubate synthesized ^{NA}Fe(III)-OC coprecipitates in the peeper cells under ambient conditions over the subarctic summer period in the fen area in Stordalen Mire. A set of 3 peepers were inserted into the soil in July 2022, on plots with similar vegetation and ca. 1 m apart from each other. Cells of the peepers were filled with anoxic, deionized water through attached butyl rubber tubing prior to installation in the soil. The peepers were equilibrated for 4 d in the soil, after which an anoxic suspension of 280 mg L^{-1} Fe as ^{NA}Fe(III)-OC coprecipitates was added via the tubing to two of the peepers. The suspension was added into every second cell in the following depths from the soil surface: 4-5, 8-9, 12-13, 16-17, and 20-21 cm. Details on dimensions of the peepers and individual components are shown in Text S9 and Figure S7. We chose a membrane with 8 μm pore size in the peeper in order to facilitate microbial access to the ^{NA}Fe(III)-OC coprecipitates. It was also tested whether the ^{NA}Fe(III)-OC coprecipitates would pass the membrane in case of lower aggregate size. To test this, we placed the membrane inside filter cups (25 mm, Millipore) and filtered through 1 mL of initial coprecipitate suspension. The filtrate was acidified with 1 M HCl and total Fe concentration was measured as described in section Geochemical analyses.

Sampling and analysis of field experiment

Greenhouse gas emissions were determined above the peepers by placing static, non-flow gas chambers over them. Emissions were measured as described previously[67], with the following adjustments: (i) the chambers were wrapped in aluminum foil to exclude photosynthic processes, (ii) incubation time was 20 min and samples were taken every 5 min by a gas-tight

50 mL syringe. Each gas sample (18 mL) was injected into pre-evacuated 12 mL Exetainer® vials. Gas fluxes were measured in triplicate in July (2, 20 and 21 h after addition of coprecipitates) and then at the end of the summer season (September, after 53 d). One peeper containing the $^{NA}Fe(III)$-OC coprecipitates ("+ cop") and one containing only deionized water ("- cop") were selected for the gas measurements. Gas concentrations of CO_2 and CH_4 were measured as described in section Geochemical analyses.

The equilibrated porewater and/or remaining $^{NA}Fe(III)$-OC coprecipitate suspensions in the peepers were sampled after 53 days of incubation in September 2022. A N_2-filled 20 mL syringe was attached to one side of the butyl tubing of each cell, while another N_2-flushed, empty syringe was attached to the outlet side. The outlet-syringe was pulled to capture the anoxic solution in the peepers and the inlet syringe was simultaneously pushed to avoid underpressure and flow of new porewater into the peeper cell. The contents of the syringe were distributed in the following way: 7 mL were transferred to an N_2-flushed, gas tight 50 mL serum vial and stored at 4°C until measurement of dissolved and solid Fe speciation. An aliquot of 3 mL was added to a He-filled 11 mL headspace vial to measure dissolved porewater gases (CO_2, CH_4). For that purpose, the vials were vigorously shaken for 2 min after which 3 mL of the headspace gas was transferred to a He-flushed, 12 mL Exetainer® vial. The remaining volume (1-2 mL) was filtered (0.22 μm, PES, Carl Roth; pre-rinsed with 50 mL DDI) and frozen (-20°C) until measurement of DOC.

Samples for measurement of aqueous and solid Fe speciation were prepared in an anoxic glovebox. An aliquot of 1 mL was filtered (0.22 μm, PES, Carl Roth) and stabilized with 1 mL of 2 M HCl to quantify aqueous Fe speciation. Total Fe in initial suspensions was determined by dissolving 0.8 mL unfiltered sample in 0.8 mL 2 M HCl. The solid Fe content and speciation was calculated by subtraction of aqueous from total concentrations. Analytical methods for determination of Fe speciation and concentration, dissolved porewater gases, and DOC concentration are described in section Geochemical analyses.

Results and Discussion

Extent of Fe(III) reduction in Fe(III)-OC coprecipitate-amended microcosms

Soil microcosms amended with ^{57}Fe-enriched Fe(III)-OC coprecipitates showed an increase in aqueous Fe^{2+} from 0.68±0.02 mM directly after addition to 1.01±0.02 mM after 42 days (Figure 1a), while the no-coprecipitate control had constant Fe^{2+} concentration over time (0.72±0.02 mM). This shows that there was more Fe(III) reduction in the coprecipitate-added setup than in the control. This reduction is likely microbial, based on greenhouse gas data and the presence of Fe(III)-reducing microorganisms (see below and Figure S8). Based

on the ^{57}Fe isotope data, 0.63±0.01 mM Fe were reduced and released from coprecipitates (Figure 1b) within 42 days, confirming that this excess quantity of aqueous Fe^{2+} stemmed from the added ^{57}Fe-enriched Fe(III)-OC coprecipitates. This would constitute a net dissolution of 10.2±0.2% of added coprecipitates. However, there was a small discrepancy between the estimated amount of reduced and dissolved Fe(III)-OC coprecipitates by the absolute concentrations of aqueous Fe^{2+} (4.4%) and the ^{57}Fe-based calculations.

We considered that isotope exchange of aqueous Fe^{2+} with the Fe in the added coprecipitates potentially occured. This effect would have increased the fraction of ^{57}Fe in the aqueous phase by electron transfer from the aqueous $^{56}Fe^{2+}$ to the ^{57}Fe(III) in the coprecipitates and released $^{57}Fe^{2+}$. We tested the importance of isotope exchange by adding the same concentration of Fe(III)-OC coprecipitates to sterile-filtered solution from the microcosms, containing dissolved Fe^{2+}. Results showed rapid isotope exchange immediately after addition of Fe(III)-OC coprecipiates to the solution while absolute aqueous Fe concentrations stayed constant over 48 hours (Figure S9). Concentrations of aqueous Fe^{2+} also immediately decreased due to adsorption onto the coprecipitate surface, as detected in the main experiment at t_0 (Figure 1a). This is in line with other studies, showing that electron transfer between aqueous Fe(II) and Fe(III)-OC coprecipitates[68] and at acidic pH values (pH<6, in this study pH 4.9-5.7) is possible[69,70]. The initial increase in aqueous Fe from coprecipitates within one day (0.35 mM, Figure 1b) is therefore attributable to partial isotope exchange, while the remaining increase likely constitutes microbial Fe(III) reduction. The estimated amount of reduced and dissolved Fe(III)-OC coprecipitates is then equal to 4.7±0.2% after accounting for the initial abiotic isotope exchange. Thus, the increase in aqueous Fe^{2+} in the coprecipitate-added setup is fully explained by the reduction of added Fe(III)-OC coprecipitates and not of the native Fe(III) minerals. Together with a concurrent decrease in 0.5 M HCl-extractable Fe(III) in the solid phase of the coprecipitate-added setup in comparison to the no-coprecipitate control (Figure S10), this unambiguously proves that the added Fe(III)-OC coprecipitates were microbially reduced.
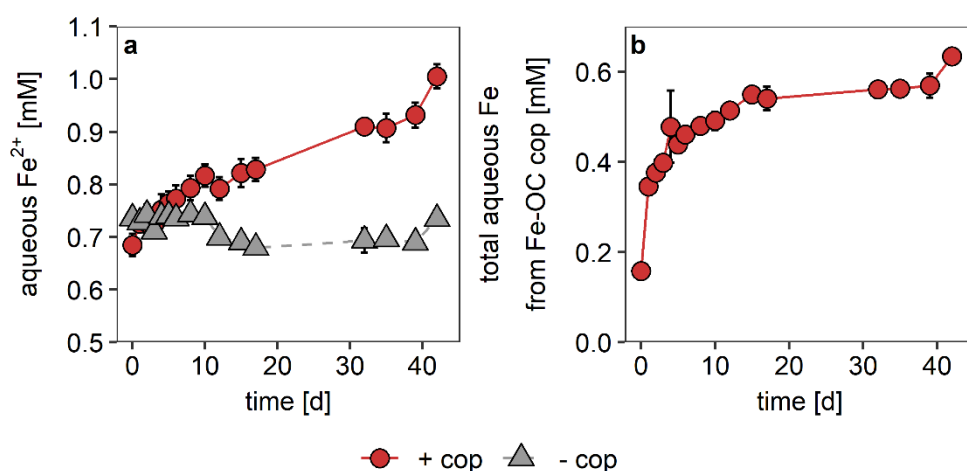
Figure 1. Increase in aqueous Fe over time. Measured concentrations of dissolved Fe^{2+} in setups with Fe(III)-OC coprecipitate addition ("+ cop", red circles) and the no-coprecipitate control ("- cop", grey triangles) (a). Calculated concentration of total aqueous Fe from Fe(III)-OC coprecipitates based on ^{57}Fe isotope measurements (b). All data symbols and error bars represent the average and standard deviation of experimental triplicates respectively.

In the solid phase, we quantified the extent of Fe(III) reduction using ^{57}Fe Mössbauer spectroscopy and a selective 0.5 M HCl extraction targeting the poorly crystalline fraction of Fe minerals[44,45]. Due to the enrichment of ^{57}Fe in the Fe(III)-OC coprecipitates, 51% of the signal within the Mössbauer spectra originated from the coprecipitates (see calculation in Text S10), while the theoretical fraction of coprecipitate Fe in the total soil Fe is 17%.

We measured ^{57}Fe Mössbauer spectra of soil with and without addition of ^{57}Fe-enriched coprecipitates at 77 and 6 K. Spectra at 6 K allowed for a more precise identification of Fe phases, while spectra at 77 K gave overall information on Fe speciation (see Figure S11, Text S11). In all 6 K spectra, we detected an Fe(II)-doublet, Fe(III)-doublet, and Fe(II)-octet (Figure 2). The Fe(II)-doublet at 6 K is representative of Fe(II) in phyllosilicates and/or Fe(II) adsorbed to other minerals[71–73]. The Fe(III)-doublet represents Fe(III) in phyllosilicates or bound to organic matter[72,74]. The Fe(II)-octet is representative for Fe(II) in Fe-rich phyllosilicates[75–77] and was included since XRD patterns (Figure S12) and Fe K-edge EXAFS data (Figure S3) of the initial soil showed high abundances of Fe in phyllosilicates. An additional Fe(III) sextet component was observed exclusively in the samples with addition of ^{57}Fe-enriched coprecipitates (Figure 2a, e). The Fe(III) sextet had parameters characteristic for poorly crystalline Fe(III) (oxyhydr)oxides (Table S4), such as ferrihydrite[78,79]. The relative area of the Fe(III) sextet in the sample at t_0 was 44%, close to the calculated initial contribution of ^{57}Fe-enriched coprecipitates to the overall signal (Text S10). Furthermore, the spectra of initial coprecipitates also show formation of a sextet component at lower temperatures (Figure S2).

This suggests that the entire Fe(III) sextet component is indicative of the contribution of coprecipitates to the solid ^{57}Fe pool. After 42 days of incubation, the area of the Fe(III) sextet decreased to 34% (Figure 2b, e). The difference in relative abundance compared to t_0 thus indicates that the added Fe(III)-OC coprecipitates were reduced by 22%. We also detected a decrease in 0.5 M HCl-extractable Fe(III) contents of 1.38±0.89 mg Fe(III) g^{-1} dry soil (Figure S10) from 0 to 42 d (reduction extent of Fe(III)-OC coprecipitates: 33±21%), which agrees well with the reduction extent based on Mössbauer spectroscopy (22%). In contrast, no Fe(III) reduction was detected in the no-coprecipitate setup based on 6 K spectra (Figure 2c, d, e) and 0.5 M HCl extractions (Figure S10). We can thus conclude that the decrease in Fe(III) content is fully attributable to the reduction of added coprecipitates, fitting to the aqueous Fe data. The native, bioavailable Fe(III) minerals in the soil were likely already reduced during the 35 day incubation period before addition of the coprecipitates.
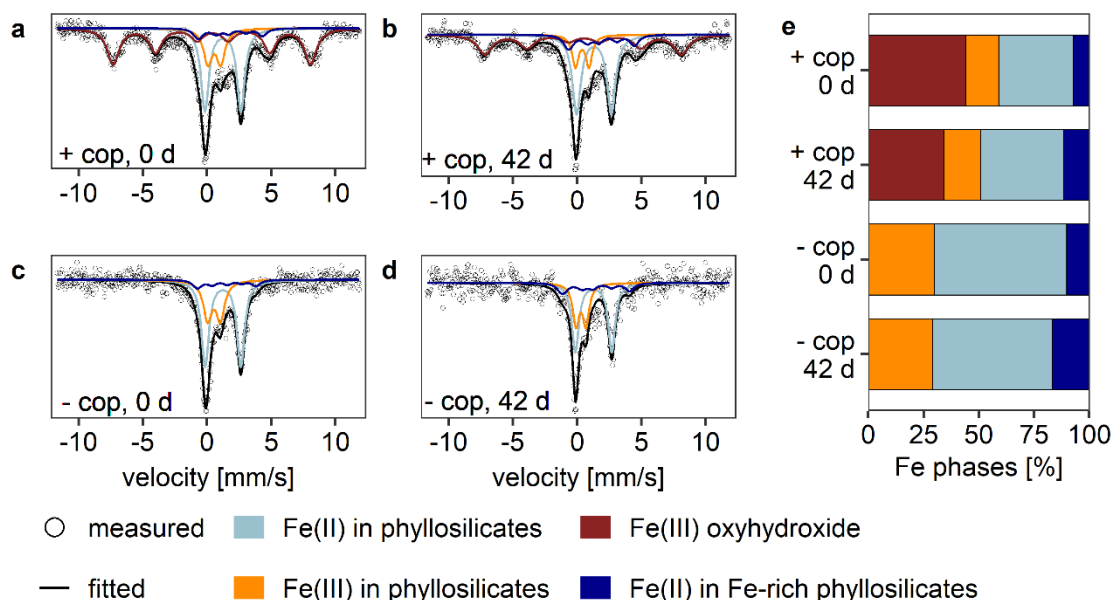
Figure 2. Solid-phase Fe speciation in soil from microcosm experiment measured by ^{57}Fe Mössbauer spectroscopy at 6 K. Subplots display spectra of soil with addition of ^{57}Fe-enriched Fe(III)-OC coprecipitates at t_0 (a) and after 42 days (b) as well as a no-coprecipitate control at t_0 (c) and after 42 days (d). All spectra show the measured data (open circles), the fit (black line) and individual components (coloured lines). The following components were assigned: Fe(II) in phyllosilicates and/or adsorbed Fe(II) (light blue), Fe(III) in phyllosilicates (orange), poorly crystalline Fe(III) oxyhydroxides (dark red), Fe(II) in Fe-rich phyllosilicates (dark blue). Fitting parameters are given in Table S4. The relative share of each component based on area (e).

Greenhouse gas emissions in microcosm experiments

Greenhouse gas fluxes of CH_4 and CO_2 were measured throughout the microcosm experiment. During the incubation period before coprecipitate addition (35 days) both soils had similar gas fluxes (Figure S13). Until 8 days after addition of ^{57}Fe-enriched coprecipitates, no CH_4 emissions were detected in that setup as well as in the no-coprecipitate controls. After 8 days, CH_4 fluxes started to increase in the no-coprecipitate setup from 0.03 ± 0.01 to 0.27 ± 0.04 $\mu mol\ d^{-1}\ g^{-1}$ dry weight after 42 d (Figure S13). Resulting cumulative fluxes reached 4.61 ± 0.62 $\mu mol\ g^{-1}$ dry weight after 42 d (Figure 3a). In contrast, CH_4 fluxes in the setup with added coprecipitates stayed significantly lower between 8 d and 42 d (ANOVA, $p < 0.05$) and reached a cumulative flux of 0.27 ± 0.03 $\mu mol\ g^{-1}$ dry weight after 42 d. This constitutes a suppression of methane emissions by 94% compared to the no-coprecipitate setup (Figure 3a).
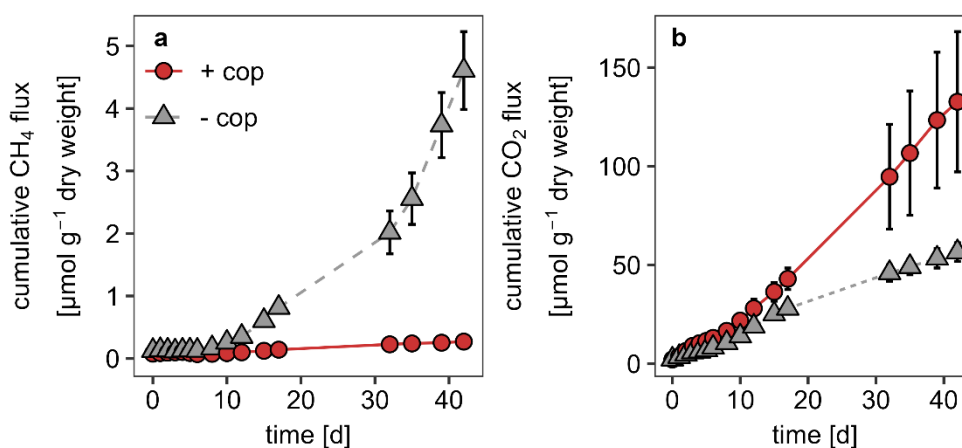
Figure 3. Cumulative greenhouse gas emissions of CH_4 (a) and CO_2 (b) in microcosm experiments with addition of ^{57}Fe-enriched Fe(III)-OC coprecipitates ("+ cop") and without ("-cop") over time. All data symbols and error bars represent the average and standard deviation of experimental triplicates respectively.

Microbial Fe(III) reduction likely inhibited methanogenesis, as shown in other studies based on field measurements and addition of Fe minerals to peatland soils[15–17]. Previously reported methane emission rates were decreased by 37-54% due to Fe(III) addition in the form of dissolved Fe(III)-NTA[16] and poorly crystalline ferrihydrite[17]. Our detected suppression effect might be considerably higher due to low DOC concentrations (Figure S14), indicative of low substrate availability, which can intensify the suppression effect[23]. The stronger decrease in CH_4 emission might also be due to anaerobic oxidation of CH_4 coupled to either Fe(III) reduction or to OC reduction which was present within the coprecipitates. It has been shown that addition of complex OC can decrease CH_4 fluxes[16,80,81], with reasons being (i)

thermodynamic favourability of reduction of redox-active OC functional groups in comparison to methanogenesis[82,83], (ii) metabolic flexibility of anaerobic methanotrophs to use oxidized OC as a terminal electron acceptor[84], or (iii) an electron shuttling effect by the released OC between methanotrophs and Fe(III) minerals[85].

Cumulative CO_2 emissions continuously increased in both setups (Figure 3b). There was a significantly higher cumulative flux after 42 days in the setup with added coprecipitates than in the no-coprecipitate control (132.7 ± 35.5 compared to 56.6 ± 4.7 µmol g^{-1} dry weight, ANOVA, $p<0.05$). The overall global warming potential was still 24% lower in the coprecipitate-added setup than in the no-coprecipitate control (Figure S15). The addition of Fe(III)-OC coprecipitates thus increased cumulative CO_2 emission by 134%, demonstrating that Fe-based anaerobic respiration was likely the dominant pathway for OC decomposition in our anoxic peatland soil. Assuming that 4 mol of Fe(III) are reduced per 1 mol CO_2 produced[18,86,87], we calculated the contribution of Fe(III) reduction to overall anaerobic respiration using our data from the microcosm experiment. Direct oxidation of OC to CO_2 via Fe(III) reduction of the coprecipitates could account for 26-64% of the additionally produced cumulative CO_2 flux after 42 days in the coprecipitate-added setup compared to the no-coprecipitate control. The remaining share therefore could stem from the release of previously Fe-bound OC to the aqueous phase, which could have served as an electron donor for many other microorganisms, leading to higher CO_2 production.

Shift in microbial community and methane-cycling microorganisms

We analyzed the change in overall microbial community using 16S rRNA (gene) amplicon sequencing and compared relative abundances of known methanogens and methanotrophs. Detected methanogens generally had a significantly lower relative abundance in coprecipitate-added setups than in the no-coprecipitate control (unpaired t-test, $p<0.001$), with the highest difference in RNA-based abundances after 42 days (1.57 ± 0.13% compared to 2.69 ± 0.19%, $p<0.001$, Figure 4a). Relative abundances of genera *Methanosaeta* and *Methanoregula* were decreased on average by 45 and 51%, respectively, compared to the no-coprecipitate control. *Methanosarcina* sp. had significantly lower RNA-based relative abundances in coprecipitate-added setups after 42 days compared to control setups (0.08 ± 0.00% to 0.30 ± 0.16%, one-way ANOVA, $p<0.05$).

Concurrently, we also found differences in gene copy numbers of *mcrA* between the coprecipitate-added setup and the no-coprecipitate control using a qPCR-based analysis (Figure 4b). DNA- and RNA-based copy numbers of the *mcrA* gene decreased over time in the setup with added coprecipitates relative to the no-coprecipitate control. The decrease relative

to the control was highest after 42 days for both DNA- and RNA-based abundances (log_2FC: -0.50±0.21 and -2.54±0.64, respectively, Figure 4b). Together with the changes in methanogen community composition, this suggests that methanogen activity and abundance were suppressed by microbial Fe(III) reduction following the addition of Fe(III)-OC coprecipitates. Known acetoclastic methanogens, like genera *Methanosaeta* and *Methanosarcina*[88], were likely more affected compared to other hydrogenotrophic or possibly methylotrophic prokaryotes (*Methanobacterium* spp.) due to substrate competiton with Fe(III)-reducing microorganisms using acetate. We did detect a few Fe(III)-reducing taxa capable of utilizing acetate (*Geobacter*, *Rhodoferax*, *Geothrix*, see Figure S8)[89–91] which supports this hypothesis. There could also have been an indirect effect on methanogen activity due to pH changes, but since pH differences were small between the setups (5.7±0.0 in coprecipitate-added setup compared to 5.5±0.2 in control after 42 days, Figure S16), we consider this effect negligible.

We detected both canonically aerobic methanotrophs and (putatively) anaerobic methanotrophs. Prominent aerobic methanotrophs (>0.1%) belonged to the genera of *Methylobacter* and *Crenothrix* of the order *Methylococcales* (Figure 4a). Their RNA-based relative abundance stayed constant across the incubation of both setups (*Methylococcales*: 0.53±0.09%), meaning that they were likely active despite the persistent anoxic conditions. Especially *Methylobacter* sp. has previously been detected in other anoxic environments and was therefore suggested to be metabolically flexible[92–94]. Within the microcosm experiment, it is possible that the methanotrophs used fermentation or Fe(III) reduction for anaerobic respiration instead of aerobic respiration[95,96].

The most prominent anaerobic methanotroph detected in our experiments was a member of the order *Methylomirabilales* (genus: Sh765B-TzT-35). Members of the *Methylomirabilales* taxa had a higher relative abundance in the coprecipitate added setup compared to the control after 8 days (1.12±0.06% compared to 0.64±0.41%) and 42 days (1.26±0.05% compared to 0.93±0.07%). Although these differences were not statistically significant (Kruskal-Wallis test, p=0.15), it is interesting to note that the RNA-based copy numbers of the *pmoA* gene were also slightly elevated at the same time points compared to the no-coprecipitate control (log_2FC: 0.75±0.81 and 0.54±0.36 after 8 and 42 days, respectively, Figure 4b). The available genomes of *Methylomirabilales* contain genes encoding for particulate methane monooxygenase[97], meaning that they could have contributed to the higher *pmoA* gene copy numbers. It has been found that one member of the *Methylomirabilales* taxa, Candidatus *Methylomirabilis oxyfera*, is capable of producing dioxygen (O_2) intercellularly from nitrite to oxidize CH_4 under anoxic conditons[98]. The *Methylomirabilales* members here could have used a similar mechanism and were recently also linked to anoxic methane oxidation in arctic thermokarst lagoons[94]. Additionally, it has been found that Fe(III)

oxyhydroxides can serve as an electron acceptor for methanotrophs capable of extracellular electron transfer, as shown for *Methylococcales*[99]. We therefore speculate that anaerobic methane oxidation coupled to Fe(III) or OC reduction stemming from the coprecipitates could have played a role in further inhibiting net methane release. The overall data, however, suggests that methanogenesis inhibition due to substrate competition with Fe(III)-reducers was the dominating process in decreasing methane emissions.
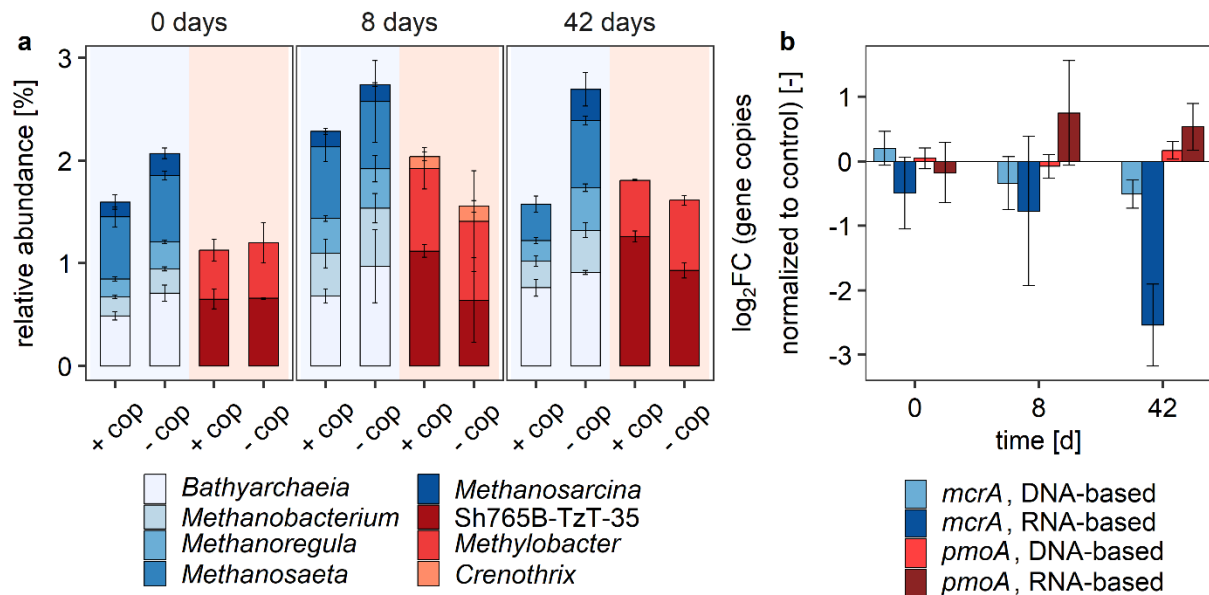
Figure 4. Changes in potential activity of methanogens and methanotrophs based on 16S rRNA sequencing and functional gene abundance in the microcosm experiment after 0, 8, and 42 days after addition of Fe(III)-OC coprecipitates. Relative 16S rRNA abundances of likely active (RNA-based) microbial taxa related to methane production (blue) and methane oxidation (red) per timepoint and setup (+cop: with addition of Fe(III)-OC coprecipitates, -cop: no-coprecipitate control) (a). Taxa with an abundance lower than 0.1% were not included. Taxa are labelled at the genus-level, except for *Bathyarchaeia* for which no genus could be classified. DNA-based 16S rRNA abundances show similar trends and are given in Figure S17. Data bars and error bars represent the average and standard deviation of experimental triplicates, respectively. Quantitative PCR results of DNA- and RNA-based *mcrA* and *pmoA* gene copies in samples taken immediately after addition of coprecipitates (t_0), after 8 days, and 42 days (b). Changes in the coprecipitate-added setup are displayed as the $\log_2$ fold change (FC) of the mean copy numbers of "+ cop" setup to the mean of the no-coprecipitate control [copies$_{+cop}$ g^{-1} dry soil/ copies$_{-cop}$ g^{-1} dry soil] at the same time point. Absolute gene copy numbers are displayed in Figure S18. Data bars and error bars represent the average and 95% confidence interval of experimental triplicates, respectively.

Concentrations of methanogenesis substrates and fermentation intermediates

The concentrations of different organic metabolites relevant for methanogenesis (direct substrates and fermentation intermediates) were quantified using targeted GC-MS. Concentrations of acetate, which is a fermentation product and both a substrate for methanogenesis and Fe(III) reduction, remained approximately constant over time in the coprecipitate-added setup and the non-amended control (Figure 5). We thus cannot conclude any preferential utilization within the two different setups. However, since acetoclastic methanogenesis based on molecular biology data was suppressed, a higher proportion of acetate in the coprecipitate-added setup was likely used for Fe(III) reduction. Methanol concentrations generally increased over time (Figure 5) from 1.73 ± 0.74 µM at t_0 to 3.78 ± 1.10 µM after 42 days (Figure S19), but also did not vary between setups (Figure 5). We expect that methylotrophic methanogenesis does play a role in the fen soil based on published microbial data[100]. However, the lack of difference in the concentrations between setups could indicate that methylotrophs are unaffected by changes in Fe(III) cycling due to their wide range of usable substrates[88,101] independent of substrates used for Fe(III) reduction. Butyrate is also a substrate for methanogenesis via syntrophic butyrate oxidation[102]. Butyrate concentrations significantly decreased over time in the coprecipitate added setup (3.00 ± 0.18 µM at day 0 compared to 2.56 ± 0.07 µM at day 42, $p<0.05$) in contrast to constant concentrations in the no-coprecipitate control (2.66 ± 0.10 µM, Figure S19). The observed decrease in the coprecipitate-added setup might stem from fermentative Fe(III)-reducers using Fe(III) as a sink for excess reducing equivalents, instead of producing butyrate during fermentation[103–105]. Thus, less butyrate may have been produced, decreasing the potential for methanogenesis. Lactate and pyruvate concentrations were increased slightly in the coprecipitate-added setup compared to the control (Figure 5), which could indicate an increased fermentation activity stimulated due to the release of Fe-bound OC.
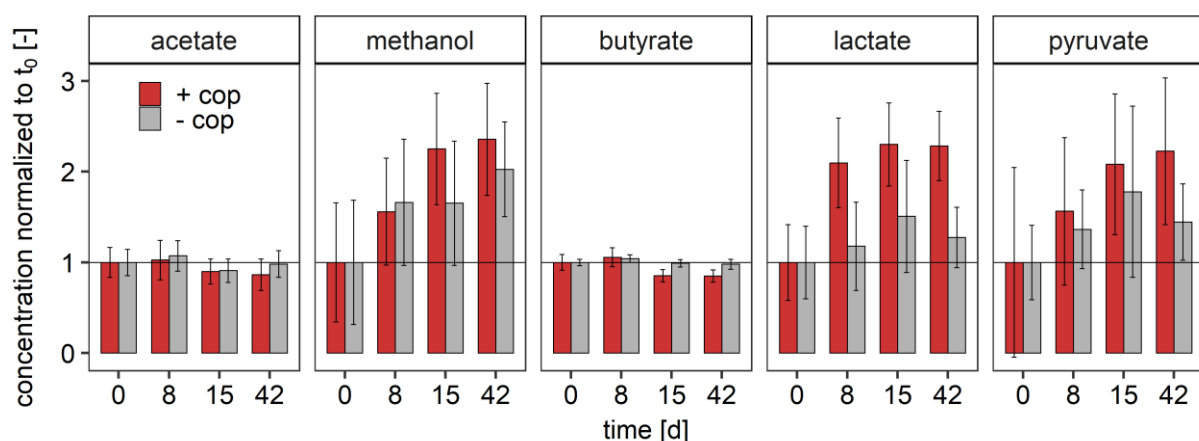
Figure 5. Changes in concentration of microbial metabolites relevant for fermentation and methanogenesis in microcosm setups with addition of ^{57}Fe-enriched Fe(III)-OC coprecipitates ("+ cop", red) and in a no-coprecipitate control ("- cop", grey). Data is displayed as the ratio of concentrations for each metabolite after 8, 15, and 42 days relative to their respective concentration at time 0 [μM /μM]. Absolute data is displayed in Figure S19. Data bars and error bars represent the average and standard deviation of experimental triplicates.

Fe(III) reduction extent and changes in net CH_4 emissions under *in situ* conditions

To test whether our results from the microcosm experiment also apply in the environment, we incubated ^{NA}Fe(III)-OC coprecipitates in passive porewater samplers ("peepers") over a growing season in the fen area of Stordalen Mire. After the incubation time of 53 days (from July to September 2022), the solid-phase data showed that the majority of added Fe in the coprecipitate-added plots was not recovered from the peepers. Suspension concentrations of total Fe were 29.6±12.7 mg L^{-1} per cell across all depths (Figure S20) compared to the initial addition of 280 mg L^{-1} Fe. Over depth, solid total Fe concentrations increased from 17.6±8.4 mg L^{-1} at 4 cm depth to 42.1±8.34 mg L^{-1} at 20 cm depth (Figure S20). The Fe oxidation state of the remaining ^{NA}Fe(III)-OC coprecipitates was 14-49% Fe(II) (Figure 6a). Assuming that the loss in total Fe and solid-phase Fe(II) content represents the combined extent of reductive dissolution of ^{NA}Fe(III)-OC coprecipitates, 92±4.0% of Fe in coprecipitates was reduced across all depths (Figure 6a).

We also considered that some Fe(III)-OC coprecipitates might have also passed the 8 μm membrane due to potentially lower aggregate size. However, in a control experiment we found that 98.9% of the initial ^{NA}Fe(III)-OC coprecipitate suspension was retained on the membrane, suggesting that the majority of the loss in Fe(III)-OC was due to reductive dissolution. The control peeper, in which no Fe(III) was added, contained lower concentrations of solid, primarily ferrous, Fe (0.65-6.31 mg L^{-1}, Figure S20) across all depths. This suggests that there was a low background concentration of particulate-bound Fe in the porewater. We did not detect any large differences in dissolved species concentrations between the two setups at the end of the experiment. Aqueous Fe^{2+}, dissolved CH_4 and DOC did not vary in comparison to the no-coprecipitate setup (Figure S21). It is likely that any initial changes in porewater chemistry inside the peeper cells due to Fe(III) reduction were overridden by re-equilibration with the soil porewater.

The reduction extent of our added Fe(III)-OC coprecipitates under *in situ* conditions was thus substantially larger than in the microcosm experiment. The following factors might have played a role: (i) The *in situ* DOC concentrations detected in all three peepers were, on average, at least three times higher in the field compared to the microcosm experiment

(31.9±8.6 mg C L^{-1} compared to 8.8±5.7 mg C L^{-1}, respectively). The higher DOC concentrations might have facilitated more Fe(III) reduction via OC oxidation relative to the microcosm experiment. Additionally, redox-active organic groups in DOC can be used as electron shuttles between Fe(III)-reducing microorganisms and solid phase Fe(III)[105], which could also increase the rates and extent of reduction in the field experiment. (ii) The peepers reached until a depth of 21 cm from the soil surface, while the soil used for the microcosm experiment came from a depth of 30 cm. Thus, the geochemical parameters (such as OC content, pH, presence of other nutrients like phosphate and nitrate) and the microbial community might have slightly differed. (iii) Under ambient conditions, there is constant exchange of nutrients via root exudates[106,107], permafrost runoff or river flow[108,109] such that conditions for microbial Fe(III) reduction might be more favorable. (iv) The microbial community in thawed permafrost soils is likely adapted to cold conditions[110,111] and might perform Fe(III) reduction at a lower rate when exposed to higher temperatures in the laboratory (room temperature).
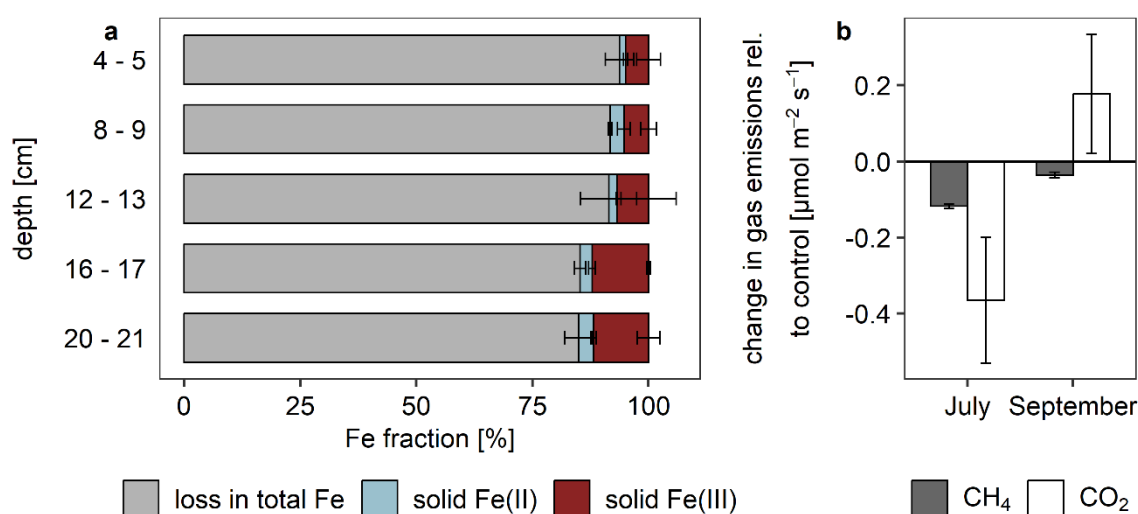
Figure 6. *In situ* loss and speciation of [NA]Fe(III)-OC coprecipitates and the net impact on greenhouse gas emissions over a growing season in the fen area of Stordalen Mire. The Fe speciation in the solid (measured) and the loss of total Fe compared to initial addition (calculated) is displayed over depth from the soil surface (a). Changes in CH_4 and CO_2 emissions [μmol m^{-2} s^{-1}] within one day after addition of [NA]Fe(III)-OC coprecipitates (July) and after 53 days (September) are shown relative to a no-coprecipitate plot in which only deionized water was added (b). Absolute Fe concentrations and gas flux data are provided in Figure S20 and S22, respectively. Data bars and error bars represent the average and range of experimental duplicates in case of the Fe speciation data, and the average and standard

deviation of triplicate measurements of one "+ cop" plot and one control plot in case of the gas data.

The GHG fluxes measured above the different peeper setups changed significantly depending on the season (ANOVA, $p < 0.05$), with lower CH_4 and CO_2 emissions in September than in July (Figure S22). We thus examined the differences in net fluxes of the coprecipitate-added and no-coprecipitate plot at each sampling time. Net CH_4 emission in the coprecipitated plot relative to the no-coprecipitate plot decreased significantly by 40% within one day after addition of coprecipitates (change of -0.12 ± 0.01 μmol m^{-2} s^{-1}) and by 33% at the end of the growing season (-0.04 ± 0.01 μmol m^{-2} s^{-1}, Figure 6b). Methanogenesis was thus inhibited likely due to Fe(III) reduction of added ^{NA}Fe(III)-OC coprecipitates, matching with the results of our microcosm experiment. The suppression effect was less pronounced under *in situ* conditions (33-40% compared to 93 ± 5% lower CH_4 flux between the setups). Possible reasons could be the higher DOC concentrations, measured at the end of the incubation period, and thus higher substrate availability and the relatively lower amount of Fe(III)-OC coprecipitates added to soil in comparison to the microcosm experiment. The decrease in suppression intensity over time also indicates that this effect is only temporary.

Fluxes of CO_2 measured under dark conditions (excluding photosynthesis) initially slightly decreased as a consequence of ^{NA}Fe(III)-OC coprecipitate addition by 25% (-0.37 ± 0.17 μmol m^{-2} s^{-1}, Figure 6b) relative to the no-coprecipitate plot. In September, fluxes were on average 36% higher relative to the no-coprecipitate control (0.18 ± 0.15 μmol m^{-2} s^{-1}). It is likely the ^{NA}Fe(III)-OC coprecipitates initially bound additional DOC, as detected in the microcosm experiment (Figure S14). This could have decreased CO_2 fluxes, which are often controlled by DOC concentrations[112]. As ^{NA}Fe(III)-OC coprecipitates were reductively dissolved, they likely re-released this adsorbed OC again, contributing to an increased CO_2 flux together with microbial Fe(III) reduction coupled to OC oxidation.

Conclusions

This study demonstrated that the addition of Fe(III)-OC associations (in the form of coprecipitates) in anoxic permafrost peatland soils decreases net CH_4 emissions. In both our microcosm and field experiment with fully thawed permafrost peatland soil, addition of synthesized Fe(III)-OC coprecipitates lowered fluxes of CH_4 compared to control setups without the coprecipitates. Decrease in CH_4 fluxes was mainly due to inhibition of methanogenesis, likely of acetoclastic methanogens (e.g., *Methanosaeta* and *Methanosarcina*) by substrate competition with Fe(III)-reducers which reduced added Fe(III)-OC coprecipitates. Methanotrophy coupled to Fe(III) or OC reduction might have played a

minor role, as suggested by the increase in relative abundance of *Methylomirabilales* spp. upon Fe(III)-OC coprecipitate addition.

The results of our study can be used to gain insights into future coupled Fe-CH$_4$ cycling in (permafrost) peatlands. The areal cover of fens at Stordalen Mire has already increased by 100% in the last 50 years[7] with this trend projected to continue in the future. Therefore, a large proportion of oxic soils could abruptly thaw and collapse[113], establishing anoxic conditions. The native Fe(III)-OC associations could then attenuate CH$_4$ release for a certain time frame and thus lower the global warming potential of the emitted greenhouse gases. The timescale of this attenuation is still highly uncertain due to limiting data on Fe stocks in permafrost peatlands[29,37] and the estimated *in situ* Fe reduction rates[87]. In addition, Fe(II)-oxidizing microorganisms could play a role in replenishing the content of Fe(III)-OC associations in permanently anoxic soils, as they have been detected in other Arctic habitats[114]. The results of our two experiments also showcase the sensitivity of CH$_4$ release on substrate availability and microbial composition of methane-cycling and Fe-cycling communities. If higher substrate concentrations are available and/or methanogenic communitites are made up of metabolically flexible members, competition with Fe(III)-reducing microorganisms might be decreased and methanogenesis suppression might be less severe. Our work also has implications for other flooded soils in which high OC contents, Fe minerals, and methanogenesis are expected, such as paddy soils or coastal marshes. Since these soils experience periodic flooding, abiotic or microbial re-oxidation of Fe(II) might regenerate Fe(III)-OC associations that may suppress CH$_4$ emission long term. Thus, Fe(III)-OC associations may play a major role in CH$_4$ emissions from a range of flooded (or redox-dynamic) soils.

References

1. Saunois, M., Stavert, A. R., Poulter, B., Bousquet, P., Canadell, J. G., Jackson, R. B., Raymond, P. A., Dlugokencky, E. J., Houweling, S., Patra, P. K., Ciais, P., Arora, V. K., Bastviken, D., Bergamaschi, P., Blake, D. R., Brailsford, G., Bruhwiler, L., Carlson, K. M., Carrol, M., … Zhuang, Q. (2020). The Global Methane Budget 2000–2017. *Earth System Science Data*, *12*(3), 1561–1623. https://doi.org/10.5194/essd-12-1561-2020

2. Kleinen, T., Gromov, S., Steil, B., & Brovkin, V. (2021). Atmospheric methane underestimated in future climate projections. *Environmental Research Letters*, *16*(9), 094006. https://doi.org/10.1088/1748-9326/ac1814

3. Lim, A. G., Loiko, S. V., & Pokrovsky, O. S. (2022). Sizable pool of labile organic carbon in peat and mineral soils of permafrost peatlands, western Siberia. *Geoderma*, *409*, 115601. https://doi.org/10.1016/j.geoderma.2021.115601

4. Mueller, C. W., Rethemeyer, J., Kao-Kniffin, J., Löppmann, S., Hinkel, K. M., & G. Bockheim, J. (2015). Large amounts of labile organic carbon in permafrost soils of northern A laska. *Global Change Biology*, *21*(7), 2804–2817. https://doi.org/10.1111/gcb.12876

5. Farquharson, L. M., Romanovsky, V. E., Cable, W. L., Walker, D. A., Kokelj, S. V., & Nicolsky, D. (2019). Climate Change Drives Widespread and Rapid Thermokarst Development in Very Cold Permafrost in the Canadian High Arctic. *Geophysical Research Letters*, *46*(12), 6681–6689. https://doi.org/10.1029/2019GL082187

6. Kokelj, S. V., & Jorgenson, M. T. (2013). Advances in Thermokarst Research. *Permafrost and Periglacial Processes*, *24*(2), 108–119. https://doi.org/10.1002/ppp.1779

7. Varner, R. K., Crill, P. M., Frolking, S., McCalley, C. K., Burke, S. A., Chanton, J. P., Holmes, M. E., Saleska, S., & Palace, M. W. (2022). Permafrost thaw driven changes in hydrology and vegetation cover increase trace gas emissions and climate forcing in Stordalen Mire from 1970 to 2014. *Philosophical transactions. Series A, Mathematical, physical, and engineering sciences*, *380*(2215), 20210022. https://doi.org/10.1098/rsta.2021.0022

8. Woo, M., & Young, K. L. (2006). High Arctic wetlands: Their occurrence, hydrological characteristics and sustainability. *Journal of Hydrology*, *320*(3–4), 432–450. https://doi.org/10.1016/j.jhydrol.2005.07.025

9. Knoblauch, C., Beer, C., Liebner, S., Grigoriev, M. N., & Pfeiffer, E.-M. (2018). Methane production as key to the greenhouse gas budget of thawing permafrost. *Nature Climate Change*, *8*(4), 309–312. https://doi.org/10.1038/s41558-018-0095-z

10. Rößger, N., Sachs, T., Wille, C., Boike, J., & Kutzbach, L. (2022). Seasonal increase of methane emissions linked to warming in Siberian tundra. *Nature Climate Change*, *12*(11), 1031–1036. https://doi.org/10.1038/s41558-022-01512-4

11. Turetsky, M. R., Treat, C. C., Waldrop, M. P., Waddington, J. M., Harden, J. W., & McGuire, A. D. (2008). Short-term response of methane fluxes and methanogen activity to water table and soil warming manipulations in an Alaskan peatland. *Journal of Geophysical Research: Biogeosciences*, *113*(G3), 2007JG000496. https://doi.org/10.1029/2007JG000496

12. Bridgham, S. D., Cadillo-Quiroz, H., Keller, J. K., & Zhuang, Q. (2013). Methane emissions from wetlands: Biogeochemical, microbial, and modeling perspectives from local to global scales. *Global Change Biology*, *19*(5), 1325–1346. https://doi.org/10.1111/gcb.12131

13. Achtnich, C., Bak, F., & Conrad, R. (1995). Competition for electron donors among nitrate reducers, ferric iron reducers, sulfate reducers, and methanogens in anoxic paddy soil. *Biology and Fertility of Soils*, *19*(1), 65–72. https://doi.org/10.1007/BF00336349

14. Stams, A. J. M., Elferink, S. J. W. H. O., & Westermann, P. (2003). Metabolic Interactions Between Methanogenic Consortia and Anaerobic Respiring Bacteria. In B. K. Ahring, I. Angelidaki, E. C. De Macario, H. N. Gavala, J. Hofman-Bang, A. J. L. Macario, S. J. W. H. O. Elferink, L. Raskin, A. J. M. Stams, P. Westermann, & D. Zheng (Hrsg.), *Biomethanation I* (Bd. 81, S. 31–56). Springer Berlin Heidelberg. https://doi.org/10.1007/3-540-45839-5_2

15. Lipson, D. A., Zona, D., Raab, T. K., Bozzolo, F., Mauritz, M., & Oechel, W. C. (2012). Water-table height and microtopography control biogeochemical cycling in an Arctic coastal tundra ecosystem. *Biogeosciences*, *9*(1), 577–591. https://doi.org/10.5194/bg-9-577-2012

16. Miller, K. E., Lai, C.-T., Friedman, E. S., Angenent, L. T., & Lipson, D. A. (2015). Methane suppression by iron and humic acids in soils of the Arctic Coastal Plain. *Soil Biology and Biochemistry*, *83*, 176–183. https://doi.org/10.1016/j.soilbio.2015.01.022

17. Reiche, M., Torburg, G., & Küsel, K. (2008). Competition of Fe(III) reduction and methanogenesis in an acidic fen. *FEMS microbiology ecology*, *65*(1), 88–101. https://doi.org/10.1111/j.1574-6941.2008.00523.x

18. Roden, E. E., & Wetzel, R. G. (1996). Organic carbon oxidation and suppression of methane production by microbial Fe(III) oxide reduction in vegetated and unvegetated freshwater wetland sediments. *Limnology and Oceanography*, *41*(8), 1733–1748. https://doi.org/10.4319/lo.1996.41.8.1733

19. Megonigal, J. P., Hines, M. E., & Visscher, P. T. (2003). Anaerobic Metabolism: Linkages to Trace Gases and Aerobic Processes. In *Treatise on Geochemistry* (S. 317–424). Elsevier. https://doi.org/10.1016/B0-08-043751-6/08132-9

20. Roden, E. E., & Wetzel, R. G. (2003). Competition between Fe(III)-Reducing and Methanogenic Bacteria for Acetate in Iron-Rich Freshwater Sediments. *Microbial Ecology*, *45*(3), 252–258. https://doi.org/10.1007/s00248-002-1037-9

21. Bar-Or, I., Elvert, M., Eckert, W., Kushmaro, A., Vigderovich, H., Zhu, Q., Ben-Dov, E., & Sivan, O. (2017). Iron-Coupled Anaerobic Oxidation of Methane Performed by a Mixed Bacterial-Archaeal Community Based on Poorly Reactive Minerals. *Environmental Science & Technology*, *51*(21), 12293–12301. https://doi.org/10.1021/acs.est.7b03126

22. Ettwig, K. F., Zhu, B., Speth, D., Keltjens, J. T., Jetten, M. S. M., & Kartal, B. (2016). Archaea catalyze iron-dependent anaerobic oxidation of methane. *Proceedings of the National Academy of Sciences*, *113*(45), 12792–12796. https://doi.org/10.1073/pnas.1609534113

23. Sulman, B. N., Yuan, F., O'Meara, T., Gu, B., Herndon, E. M., Zheng, J., Thornton, P. E., & Graham, D. E. (2022). Simulated Hydrological Dynamics and Coupled Iron Redox Cycling Impact Methane Production in an Arctic Soil. *Journal of Geophysical Research: Biogeosciences*, *127*(10), e2021JG006662. https://doi.org/10.1029/2021JG006662

24. Wagner, R., Zona, D., Oechel, W., & Lipson, D. (2017). Microbial community structure and soil p H correspond to methane production in A rctic A laska soils. *Environmental Microbiology*, *19*(8), 3398–3410. https://doi.org/10.1111/1462-2920.13854

25. Fu, L., Zhou, T., Wang, J., You, L., Lu, Y., Yu, L., & Zhou, S. (2019). NanoFe3O4 as Solid Electron Shuttles to Accelerate Acetotrophic Methanogenesis by Methanosarcina barkeri. *Frontiers in Microbiology*, *10*, 388. https://doi.org/10.3389/fmicb.2019.00388

26. Wang, H., Byrne, J. M., Liu, P., Liu, J., Dong, X., & Lu, Y. (2020). Redox cycling of Fe(II) and Fe(III) in magnetite accelerates aceticlastic methanogenesis by *Methanosarcina mazei*. *Environmental Microbiology Reports*, *12*(1), 97–109. https://doi.org/10.1111/1758-2229.12819

27. Xiao, L., Wei, W., Luo, M., Xu, H., Feng, D., Yu, J., Huang, J., & Liu, F. (2019). A potential contribution of a Fe(III)-rich red clay horizon to methane release: Biogenetic magnetite-mediated methanogenesis. *CATENA*, *181*, 104081. https://doi.org/10.1016/j.catena.2019.104081

28. Dong, H., Zeng, Q., Sheng, Y., Chen, C., Yu, G., & Kappler, A. (2023). Coupled iron cycling and organic matter transformation across redox interfaces. *Nature Reviews Earth & Environment*, *4*(9), 659–673. https://doi.org/10.1038/s43017-023-00470-5

29. Patzner, M. S., Mueller, C. W., Malusova, M., Baur, M., Nikeleit, V., Scholten, T., Hoeschen, C., Byrne, J. M., Borch, T., Kappler, A., & Bryce, C. (2020). Iron mineral dissolution releases iron and associated organic carbon during permafrost thaw. *Nature communications*, *11*(1), 6329. https://doi.org/10.1038/s41467-020-20102-6

30. Sun, F.-S., Ma, C., Yu, G.-H., Kuzyakov, Y., Lang, Y.-C., Fu, P.-Q., Guo, L.-J., Teng, H. H., & Liu, C.-Q. (2023). Organic carbon preservation in wetlands: Iron oxide protection vs. thermodynamic limitation. *Water Research*, *241*, 120133. https://doi.org/10.1016/j.watres.2023.120133

31. Wang, Y., Liu, X., Zhang, X., Dai, G., Wang, Z., & Feng, X. (2022). Evaluating wetland soil carbon stability related to iron transformation during redox oscillations. *Geoderma*, *428*, 116222. https://doi.org/10.1016/j.geoderma.2022.116222

32. Adhikari, D., Zhao, Q., Das, K., Mejia, J., Huang, R., Wang, X., Poulson, S. R., Tang, Y., Roden, E. E., & Yang, Y. (2017). Dynamics of ferrihydrite-bound organic carbon during microbial Fe reduction. *Geochimica et Cosmochimica Acta*, *212*, 221–233. https://doi.org/10.1016/j.gca.2017.06.017

33. Cooper, R. E., Eusterhues, K., Wegner, C.-E., Totsche, K. U., & Küsel, K. (2017). Ferrihydrite-associated organic matter (OM) stimulates reduction by Shewanella oneidensis MR-1 and a complex microbial consortia. *Biogeosciences*, *14*(22), 5171–5188. https://doi.org/10.5194/bg-14-5171-2017

34. Drake, H. L., Horn, M. A., & Wüst, P. K. (2009). Intermediary ecosystem metabolism as a main driver of methanogenesis in acidic wetland soil. *Environmental Microbiology Reports*, *1*(5), 307–318. https://doi.org/10.1111/j.1758-2229.2009.00050.x

35. Eusterhues, K., Hädrich, A., Neidhardt, J., Küsel, K., Keller, T. F., Jandt, K. D., & Totsche, K. U. (2014). Reduction of ferrihydrite with adsorbed and coprecipitated organic matter: Microbial reduction by Geobacter bremensis vs. Abiotic reduction by Na-dithionite. *Biogeosciences*, *11*(18), 4953–4966. https://doi.org/10.5194/bg-11-4953-2014

36. Liu, F., Qin, S., Fang, K., Chen, L., Peng, Y., Smith, P., & Yang, Y. (2022). Divergent changes in particulate and mineral-associated organic carbon upon permafrost thaw. *Nature communications*, *13*(1), 5073. https://doi.org/10.1038/s41467-022-32681-7

37. Mu, C. C., Zhang, T. J., Zhao, Q., Guo, H., Zhong, W., Su, H., & Wu, Q. B. (2016). Soil organic carbon stabilization by iron in permafrost regions of the Qinghai-Tibet Plateau. *Geophysical Research Letters*, *43*(19), 10286–10294. https://doi.org/10.1002/2016GL070071

38. Monhonval, A., Strauss, J., Thomas, M., Hirst, C., Titeux, H., Louis, J., Gilliot, A., Du Bois d'Aische, E., Pereira, B., Vandeuren, A., Grosse, G., Schirrmeister, L., Jongejans, L. L., Ulrich, M., & Opfergelt, S. (2022). Thermokarst processes increase the supply of stabilizing surfaces and elements (Fe, Mn, Al, and Ca) for mineral–organic carbon interactions. *Permafrost and Periglacial Processes*, *33*(4), 452–469. https://doi.org/10.1002/ppp.2162

39. Patzner, M. S., Logan, M., McKenna, A. M., Young, R. B., Zhou, Z., Joss, H., Mueller, C. W., Hoeschen, C., Scholten, T., Straub, D., Kleindienst, S., Borch, T., Kappler, A., & Bryce, C. (2022). Microbial iron cycling during palsa hillslope collapse promotes

greenhouse gas emissions before complete permafrost thaw. *Communications Earth & Environment*, *3*(1). https://doi.org/10.1038/s43247-022-00407-8

40. Burke, S. A., Wik, M., Lang, A., Contosta, A. R., Palace, M., Crill, P. M., & Varner, R. K. (2019). Long-Term Measurements of Methane Ebullition From Thaw Ponds. *Journal of Geophysical Research: Biogeosciences*, *124*(7), 2208–2221. https://doi.org/10.1029/2018JG004786

41. Malmer, N., Johansson, T., Olsrud, M., & Christensen, T. R. (2005). Vegetation, climatic changes and net carbon sequestration in a North-Scandinavian subarctic mire over 30 years. *Global change biology*, *0*(0), 051006062331004-. https://doi.org/10.1111/j.1365-2486.2005.01042.x

42. Stookey, L. L. (1970). Ferrozine—A new spectrophotometric reagent for iron. *Analytical Chemistry*, *42*(7), 779–781. https://doi.org/10.1021/ac60289a016

43. Kim, D.-G., Vargas, R., Bond-Lamberty, B., & Turetsky, M. R. (2012). Effects of soil rewetting and thawing on soil gas fluxes: A review of current literature and suggestions for future research. *Biogeosciences*, *9*(7), 2459–2483. https://doi.org/10.5194/bg-9-2459-2012

44. Heron, Gorm., Crouzet, Catherine., Bourg, A. C. M., & Christensen, T. H. (1994). Speciation of Fe(II) and Fe(III) in Contaminated Aquifer Sediments Using Chemical Extraction Techniques. *Environmental Science & Technology*, *28*(9), 1698–1705. https://doi.org/10.1021/es00058a023

45. Kostka, J. E., & Luther, G. W. (1994). Partitioning and speciation of solid phase iron in saltmarsh sediments. *Geochimica et Cosmochimica Acta*, *58*(7), 1701–1710. https://doi.org/10.1016/0016-7037(94)90531-2

46. R Core Team. (2024). *R: A language and environment for statistical computing* (Vienna, Austria). R Foundation for Statistical Computing. https://www.R-project.org/

47. Otte, J. M., Blackwell, N., Soos, V., Rughöft, S., Maisch, M., Kappler, A., Kleindienst, S., & Schmidt, C. (2018). Sterilization impacts on marine sediment—Are we able to inactivate microorganisms in environmental samples? *FEMS Microbiology Ecology*, *94*(12). https://doi.org/10.1093/femsec/fiy189

48. Parada, A. E., Needham, D. M., & Fuhrman, J. A. (2016). Every base matters: Assessing small subunit RRNA primers for marine microbiomes with mock communities, time series and global field samples. *Environmental Microbiology*, *18*(5), 1403–1414. https://doi.org/10.1111/1462-2920.13023

49. Apprill, A., McNally, S., Parsons, R., & Weber, L. (2015). Minor revision to V4 region SSU rRNA 806R gene primer greatly increases detection of SAR11 bacterioplankton. *Aquatic Microbial Ecology*, *75*(2), 129–137. https://doi.org/10.3354/ame01753

50. Straub, D., Tångrot, J., Peltzer, A., Lundin, D., emnilsson, nf-core bot, Sateesh_Peri, Adam Bennett, John Sundh, DiegoBrambilla, Asaf Peer, Till E, Lokeshwaran Manoharan, Maxime U Garcia, Sam Minot, PhilPalmer, Harshil Patel, Venkat Malladi, Matthew, … Kevin Menden. (2024). *nf-core/ampliseq: Ampliseq Version 2.8.0* (2.8.0) [Software]. [object Object]. https://doi.org/10.5281/ZENODO.1493841

51. Straub, D., Blackwell, N., Langarica-Fuentes, A., Peltzer, A., Nahnsen, S., & Kleindienst, S. (2020). Interpretations of Environmental Microbial Community Studies Are Biased by the Selected 16S rRNA (Gene) Amplicon Sequencing Pipeline. *Frontiers in Microbiology*, *11*, 550420. https://doi.org/10.3389/fmicb.2020.550420

52. Ewels, P. A., Peltzer, A., Fillinger, S., Patel, H., Alneberg, J., Wilm, A., Garcia, M. U., Di Tommaso, P., & Nahnsen, S. (2020). The nf-core framework for community-curated bioinformatics pipelines. *Nature Biotechnology*, *38*(3), 276–278. https://doi.org/10.1038/s41587-020-0439-x

53. Friedrich, M. W. (2005). Methyl-Coenzyme M Reductase Genes: Unique Functional Markers for Methanogenic and Anaerobic Methane-Oxidizing Archaea. In *Methods in Enzymology* (Bd. 397, S. 428–442). Elsevier. https://doi.org/10.1016/S0076-6879(05)97026-2

54. Juottonen, H., Galand, P. E., & Yrjälä, K. (2006). Detection of methanogenic Archaea in peat: Comparison of PCR primers targeting the mcrA gene. *Research in Microbiology*, *157*(10), 914–921. https://doi.org/10.1016/j.resmic.2006.08.006

55. McDonald, I. R., Bodrossy, L., Chen, Y., & Murrell, J. C. (2008). Molecular Ecology Techniques for the Study of Aerobic Methanotrophs. *Applied and Environmental Microbiology*, *74*(5), 1305–1315. https://doi.org/10.1128/AEM.02233-07

56. Welte, C. U., Rasigraf, O., Vaksmaa, A., Versantvoort, W., Arshad, A., Op Den Camp, H. J. M., Jetten, M. S. M., Lüke, C., & Reimann, J. (2016). Nitrate- and nitrite-dependent anaerobic oxidation of methane. *Environmental Microbiology Reports*, *8*(6), 941–955. https://doi.org/10.1111/1758-2229.12487

57. Großkopf, R., Janssen, P. H., & Liesack, W. (1998). Diversity and Structure of the Methanogenic Community in Anoxic Rice Paddy Soil Microcosms as Examined by Cultivation and Direct 16S rRNA Gene Sequence Retrieval. *Applied and Environmental Microbiology*, *64*(3), 960–969. https://doi.org/10.1128/AEM.64.3.960-969.1998

58. Hales, B. A., Edwards, C., Ritchie, D. A., Hall, G., Pickup, R. W., & Saunders, J. R. (1996). Isolation and identification of methanogen-specific DNA from blanket bog peat by PCR amplification and sequence analysis. *Applied and Environmental Microbiology*, *62*(2), 668–675. https://doi.org/10.1128/aem.62.2.668-675.1996

59. Holmes, A. J., Costello, A., Lidstrom, M. E., & Murrell, J. C. (1995). Evidence that participate methane monooxygenase and ammonia monooxygenase may be evolutionarily related. *FEMS Microbiology Letters*, *132*(3), 203–208. https://doi.org/10.1111/j.1574-6968.1995.tb07834.x

60. Muyzer, G., Teske, A., Wirsen, C. O., & Jannasch, H. W. (1995). Phylogenetic relationships ofThiomicrospira species and their identification in deep-sea hydrothermal vent samples by denaturing gradient gel electrophoresis of 16S rDNA fragments. *Archives of Microbiology*, *164*(3), 165–172. https://doi.org/10.1007/BF02529967

61. Nadkarni, M. A., Martin, F. E., Jacques, N. A., & Hunter, N. (2002). Determination of bacterial load by real-time PCR using a broad-range (universal) probe and primers set. *Microbiology*, *148*(1), 257–266. https://doi.org/10.1099/00221287-148-1-257

62. Stahl, D., & Amann, R. (1991). Development and application of nucleic acid probes in bacterial systematics. In *Nucleic acid techniques in bacterial systematics* (S. 205–248). John Wiley & Sons Ltd.

63. Winkel, M., Mitzscherling, J., Overduin, P. P., Horn, F., Winterfeld, M., Rijkers, R., Grigoriev, M. N., Knoblauch, C., Mangelsdorf, K., Wagner, D., & Liebner, S. (2018). Anaerobic methanotrophic communities thrive in deep submarine permafrost. *Scientific Reports*, *8*(1), 1291. https://doi.org/10.1038/s41598-018-19505-9

64. Bowes, H. L., & Hornibrook, E. R. C. (2006). Emission of highly [13] C-depleted methane from an upland blanket mire. *Geophysical Research Letters*, *33*(4), 2005GL025209. https://doi.org/10.1029/2005GL025209

65. Hesslein, R. H. (1976). An in situ sampler for close interval pore water studies. *Limnology and Oceanography*, *21*(6), 912–914. https://doi.org/10.4319/lo.1976.21.6.0912

66. Lei, P., Chen, M., Rong, N., Tang, W., & Zhang, H. (2024). A passive sampler for synchronously measuring inorganic and organic pollutants in sediment porewater: Configuration and field application. *Journal of Environmental Sciences*, *136*, 201–212. https://doi.org/10.1016/j.jes.2023.02.019

67. Liebner, S., Ganzert, L., Kiss, A., Yang, S., Wagner, D., & Svenning, M. M. (2015). Shifts in methanogenic community composition and methane fluxes along the degradation of discontinuous permafrost. *Frontiers in Microbiology*, *6*. https://doi.org/10.3389/fmicb.2015.00356

68. Zhou, Z., Latta, D. E., Noor, N., Thompson, A., Borch, T., & Scherer, M. M. (2018). Fe(II)-Catalyzed Transformation of Organic Matter-Ferrihydrite Coprecipitates: A Closer Look Using Fe Isotopes. *Environmental science & technology*, *52*(19), 11142–11150. https://doi.org/10.1021/acs.est.8b03407

69. Handler, R. M., Frierdich, A. J., Johnson, C. M., Rosso, K. M., Beard, B. L., Wang, C., Latta, D. E., Neumann, A., Pasakarnis, T., Premaratne, W. A. P. J., & Scherer, M. M. (2014). Fe(II)-Catalyzed Recrystallization of Goethite Revisited. *Environmental Science & Technology*, *48*(19), 11302–11311. https://doi.org/10.1021/es503084u

70. Reddy, T. R., Frierdich, A. J., Beard, B. L., & Johnson, C. M. (2015). The effect of pH on stable iron isotope exchange and fractionation between aqueous Fe(II) and goethite. *Chemical Geology*, *397*, 118–127. https://doi.org/10.1016/j.chemgeo.2015.01.018

71. Dyar, M. D., Schaefer, M. W., Sklute, E. C., & Bishop, J. L. (2008). Mössbauer spectroscopy of phyllosilicates: Effects of fitting models on recoil-free fractions and redox ratios. *Clay Minerals*, *43*(1), 3–33. https://doi.org/10.1180/claymin.2008.043.1.02

72. Murad, E., & Cashion, J. (2011). Mössbauer Spectroscopy of Environmental Materials and Their Industrial Utilization. Springer.

73. Williams, A. G. B., & Scherer, M. M. (2004). Spectroscopic Evidence for Fe(II)−Fe(III) Electron Transfer at the Iron Oxide−Water Interface. *Environmental Science & Technology*, *38*(18), 4782–4790. https://doi.org/10.1021/es049373g

74. Schwertmann, U., Wagner, F., & Knicker, H. (2005). Ferrihydrite–Humic Associations. *Soil Science Society of America Journal*, *69*(4), 1009–1015. https://doi.org/10.2136/sssaj2004.0274

75. Rancourt, D. G., Christie, I. A. D., Lamarche, G., Swainson, I., & Flandrois, S. (1994). Magnetism of synthetic and natural annite mica: Ground state and nature of excitations in an exchange-wise two-dimensional easy-plane ferromagnet with disorder. *Journal of Magnetism and Magnetic Materials*, *138*(1–2), 31–44. https://doi.org/10.1016/0304-8853(94)90396-4

76. Ribeiro, F. R., Fabris, J. D., Kostka, J. E., Komadel, P., & Stucki, J. W. (2009). Comparisons of structural iron reduction in smectites by bacteria and dithionite: II. A variable-temperature Mössbauer spectroscopic study of Garfield nontronite. *Pure and Applied Chemistry*, *81*(8), 1499–1509. https://doi.org/10.1351/PAC-CON-08-11-16

77. Rothwell, K. A., Pentrak, M. P., Pentrak, L. A., Stucki, J. W., & Neumann, A. (2023). Reduction Pathway-Dependent Formation of Reactive Fe(II) Sites in Clay Minerals. *Environmental Science & Technology*, *57*(28), 10231–10241. https://doi.org/10.1021/acs.est.3c01655

78. Byrne, J. M., & Kappler, A. (2022). A revised analysis of ferrihydrite at liquid helium temperature using Mössbauer spectroscopy. *American Mineralogist*, *107*(8), 1643–1651. https://doi.org/10.2138/am-2021-7802

79. Cornell, R. M., & Schwertmann, U. (2003). *The iron oxides* (2., completely rev. and extended ed.). Wiley-VCH. https://doi.org/10.1002/3527602097

80. Blodau, C., & Deppe, M. (2012). Humic acid addition lowers methane release in peats of the Mer Bleue bog, Canada. *Soil Biology and Biochemistry*, *52*, 96–98. https://doi.org/10.1016/j.soilbio.2012.04.023

81. Ye, R., Keller, J. K., Jin, Q., Bohannan, B. J. M., & Bridgham, S. D. (2016). Peatland types influence the inhibitory effects of a humic substance analog on methane production. *Geoderma*, *265*, 131–140. https://doi.org/10.1016/j.geoderma.2015.11.026

82. Cervantes, F. J., Velde, S., Lettinga, G., & Field, J. A. (2000). Competition between methanogenesis and quinone respiration for ecologically important substrates in anaerobic consortia. *FEMS Microbiology Ecology*, *34*(2), 161–171. https://doi.org/10.1111/j.1574-6941.2000.tb00766.x

83. Heitmann, T., Goldhammer, T., Beer, J., & Blodau, C. (2007). Electron transfer of dissolved organic matter and its potential significance for anaerobic respiration in a northern bog. *Global Change Biology*, *13*(8), 1771–1785. https://doi.org/10.1111/j.1365-2486.2007.01382.x

84. Valenzuela, E. I., Prieto-Davó, A., López-Lozano, N. E., Hernández-Eligio, A., Vega-Alvarado, L., Juárez, K., García-González, A. S., López, M. G., & Cervantes, F. J. (2017). Anaerobic Methane Oxidation Driven by Microbial Reduction of Natural Organic Matter in a Tropical Wetland. *Applied and Environmental Microbiology*, *83*(11), e00645-17. https://doi.org/10.1128/AEM.00645-17

85. Valenzuela, E. I., Avendaño, K. A., Balagurusamy, N., Arriaga, S., Nieto-Delgado, C., Thalasso, F., & Cervantes, F. J. (2019). Electron shuttling mediated by humic substances fuels anaerobic methane oxidation and carbon burial in wetland sediments. *Science of The Total Environment*, *650*, 2674–2684. https://doi.org/10.1016/j.scitotenv.2018.09.388

86. Küsel, K., Blöthe, M., Schulz, D., Reiche, M., & Drake, H. L. (2008). Microbial reduction of iron and porewater biogeochemistry in acidic peatlands. *Biogeosciences*, *5*(6), 1537–1549. https://doi.org/10.5194/bg-5-1537-2008

87. Lipson, D. A., Raab, T. K., Goria, D., & Zlamal, J. (2013). The contribution of Fe(III) and humic acid reduction to ecosystem respiration in drained thaw lake basins of the Arctic Coastal Plain. *Global Biogeochemical Cycles*, *27*(2), 399–409. https://doi.org/10.1002/gbc.20038

88. Kurth, J. M., Op Den Camp, H. J. M., & Welte, C. U. (2020). Several ways one goal—Methanogenesis from unconventional substrates. *Applied Microbiology and Biotechnology*, *104*(16), 6839–6854. https://doi.org/10.1007/s00253-020-10724-7

89. Coates, J. D., Phillips, E. J., Lonergan, D. J., Jenter, H., & Lovley, D. R. (1996). Isolation of Geobacter species from diverse sedimentary environments. *Applied and Environmental Microbiology*, *62*(5), 1531–1536. https://doi.org/10.1128/aem.62.5.1531-1536.1996

90. Coates, J. D., Ellis, D. J., Gaw, C. V., & Lovley, D. R. (1999). Geothrix fermentans gen. Nov., sp. Nov., a novel Fe(III)-reducing bacterium from a hydrocarbon-contaminated aquifer. *International Journal of Systematic and Evolutionary Microbiology*, *49*(4), 1615–1622. https://doi.org/10.1099/00207713-49-4-1615

91. Finneran, K. T. (2003). Rhodoferax ferrireducens sp. Nov., a psychrotolerant, facultatively anaerobic bacterium that oxidizes acetate with the reduction of Fe(III). *INTERNATIONAL JOURNAL OF SYSTEMATIC AND EVOLUTIONARY MICROBIOLOGY*, *53*(3), 669–673. https://doi.org/10.1099/ijs.0.02298-0

92. Graef, C., Hestnes, A. G., Svenning, M. M., & Frenzel, P. (2011). The active methanotrophic community in a wetland from the High Arctic. *Environmental Microbiology Reports*, *3*(4), 466–472. https://doi.org/10.1111/j.1758-2229.2010.00237.x

93. Martinez-Cruz, K., Leewis, M.-C., Herriott, I. C., Sepulveda-Jauregui, A., Anthony, K. W., Thalasso, F., & Leigh, M. B. (2017). Anaerobic oxidation of methane by aerobic

methanotrophs in sub-Arctic lake sediments. *Science of The Total Environment*, *607–608*, 23–31. https://doi.org/10.1016/j.scitotenv.2017.06.187

94. Yang, S., Anthony, S. E., Jenrich, M., in 't Zandt, M. H., Strauss, J., Overduin, P. P., Grosse, G., Angelopoulos, M., Biskaborn, B. K., Grigoriev, M. N., Wagner, D., Knoblauch, C., Jaeschke, A., Rethemeyer, J., Kallmeyer, J., & Liebner, S. (2023). Microbial methane cycling in sediments of Arctic thermokarst lagoons. *Global Change Biology*, *29*(10), 2714–2731. https://doi.org/10.1111/gcb.16649

95. Kalyuzhnaya, M. G., Yang, S., Rozova, O. N., Smalley, N. E., Clubb, J., Lamb, A., Gowda, G. A. N., Raftery, D., Fu, Y., Bringel, F., Vuilleumier, S., Beck, D. A. C., Trotsenko, Y. A., Khmelenina, V. N., & Lidstrom, M. E. (2013). Highly efficient methane biocatalysis revealed in a methanotrophic bacterium. *Nature Communications*, *4*(1), 2785. https://doi.org/10.1038/ncomms3785

96. Van Grinsven, S., Sinninghe Damsté, J. S., Abdala Asbun, A., Engelmann, J. C., Harrison, J., & Villanueva, L. (2020). Methane oxidation in anoxic lake water stimulated by nitrate and sulfate addition. *Environmental Microbiology*, *22*(2), 766–782. https://doi.org/10.1111/1462-2920.14886

97. Versantvoort, W., Guerrero-Cruz, S., Speth, D. R., Frank, J., Gambelli, L., Cremers, G., Van Alen, T., Jetten, M. S. M., Kartal, B., Op Den Camp, H. J. M., & Reimann, J. (2018). Comparative Genomics of Candidatus Methylomirabilis Species and Description of Ca. Methylomirabilis Lanthanidiphila. *Frontiers in Microbiology*, *9*, 1672. https://doi.org/10.3389/fmicb.2018.01672

98. Ettwig, K. F., Butler, M. K., Le Paslier, D., Pelletier, E., Mangenot, S., Kuypers, M. M. M., Schreiber, F., Dutilh, B. E., Zedelius, J., De Beer, D., Gloerich, J., Wessels, H. J. C. T., Van Alen, T., Luesken, F., Wu, M. L., Van De Pas-Schoonen, K. T., Op Den Camp, H. J. M., Janssen-Megens, E. M., Francoijs, K.-J., … Strous, M. (2010). Nitrite-driven anaerobic methane oxidation by oxygenic bacteria. *Nature*, *464*(7288), 543–548. https://doi.org/10.1038/nature08883

99. Rissanen, A. J., Saarela, T., Jäntti, H., Buck, M., Peura, S., Aalto, S. L., Ojala, A., Pumpanen, J., Tiirola, M., Elvert, M., & Nykänen, H. (2021). Vertical stratification patterns of methanotrophs and their genetic controllers in water columns of oxygen-stratified boreal lakes. *FEMS Microbiology Ecology*, *97*(2), fiaa252. https://doi.org/10.1093/femsec/fiaa252

100. Ellenbogen, J. B., Borton, M. A., McGivern, B. B., Cronin, D. R., Hoyt, D. W., Freire-Zapata, V., McCalley, C. K., Varner, R. K., Crill, P. M., Wehr, R. A., Chanton, J. P., Woodcroft, B. J., Tfaily, M. M., Tyson, G. W., Rich, V. I., & Wrighton, K. C. (2024). Methylotrophy in the Mire: Direct and indirect routes for methane production in thawing permafrost. *mSystems*, *9*(1), e00698-23. https://doi.org/10.1128/msystems.00698-23

101. Söllinger, A., & Urich, T. (2019). Methylotrophic methanogens everywhere—Physiology and ecology of novel players in global methane cycling. *Biochemical Society Transactions*, *47*(6), 1895–1907. https://doi.org/10.1042/BST20180565

102. Meng, X., Cao, Q., Sun, Y., Huang, S., Liu, X., & Li, D. (2022). 16S rRNA genes- and metagenome-based confirmation of syntrophic butyrate-oxidizing methanogenesis enriched in high butyrate loading. *Bioresource Technology*, *345*, 126483. https://doi.org/10.1016/j.biortech.2021.126483

103. Lehours, A.-C., Rabiet, M., Morel-Desrosiers, N., Morel, J.-P., Jouve, L., Arbeille, B., Mailhot, G., & Fonty, G. (2010). Ferric Iron Reduction by Fermentative Strain BS2 Isolated From an Iron-Rich Anoxic Environment (Lake Pavin, France). *Geomicrobiology Journal*, *27*(8), 714–722. https://doi.org/10.1080/01490451003597663

104. List, C., Hosseini, Z., Lederballe Meibom, K., Hatzimanikatis, V., & Bernier-Latmani, R. (2019). Impact of iron reduction on the metabolism of *Clostridium acetobutylicum*. *Environmental Microbiology*, *21*(10), 3548–3563. https://doi.org/10.1111/1462-2920.14640

105. Lovley, D. R., Holmes, D. E., & Nevin, K. P. (2004). Dissimilatory Fe(III) and Mn(IV) reduction. In *Advances in microbial physiology* (S. 212–286).

106. Blume-Werry, G., Milbau, A., Teuber, L. M., Johansson, M., & Dorrepaal, E. (2019). Dwelling in the deep – strongly increased root growth and rooting depth enhance plant interactions with thawing permafrost soil. *New Phytologist*, *223*(3), 1328–1339. https://doi.org/10.1111/nph.15903

107. Wild, B., Gentsch, N., Čapek, P., Diáková, K., Alves, R. J. E., Bárta, J., Gittel, A., Hugelius, G., Knoltsch, A., Kuhry, P., Lashchinskiy, N., Mikutta, R., Palmtag, J., Schleper, C., Schnecker, J., Shibistova, O., Takriti, M., Torsvik, V. L., Urich, T., … Richter, A. (2016). Plant-derived compounds stimulate the decomposition of organic matter in arctic permafrost soils. *Scientific Reports*, *6*(1), 25607. https://doi.org/10.1038/srep25607

108. Guo, Y. D., Song, C. C., Wan, Z. M., Lu, Y. Z., Qiao, T. H., Tan, W. W., & Wang, L. L. (2015). Dynamics of dissolved organic carbon release from a permafrost wetland catchment in northeast China. *Journal of Hydrology*, *531*, 919–928. https://doi.org/10.1016/j.jhydrol.2015.10.008

109. Olefeldt, D., & Roulet, N. T. (2012). Effects of permafrost and hydrology on the composition and transport of dissolved organic carbon in a subarctic peatland complex. *Journal of Geophysical Research: Biogeosciences*, *117*(G1), 2011JG001819. https://doi.org/10.1029/2011JG001819

110. Mangelsdorf, K., Finsel, E., Liebner, S., & Wagner, D. (2009). Temperature adaptation of microbial communities in different horizons of Siberian permafrost-affected soils from the Lena Delta. *Geochemistry*, *69*(2), 169–182. https://doi.org/10.1016/j.chemer.2009.02.001

111. Rivkina, E. M., Fedorov-Davydov, D. G., Zakharyuk, A. G., Shcherbakova, V. A., & Vishnivetskaya, T. A. (2020). Free Iron and Iron-Reducing Microorganisms in Permafrost and Permafrost-Affected Soils of Northeastern Siberia. *Eurasian Soil Science*, *53*(10), 1455–1468. https://doi.org/10.1134/S1064229320100166

112. Algesten, G., Sobek, S., Bergström, A.-K., Jonsson, A., Tranvik, L. J., & Jansson, M. (2005). Contribution of Sediment Respiration to Summer CO2 Emission from Low Productive Boreal and Subarctic Lakes. *Microbial Ecology*, *50*(4), 529–535. https://doi.org/10.1007/s00248-005-5007-x

113. Turetsky, M. R., Abbott, B. W., Jones, M. C., Anthony, K. W., Olefeldt, D., Schuur, E. A. G., Grosse, G., Kuhry, P., Hugelius, G., Koven, C., Lawrence, D. M., Gibson, C., Sannel, A. B. K., & McGuire, A. D. (2020). Carbon release through abrupt permafrost thaw. *Nature Geoscience*, *13*(2), 138–143. https://doi.org/10.1038/s41561-019-0526-0

114. Emerson, D., Scott, J. J., Benes, J., & Bowden, W. B. (2015). Microbial Iron Oxidation in the Arctic Tundra and Its Implications for Biogeochemical Cycling. *Applied and Environmental Microbiology*, *81*(23), 8066–8075. https://doi.org/10.1128/AEM.02832-15

115. Raiswell, R., Canfield, D. E., & Berner, R. A. (1994). A comparison of iron extraction methods for the determination of degree of pyritisation and the recognition of iron-limited pyrite formation. *Chemical Geology*, *111*(1–4), 101–110. https://doi.org/10.1016/0009-2541(94)90084-1

116. Hahn-Weinheimer, P., Hirner, A., & Weber-Diefenbach, K. (1984). *Grundlagen und praktische Anwendung der Röntgenfluoreszenzanalyse (RFA)*. Vieweg+Teubner Verlag. https://doi.org/10.1007/978-3-663-14098-6

117. Chen, C., Dynes, J. J., Wang, J., & Sparks, D. L. (2014). Properties of Fe-organic matter associations via coprecipitation versus adsorption. *Environmental science & technology*, *48*(23), 13751–13759. https://doi.org/10.1021/es503669u

118. Minh, D. D., Macdonald, B., Warneke, S., & White, I. (2018). Fluxes of greenhouse gases from incubated soils using different lid-closure times. *Soil Research*, *56*(1), 39. https://doi.org/10.1071/SR17050

119. Notini, L., Schulz, K., Kubeneck, L. J., Grigg, A. R. C., Rothwell, K. A., Fantappiè, G., ThomasArrigo, L. K., & Kretzschmar, R. (2023). A New Approach for Investigating Iron Mineral Transformations in Soils and Sediments Using [57] Fe-Labeled Minerals and [57] Fe Mössbauer Spectroscopy. *Environmental Science & Technology*, *57*(27), 10008–10018. https://doi.org/10.1021/acs.est.3c00434

120. Lagarec, K., & Rancourt, D. G. (1997). Extended Voigt-based analytic lineshape method for determining N-dimensional correlated hyperfine parameter distributions in Mössbauer spectroscopy. *Nuclear Instruments and Methods in Physics Research Section B: Beam Interactions with Materials and Atoms*, *129*(2), 266–280. https://doi.org/10.1016/s0168-583x(97)00284-x

121. Blaes, N., Fischer, H., & Gonser, U. (1985). Analytical expression for the Mössbauer line shape of 57Fe in the presence of mixed hyperfine interactions. *Nuclear Instruments and Methods in Physics Research Section B: Beam Interactions with Materials and Atoms*, *9*(2), 201–208. https://doi.org/10.1016/0168-583X(85)90683-4

122. Ravel, B., & Newville, M. (2005). ATHENA and ARTEMIS Interactive Graphical Data Analysisusing IFEFFIT. *Physica Scripta*, *2005*(T115), 1007. https://doi.org/10.1238/Physica.Topical.115a01007

123. Frommer, J., Voegelin, A., Dittmar, J., Marcus, M. A., & Kretzschmar, R. (2011). Biogeochemical processes and arsenic enrichment around rice roots in paddy soil: Results from micro-focused X-ray spectroscopy. *European Journal of Soil Science*, *62*(2), 305–317. https://doi.org/10.1111/j.1365-2389.2010.01328.x

124. Martin, M. (2011). Cutadapt removes adapter sequences from high-throughput sequencing reads. *EMBnet.journal*, *17*(1), 10. https://doi.org/10.14806/ej.17.1.200

125. Callahan, B. J., McMurdie, P. J., Rosen, M. J., Han, A. W., Johnson, A. J. A., & Holmes, S. P. (2016). DADA2: High-resolution sample inference from Illumina amplicon data. *Nature Methods*, *13*(7), 581–583. https://doi.org/10.1038/nmeth.3869

126. Quast, C., Pruesse, E., Yilmaz, P., Gerken, J., Schweer, T., Yarza, P., Peplies, J., & Glöckner, F. O. (2012). The SILVA ribosomal RNA gene database project: Improved data processing and web-based tools. *Nucleic Acids Research*, *41*(D1), D590–D596. https://doi.org/10.1093/nar/gks1219

127. Bolyen, E., Rideout, J. R., Dillon, M. R., Bokulich, N. A., Abnet, C. C., Al-Ghalith, G. A., Alexander, H., Alm, E. J., Arumugam, M., Asnicar, F., Bai, Y., Bisanz, J. E., Bittinger, K., Brejnrod, A., Brislawn, C. J., Brown, C. T., Callahan, B. J., Caraballo-Rodríguez, A. M., Chase, J., … Caporaso, J. G. (2019). Reproducible, interactive, scalable and extensible microbiome data science using QIIME 2. *Nature Biotechnology*, *37*(8), 852–857. https://doi.org/10.1038/s41587-019-0209-9

128. Taylor, P. D. P., Maeck, R., & De Bièvre, P. (1992). Determination of the absolute isotopic composition and Atomic Weight of a reference sample of natural iron. *International Journal of Mass Spectrometry and Ion Processes*, *121*(1–2), 111–125. https://doi.org/10.1016/0168-1176(92)80075-C

129. Chen, C., Dong, Y., & Thompson, A. (2023). Electron Transfer, Atom Exchange, and Transformation of Iron Minerals in Soils: The Influence of Soil Organic Matter. *Environmental Science & Technology*, *57*(29), 10696–10707. https://doi.org/10.1021/acs.est.3c01876

130. Kihara, K. (1990). An X-ray study of the temperature dependence of the quartz structure. *European Journal of Mineralogy*, *2*(1), 63–77.

131. Gualtieri, A. F. (2000). Accuracy of XRPD QPA using the combined Rietveld–RIR method. *Journal of Applied Crystallography*, *33*(2), 267–278. https://doi.org/10.1107/S002188989901643X

132. Guha, R., Nag, D. K., & Iyengar, S. V. P. (1987). Structure of an amphibole from Simlipal granite, India. *Indian Minerals*.

133. Rouse, R. C., & Peacor, D. R. (1994). Maricopaite, an unusual lead calcium zeolite with an interrupted mordenite-like framework and intrachannel Pb4 tetrahedral clusters. *American Mineralogist*, *79*(1–2), 175–184.

134. Fitz Gerald, J. D., Parise, J. B., & MacKinnon, I. D. R. (1986). Average structure of an An48 plagioclase from the Hogarth Ranges. *American Mineralogist*, *71*(11–12), 1399–1408.

135. Straub, K., Kappler, A., & Schink, B. (2005). Enrichment and Isolation of Ferric-Iron- and Humic-Acid-Reducing Bacteria. In *Methods in Enzymology* (Bd. 397, S. 58–77). Elsevier. https://doi.org/10.1016/S0076-6879(05)97004-3

Supporting Information

Text S1. Methods applied for initial characterization of the mineral soil used for the microcosm experiment

Selective Fe extractions were performed to assess the content and speciation of different Fe pools in the initial soil. For that purpose, a 0.5 M HCl extraction, targeting poorly crystalline Fe(III) (oxyhydr)oxide minerals, adsorbed Fe(II), FeS and partially $FeCO_3$[44,45] and a 6 M HCl extraction, targeting more crystalline phases (goethite, magnetite and partially Fe in phyllosilicates[44,115]) were performed under anoxic conditions in experimental triplicate. The dry soil (300 mg) was added into 1 M HCl-washed 20 mL glass vials in an anoxic glovebox (MBraun Unilab Workstation, 100% N_2 atmosphere) and 14 mL of anoxic extractant solution was added. The vials were closed with butyl rubber stoppers and crimped with aluminum caps. The vials were taken outside of the glovebox and put on a rolling shaker (60 rpm) in the dark for 24 h. The samples were brought back to the glovebox and centrifuged (10,055 rcf, 5 min) after transferring them to 2 mL Eppendorf tubes. Samples were diluted in 1 M HCl (dilution factor: 4 and 50 for 0.5 M and 6 M HCl, respectively) and Fe speciation was measured by the Ferrozine assay[42]. Total Fe contents of the soil were determined by X-ray fluorescence (XRF). Dried soil (105°C, 1.5 g) was mixed with 7.5 g MERCK spectromelt A12 (mixture of 66% Li-tetraborate and 34% Li-metaborate) and melted at 1200°C to fused beads using an Oxiflux system from CBR analytical service[116]. Measurements were done using a Bruker AXS S4 Pioneer XRF device (Rh-tube at 4kW). Soil organic carbon content was quantified in analytical triplicate by elemental analysis (SoliTOC Cube, Elementar, Germany). A soil standard was used for calibration (Soil Standard OAS, Cat No B2152, Elemental Microanalysis Limited).

Text S2. Synthesis of (^{57}Fe-enriched) Fe(III)-OC coprecipitates

The coprecipitates used in the microcosm experiment were prepared from a ^{57}Fe-enriched (10%) $FeCl_3$ solution. Briefly, 100 mg ^{57}Fe(0) metal powder (97.85% ^{57}Fe, Chemgas) was added to 10 mL of 1 M HCl (Merck). The suspension was stirred overnight (300 rpm) at 70°C to facilitate ^{57}Fe(0) dissolution. The resulting ^{57}Fe(II) solution was oxidized by addition of dropwise H_2O_2 (50%, VWR Chemicals) in excess (150 μL) with ice water surrounding the bottle. The solution was stirred for 2 h to ensure complete oxidation, after which the solution was filtered (0.22 μm, PES, Carl Roth). The resulting ^{57}Fe(III) solution was diluted to a concentration of 150 mM and subsequently mixed with an equimolar solution of $^{NA}FeCl_3$ ($FeCl_3x6H_2O$, Sigma-Aldrich) in a ratio of 1:10, to obtain a 10% ^{57}Fe-enriched $Fe(III)Cl_3$ solution.

184

Both ^{NA}Fe- and ^{57}Fe-enriched Fe-OC coprecipitates were synthesized by mixing 1.5 L of WEOM with 20 mL of the respective FeCl$_3$ solution (initial C:Fe ratio=1), similar to Chen et. al (2014)[117]. During addition of the FeCl$_3$, it was taken care that the pH did not drop below pH 3 to avoid precipitation of OC. To keep the ionic strength constant during the synthesis, NaCl solution was added to a final concentration of 3 mM. The pH was raised by adding 100 mM NaOH dropwise until pH 6 under constant stirring (800 rpm). The suspension was left to stand for 2 h, after which the pH was readjusted to pH 6. The suspensions were washed by filling them into pre-soaked dialysis membranes (14 kDa, 43 mm wide, Sigma-Aldrich) in DDI water. The water was exchanged several times until conductivity was < 20 µS cm^{-1}. The washed suspension was centrifuged down and the solids were resuspended in 50 mL DDI water. The pH was adjusted to pH 6 and the solution was bubbled with N$_2$ (99.999%) for 15 min to make it anoxic.

Text S3. Sampling procedure of greenhouse gas fluxes in microcosm experiment

We measured greenhouse gas fluxes at each sampling time point. For that purpose, the rubber stopper of the bottles was pierced with 2 needles with a three-way valve attached to each. The headspace of each bottle was flushed with moistened N$_2$ gas for 10 min. Afterwards, 2 mL of headspace gas was sampled with a 3 mL syringe into a He-flushed 12 mL Exetainer® vial (Labco, UK) while there was still N$_2$ flowing. The outlet valve was then attached to a water trap to release any overpressure in the bottles and the inlet valve was closed. Once the overpressure was released, the outlet valve was closed as well and the flux incubation time started. Two more samples were taken after 30 min and 1 h, from which the gas flux was calculated. The flux incubation time was increased to 90 min after 67 days of the incubation (including the incubation time before Fe-OC coprecipitates were added).

Text S4. Calculation of greenhouse gas flux

The gas fluxes of carbon dioxide (CO$_2$) and methane (CH$_4$) were calculated according to Equation (1), similar to Minh et al. (2018)[118]:

$$R = \Delta c \, \frac{p \times V_{HS}}{R \times T \times m_{soil}} \qquad \text{Eq (1)}$$

where R is the flux (µmol d^{-1} g^{-1} dry soil), Δc is the slope of the measured gas concentrations over time (ppm d^{-1}), p is the pressure (101325 Pa), V_{HS} is the headspace volume in the incubation bottle (m^3), R is the ideal gas constant (8.31 J mol^{-1} K^{-1}), T is the temperature (293 K) and m_{soil} is the mass of dry soil left in the incubation bottle (g dry weight).

The V_{HS} and m_{soil} were adjusted after each sampling, depending on the volume of the sampled suspension and the soil to solution ratio.

The cumulative gas flux was calculated based on a simple interpolation:

$$R_{cum,n} = \Delta t_{n-k} \times \frac{1}{2} \times (R_k + R_n) + R_{cum,k} \qquad \text{Eq (2)}$$

where $R_{cum,n}$ is the cumulative flux at a given timepoint n (µmol g^{-1} dry soil), Δt_{k-n} is the timeframe between timepoint n and the prior timepoint k (d), R_k and R_n are the fluxes at timepoint k and n (µmol d^{-1} g^{-1} dry soil), respectively, and $R_{cum,k}$ is the cumulative flux at timepoint k (µmol g^{-1} dry soil). The first cumulative flux at timepoint 0 was calculated by including a measurement which was done one day prior addition of coprecipitates.

Text S5. Calculation of aqueous and solid (0.5 M HCl extractable) Fe from ^{57}Fe-enriched Fe-OC coprecipitates

To directly determine the reduction of ^{57}Fe-enriched Fe-OC coprecipitates in the microcosms, we calculated the share of aqueous Fe stemming from added coprecipitates based on the isotope signature, as described in Notini et. al (2023)[119]. We know that the fraction of ^{57}Fe to ^{56}Fe+^{57}Fe ($f^{57}Fe_{+cop}$), which is measured by ICP-MS, can also be described as

$$f^{57}Fe_{+cop} = \frac{f^{57}Fe_{Fe-OC} \times f_{Fe-OC} + f^{57}Fe_{soil} \times (100 - f_{Fe-OC})}{100} \qquad \text{Eq (3)}$$

In which $f^{57}Fe_{Fe-OC}$ is the known fraction of ^{57}Fe to ^{56}Fe+^{57}Fe in the labelled coprecipitates (10.47%), $f Fe_{Fe-OC}$ is the fraction of aqueous Fe coming from coprecipitates [%] and $f^{57}Fe_{soil}$ is the measured fraction of ^{57}Fe to ^{56}Fe+^{57}Fe in the no-coprecipitate control setup. By re-arranging for $f Fe_{Fe-OC}$, we get:

$$f_{Fe-OC} = \frac{100 \times (f^{57}Fe_{+cop} - f^{57}Fe_{soil})}{f^{57}Fe_{Fe-OC} - f^{57}Fe_{soil}} \qquad \text{Eq (4)}$$

We then multiply the fraction with the absolute concentration of total aqueous Fe measured by the ferrozine assay (c(Fe$_{aq}$), [mM]) to get the amount of aqueous Fe derived from the reductive dissolution of ^{57}Fe-enriched Fe-OC coprecipitates c_{Fe-OC} [mM], which is displayed in Figure 1b:

$$c_{Fe-OC} = c(Fe_{aq}) \times f_{Fe-OC} \qquad \text{Eq (5)}$$

The contribution of ^{57}Fe-enriched Fe-OC coprecipitates to the 0.5 M HCl-extractable solid Fe pool was calculated in the same way but measured fraction values of the solid extracts were used. The data is displayed in Figure S4.

186

Text S6. Iron speciation analysis by [57]Fe Mössbauer spectroscopy and Fe *K*-edge X-ray absorption spectra collection and data analysis

Mössbauer spectra were taken using a constant acceleration drive system (WissEL) in transmission mode with a [57]Co/Rh source. All spectra were calibrated against an α-[57]Fe foil measured at room temperature. Data analysis was performed using Recoil (University of Ottawa) and the Voigt based fitting routine[120] was used for initial coprecipitates while the Full Static Hamiltonian Site Analysis[121] was used for microcosm samples. This latter fitting routine was necessary to include the Fe(II)-octet component from Fe-bearing phyllosilicate minerals. The half width at half maximum was constrained to 0.116 mm s^{-1} during fitting.

The Fe oxidation state and binding environment of initial synthesized [57]Fe-enriched coprecipitates and initial soil used for the microcosm experiment was analyzed by Fe *K*-edge X-ray absorption spectroscopy (XAS) at SAMBA beamline (SOLEIL). Transmission spectra were recorded at 77 K using a N$_2$(l) cryostat. A Si(220) monochromator was used and calibrated to the first derivative maximum of the *K*-edge absorption of an Fe(0) foil. Harmonic rejection was performed by two Si mirrors coated in Pd. Between 8 and 16 scans per sample were collected in continuous scan mode and merged. The final spectra were used for analysis of Fe *K*-edge X-ray absorption near edge structure (XANES) and extended X-ray absorption fine structure (EXAFS). Data processing included energy calibration, pre-edge subtraction, and post-edge normalization done in Athena[122]. The Fe redox state was estimated by linear combination fitting (LCF) of the XANES region from -20 to +30 eV around the edge energy. References for XANES spectra included ferrihydrite (representative for Fe(III)) and chlorite CCa-2[123] (representative for Fe(II)) for initial coprecipitates. Speciation of Fe was examined by LCF of the k^3-weighted EXAFS region in a *k* range from 2 to 11 Å^{-1}. The edge energy of all samples and references was set to 7128 eV. The following reference compounds were selected for EXAFS analysis: ferrihydrite, Fe(III)-citrate, Fe(III)-catechol, illite IMt-1, chlorite CCa-2, Fe(II)-citrate, Fe(II)-catechol, mackinawite. Components were constrained between 0 and 100% during fitting, but no constraints were set on the sum of components. Initial fractions of detected Fe phases were re-calculated to sum up to 100% and fractions below 5% were excluded. All data processing and analysis were done in Athena software[122].

Text S7. Details of molecular biology analysis

Total DNA and RNA of soil samples from the microcosm experiment were extracted in experimental triplicate using the RNeasy PowerSoil® Total RNA Kit with DNA Elution (Qiagen). The following adjustments were made to the manufacturer's instructions: 1-1.5 g of soil (wet weight) was added to the bead tube; 10 min bead-beating; all centrifugation steps (of 15 mL

tubes) at 7000 rcf at 4°C; incubation time at -20°C for 1.5 h; final pellets were dried on a clean bench and resuspended in 50 µL RNase or DNase-free water. The quality of the extracted RNA and DNA was examined using Nanodrop (NanoDrop 1000, Thermo Scientific, USA) and concentrations were quantified using Qubit® 2.0 Fluorometer with RNA and DNA HS kits (Life Technologies, USA). Remaining DNA in the RNA samples was digested and the RNA was reverse transcribed using commercial kits (Invitrogen, Life Technologies, USA) as described in Otte et al. (2018)[47]. Complete digestion of DNA and transcription of RNA to cDNA was confirmed using agarose gel electrophoresis after polymerase chain reaction (PCR) with primers specific for the 16S rRNA gene of bacteria (341f, 907r).

Library preparation steps (Nextera, Illumina) and sequencing were performed using Illumina MiSeq sequencing system (Illumina, USA) at the Institute for Medical Microbiology and Hygiene of the University of Tübingen. In total 12,854,425 paired-end reads with length 250 bp were obtained for 108 samples, of which 36 samples with 4,707,718 read pairs are discussed here (78,280 to 213,458 read pairs per sample, in average 130,770). Data processing, including quality control, reconstruction of sequences and taxonomic annotation was done using nf-core/ampliseq version 2.8.0[50,51] of the nf-core collection of workflows[52]. Primers were trimmed using Cutadapt v3.4[124] and untrimmed sequences were discarded. Less than 22% of sequences were discarded per sample and 86.6% of sequences passed the filtering on average. Adapter and primer-free sequences were pooled with DADA2 v1.28[125] to eliminate PhiX contamination, trim reads (forward reads at 231 bp and reverse reads at 207 bp), discard reads with >2 expected errors, correct errors, merge read pairs, and remove PCR chimeras. Ultimately, 10,565 amplicon sequencing variants (ASVs) were obtained across all samples. Between 73.2% and 80.2% reads per sample (average 77.6%) were retained. ASVs with length lower than 240 or above 270 bp were removed (76 of 10,565). Taxonomic classification was performed by DADA2 and the database 'Silva 138.1 prokaryotic SSU'[126]. Of 10489 ASVs, 36 ASVs designated as mitochondria or chloroplasts were removed within QIIME2 version 2023.7.[127]. Finally, 10,453 amplicon sequencing variants (ASVs) with between 51,392 and 148,556 counts (average 88,453) per sample were obtained.

Text S8. Quantification of microbial metabolites by gas chromatography coupled to mass spectrometry (GC-MS)

The concentration of metabolites, including small sugars, organic acids, and amino acids (full list in Table S3) were quantified using GC-MS (Shimadzu GC/MS TQ 8040, Japan) operated in Electron Ionisation mode (EI). Metabolites were measured either by headspace injection (MS acquisition mode: Scan) or as a liquid sample after derivatization (MS acquisition

mode: MRM). For derivatization, samples were thawed on ice and 3000 pmol ^{13}C-glucose was added as an internal standard to 250 µL sample prior to freeze-drying. The solids were re-dissolved with 50 µL methoxamine (20 mg mL^{-1} pyridine), ultrasonicated for 10 min and subsequently incubated at 30° C for 90 min. Next, 70 µL N-methyl-N-(trimethylsilyl)-trifluor-acetamid (MSTFA) was added and samples were incubated at 40°C for 60 min, after which they were kept at room temperature for 2 h. A volume of 1 µL was used for injection in splitted mode on a Restek SH-Rxi-5SIL MS column (30 m; film 0.25 µm; diameter 0.25 mm). The injection port was heated to 280°C. For chromatographic separation a He flow rate of 1.1 mL min^{-1} and a temperature increase of 10°C min^{-1} from 100 to 320°C were employed. For the measurement via the headspace method, 250 µL of thawed sample together with 2500 pmol octanol as internal standard were added into glass vials with closed lids. A volume of 1 ml of headspace gas was injected onto the column Stabilwax-DA from Restek. The He flow rate was 1.1 mL min^{-1} and the column temperature increased by 10°C min^{-1} from 40 to 240°C. Concentrations were quantified with a 8-point external calibration containing standards of all targeted analytes, ranging from 20 to max. 10^7 pmol per 250 µL.

Text S9. Design of passive porewater samplers ("peepers")

The passive porewater samplers (25 x 25 x 2 cm, width x height x depth) contained 10 x 1 cm high cells each, spaced 1 cm apart. Each cell had a volume of 12 mL. A membrane (PETE, 8 µm pore size, 30x300 cm roll, Sterlitech, USA) was placed between the inner panel (containing the cells) and the outer panel. Plastic screws were used to tighten all compartments together and prevent leakage. Each cell was connected on both ends to butyl rubber tubing (4 mm inner, 7 mm outer diameter, NBR, Reichelt Chemietechnik, Germany) with a thread-to-tubing adapter (brass, 4mm inner diameter, M5 thread). Butyl rubber tubing was placed inside an additional compartment and led above the peeper cells so that it was accessible while the peeper was placed in the soil. Luer-lock syringes were attached to the butyl rubber tubing via a female luer-thread connector (4 mm inner diameter, polypropylene).

Text S10. Calculation of contribution of ^{57}Fe-enriched Fe(III)-OC coprecipitates to total signal in Mössbauer spectra

The contribution of ^{57}Fe-enriched Fe-OC coprecipitates to the total signal in ^{57}Fe Mössbauer spectra was calculated knowing the absolute total and individual masses of ^{57}Fe in the two pools (from initial soil and coprecipitates):

Soil per bottle (dry weight):	12	g
Fe content in soil:	20.20	mg/g (measured by XRF)
Natural abundance of ^{57}Fe in soil:	2.12	%[128]
^{57}Fe content in soil:	20.2 mg/g * 2.1/100 =	0.42 mg/g
Total ^{57}Fe per bottle initially:	12 g * 0.42 mg/g=	5.09 mg
^{57}Fe abundance in coprecipitate:	10.47	%
Added ^{57}Fe from coprecipitate:	5.22	mg
Total ^{57}Fe per bottle:	5.09 mg + 5.22 mg =	10.31 mg
Share of ^{57}Fe from soil:	5.09 mg/10.31 mg*100% =	49.3 %
Share of ^{57}Fe from coprecipitate:	5.22 mg/10.31 mg*100% =	50.6 %

Text S11. Interpretation of 77 K spectra Mössbauer spectroscopy results

The Mössbauer spectra collected at 77 K give an indication on overall Fe speciation (Figure S11). We found two doublet features with parameters characteristic of (i) adsorbed Fe(II), siderite and/or Fe(II) in phyllosilicates[71–73] and (ii) Fe(III) bound in phyllosilicates or to organic matter and/or in poorly crystalline Fe(III) (oxyhydr)oxides[71,74,79]. The absence of sextet components at 77 K indicates that no higher crystalline Fe minerals (such as goethite, lepidocrocite, magnetite) were present in substantial fractions (>5%). In the soil with added coprecipitates, the Fe(II) and Fe(III) components make up 41% and 59%, respectively. In contrast, the Fe(II) component made up 62% and Fe(III) was equal to 38% in the no-coprecipitate control. The difference in relative fraction of Fe(III) thus reflects the addition of the Fe(III)-OC coprecipitates. The speciation in both setups did not change substantially for the 77 K spectra taken after 42 days of anoxic incubation (Figure S11).
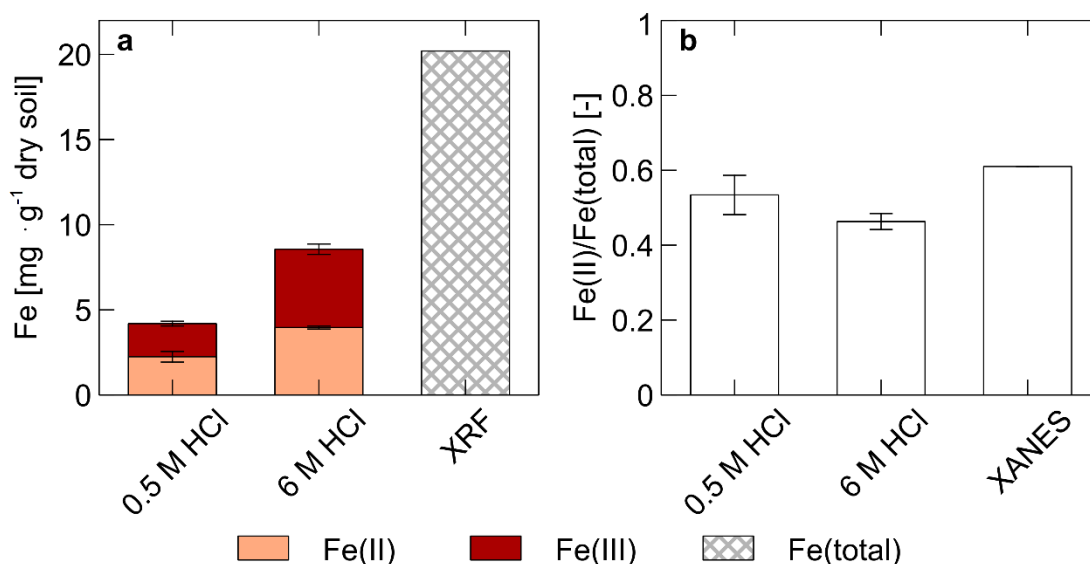
Figure S1. Initial Fe content and speciation of mineral soil from fen used for the microcosm experiment. Fe(II) and Fe(III) contents are displayed based on selective extractions: anoxic 0.5 M HCl extractions (targeting poorly crystalline Fe(III) (oxyhydr)oxides, adsorbed Fe(II), FeS and partially $FeCO_3$[44,45]), anoxic 6 M HCl extractions (targeting more crystalline Fe mineral phases, such as goethite, magnetite and partially Fe in phyllosilicates[44] as well as total Fe content measured by X-ray fluorescence (XRF). Data and error bars show the mean and standard deviation of experimental triplicates in case of HCl-based extractions (a). The Fe(II)/Fe(total) ratio in extracts is compared to the result by linear combination fitting of X-ray absorption near edge structure (XANES), see fitting parameters in Table S6 (b).
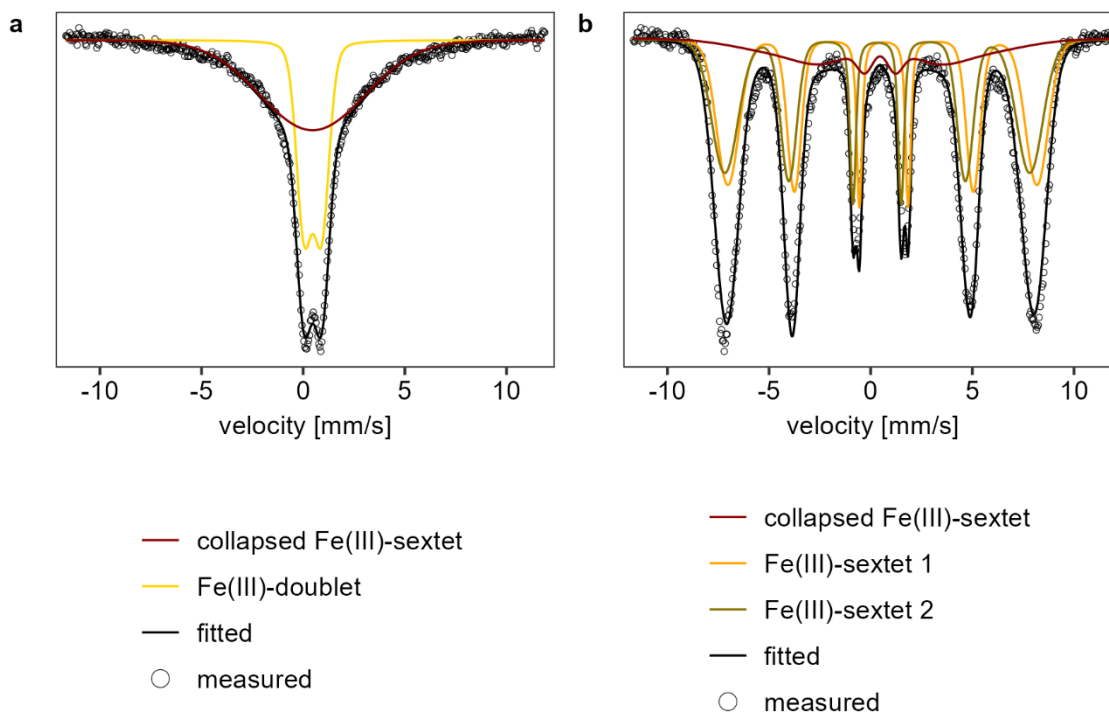
Figure S2. ^{57}Fe Mössbauer spectra of initial ^{57}Fe-enriched Fe-OC coprecipitates collected at 30 K (a) and 6 K (b). Spectra display the measured data (open circles), the fit (black line) and individual components (coloured lines). The following components were assigned at 30 K: Fe(III)-doublet = very poorly crystalline ferrihydrite, collapsed Fe(III)-sextet = poorly crystalline ferrihydrite, near the Neél-temperature. Components at 6 K included: 2 Fe(III)-sextets = very poorly crystalline ferrihydrite, collapsed Fe(III)-sextet = very poorly crystalline Fe(III) (oxyhydr)oxide[129]. Parameters are given in Table S5. Spectra were collected at 30 K to determine whether there is a minor fraction of lepidocrocite in the coprecipitates, which was detected by Fe *K*-edge EXAFS analysis.
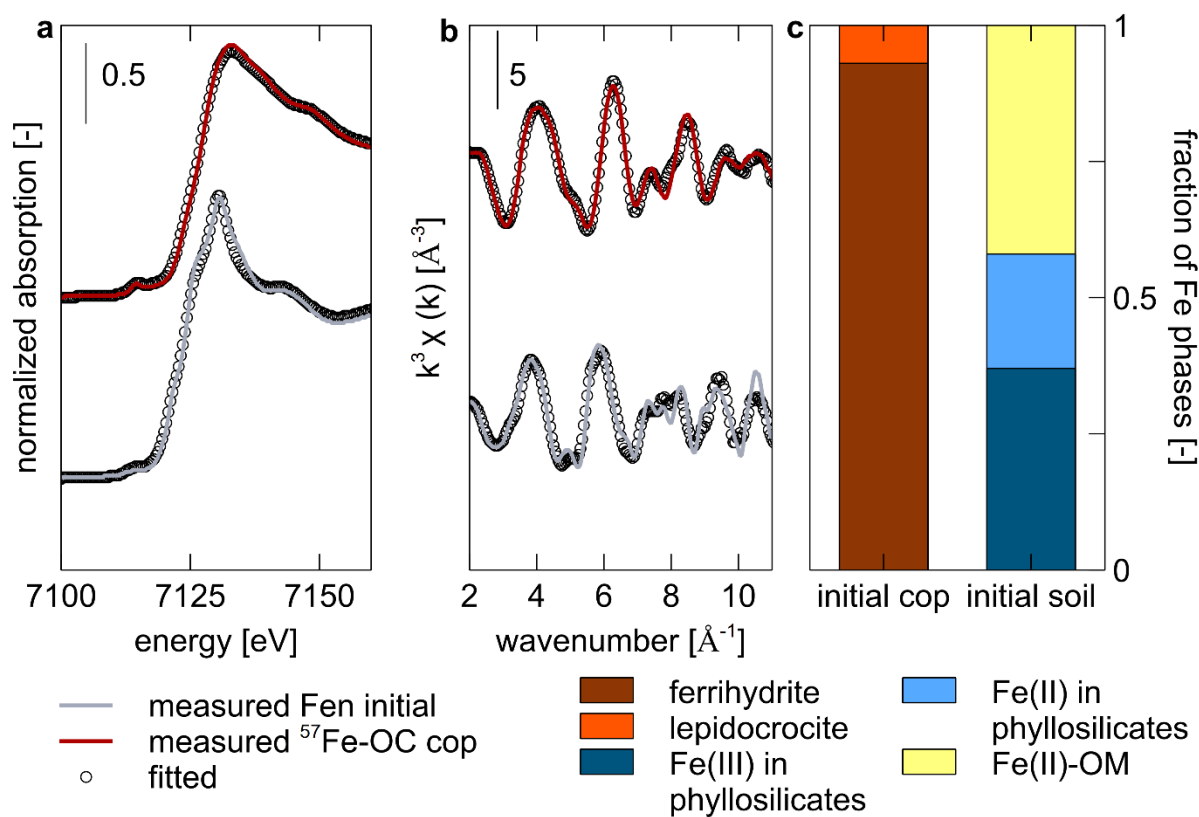
Figure S3. Linear combination fitting results of Fe *K*-edge XANES spectra (a), k^3-weighted Fe *K*-edge EXAFS spectra (b) and the resulting fraction of fitted Fe phases (c) of initial synthesized [57]Fe-enriched Fe-OC coprecipitates (red) and the initial fen mineral soil (grey). The coloured lines show measured data and open circles show the fit. The fitting parameters and resulting Fe speciation are given in Table S6 and Table S7.
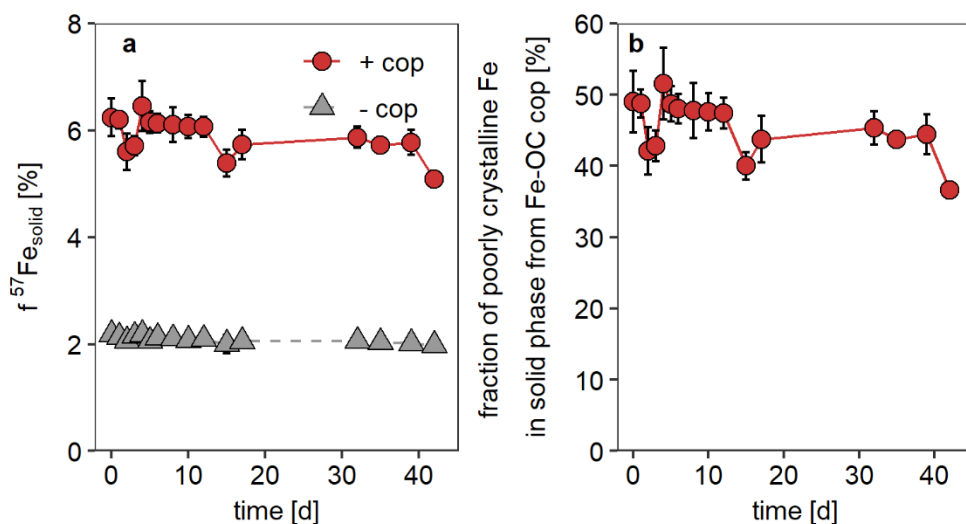
Figure S4. Fraction of ^{57}Fe (^{57}Fe to $^{56}Fe+^{57}Fe$) in solid (0.5 M HCl-extractable) phase of microcosm setups with addition of ^{57}Fe-enriched Fe-OC coprecipitates ("+ cop") and of a no-coprecipitate control ("- cop") over time (a). The percentage of Fe stemming directly from the ^{57}Fe-enriched Fe-OC coprecipitates is displayed over time (b). Data points and error bars show the mean and standard deviation of experimental triplicates.
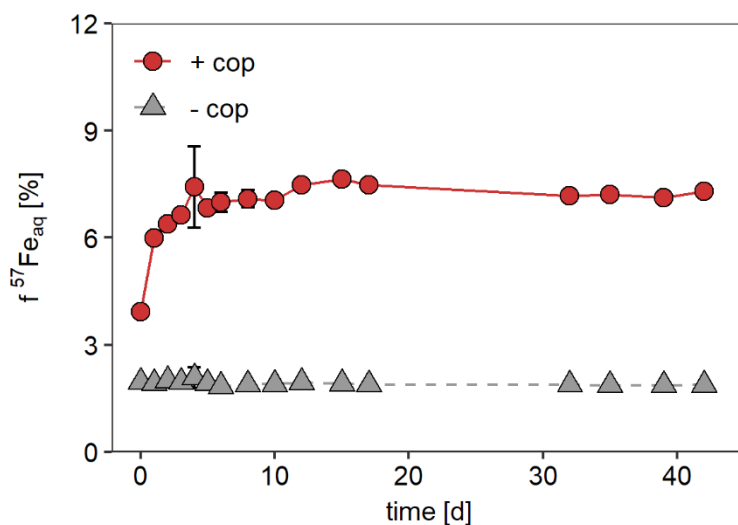
Figure S5. Fraction of ^{57}Fe (^{57}Fe to $^{56}Fe+^{57}Fe$) in aqueous phase of microcosm setups with addition of ^{57}Fe-enriched Fe-OC coprecipitates ("+ cop") and of a no-coprecipitate control ("- cop") over time. Data points and error bars show the mean and standard deviation of experimental triplicates.

194
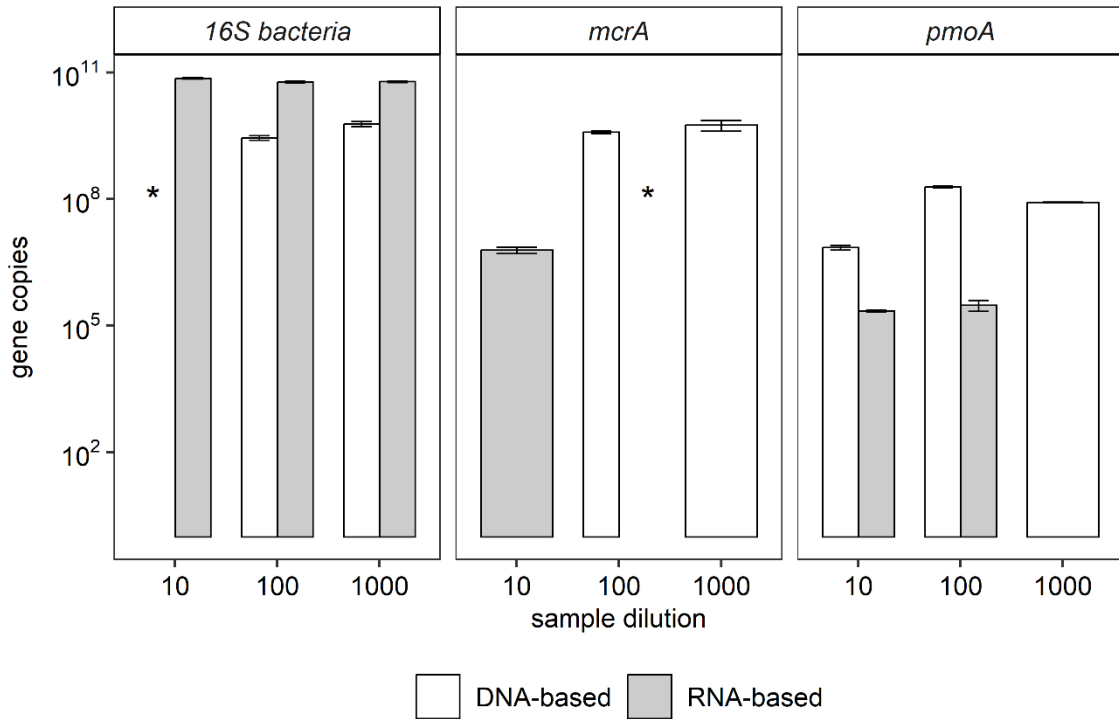
Figure S6. Results of quantitative PCR assays for DNA- and RNA-based bacterial 16S, mcrA and pmoA gene copies using different dilutions (10x, 100x, 1000x) of a representative sample. Asterisks denote measurements for which no amplification was possible (likely due to high concentration of inhibiting compounds or too low abundance of gene copies). If gene copy numbers were comparable between two dilutions, the lower dilution was chosen for the whole assay. Data and error bars show the mean and standard deviation of analytical triplicates.
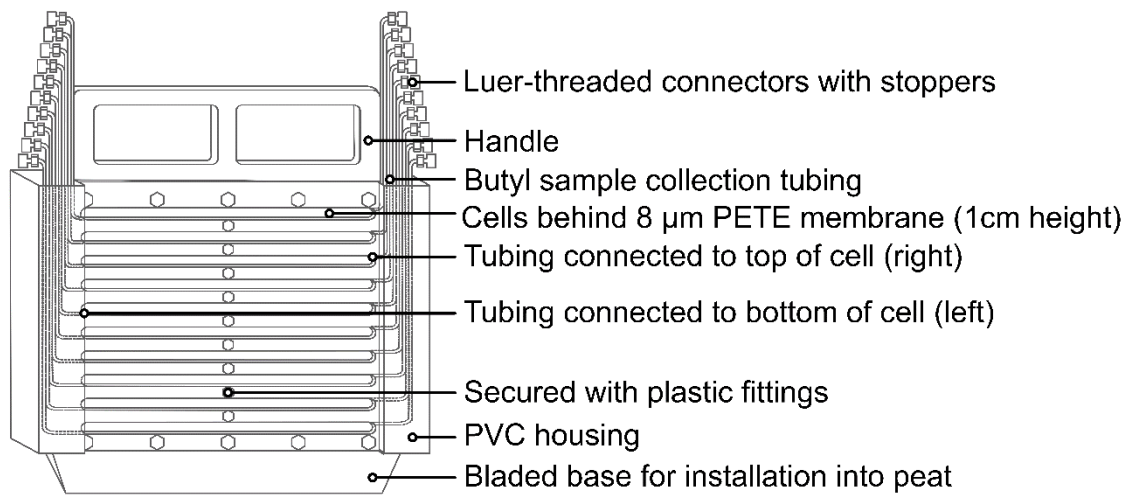
Figure S7. Schematic of passive porewater sampler constructed according to Bowes & Hornibrook (2006)[64] after Hesslein (1976)[65].
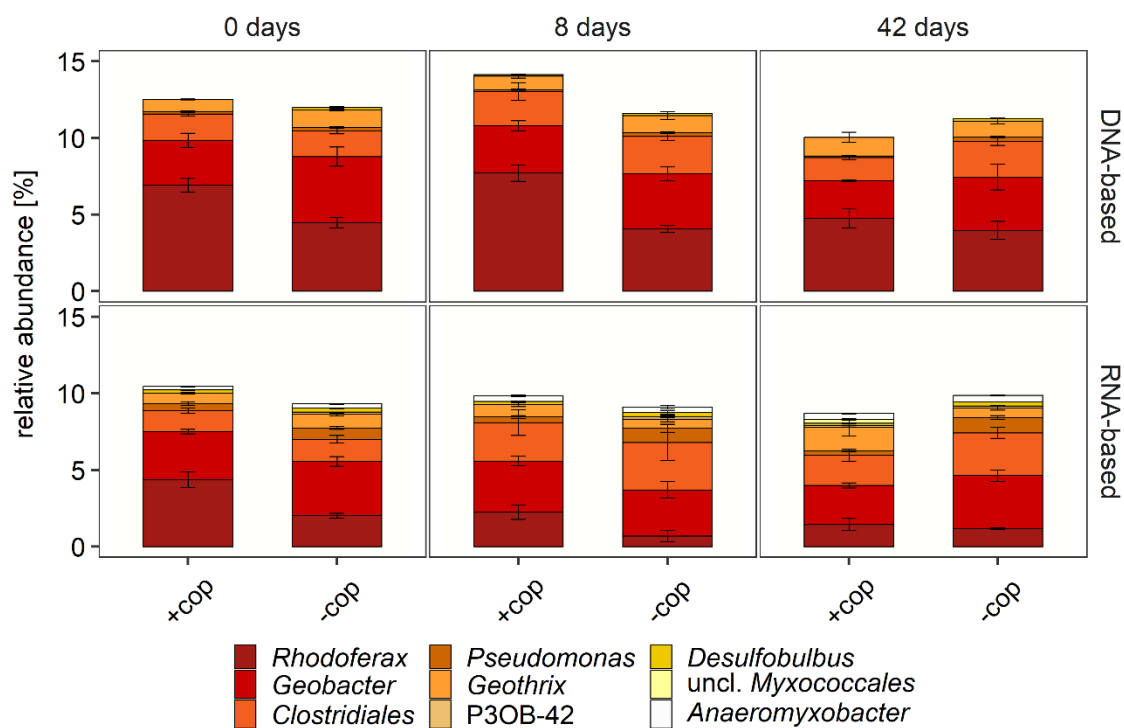
Figure S8. Relative 16S rRNA abundances of present (DNA-based) and likely active (RNA-based) microbial taxa related to Fe(III) reduction per timepoint (0, 8, 42 days) and setup (with added Fe-OC coprecipitates: +cop, no-coprecipitate control: -cop) in the microcosm experiment. Taxa with an abundance lower than 0.1% were not included. Taxa are labelled at the genus-level except for unclassified *Myxococcales*. All data bars and error bars represent the average and standard deviation of experimental triplicates.
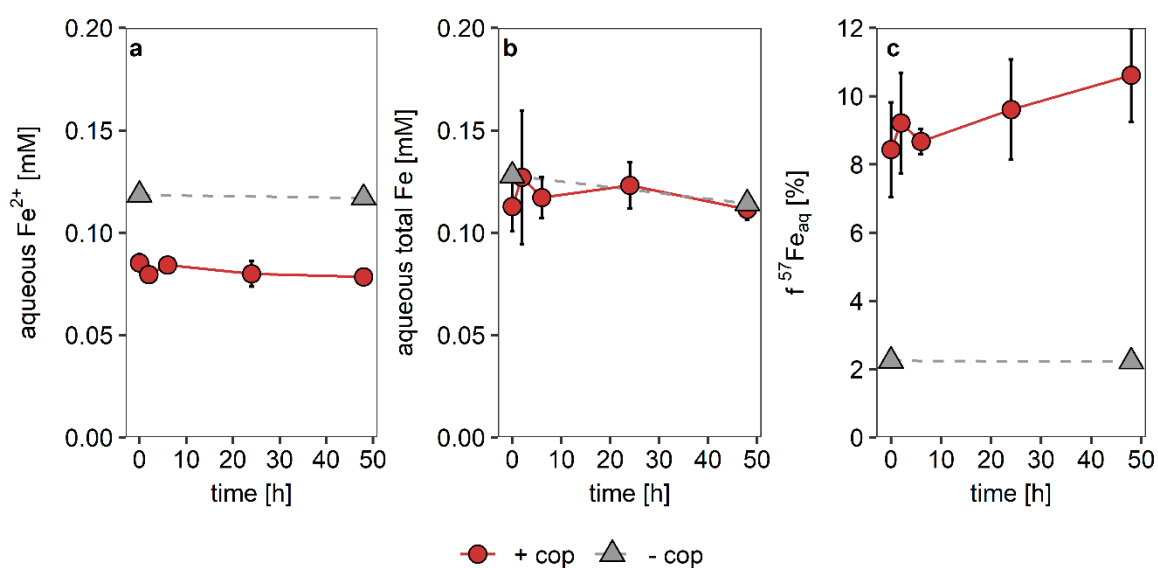
Figure S9. Results of the abiotic control experiment to quantify isotope exchange between the aqueous $^{56}Fe^{2+}$ and the $^{57}Fe(III)$ in the Fe(III)-OC coprecipitates. The concentrations of aqueous Fe^{2+} (a), aqueous total Fe (b) and the fraction of ^{57}Fe (^{57}Fe to $^{56}Fe+^{57}Fe$) in the aqueous phase are displayed over 48 h within a setup of added ^{57}Fe-enriched Fe-OC coprecipitates (+ cop) and only sterile filtered, fen-derived porewater (- cop). Data points and error bars represent the average and standard deviation of experimental triplicates in case of the "+ cop" setup and the average and range of experimental duplicates in case of the "- cop" setup.
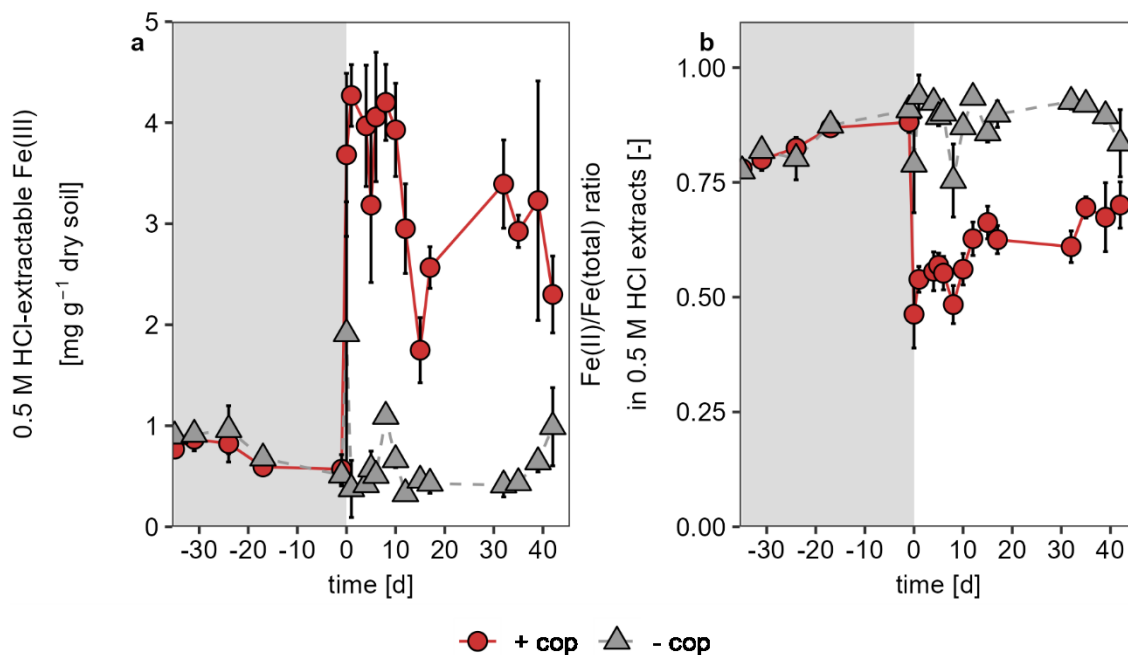
Figure S10. Solid phase (0.5 M HCl-extractable) Fe(III) contents [mg g^{-1} dry soil] in microcosm setups with addition of ^{57}Fe-enriched Fe-OC coprecipitates ("+ cop") and in a no-coprecipitate control ("- cop") over time (a). Fe speciation (Fe(II)/Fe(total) ratio) in 0.5 M HCl extracts is displayed over time for both setups. Data points and error bars show the mean and standard deviation of experimental triplicates. The grey area represents the incubation time before coprecipitates were added.
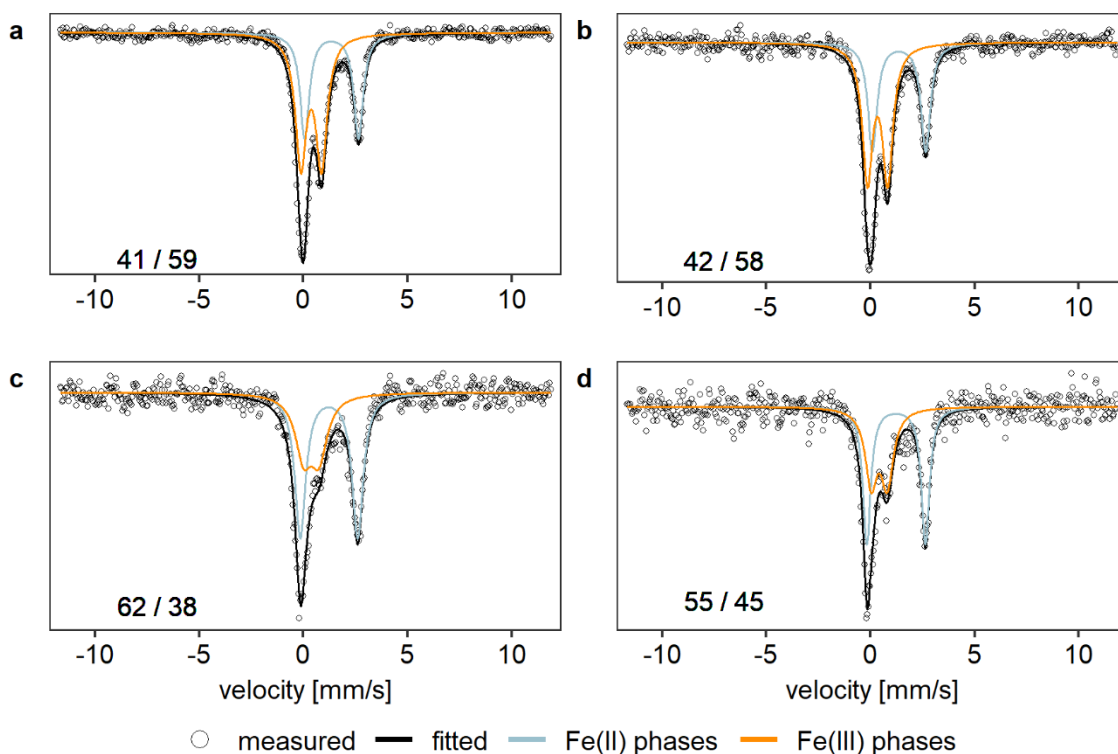
**Figure S11**. Solid-phase Fe speciation of soil in microcosm experiments measured by ^{57}Fe Mössbauer spectroscopy at 77 K. The subplots display spectra of soil with addition of ^{57}Fe-enriched Fe-OC coprecipitates at t0 (a) and after 42 days (b) as well as a no-coprecipitate control at t0 (c) and after 42 days (d). The numbers in the plot stand for the relative fractions of Fe(II) and Fe(III) in %. Spectra display the measured data (open circles), the fit (black line) and individual components (coloured lines) (a-d). The following components were assigned: Fe(II) phases = adsorbed Fe(II) or Fe(II) in phyllosilicates, Fe(III) phases = Fe(III) in phyllosilicates, poorly crystalline Fe(III) oxyhydroxides. Fitting parameters are given in Table S4.
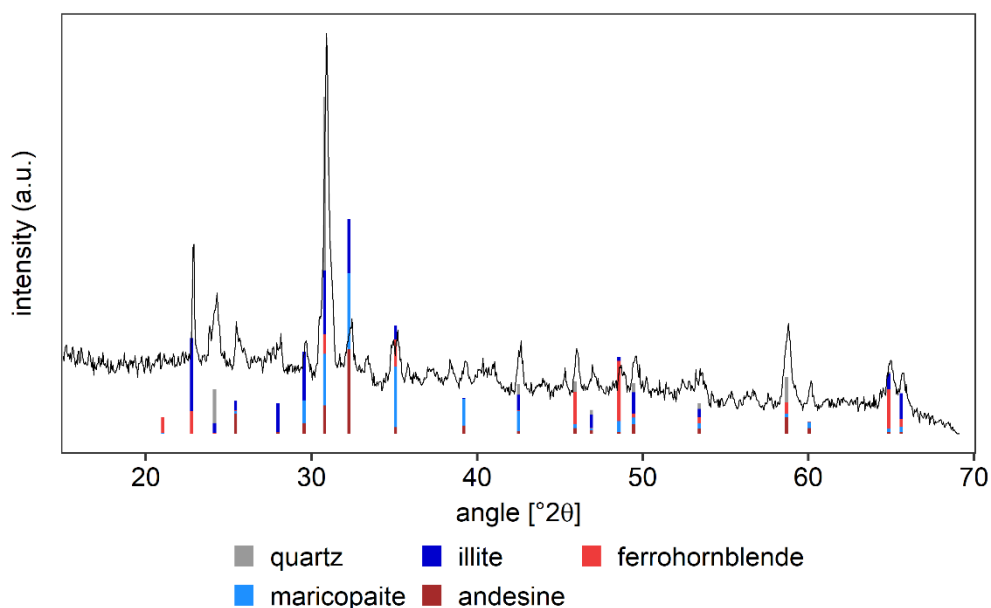
Figure S12. X-ray diffraction (XRD) spectra of initial fen soil, indicated as black lines, with identified reflections as coloured bars. Published structure files of quartz[130], illite[131], ferrohornblende[132], maricopaite[133] and andesine[134] were used.
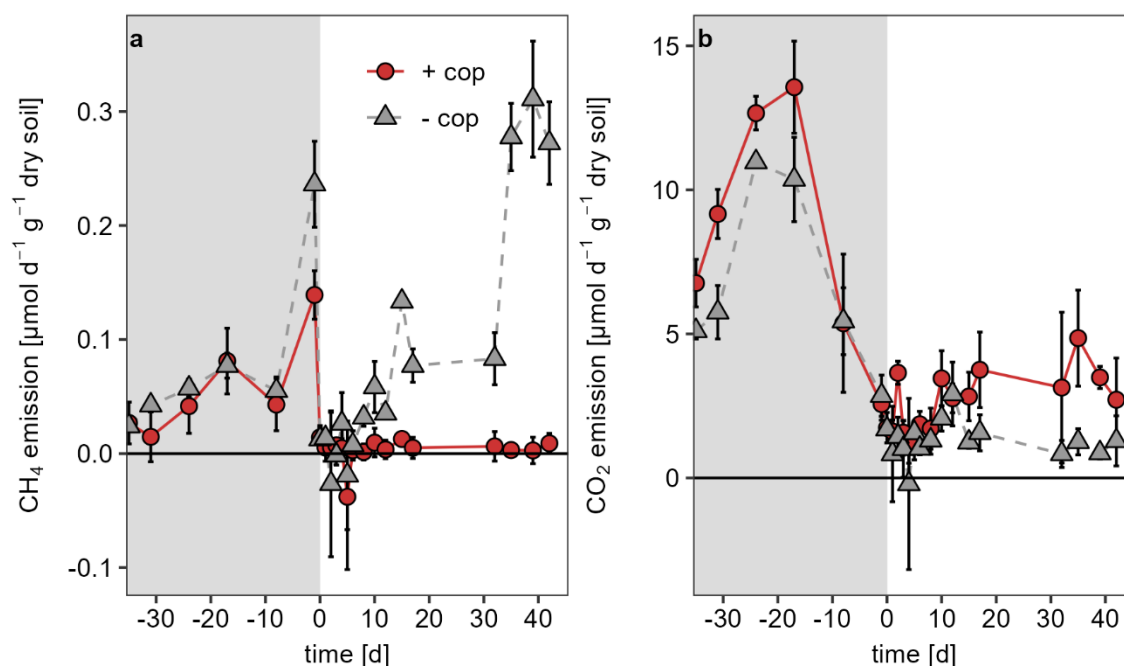
Figure S13. Greenhouse gas fluxes of CH_4 (a) and CO_2 (b) [µmol d^{-1} g^{-1} dry soil] in microcosm setups with addition of ^{57}Fe-enriched Fe-OC coprecipitates ("+ cop") and in a no-coprecipitate control ("- cop") over time. Data points and error bars show the mean and standard deviation of experimental triplicates. The grey area represents the incubation time before coprecipitates were added.
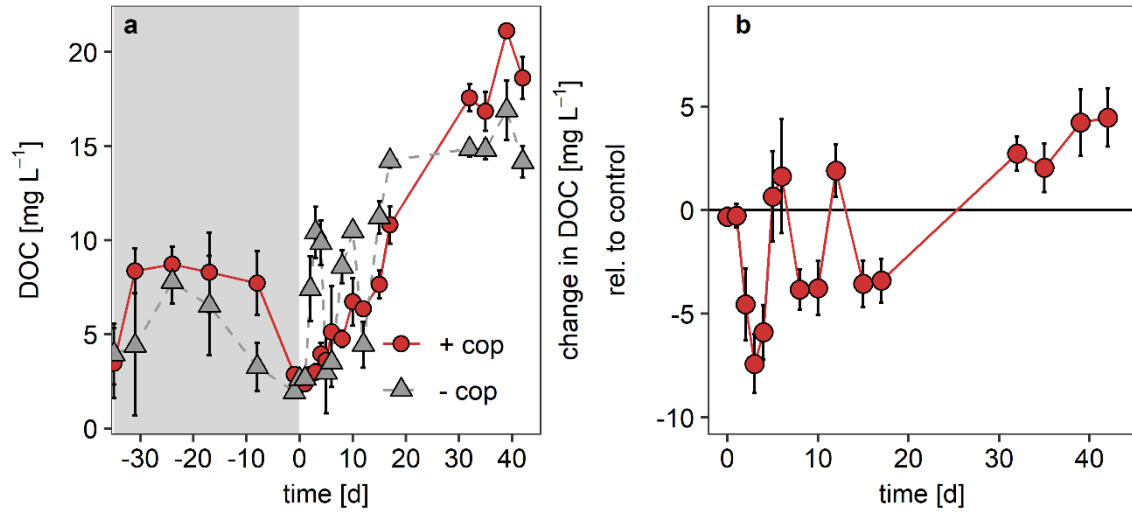
Figure S14. Dissolved organic carbon (DOC) in microcosm setups with addition of ^{57}Fe-enriched Fe-OC coprecipitates ("+ cop") and in a no-coprecipitate control ("- cop") over time. The absolute concentrations in both setups are displayed in (a) and difference of the coprecipitate-added setup to the no-coprecipitate control is shown in (b). Data points and error bars show the mean and standard deviation of experimental triplicates. Errors in (b) were propagated. The grey area represents the incubation time before coprecipitates were added.
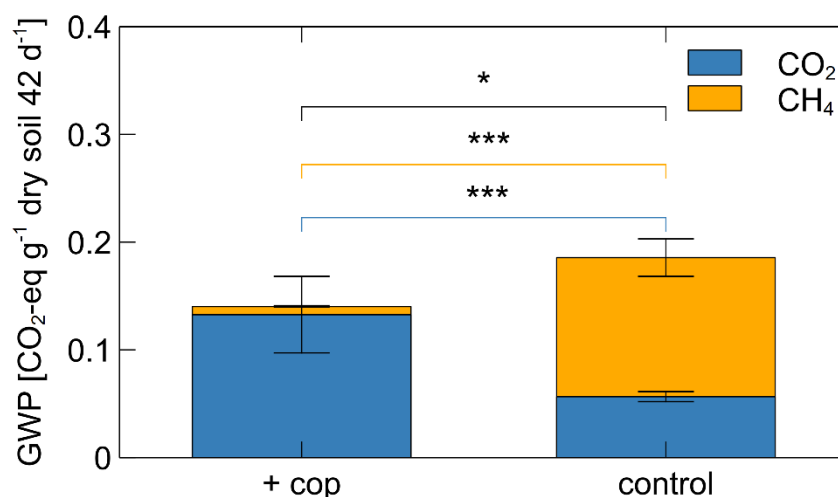
Figure S15. Calculated global warming potential (GWP) using the cumulative CH_4 and CO_2 fluxes in setups with added (^{57}Fe-enriched) Fe-OC coprecipitates ("+ cop") and in no-coprecipitate controls at the end of the microcosm experiment. Symbols above the bars denote the level of significant difference between the two setups for each experiment (one-way ANOVA, Tukey's HSD test): $p > 0.1$ – not significant (ns), $p \leq 0.1$ -*, $p \leq 0.05$ - **, $p \leq 0.001$ - ***. The symbol on top of the black line signifies the difference of the total GWP, the yellow line of the contribution of CH_4 and the blue line of the contribution of CO_2 to the GWP. Data and error bars represent the average and standard deviation of experimental triplicates.
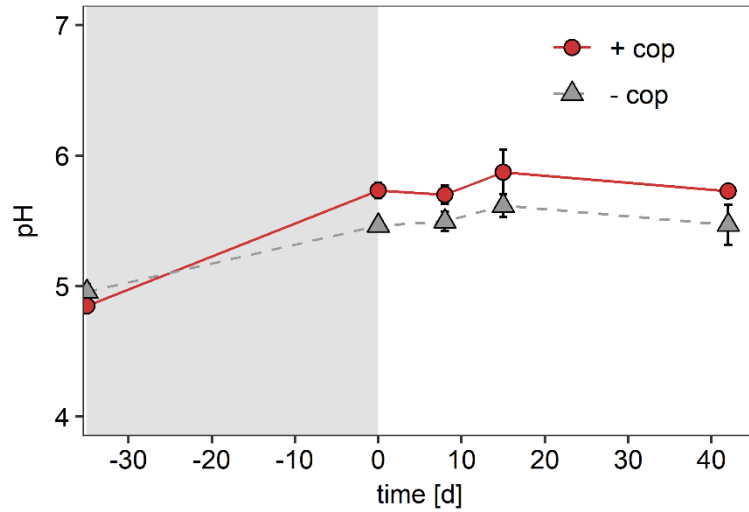
Figure S16. pH in soil microcosm setups with addition of ^{57}Fe-enriched Fe-OC coprecipitates ("+ cop") and in a no-coprecipitate control ("- cop") over time. Data points and error bars show the mean and standard deviation of experimental triplicates. The grey area represents the incubation time before coprecipitates were added.
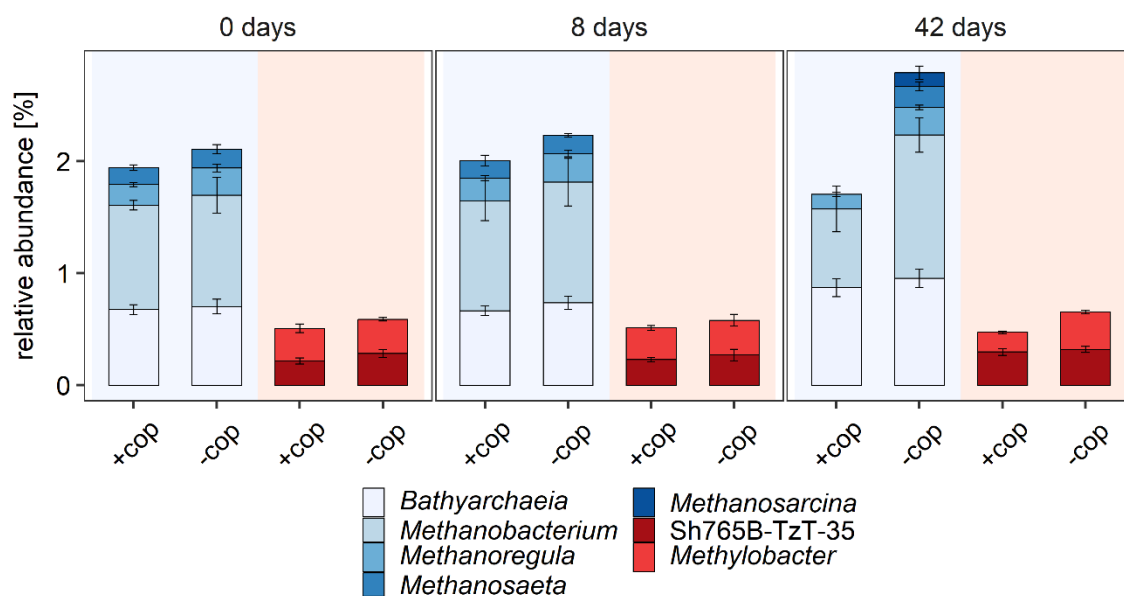
Figure S171. Relative 16S rRNA abundances of present (DNA-based) microbial taxa related to methane production (in blue colours) and methane oxidation (in red colour) per timepoint (0, 8, 42 days) and setup (with added Fe-OC coprecipitates: +cop, no-coprecipitate control: -cop) in the microcosm experiment. Taxa with an abundance lower than 0.1% were not included. Taxa are labelled at the genus-level except for *Bathyarchaeia* for which no genus could be identified. All data bars and error bars represent the average and standard deviation of experimental triplicates.
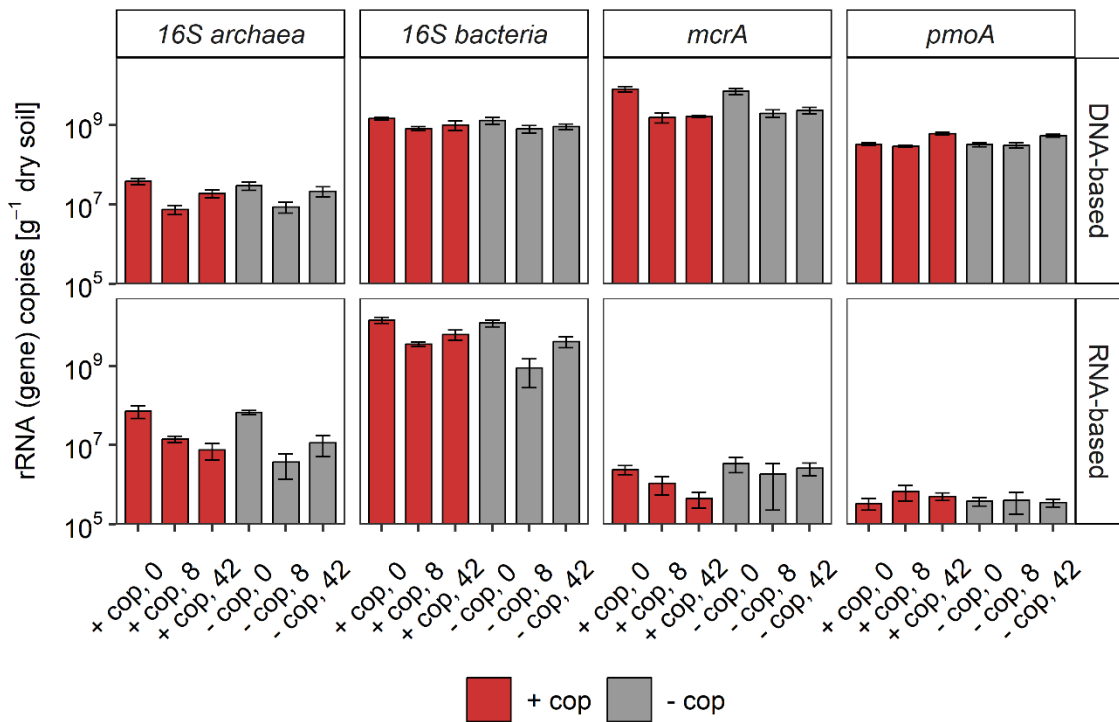
Figure S18. Full results of quantitative PCR data. Absolute values of DNA- and RNA-based rRNA (gene) copy numbers in microcosm setups with addition of ^{57}Fe-enriched Fe-OC coprecipitates ("+ cop") and in a no-coprecipitate control ("- cop") are displayed over time. Samples were collected immediately after addition of ^{57}Fe-enriched Fe-OC coprecipitates (0), after 8 days and after 42 days. The total bacterial and archaeal 16S rRNA (gene) copies as well as gene copies relating to methanogenesis (mcrA) and methanotrophy (pmoA) were quantified. Data and error bars show the mean and standard deviation of experimental triplicates.
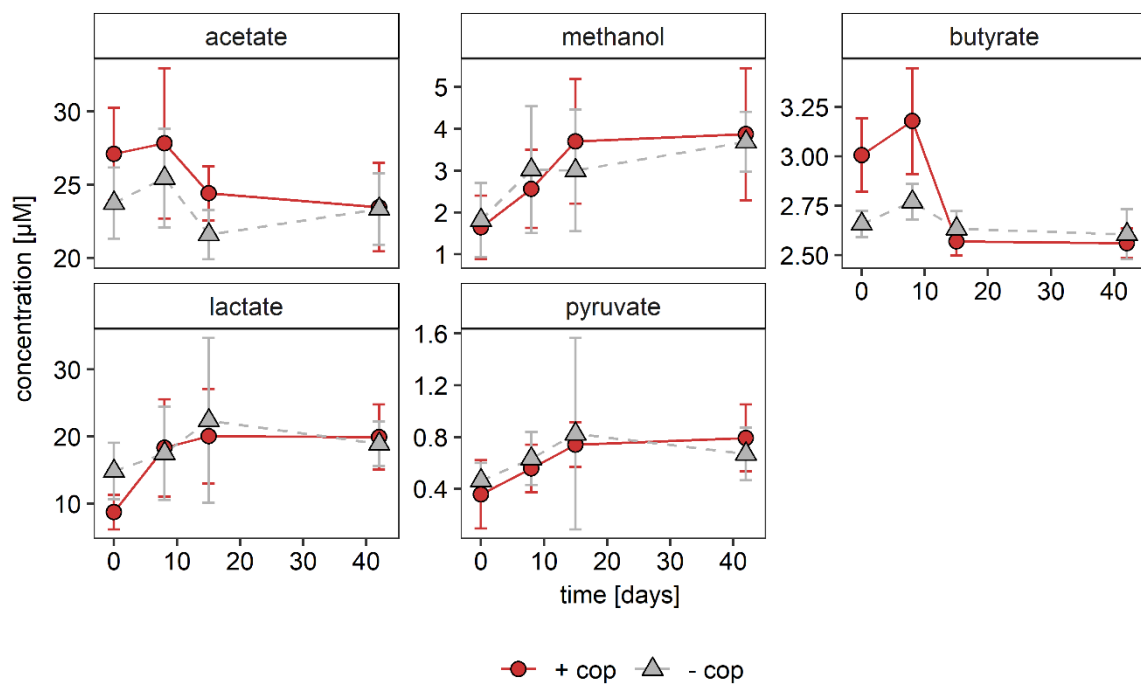
Figure S19. Measured concentrations of selected microbial metabolites in microcosm experiment with addition of ^{57}Fe-enriched Fe-OC coprecipitates ("+ cop") and in a no-coprecipitate control ("- cop") over time. Note the different scaling of the y-axis for every analyte. Data points and error bars show the mean and standard deviation of experimental triplicates.
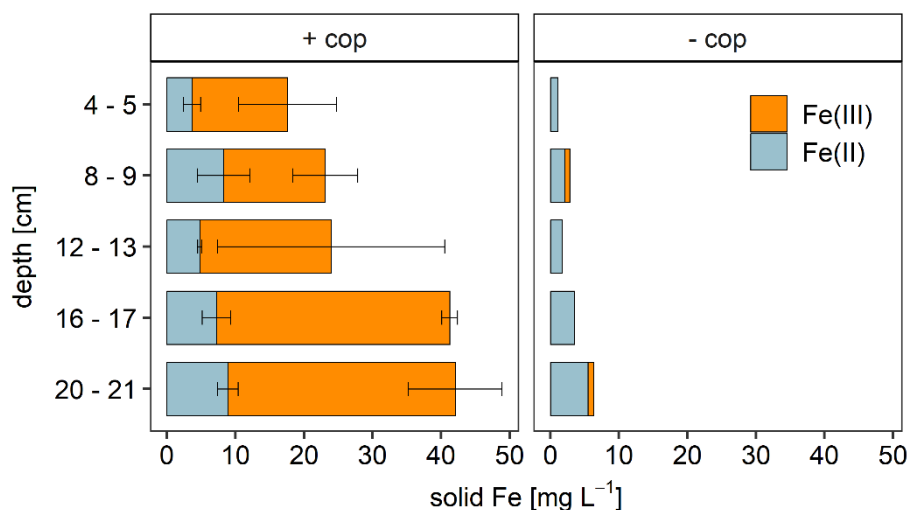
Figure S20. Absolute concentration of solid Fe(II) and Fe(III) detected in field experiment over depth. Synthesized [NA]Fe-OC coprecipitates (5 mM initially) were incubated inside passive porewater samplers ("+ cop") placed in the fen area of Stordalen Mire for 53 days. Data and error bars represent the average and range of experimental duplicates in case of the samplers with added [NA]Fe-OC coprecipitates and data of one replicate in case of the no-coprecipitate control ("- cop").
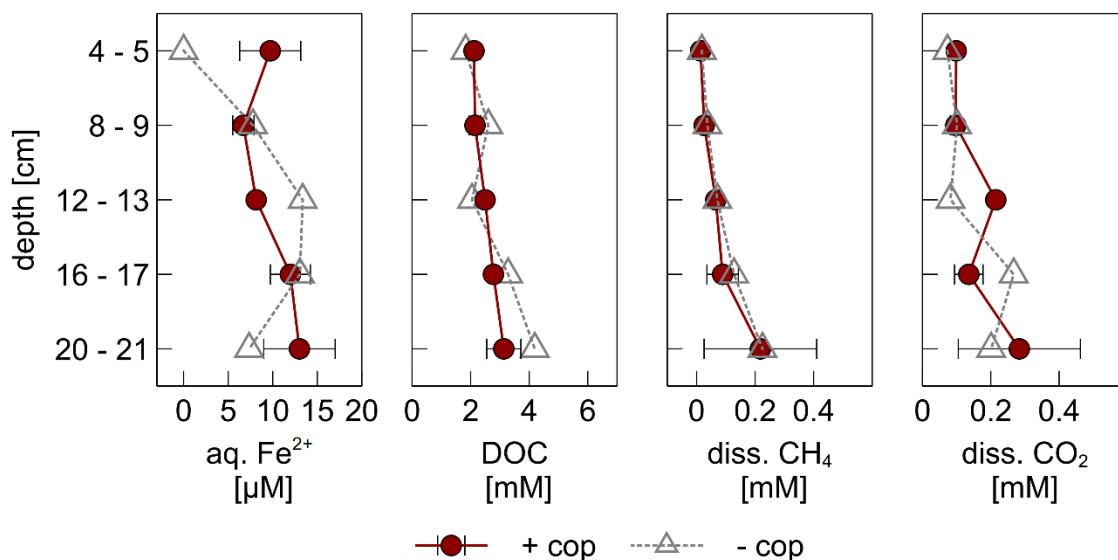
Figure S21. Dissolved species concentrations in porewater of passive porewater samplers over depth. Concentrations of aqueous Fe^{2+}, dissolved organic carbon (DOC), dissolved CH_4 and dissolved CO_2 are displayed for setups with added ^{NA}Fe-OC coprecipitates ("+ cop") and without ("- cop") after 53 days of in situ incubation. Concentrations of nitrite and nitrate were below detection limit. Data points and error bars represent the average and range of experimental duplicates in case of the "+ cop" setup and data of one replicate in case of the "- cop" setup.
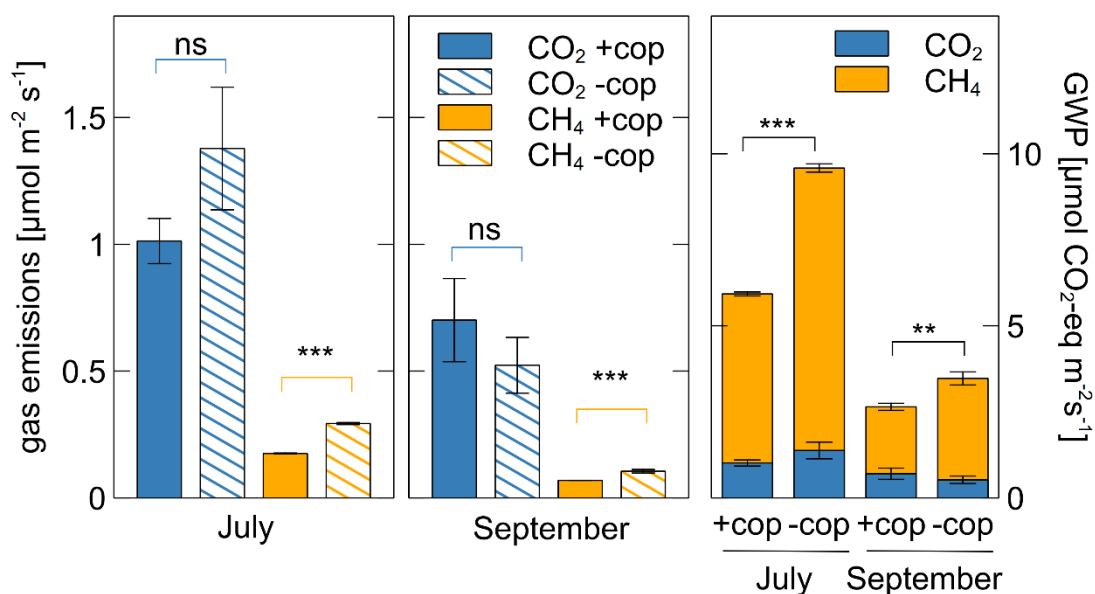
Figure S22. Absolute measured greenhouse gas fluxes (left and middle panel) and calculated global warming potential (GWP, right panel) of the field experiment. Measurements were taken 2, 20 and 21 h after ^{NA}Fe-OC coprecipitates were added to the passive porewater samplers (July) and after 53 days (September). Gas fluxes were determined on top of one passive porewater sampler containing the ^{NA}Fe-OC coprecipitates ("+ cop") and one sampler containing deionized water as a control ("- cop"). Symbols above the bars denote the level of significant difference between the two setups at a given time (one-way ANOVA, Tukey's HSD test): $p > 0.1$ – not significant (ns), $p ≤ 0.1$ -*, $p ≤ 0.05$ - **, $p ≤ 0.001$ - ***. Data and error bars represent the average and standard deviation of triplicate measurements of one "+ cop" plot and one "- cop" plot.

Table S1. Composition of artificial porewater used in microcosm experiment. The composition was modified from a mineral medium [135]. Concentrations were 100x diluted but the concentration of $CaCl_2$ was kept at 2 mM to provide a constant ionic strength.

Salt	Final concentration in bottles [mM]
KH_2PO_4	0.04
NH_4Cl	0.06
$MgSO_4x7H_2O$	0.02
$CaCl_2x2H_2O$	2.00

Table S2. List of performed quantitative PCR assays to quantify DNA- and RNA-based copy numbers. The assays and their used primers, primer sequences, thermal programs and sample dilution are given.

Assay	Primer	Primer sequence (5´- 3´)	Thermal program	dilution factor	References
16S rRNA gene Bacteria	341f	CCTACGGGAGGCAGCAG	95°C - 3´; (95°C - 10´´; 55°C - 30´´) x 40; 60-95°C by 0.5°C - 5´´	DNA: 1000, RNA-based: 10	Muyzer et al. (1995)[60]
	797r	ATTACCGCGGCTGCTGG			Nadkarni et al (2002)[61]
16S rRNA gene Archaea	Ar109f	ACKGCTGAGTAACACGT	95°C - 3´; (95°C - 10´´; 52°C - 45´´; 72°C - 30´´) x 40; 60-95°C by 0.5°C - 5´´	DNA: 1000, RNA-based: 10	Großkopf et al. (1998)[57]
	Ar915r	GTGCTCCCCCGCCAATT CCT			Stahl & Amann (1991)[62]
pmoA	A189f	GGNGACTGGGACTTC TGG	96°C - 5´; (94°C - 1´; 55°C - 1´; 72°C - 1´) x 40; 72°C - 5´; 94°C - 2´, 65-95°C by 0.5°C - 5´´	DNA: 100, RNA-based: 10	Holmes et al. (1995)[59]
	A682r	GAASGCNGAGAAGAA SGC			
mcrA	ME1f	GCMATGCARATHGGWAT GTC	95°C - 5´; (95°C - 30´´; 48°C - 45´´) x 6; (95°C - 30´´; 55°C - 45´´; 72°C - 30´) x 40; 65-95°C by 0.5°C - 5´´	DNA: 100, RNA-based: 10	Hales et al. (1996)[58]
	ME1r	TCATKGCRTAGTTDGGRT AGT			

Table S3. Overview of analyzed microbial metabolites, their chemical classification and injection method by gas chromatography coupled to mass spectrometry (GC-MS). Metabolites which were detected at least at one time point in all three experimental replicates over the course of the microcosm experiment are marked with an "x".

metabolite	chemical class	detected in samples?	injection method
alanine	amino acid	x	liquid
cysteine	amino acid		liquid
glutamic acid	amino acid	x	liquid
glycine	amino acid	x	liquid
histidine	amino acid		liquid
isoleucine	amino acid	x	liquid
lysine	amino acid	x	liquid
methionine	amino acid		liquid
phenylalanine	amino acid	x	liquid
proline	amino acid	x	liquid
serine	amino acid	x	liquid
threonine	amino acid	x	liquid
tyrosine	amino acid	x	liquid
valine	amino acid	x	liquid
aspargine	amino acid		liquid
methanol	alcohol	x	headspace
formic acid	organic acid		headspace
acetic acid	organic acid	x	headspace
propionic acid	organic acid	x	headspace
butyric acid	organic acid	x	headspace
pentanoic acid	organic acid	x	headspace
oxalic acid	organic acid		liquid
citric acid	organic acid		liquid
fumaric acid	organic acid	x	liquid
lactic acid	organic acid	x	liquid
pyruvic acid	organic acid	x	liquid
malic acid	organic acid		liquid
malonic acid	organic acid		liquid
succinic acid	organic acid	x	liquid
tartaric acid	organic acid	x	liquid
valeric acid	organic acid		headspace
3-hydroxybenzoic acid	phenol derivative	x	liquid
4-hydroxybenzoic acid	phenol derivative		liquid
hydroquinone	phenol derivative	x	liquid
galacitol	sugar alcohol		liquid
inositol	sugar alcohol	x	liquid
galacturonic acid	sugar acid		liquid
saccharic acid	sugar acid		liquid
fructose	sugar	x	liquid
fucose	sugar	x	liquid

glucose	sugar	x	liquid
mannose	sugar	x	liquid
sucrose	sugar	x	liquid
xylose	sugar	x	liquid

Table S4. Overview of ^{57}Fe Mössbauer spectroscopy fitting parameters (using the Full Static Hamiltonian model) of soil with addition of ^{57}Fe-enriched Fe-OC coprecipitates ("+ cop") and without ("- cop").

Sample	T [K]	site	CS[a] [mm s^{-1}]	QS[b] [mm s^{-1}]	H[c] [T]	η[d] [-]	Θ[e] [-]	Relative area [%]	χ^{2,f}
+ cop,0 d	77	Fe(II) doublet	1.36	2.59		0*	0*	41	1.25
		Fe(III) doublet	0.38	1.00		0*	0*	59	
	6	Fe(II) doublet	1.23	2.80		0*	0*	34	
		Fe(III) doublet	0.56	1.00*		0*	0*	15	0.85
		Fe(III) sextet	0.4*	-0.08	47.66	0*	0*	44	
		Fe(II) octet	1.5*	-2.6*	11.30	0.2*	90*	8	
- cop,0 d	77	Fe(II) doublet	1.23	2.76		0*	0	62	0.75
		Fe(III) doublet	0.38	0.75		0*	0	38	
	6	Fe(II) doublet	1.23	2.77		0*	0*	60	
		Fe(III) doublet	0.53	0.99		0*	0*	30	0.61
		Fe(II) octet	1.25	-2.6*	9.40	0.2*	90*	11	
+ cop, 42 d	77	Fe(II) doublet	1.38	2.56		0*	0	34	0.68
		Fe(III) doublet	0.35	0.98		0*	0	15	
	6	Fe(II) doublet	1.30	2.71		0*	0*	41	
		Fe(III) doublet	0.40	1.08		0*	0*	12	0.94
		Fe(III) sextet	0.48	-0.07	47.39	0*	0*	34	
		Fe(II) octet	1.35	-2.6*	9.96	0.2*	90*	12	
- cop,42 d	77	Fe(II) doublet	1.23	2.82		0*	0	55	0.60
		Fe(III) doublet	0.43	0.78		0*	0	45	
	6	Fe(II) doublet	1.27	2.83		0*	0*	54	
		Fe(III) doublet	0.29	0.78*		0*	0*	29	0.61
		Fe(II) octet	1.13	-2.6*	12.30	0.2*	90*	17	

[a]center shift
[b]quadrupole split in paramagnetic state or quadrupole shift
[c]hyper fine field
[d]asymmetry parameter
[e]polar angle between the electric field gradient (EFG) axis of symmetry with hyperfine field
[f]goodness of fit parameter
*indicates that parameters were fixed during fitting process

Table S5. Overview of ^{57}Fe Mössbauer spectroscopy fitting parameters (using Voigt-based fitting) of ^{57}Fe-enriched Fe-OC coprecipitates.

sample	T [K]	site	CS[a] [mm s^{-1}]	QS[b] [mm s^{-1}]	H[c] [T]	Relative area [%]	$\chi^{2,d}$
^{57}Fe Fe-OC cop	30	Fe(III) doublet	0.47	0.92		40	1.38
		Collapsed Fe(III) sextet	0.46	4.09		60	
	6	Fe(III) sextet 1	0.61	-0.03	47.2	42	
		Fe(III) sextet 2	0.32	0.01	46.4	44	3.35
		Collapsed Fe(III) sextet	0.45	-0.01	29.3	14	

[a]center shift
[b]quadrupole split in paramagnetic state or quadrupole shift
[c]hyper fine field
[d]goodness of fit parameter

Table S6. Linear combination fit results for Fe K-edge XANES spectra of the initial synthesized ^{57}Fe-enriched Fe-OC coprecipitates and the initial fen soil used in the microcosm experiment. The used references were ferrihydrite for Fe(III), and chlorite CCa-2 and Fe(II)-citrate for Fe(II). Fe(II)-citrate was used for the initial Fe-OC coprecipitate sample, while chlorite CCa-2 was used for initial soil.

sample	Fe(III) [-]	Fe(II) [-]	NSSR[a] [%]	red $\chi^{2,b}$ [%]
^{57}FeOC_initial	1.00	0.00	0.138	0.033
soil initial	0.39	0.61	0.713	0.185

[a] normalized sum of of squared residuals (residuals (100 $\sum_i$ (data$_i$-fit$_i$)^2/$\sum_i$ data^2)
[b] measure of fit accuracy ((N_{idp} /N_{pts}) $\sum_i$ ((data$_i$-fit$_i$)/ε_i)^2(N_{idp}-N_{var})$^{-1}$)). N_{idp} /N_{pts} and N_{var} are the number of independent points in the model fit (37.5), the total number of data points (250) and the number of fit variables (2), respectively.

Table S7. Linear combination fit results for k^3-weighted Fe K-edge EXAFS spectra of the initial synthesized ^{57}Fe-enriched Fe-OC coprecipitates and the initial mineral fen soil. The reference of Fe(II)-catechol was used for Fe(II)-OM.

Sample	Fh[a] [%]	Lp[b] [%]	chlorite [%]	illite [%]	Fe(II)-OM [%]	NSSR[c] [%]	red. $X^{2,d}$ [%]
^{57}FeOC_initial	93	7	0	0	0	2.2	10.8
soil initial	0	0	42	37	21	9.8	37.8

[a]Ferrihydrite
[b]Lepidocrocite
[c] Normalized sum of of squared residuals (residuals (100 $\sum_i$ (data$_i$-fit$_i$)^2/$\sum_i$ data^2)
[d] Measure of fit accuracy ((N_{idp} /N_{pts}) $\sum_i$ ((data$_i$-fit$_i$)/ε_i)^2(N_{idp}-N_{var})$^{-1}$)). N_{idp} /N_{pts} and N_{var} are the number of independent points in the model fit (18.1), the total number of data points (181) and the number of fit variables (2-5), respectively.

Chapter 5:

Conclusion and outlook

Interactions of iron (Fe) and organic carbon (OC) have been previously studied in many different environments, including marine sediments[1,2], paddy fields[3–5], forests[6,7] and wetlands[8–10]. High-organic carbon permafrost peatlands are often overlooked in this context due to the assumption that they contain very small inorganic element contents, such as Fe. Instead, previous studies have indicated that Fe(III)-OC associations are wide-spread in permafrost environments and have quantified the present Fe contents and bound OC[11–14]. Previous work at Stordalen Mire and other Arctic permafrost peatlands has therefore laid the foundation for this work by providing results of many *in situ* measurements and experiments as well as characterization of collected samples from the field[11,12,15–18]. Based on these data, we could design experiments that allowed us to move from field-based observations and correlations of geochemical parameters to a more fundamental, mechanistic understanding of the biogeochemical processes at play. Within this PhD work, we have elucidated the changes to Fe(III)-OC associations during permafrost thaw. We focused on initial composition of Fe-bound OC and greenhouse gas (GHG) emissions due to the reductive dissolution of Fe(III)-OC associations. The results of this work, therefore, have implications for thawing permafrost peatlands which will experience inundation and anoxia due to climate change, but also for anoxic non-permafrost peatlands and other wetlands. These conclusions and implications will be summarized per chapter in the following paragraphs. Further potential follow-up experiments based on unresolved knowledge gaps will be described in the outlook.

General conclusions

In **Chapter 2**, the potential quantity and composition of OC bound to Fe minerals were determined along a thaw gradient in order to understand how much and which OC classes are selectively bound to poorly crystalline Fe(III) (oxyhydr)oxides in permafrost soils. We found that the quantity of potentially adsorbed water-extractable OC to poorly crystalline Fe(III) (oxyhydr)oxides decreased from palsa and bog to fen. The efficiency of poorly crystalline Fe(III) (oxyhydr)oxides to adsorb OC and consequently limit microbial OC degradation, therefore decreases along the thaw gradient. Abiotic coprecipitation of initially anoxic, water-extractable OC from palsa and bog soils and dissolved Fe(II) led to much higher quantities of bound OC than by adsorption. Since high C:Fe ratios (based on soil extractions) are also found in the soils, coprecipitation at redox interfaces is likely the dominant mechanism trapping OC. During both adsorption and coprecipitation, we have shown that preferential binding of more oxidized, aromatic, and high molecular weight OC compounds takes place. Preferential binding,

therefore, imposes a bias on the remaining OC in solution, which is likely composed of inherently more bioavailable OC compounds. Therefore, a higher portion of dissolved OC (DOC) after binding could still be respired by microorganisms compared to the initial DOC composition. This has implications for the C cycle before and after thawing. In oxic soil layers of palsa and bog soils, high quantities of OC may be captured by Fe(III) (oxyhydr)oxides, but inherently easier-to-degrade OC may be disproportionately left in solution. This could lead to higher CO_2 emissions than expected. In anoxic soil layers, Fe(III)-OC associations could be reductively dissolved, and the release of previously Fe-bound OC could contribute to OC mobilization in the form of CO_2 emissions. However, the respiration of the mobilized, yet less bioavailable OC from Fe(III) (oxyhydr)oxides might be limited, especially under anoxic conditions in which thermodynamic constraints on degradation exist[19]. In conclusion, the potential of Fe(III) (oxyhydr)oxides to bind OC is dynamic along the thaw gradient, changing both in maximum quantity and intensity of preferential binding due to vegetation- and redox-driven changes in OC composition.

In both **Chapter 3** and **Chapter 4**, we aimed to understand to which extent Fe(III)-OC associations are reductively dissolved in thawing, anoxic permafrost soils and how they may contribute to GHG release. Specifically, in **Chapter 3**, we focused on the fate of Fe(III)-OC associations during initial permafrost thaw, their contribution to CO_2 release, and the possible microbial players involved in the reduction of Fe(III)-OC associations and following OC degradation. We found that Fe(III)-OC coprecipitates, which were used as representative phases for Fe(III)-OC associations, were only stable in palsa soils under *in situ*, and therefore oxic, conditions. Once anoxic conditions develop, as simulated in the microcosm experiments, coprecipitates were fully reduced within several weeks in both palsa and bog soils. Their reduction increased cumulative CO_2 emissions by 43±16% in the anoxic palsa soil, demonstrating that they can make up a significant portion of anaerobic respiration upon permafrost soil collapse. The results, therefore, show that oxic, low-land permafrost areas are likely losing their Fe(III)-OC associations upon permafrost thaw if anoxic conditions develop. Based on estimations of low-land permafrost areal extent[20,21], the available data on Fe stocks[12,13,15], and our estimated ratio of CO_2 release per reduced Fe(III) (ca. 1:1), the reduction of Fe(III)-OC associations could release 94-1144 Tg of CO_2-C. In bog soils, Fe(III)-OC coprecipitates were also fully reduced. We could not determine direct contributions of this reduction to anaerobic respiration due to counter-acting effects on CO_2 emissions. Phenolic-rich OC compounds, which are produced by *Sphagnum* spp. in bogs, were likely released from the added coprecipitates and could have inhibited microbial activity. Therefore, in cases where permafrost thaw favors growth of *Sphagnum* spp., CO_2 release due to dissolution of Fe(III)-

OC associations could be mitigated. Nevertheless, our findings show that Fe(III)-OC associations are no stable OC sink during thaw of low-land permafrost areas.

Within **Chapter 4**, our specific goal was to investigate how methane (CH_4) emissions in fully thawed permafrost soils will be affected by Fe(III)-OC associations. In both field and lab experiments, we found that Fe(III)-OC coprecipitates were microbially reduced, as they provided an easily reducible Fe pool compared to Fe in phyllosilicates for the present Fe(III)-reducing microorganisms. The resulting net CH_4 emissions from anoxic fen soil were decreased due to the addition of Fe(III)-OC coprecipitates. Based on molecular biological techniques, we determined that a majority of the decrease in CH_4 emissions stemmed from thermodynamic inhibition of methanogenesis due to microbial Fe(III) reduction and a minority from anaerobic methane oxidation. The net decrease of CH_4 emissions lowered the overall global warming potential of emitted GHGs in treatments with coprecipitate addition compared to no-coprecipitate controls, even while more CO_2 was released. Fe(III)-OC associations could, therefore, play an integral part in lowering the radiative forcing of future thawed permafrost peatlands. Under natural conditions, this function could be sustained due to continuous production of Fe(III)-OC associations in the soil. For example, root radial oxygen loss of sedges could induce coprecipitation of dissolved Fe(II) and DOC and provide niches for microaerophilic Fe(II)-oxidizing microorganisms. Similarly, phototrophic or nitrate-reducing Fe(II)-oxidizers, which have been shown to be present in the fen soil based on microbial enrichment attempts (by Katrin Wunsch), could biotically form Fe(III)-OC associations. The future CH_4 emissions of thawed permafrost peatlands, therefore, depend on the presence of Fe(III)-OC associations.

Outlook

Coprecipitation of permafrost organic carbon with dissolved iron(II) – role of abiotic vs biotic processes

Coprecipitation processes of DOC from various ecosystems with dissolved Fe(III)[24–27] as well as with dissolved Fe(II) at circumneutral pH[28,29] have already been investigated in order to understand the OC binding capacities of Fe(III)-OC coprecipitates. In this PhD work, we expanded this knowledge by using permafrost-derived water-extractable OC and initially anoxic, dissolved Fe(II) to simulate coprecipitation in permafrost environments at redox transitions (**Chapter 2**). We found high OC binding capacities of up to 925 and 1532 mg C g^{-1} Fe for palsa and bog environments, respectively. The produced C:Fe ratios in the solids were higher than in other studies using dissolved Fe(III) due to the higher solubility of Fe(II) at acidic

pH (pH 4.5) and slower Fe oxidation rate[30]. However, only abiotic coprecipitation was simulated in this work and only at one pH value. Since coprecipitation is rarely simulated at acidic pH values (< pH 5.5) and with dissolved Fe(II) as a starting material, it could be useful to continue research in this direction. The role of other abiotic processes, such as radical formation (in the dark) during oxygenation of dissolved Fe(II)[31,32] or complexation of Fe(II) by DOC, as well as formation by biotic coprecipitation pathways (Figure 1), was also not evaluated in this work. The following questions therefore remain to be answered:

(i)   How much DOC is immobilized during oxidation of dissolved Fe(II) across different pH ranges, representative for palsa and bog (pH 3.5-5) and for fen environments (pH 6-7)?

(ii)   What role does (dark) radical formation and Fe complexation by OC play in changing the OC composition during the coprecipitation process?

(iii)   How does biotic Fe(II) oxidation change the binding capacities of OC during microbial Fe(II) oxidation?

To answer these questions, coprecipitation experiments using anoxic, water-extractable OC from different permafrost thaw stages and dissolved Fe(II) could be performed at varying pH values. The solid phase OC composition could be characterized by FTIR or C X-ray absorption spectroscopy (XAS) and the bound OC content quantified by analysis of remaining DOC in solution. During the abiotic oxidation process, radical oxygen species and intermediates (e.g., $^{\bullet}OH$, H_2O_2) could be quantified, and OC composition could be analyzed by specific ultraviolet absorption spectroscopy (SUVA), ^{13}C nuclear magnetic resonance spectroscopy (^{13}C-NMR) and Fourier-transform ion cyclotron resonance mass spectrometry (FT-ICR-MS). Presence of Fe-OC complexes could be determined by modeling using geochemical modeling software (e.g. PHREEQC). Biotic Fe(II) oxidation could be simulated by using phototrophic or microaerophilic Fe(II)-oxidizing enrichment cultures (enriched from Stordalen Mire by Katrin Wunsch). Cultures could be pre-grown in typical media and then transferred to minimal media, amended with water-extractable OC and low concentration of other cations, to simulate environmental conditions. Lower cation concentrations would ensure a higher probability of Fe(II)-OC complex formation, which has been shown to affect biotic Fe(II) oxidation rates[33]. The final OC binding capacities in microbially formed Fe(III)-OC coprecipitates could then be compared to those formed abiotically.

Phyllosilicates and manganese (hydr)oxides as potential organic matter sinks across thawing permafrost soils

While this PhD work focused mainly on Fe(III)-OC associations as a subset of mineral-OC associations in permafrost peatlands, other minerals could also function as sinks for OC. Phyllosilicates and their bound OC pool are frequently studied in the context of temperate or agricultural soils[34,35], but less in permafrost soils[36]. While their reported maximum binding capacities of OC per g mineral are much lower than for poorly crystalline Fe(III) (oxyhydr)oxides[37], they might be more abundant in mineral subsoils of permafrost areas. Additionally, they are not susceptible to full reductive dissolution and instead undergo structural rearrangements due to Fe reduction[38], thereby forming more stable associations with OC. Therefore, as Fe(III)-OC associations are reduced due to anoxic conditions during thaw (**Chapter 3 and 4**), phyllosilicates could partly recapture the released OC (Figure 1). Manganese (Mn) (hydr)oxides are redox-active and could bind similar OC quantities in oxic soil layers and oxic-anoxic transitions as Fe (oxyhydr)oxides[39]. While Mn contents in soils are often several orders of magnitude smaller than Fe contents[40] (within this work: 0.18-1.28 µmol Mn g^{-1} soil vs 70-170 µmol Fe g^{-1} soil), Mn coatings on other minerals could still affect OC binding behavior. Interaction of Mn (hydr)oxides with OC leads to oxidation of OC and production of low molecular weight compounds, or even CO_2, while Mn is being reduced[41–43]. Furthermore, both phyllosilicates and Mn (hydr)oxides could exhibit different preferential binding behaviors compared to Fe(III) (oxyhydr)oxides[37,44]. With regards to the role of these two minerals in permafrost soils, the following knowledge gaps exist:

(i)   How abundant are phyllosilicates and Mn (hydr)oxides in permafrost peatlands and what is their speciation?

(ii)   What are the maximum OC adsorption or coprecipitation (in case of Mn) capacities to phyllosilicates and Mn-coated Fe(III) (oxyhydr)oxides across conditions of permafrost thaw?

(iii)   What kind of preferential binding effect is induced on OC by adsorption to or coprecipitation (in case of Mn) with phyllosilicates and Mn-coated Fe(III) (oxyhydr)oxides?

To tackle these research gaps, soil cores could be collected from a variety of permafrost peatlands, spanning different thaw stages and mineralogies, and extractions targeting Mn (hydr)oxides (dithionite-citrate-bicarbonate extraction) could be performed on different soil layers. The residues could be washed and analyzed by X-ray diffractometry to identify phyllosilicate minerals, and the TOC could be quantified to draw conclusions on the potentially phyllosilicate-bound OC in the residue. Initial soil samples could be further analyzed by Mn XAS to determine the Mn oxidation state and binding environment. Using water-extractable

OC from the soils of the different sites, adsorption and coprecipitation experiments could be performed with synthesized Mn-coated Fe(III) (oxyhydr)oxides and purchased phyllosilicate minerals to quantify the OC binding capacity. Different techniques could be used to estimate preferential binding effects to these minerals, such as SUVA, Fourier transform infrared spectroscopy (FTIR), ^{13}C-NMR, and FT-ICR-MS.

Role of redox-active groups in particulate organic matter for mediating microbial iron(III) reduction

It has been shown that redox-active OC functional groups in sediment-derived particulate organic matter (POM) can serve as an electron shuttle for microorganisms, thereby enhancing Fe(III) reduction[45]. Within this PhD work, we observed rapid (within 1 day) dissolution and reduction of Fe(III)-OC coprecipitates (15% and 11% in palsa and bog soils, respectively) (**Chapter 3**). In a control experiment, we showed that this process was not induced by abiotic reduction due to redox-active groups in DOC. As palsa and bog soils likely contain a majority of their OC pool as POM, it is reasonable to assume that reduced redox-active groups in POM could have facilitated Fe(III) reduction together with microorganisms (Figure 1). However, no conclusive answers can be drawn since this process was not experimentally investigated further. Therefore, a few questions remain, such as:

(i)   What is the oxidation state of POM *in situ*? Does it change over the thaw gradient?

(ii)   Does electron shuttling of redox-active POM between microorganisms and Fe(III) minerals play a role for Fe(III) reduction in permafrost peatlands?

(iii) What is the extent of abiotic Fe(III) reduction by reduced redox-active POM compared to microbially-mediated Fe(III) reduction with POM as electron shuttle in permafrost peatlands?

These questions could be investigated by first characterizing the POM over the thaw gradient and depth. Soil cores could be taken per thaw stage and stored in anoxic conditions until soil layers are split and homogenized in an anoxic glovebox. POM could then be isolated using density or size fractionation techniques[46,47]. Another alternative would be to strip the peat of its poorly crystalline Fe content by a dithionite-citrate-bicarbonate extraction, thereby removing most of the mineral-associated OC and redox-active Fe[45]. However, this would likely also reduce the functional groups of POM, such that the *in situ* redox state would not be preserved. The electron accepting capacity of POM could be determined by indirect spectrophotometric assays after addition of Fe(III)-NTA[45] or ZiV[48] or by electrochemical mediated reduction and oxidation[49]. The OC composition within POM could be analyzed by ^{13}C-NMR and C XAS, in order to determine the contribution of phenolic groups, which are often

linked to abiotic Fe(III) reduction[27,50,51]. To estimate the importance of redox-active POM for Fe(III) reduction, POM could be added to a previously enriched *Geobacter* culture from Stordalen[17] in minimal media together with synthesized ferrihydrite or Fe(III)-OC associations. An abiotic control without the *Geobacter* inoculum would be used to determine potential abiotic Fe(III) reduction. Alternatively, the experiment could be performed by using a soil suspension as inoculum.

Fate of iron-bound organic carbon by use of isotope labeling

The fate of mineral-bound OC is subject of increasing research, as many studies suggest that mineral-bound OC could be the key for storing more OC in soils over long time scales[52–54]. Many studies use ^{13}C-labelled simple sugars, organic acids, or amino acids to synthesize mineral-organic carbon associations and track their fate through the aqueous, gaseous, and solid phase[5,55–57]. Within this work, we synthesized Fe(III)-OC coprecipitates to imitate a subset of the natural mineral-OC associations that would occur in permafrost soils. We demonstrated that Fe(III) minerals do not provide protection for OC during permafrost thaw due to their reductive dissolution (**Chapters 3 and 4**). Based on results in **Chapter 1**, we know that relatively less bioavailable OC compounds are preferentially coprecipitated with Fe(III) (oxyhydr)oxides. However, we could not directly quantify how much previously Fe-bound OC contributed to GHG emissions (Figure 1). The use of water-extractable OC for the synthesis provided an environmentally relevant OC mix but also prohibited us from using a ^{13}C-labeled substance, as ^{13}C labeling of the peat itself is not attainable. Therefore, the following questions are still unanswered:

(i) What is the contribution of released, previously Fe-bound OC upon reductive dissolution of Fe(III)-OC associations to CO_2 and CH_4 emissions? Does this contribution change in soils along the thaw gradient?

(ii) Does the release of Fe-bound OC induce a priming effect in permafrost soils?

(iii) How much previously Fe-bound OC is retained in the solid phase, bound to other minerals or taken up in microbial biomass?

These knowledge gaps could be answered by performing a similar laboratory experiment as in **Chapters 3 and 4**. However, using a ^{13}C-labeled OC source for synthesizing Fe(III)-OC associations would be necessary. Besides a mix of ^{13}C-labeled small OC compounds, it could also be feasible to use ^{13}C-labeled plant parts of species native to permafrost peatlands. Plants growing at Stordalen Mire, such as the shrubs in palsa areas (*Betula nana*, *Andromeda polifolia*) or sedges in fen areas (*Eriophorium* spp. or *Carex* spp.), control much of the litter inputs to the soil[58] and would therefore provide a suitable OC source for the coprecipitate

synthesis. The plants could be exposed to $^{13}CO_2$ pulse labeling, possibly in collaboration with other groups working at Stordalen Mire who study C allocation in plants. The labeled material of plants (leaves, roots) could then be dried and ground up prior to performing a water extraction. The resulting extract could be used to synthesize Fe(III)-OC associations. Isotope-specific methods, such as gas chromatography coupled to mass spectrometry (GC-MS) and isotope ratio mass spectrometry (IRMS), could be utilized to track the distribution of Fe-associated OC to the gas phase, liquid phase, and solid phase (after extractions). Visualization of the previously Fe-bound OC in the solid phase and, therefore, co-localization with other mineral phases could be performed using nanoscale secondary ion mass spectrometry (nanoSIMS).

The role of anaerobic methane oxidation in thawing permafrost peatlands

High CO_2:CH_4 ratios of net GHG emissions are detected in many cases in Arctic peatlands[59–61]. This ratio should theoretically be 1:1 in anoxic systems[62], meaning that higher ratios could imply the presence of additional processes decreasing the net flux of CH_4. Anaerobic methane oxidation (ANME) could be the reason (Figure 1), as this process is known to play a major role in marine sediments[63] and was recently demonstrated to occur in various terrestrial environments[64-67]. We could detect several canonically aerobic methanotrophic microorganisms in soils across the thaw gradient in anoxic incubations (**Chapters 3 and 4**) in this PhD work. Within the bog soil, the relative abundance and potential activity (based on 16S rRNA amplicon (gene) sequencing) of aerobic methanotrophs only slightly decreased over the course of the anoxic incubation. Within the fen soil, we found constant activity of *Methylobacter* spp. and of a genus belonging to the putative anaerobic methane-oxidizing taxa *Methylomirabilales*, which displayed an increasing relative abundance upon addition of Fe(III)-OC coprecipitates. Based on these observations, the following questions therefore remain:

(i)   Are known aerobic methanotrophs still active under anoxic conditions in thawing permafrost soils? Do they use µM traces of oxygen, or do they use other electron acceptors?

(ii)   What electron acceptors (nitrate, nitrite, sulfate, Fe(III), organic matter) are used by anaerobic methane oxidizers in thawing permafrost soils?

(iii)   What are the rates of ANME across thawing permafrost soils?

Experiments to answer these research questions could involve incubations of soil slurries from the bog and fen areas under anoxic conditions with $^{13}CH_4$-amended headspace. The production of $^{13}CO_2$ and, therefore, the activity of methanotrophs could be tracked over time in order to quantify the rates of ANME. In another experiment, different electron acceptors

(nitrate, nitrite, sulfate, Fe(III) in form of ferrihydrite, organic matter in form of water-extractable OC, or isolated POM from the same soils) could be supplemented to distinguish which electron acceptors are used by methanotrophs. The oxygen concentrations could be tracked with non-invasive optical sensor foils adapted for µM concentrations. The identity and activity of methanotrophic communities could be followed by different molecular biology techniques, including fluorescence in situ hybridization (FISH), quantitative polymerase chain reaction assays (qPCR) of the *pmoA* and *mcrA* gene of ANME-bacteria[68] as well as 16S rRNA gene amplicon sequencing.
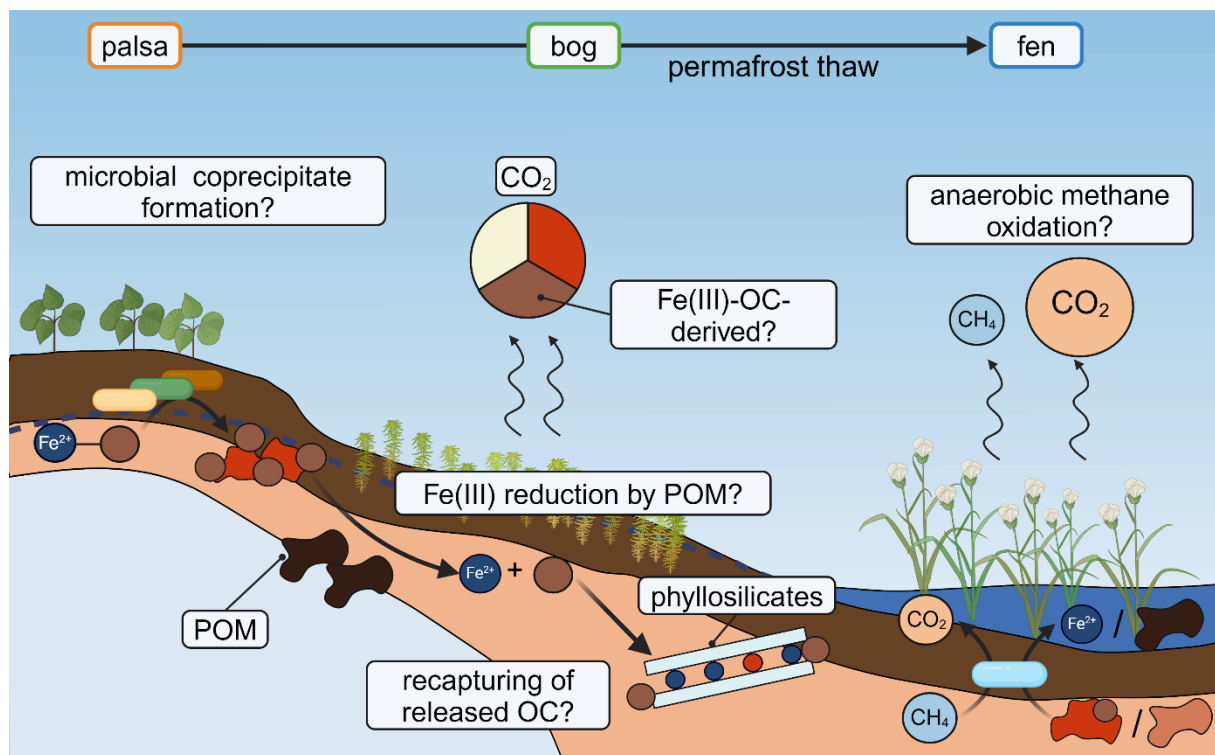
Figure 1. Illustration of a subset of unresolved knowledge gaps regarding coupled iron-organic carbon cycling in thawing permafrost peatlands. Boxes with question marks display the knowledge gaps described in the section above. The abbreviation POM stands for particulate organic matter. Graphic is made with BioRender.com.

References

1. Barber, A., Brandes, J., Leri, A., Lalonde, K., Balind, K., Wirick, S., Wang, J., & Gélinas, Y. (2017). Preservation of organic matter in marine sediments by inner-sphere interactions with reactive iron. *Scientific Reports*, *7*(1), 366. https://doi.org/10.1038/s41598-017-00494-0

2. Lalonde, K., Mucci, A., Ouellet, A., & Gélinas, Y. (2012). Preservation of organic matter in sediments promoted by iron. *Nature*, *483*(7388), 198–200. https://doi.org/10.1038/nature10855

3. Duan, X., Li, Z., Li, Y., Yuan, H., Gao, W., Chen, X., Ge, T., Wu, J., & Zhu, Z. (2023). Iron–organic carbon associations stimulate carbon accumulation in paddy soils by decreasing soil organic carbon priming. *Soil Biology and Biochemistry*, *179*, 108972. https://doi.org/10.1016/j.soilbio.2023.108972

4. Jeewani, P. H., Van Zwieten, L., Zhu, Z., Ge, T., Guggenberger, G., Luo, Y., & Xu, J. (2021). Abiotic and biotic regulation on carbon mineralization and stabilization in paddy soils along iron oxide gradients. *Soil Biology and Biochemistry*, *160*, 108312. https://doi.org/10.1016/j.soilbio.2021.108312

5. Wang, S., Gao, W., Ma, Z., Zhu, Z., Luo, Y., Wei, L., Yuan, H., Chen, S., Ying, C., Mason-Jones, K., Kuzyakov, Y., & Ge, T. (2024). Iron mineral type controls organic matter stability and priming in paddy soil under anaerobic conditions. *Soil Biology and Biochemistry*, 109518. https://doi.org/10.1016/j.soilbio.2024.109518

6. Bhattacharyya, A., Campbell, A. N., Tfaily, M. M., Lin, Y., Kukkadapu, R. K., Silver, W. L., Nico, P. S., & Pett-Ridge, J. (2018). Redox Fluctuations Control the Coupled Cycling of Iron and Carbon in Tropical Forest Soils. *Environmental Science & Technology*, *52*(24), 14129–14139. https://doi.org/10.1021/acs.est.8b03408

7. Chen, C., Meile, C., Wilmoth, J., Barcellos, D., & Thompson, A. (2018). Influence of pO_2 on Iron Redox Cycling and Anaerobic Organic Carbon Mineralization in a Humid Tropical Forest Soil. *Environmental Science & Technology*, *52*(14), 7709–7719. https://doi.org/10.1021/acs.est.8b01368

8. Riedel, T., Zak, D., Biester, H., & Dittmar, T. (2013). Iron traps terrestrially derived dissolved organic matter at redox interfaces. *Proceedings of the National Academy of Sciences of the United States of America*, *110*(25), 10101–10105. https://doi.org/10.1073/pnas.1221487110

9. ThomasArrigo, L. K., Notini, L., Shuster, J., Nydegger, T., Vontobel, S., Fischer, S., Kappler, A., & Kretzschmar, R. (2022). Mineral characterization and composition of Fe-rich flocs from wetlands of Iceland: Implications for Fe, C and trace element export. *The Science of the total environment*, *816*, 151567. https://doi.org/10.1016/j.scitotenv.2021.151567

10. Zhao, Y., Liu, C., Li, X., Ma, L., Zhai, G., & Feng, X. (2023). Sphagnum increases soil's sequestration capacity of mineral-associated organic carbon via activating metal oxides. *Nature Communications*, *14*(1), 5052. https://doi.org/10.1038/s41467-023-40863-0

11. Joss, H., Patzner, M. S., Maisch, M., Mueller, C. W., Kappler, A., & Bryce, C. (2022). Cryoturbation impacts iron-organic carbon associations along a permafrost soil chronosequence in northern Alaska. *Geoderma*, *413*, 115738. https://doi.org/10.1016/j.geoderma.2022.115738

12. Patzner, M. S., Mueller, C. W., Malusova, M., Baur, M., Nikeleit, V., Scholten, T., Hoeschen, C., Byrne, J. M., Borch, T., Kappler, A., & Bryce, C. (2020). Iron mineral dissolution releases iron and associated organic carbon during permafrost thaw. *Nature communications*, *11*(1), 6329. https://doi.org/10.1038/s41467-020-20102-6

13. Mu, C. C., Zhang, T. J., Zhao, Q., Guo, H., Zhong, W., Su, H., & Wu, Q. B. (2016). Soil organic carbon stabilization by iron in permafrost regions of the Qinghai-Tibet Plateau. *Geophysical Research Letters*, *43*(19), 10286–10294. https://doi.org/10.1002/2016GL070071

14. Liu, F., Qin, S., Fang, K., Chen, L., Peng, Y., Smith, P., & Yang, Y. (2022). Divergent changes in particulate and mineral-associated organic carbon upon permafrost thaw. *Nature communications*, *13*(1), 5073. https://doi.org/10.1038/s41467-022-32681-7

15. Lipson, D. A., Raab, T. K., Goria, D., & Zlamal, J. (2013). The contribution of Fe(III) and humic acid reduction to ecosystem respiration in drained thaw lake basins of the Arctic Coastal Plain. *Global Biogeochemical Cycles*, *27*(2), 399–409. https://doi.org/10.1002/gbc.20038

16. Lipson, D. A., Jha, M., Raab, T. K., & Oechel, W. C. (2010). Reduction of iron (III) and humic substances plays a major role in anaerobic respiration in an Arctic peat soil. *Journal of Geophysical Research*, *115*. https://doi.org/10.1029/2009JG001147

17. Patzner, M. S., Kainz, N., Lundin, E., Barczok, M., Smith, C., Herndon, E., Kinsman-Costello, L., Fischer, S., Straub, D., Kleindienst, S., Kappler, A., & Bryce, C. (2022). Seasonal Fluctuations in Iron Cycling in Thawing Permafrost Peatlands. *Environmental Science & Technology*, *56*(7), 4620–4631. https://doi.org/10.1021/acs.est.1c06937

18. Patzner, M. S., Logan, M., McKenna, A. M., Young, R. B., Zhou, Z., Joss, H., Mueller, C. W., Hoeschen, C., Scholten, T., Straub, D., Kleindienst, S., Borch, T., Kappler, A., & Bryce, C. (2022). Microbial iron cycling during palsa hillslope collapse promotes greenhouse gas emissions before complete permafrost thaw. *Communications Earth & Environment*, *3*(1), 76. https://doi.org/10.1038/s43247-022-00407-8

19. Boye, K., Noël, V., Tfaily, M. M., Bone, S. E., Williams, K. H., Bargar, J. R., & Fendorf, S. (2017). Thermodynamically controlled preservation of organic carbon in floodplains. *Nature Geoscience*, *10*(6), 415–419. https://doi.org/10.1038/ngeo2940

20. Nitzbon, J., Schneider Von Deimling, T., Aliyeva, M., Chadburn, S. E., Grosse, G., Laboor, S., Lee, H., Lohmann, G., Steinert, N. J., Stuenzi, S. M., Werner, M., Westermann, S., & Langer, M. (2024). No respite from permafrost-thaw impacts in the absence of a global tipping point. *Nature Climate Change*, *14*(6), 573–585. https://doi.org/10.1038/s41558-024-02011-4

21. Hugelius, G., Strauss, J., Zubrzycki, S., Harden, J. W., Schuur, E. A. G., Ping, C.-L., Schirrmeister, L., Grosse, G., Michaelson, G. J., Koven, C. D., O'Donnell, J. A., Elberling, B., Mishra, U., Camill, P., Yu, Z., Palmtag, J., & Kuhry, P. (2014). Estimated stocks of circumpolar permafrost carbon with quantified uncertainty ranges and identified data gaps. *Biogeosciences*, *11*(23), 6573–6593. https://doi.org/10.5194/bg-11-6573-2014

22. Andrew, R. M., & Peters, G. P. (2023). *The Global Carbon Project's fossil CO2 emissions dataset* (Version 2023v36) [Dataset]. Zenodo. https://doi.org/10.5281/ZENODO.10177738

23. Ritchie, H., & Roser, M. (2020). *CO_2 emissions* [Dataset]. https://ourworldindata.org/co2-emissions

24. Chen, C., Dynes, J. J., Wang, J., & Sparks, D. L. (2014). Properties of Fe-organic matter associations via coprecipitation versus adsorption. *Environmental science & technology*, *48*(23), 13751–13759. https://doi.org/10.1021/es503669u

25. Eusterhues, K., Rennert, T., Knicker, H., Kögel-Knabner, I., Totsche, K. U., & Schwertmann, U. (2011). Fractionation of organic matter due to reaction with ferrihydrite: Coprecipitation versus adsorption. *Environmental science & technology*, *45*(2), 527–533. https://doi.org/10.1021/es1023898

26. Mikutta, R., Lorenz, D., Guggenberger, G., Haumaier, L., & Freund, A. (2014). Properties and reactivity of Fe-organic matter associations formed by coprecipitation versus adsorption: Clues from arsenate batch adsorption. *Geochimica et Cosmochimica Acta*, *144*, 258–276. https://doi.org/10.1016/j.gca.2014.08.026

27. Possinger, A. R., Zachman, M. J., Dynes, J. J., Regier, T. Z., Kourkoutis, L. F., & Lehmann, J. (2021). Co-precipitation induces changes to iron and carbon chemistry and spatial distribution at the nanometer scale. *Geochimica et Cosmochimica Acta*, *314*, 1–15. https://doi.org/10.1016/j.gca.2021.09.003

28. Angelico, R., Ceglie, A., He, J.-Z., Liu, Y.-R., Palumbo, G., & Colombo, C. (2014). Particle size, charge and colloidal stability of humic acids coprecipitated with Ferrihydrite. *Chemosphere*, *99*, 239–247. https://doi.org/10.1016/j.chemosphere.2013.10.092

29. Sodano, M., Lerda, C., Nisticò, R., Martin, M., Magnacca, G., Celi, L., & Said-Pullicino, D. (2017). Dissolved organic carbon retention by coprecipitation during the oxidation of ferrous iron. *Geoderma*, *307*, 19–29. https://doi.org/10.1016/j.geoderma.2017.07.022

30. Morgan, B., & Lahav, O. (2007). The effect of pH on the kinetics of spontaneous Fe(II) oxidation by O2 in aqueous solution – basic principles and a simple heuristic description. *Chemosphere*, *68*(11), 2080–2084. https://doi.org/10.1016/j.chemosphere.2007.02.015

31. Chen, N., Fu, Q., Wu, T., Cui, P., Fang, G., Liu, C., Chen, C., Liu, G., Wang, W., Wang, D., Wang, P., & Zhou, D. (2021). Active Iron Phases Regulate the Abiotic Transformation of Organic Carbon during Redox Fluctuation Cycles of Paddy Soil. *Environmental Science & Technology*, *55*(20), 14281–14293. https://doi.org/10.1021/acs.est.1c04073

32. Trusiak, A., Treibergs, L. A., Kling, G. W., & Cory, R. M. (2018). The role of iron and reactive oxygen species in the production of CO2 in arctic soil waters. *Geochimica et Cosmochimica Acta*, *224*, 80–95. https://doi.org/10.1016/j.gca.2017.12.022

33. Peng, C., Bryce, C., Sundman, A., Borch, T., & Kappler, A. (2019). Organic Matter Complexation Promotes Fe(II) Oxidation by the Photoautotrophic Fe(II)-Oxidizer Rhodopseudomonas palustris TIE-1. *ACS Earth and Space Chemistry*, *3*(4), 531–536. https://doi.org/10.1021/acsearthspacechem.9b00024

34. Mikutta, R., Mikutta, C., Kalbitz, K., Scheel, T., KAISER, K., & Jahn, R. (2007). Biodegradation of forest floor organic matter bound to minerals via different binding mechanisms. *Geochimica et Cosmochimica Acta*, *71*(10), 2569–2590. https://doi.org/10.1016/j.gca.2007.03.002

35. Wang, X., Toner, B. M., & Yoo, K. (2019). Mineral vs. Organic matter supply as a limiting factor for the formation of mineral-associated organic matter in forest and agricultural soils. *Science of The Total Environment*, *692*, 344–353. https://doi.org/10.1016/j.scitotenv.2019.07.219

36. Gentsch, N., Mikutta, R., Alves, R. J. E., Barta, J., Čapek, P., Gittel, A., Hugelius, G., Kuhry, P., Lashchinskiy, N., Palmtag, J., Richter, A., Šantrůčková, H., Schnecker, J., Shibistova, O., Urich, T., Wild, B., & Guggenberger, G. (2015). Storage and transformation of organic matter fractions in cryoturbated permafrost soils across the Siberian Arctic. *Biogeosciences*, *12*(14), 4525–4542. https://doi.org/10.5194/bg-12-4525-2015

37. Young, R., Avneri-Katz, S., McKenna, A., Chen, H., Bahureksa, W., Polubesova, T., Chefetz, B., & Borch, T. (2018). Composition-Dependent Sorptive Fractionation of Anthropogenic Dissolved Organic Matter by Fe(III)-Montmorillonite. *Soil Systems*, *2*(1), 14. https://doi.org/10.3390/soilsystems2010014

38. Gorski, C. A., Klüpfel, L., Voegelin, A., Sander, M., & Hofstetter, T. B. (2012). Redox Properties of Structural Fe in Clay Minerals. 2. Electrochemical and Spectroscopic Characterization of Electron Transfer Irreversibility in Ferruginous Smectite, SWa-1. *Environmental Science & Technology*, *46*(17), 9369–9377. https://doi.org/10.1021/es302014u

39. Stuckey, J. W., Goodwin, C., Wang, J., Kaplan, L. A., Vidal-Esquivel, P., Beebe, T. P., & Sparks, D. L. (2018). Impacts of hydrous manganese oxide on the retention and lability of dissolved organic matter. *Geochemical Transactions*, *19*(1), 6. https://doi.org/10.1186/s12932-018-0051-x

40. Herndon, E. M., Yang, Z., Bargar, J., Janot, N., Regier, T. Z., Graham, D. E., Wullschleger, S. D., Gu, B., & Liang, L. (2015). Geochemical drivers of organic matter decomposition in arctic tundra soils. *Biogeochemistry*, *126*(3), 397–414. https://doi.org/10.1007/s10533-015-0165-5

41. Li, H., Santos, F., Butler, K., & Herndon, E. (2021). A Critical Review on the Multiple Roles of Manganese in Stabilizing and Destabilizing Soil Organic Matter. *Environmental Science & Technology*, *55*(18), 12136–12152. https://doi.org/10.1021/acs.est.1c00299

42. Ma, D., Wu, J., Yang, P., & Zhu, M. (2020). Coupled Manganese Redox Cycling and Organic Carbon Degradation on Mineral Surfaces. *Environmental Science & Technology*, *54*(14), 8801–8810. https://doi.org/10.1021/acs.est.0c02065

43. Trainer, E. L., Ginder-Vogel, M., & Remucal, C. K. (2021). Selective Reactivity and Oxidation of Dissolved Organic Matter by Manganese Oxides. *Environmental Science & Technology*, *55*(17), 12084–12094. https://doi.org/10.1021/acs.est.1c03972

44. Han, L., Yang, Y., Sun, K., Zhang, B., Chen, Y., Fang, L., & Xing, B. (2021). Different mechanisms driving the preferential adsorption of dissolved organic matter by goethite and montmorillonite. *Chemical Geology*, *585*, 120560. https://doi.org/10.1016/j.chemgeo.2021.120560

45. Roden, E. E., Kappler, A., Bauer, I., Jiang, J., Paul, A., Stoesser, R., Konishi, H., & Xu, H. (2010). Extracellular electron transfer through microbial reduction of solid-phase humic substances. *Nature Geoscience*, *3*(6), 417–421. https://doi.org/10.1038/ngeo870

46. Mirabito, A. J., & Chambers, L. G. (2023). Quantifying mineral-associated organic matter in wetlands as an indicator of the degree of soil carbon protection. *Geoderma*, *430*, 116327. https://doi.org/10.1016/j.geoderma.2023.116327

47. Sollins, P., Kramer, M. G., Swanston, C., Lajtha, K., Filley, T., Aufdenkampe, A. K., Wagai, R., & Bowden, R. D. (2009). Sequential density fractionation across soils of contrasting mineralogy: Evidence for both microbial- and mineral-controlled soil organic matter stabilization. *Biogeochemistry*, *96*(1–3), 209–231. https://doi.org/10.1007/s10533-009-9359-z

48. Joshi, P., Schroth, M. H., & Sander, M. (2021). Redox Properties of Peat Particulate Organic Matter: Quantification of Electron Accepting Capacities and Assessment of Electron Transfer Reversibility. *Journal of Geophysical Research: Biogeosciences*, *126*(8), e2021JG006329. https://doi.org/10.1029/2021JG006329

49. Aeschbacher, M., Sander, M., & Schwarzenbach, R. P. (2010). Novel Electrochemical Approach to Assess the Redox Properties of Humic Substances. *Environmental Science & Technology*, *44*(1), 87–93. https://doi.org/10.1021/es902627p

50. Chen, J., Gu, B., Royer, R., & Burgos, W. (2003). The roles of natural organic matter in chemical and microbial reduction of ferric iron. *The Science of The Total Environment*, *307*(1–3), 167–178. https://doi.org/10.1016/S0048-9697(02)00538-7

51. Wan, X., Xiang, W., Wan, N., Yan, S., Bao, Z., & Wang, Y. (2018). Complexation and reduction of iron by phenolic substances: Implications for transport of dissolved Fe from

peatlands to aquatic ecosystems and global iron cycling. *Chemical Geology*, *498*, 128–138. https://doi.org/10.1016/j.chemgeo.2018.09.019

52. Hemingway, J. D., Rothman, D. H., Grant, K. E., Rosengard, S. Z., Eglinton, T. I., Derry, L. A., & Galy, V. V. (2019). Mineral protection regulates long-term global preservation of natural organic carbon. *Nature*, *570*(7760), 228–231. https://doi.org/10.1038/s41586-019-1280-6

53. Rodríguez-Albarracín, H. S., Demattê, J. A. M., Rosin, N. A., Contreras, A. E. D., Silvero, N. E. Q., Cerri, C. E. P., Mendes, W. D. S., & Tayebi, M. (2023). Potential of soil minerals to sequester soil organic carbon. *Geoderma*, *436*, 116549. https://doi.org/10.1016/j.geoderma.2023.116549

54. Torn, M. S., Trumbore, S. E., Chadwick, O. A., Vitousek, P. M., & Hendricks, D. M. (1997). Mineral control of soil organic carbon storage and turnover. *Nature*, *389*(6647), 170–173. https://doi.org/10.1038/38260

55. Jilling, A., Keiluweit, M., Gutknecht, J. L. M., & Grandy, A. S. (2021). Priming mechanisms providing plants and microbes access to mineral-associated organic matter. *Soil Biology and Biochemistry*, *158*, 108265. https://doi.org/10.1016/j.soilbio.2021.108265

56. Porras, R. C., Hicks Pries, C. E., Torn, M. S., & Nico, P. S. (2018). Synthetic iron (hydr)oxide-glucose associations in subsurface soil: Effects on decomposability of mineral associated carbon. *The Science of the total environment*, *613–614*, 342–351. https://doi.org/10.1016/j.scitotenv.2017.08.290

57. ThomasArrigo, L. K., Vontobel, S., Notini, L., & Nydegger, T. (2023). Coprecipitation with Ferrihydrite Inhibits Mineralization of Glucuronic Acid in an Anoxic Soil. *Environmental Science & Technology*, *57*(25), 9204–9213. https://doi.org/10.1021/acs.est.3c01336

58. Wilson, R. M., Hough, M. A., Verbeke, B. A., Hodgkins, S. B., Chanton, J. P., Saleska, S. D., Rich, V. I., & Tfaily, M. M. (2022). Plant organic matter inputs exert a strong control on soil organic matter decomposition in a thawing permafrost peatland. *The Science of the total environment*, 152757. https://doi.org/10.1016/j.scitotenv.2021.152757

59. Duddleston, K. N., Kinney, M. A., Kiene, R. P., & Hines, M. E. (2002). Anaerobic microbial biogeochemistry in a northern bog: Acetate as a dominant metabolic end product. *Global Biogeochemical Cycles*, *16*(4). https://doi.org/10.1029/2001GB001402

60. Hines, M. E., Duddleston, K. N., Rooney-Varga, J. N., Fields, D., & Chanton, J. P. (2008). Uncoupling of acetate degradation from methane formation in Alaskan wetlands: Connections to vegetation distribution. *Global Biogeochemical Cycles*, *22*(2), 2006GB002903. https://doi.org/10.1029/2006GB002903

61. Woodcroft, B. J., Singleton, C. M., Boyd, J. A., Evans, P. N., Emerson, J. B., Zayed, A. A. F., Hoelzle, R. D., Lamberton, T. O., McCalley, C. K., Hodgkins, S. B., Wilson, R. M., Purvine, S. O., Nicora, C. D., Li, C., Frolking, S., Chanton, J. P., Crill, P. M., Saleska, S. R., Rich, V. I., & Tyson, G. W. (2018). Genome-centric view of carbon processing in thawing permafrost. *Nature*, *560*(7716), 49–54. https://doi.org/10.1038/s41586-018-0338-1

62. Conrad, R. (1999). Contribution of hydrogen to methane production and control of hydrogen concentrations in methanogenic soils and sediments. *FEMS Microbiology Ecology*, *28*(3), 193–202. https://doi.org/10.1111/j.1574-6941.1999.tb00575.x

63. Boetius, A., Ravenschlag, K., Schubert, C. J., Rickert, D., Widdel, F., Gieseke, A., Amann, R., Jørgensen, B. B., Witte, U., & Pfannkuche, O. (2000). A marine microbial consortium apparently mediating anaerobic oxidation of methane. *Nature*, *407*(6804), 623–626. https://doi.org/10.1038/35036572

64. Bar-Or, I., Elvert, M., Eckert, W., Kushmaro, A., Vigderovich, H., Zhu, Q., Ben-Dov, E., & Sivan, O. (2017). Iron-Coupled Anaerobic Oxidation of Methane Performed by a Mixed

Bacterial-Archaeal Community Based on Poorly Reactive Minerals. *Environmental Science & Technology*, *51*(21), 12293–12301. https://doi.org/10.1021/acs.est.7b03126

65. Schorn, S., Graf, J. S., Littmann, S., Hach, P. F., Lavik, G., Speth, D. R., Schubert, C. J., Kuypers, M. M. M., & Milucka, J. (2024). Persistent activity of aerobic methane-oxidizing bacteria in anoxic lake waters due to metabolic versatility. *Nature Communications*, *15*(1), 5293. https://doi.org/10.1038/s41467-024-49602-5

66. Fan, L., Dippold, M. A., Ge, T., Wu, J., Thiel, V., Kuzyakov, Y., & Dorodnikov, M. (2020). Anaerobic oxidation of methane in paddy soil: Role of electron acceptors and fertilization in mitigating CH4 fluxes. *Soil Biology and Biochemistry*, *141*, 107685. https://doi.org/10.1016/j.soilbio.2019.107685

67. Valenzuela, E. I., Prieto-Davó, A., López-Lozano, N. E., Hernández-Eligio, A., Vega-Alvarado, L., Juárez, K., García-González, A. S., López, M. G., & Cervantes, F. J. (2017). Anaerobic Methane Oxidation Driven by Microbial Reduction of Natural Organic Matter in a Tropical Wetland. *Applied and Environmental Microbiology*, *83*(11), e00645-17. https://doi.org/10.1128/AEM.00645-17

68. Vaksmaa, A., Jetten, M. S. M., Ettwig, K. F., & Lüke, C. (2017). McrA primers for the detection and quantification of the anaerobic archaeal methanotroph 'Candidatus Methanoperedens nitroreducens'. *Applied Microbiology and Biotechnology*, *101*(4), 1631–1641. https://doi.org/10.1007/s00253-016-8065-8

Statement of personal contribution

This work was funded by the German Research Foundation (DFG, KA 1736/66-1), with the grant awarded to A. Kappler. The project was initially conceptualized by A. Kappler and C. Bryce. Final experiments were generally designed by A. Kappler, P. Joshi, C. Bryce (in early stages of the work), and myself. Data acquisition was performed by myself in collaboration with P. Schmitt-Kopplin, L. ThomasArrigo, J. Kilian, D. Straub, M. Friedel and, M. Bottaro. The resulting data was formally analyzed by A. Kappler, P. Joshi, M. Friedel and myself in collaboration with P. Schmitt-Kopplin, ThomasArrigo, J. Kilian, D. Straub, and M. Stahl. Visualization of the data and writing of the original manuscripts was done by myself. Detailed contributions per chapter are as follows:

Chapter 2: The study was conceptualized by A. Kappler, C. Bryce, P. Joshi and myself. A. Kappler acquired the funding. The methodology was designed by P. Schmitt-Kopplin, A. Kappler, P. Joshi and myself. I collected the samples and performed the experiments. The resulting data was formally analyzed by myself, P. Schmitt-Kopplin (regarding FT-ICR-MS data), L. ThomasArrigo and P. Joshi (regarding synchrotron spectra). Resources regarding access to synchrotron beamtime were provided by L. ThomasArrigo and P. Joshi. Visualization of the data and writing of the original draft of the manuscript was performed by me. Supervision was provided by P. Joshi and A. Kappler. All authors contributed to the review and editing of the final manuscript.

Chapter 3: The study was conceptualized by A. Kappler, P. Joshi and myself. A. Kappler acquired the funding. The experiments were designed by A. Kappler, P. Joshi and myself. I performed the experiments. D. Straub and myself formally analyzed the 16S rRNA amplicon sequencing data. M. Friedel collected samples from the field campaign and formally analyzed geochemical parameters. The GC-MS data was acquired by J. Kilian and analyzed by J. Kilian and M. Stahl and myself. L. ThomasArrigo, P. Joshi and myself analyzed the synchrotron spectra. Visualization of the data and writing of the original draft of the manuscript was performed by myself. Supervision was provided by P. Joshi and A. Kappler. All authors contributed to the review and editing of the final manuscript.

Chapter 4: The study was conceptualized by A. Kappler, P. Joshi and myself. A. Kappler acquired the funding. The experiments were designed by A. Kappler, P. Joshi and myself. F. Ring-Hrubesh and C. Bryce contributed towards the experiment design regarding the field

experiment. I performed the experiments. M. Bottaro measured the samples for ICP-MS and contributed to the data analysis. D. Straub and myself formally analyzed the 16S rRNA amplicon sequencing data. The GC-MS data was acquired by J. Kilian and formally analyzed by J. Kilian and M. Stahl and myself. L. ThomasArrigo, P. Joshi and myself analyzed the synchrotron spectra. Visualization of the data and writing of the original draft of the manuscript was performed by myself. Supervision was provided by P. Joshi and A. Kappler. All authors contributed to the review and editing of the final manuscript.

I hereby state that I have not plagiarized or copied any text. Chapter 3 and 4 are still in the publication process, such that final published versions of the manuscripts may slightly differ from the versions in this thesis.

Without his help, designing and constructing them would have been a more difficult process. But I especially appreciate the fun conversations we had during the field campaign, specifically his story about the aggressive, territorial "bog chicken" at his field site. I will for sure remember this story for years to come.

Thank you also to the whole Abisko Research Station team, specifically Jennie Wikström, Emily Pederson, Erik Lundin, and Niklas Rakos who helped to coordinate the three field campaigns that I was a part of. They were a massive help during the "great dry ice shortage" of September 2022, when our scheduled delivery of dry ice would have arrived too late for us to store our samples permanently frozen during the trip home. So they organized another pick-up of dry ice in Kiruna, just so that we had it in time. They really saved the day!

A major thanks goes to the entire "Permafrosties" team: Ankita Chauhan, Katrin Wunsch, Anne Eberle, and Marie Mollenkopf, along with many Master and Bachelor students over the years. Being part of a group of PhD students who all research various processes across permafrost thaw at the same field site was a unique experience. It was so encouraging to be able to toss ideas around within a team meeting, get feedback on experimental outlines or just discuss which field sampling techniques would work and which would probably fail. I will never forget our sampling campaigns in summer 2022: We had cake underneath moskito hats in the field for Marie's birthday, had nerdy discussions about which element we would be, watched the polar lights at the dock by the lake, and got celebratory hot chocolate in the tourist station when the final sampling plans were done.

Thank you also to all the students that contributed to my PhD project within their Bachelor thesis or as assistants in the lab: Kari Kaphegyi, Hayley Green, Maike Friedel, Simon Ferlein, Aaron Arneke, and Simon Schad. I am grateful for all the help they provided and am very happy that some of them continued doing research in Arctic environments. It was a joy to supervise them and I am looking forward to all their future findings!

Of course, I also want to thank the entire members of the Geomicrobiology group, starting with the lab technicians: Franziska Schädel, Lars Grimm and Ellen Röhm. When I first joined this group, I was amazed at the thorough organization in the lab and I later realized that this was due to their hard work. Thank you also goes to all the former members of the group who gave me great advice or just showed me how to navigate the lab during my early times in the PhD: Christopher Schwerdhelm, Anh van Le, Natalia Jakus, Verena Nikeleit, Ulf Lüder, Markus Maisch, Yuge Bai, Monique Patzner, Lea Sauter, and Sören Drabesch. They created a great atmosphere in the group that I felt really welcomed in.

Thank you also to all the current members in the group who supported me in all various of ways: by helping me analyze my samples, giving me advice on certain techniques, repairing